

Assessment of the dynamic response of a floating pontoon bridge with a fiber reinforced polymer superstructure

C.E.M. Heuberger



Assessment of the dynamic response of a floating pontoon bridge with a fiber reinforced polymer superstructure

by

C.E.M. Heuberger

to obtain the degree of Master of Science
in Civil Engineering - Hydraulic Engineering
at the Delft University of Technology

to be defended publicly on Thursday July 5, 2018 at 10:30 a.m.

Student number: 4166272
Project duration: September 2017 - July 2018
Thesis committee: Prof. Dr. Ir. S.N. Jonkman Delft University of Technology
Dr. Ir. D.J. Peters Delft University of Technology & Royal HaskoningDHV
Dr. Ir. A. Jarquin Laguna Delft University of Technology
Ir. E. Tromp Royal HaskoningDHV
Ir. Y. Wang Royal HaskoningDHV

Cover photo by S. Hansen, *Bergsøysundbrua*

An electronic version of this thesis is available at <http://repository.tudelft.nl/>.

Preface

This thesis is the final part of my master program of Hydraulic Engineering at Delft University of Technology. My thesis is titled: "Assessment of the dynamic response of a floating pontoon bridge with a fiber reinforced polymer superstructure". Royal HaskoningDHV offered me the opportunity to work on this subject, for which I am very grateful. They provided me with the means and the motivation to complete this research.

Many people assisted me during the process of writing this thesis. Without their help, this report would not be lying in front of you. First and foremost I would like to express my gratitude towards my graduation committee. I would like to thank Bas Jonkman for chairing the committee. Your feedback and guidance during the meetings proved very helpful. Second, I want to thank Dirk Jan Peters for sharing his expertise in both hydraulic and structural engineering. Although it was sometimes difficult to my squeeze meetings in your busy schedule, you always managed to understand my problems within minutes and provided me with useful feedback as well. Third, I was very happy to have Antonio Jarquin Laguna in my committee. You always asked the right questions and helped me a great deal with my problems concerning dynamics. I want to thank Liesbeth Tromp for her enthusiasm around my thesis and her expertise regarding fiber reinforced polymers. Last but not least I want to thank Yijun Wang, who was a great support during my thesis. Besides your expertise and brilliant ability to explain the secrets behind hydrodynamics, I would like to thank you for our discussions and laughs at the office.

Besides my committee members, I want to thank all my colleagues at Royal HaskoningDHV for their interest and help with my research. I want to name two specific colleagues who always wanted to discuss and brainstorm about my thesis. Job Kramers and Ben Edmondson, thank you for your help and for making my time at the company much more enjoyable. Furthermore, I would like to thank Øyvind Wiig Petersen, a PhD candidate at NTNU, who provided me with the data of the Bergsøysund bridge and always answered my questions about this bridge.

Last, I would like to thank my family and friends for their support during this journey. Especially Carla, for coping with all of my struggles and for always being there for me.

*C.E.M. Heuberger
Delft, july 2018*

Abstract

Floating bridges are found at locations where deep water must be crossed for a long distance, such as in Norwegian fjords. The Norwegian government plans to make the European highway E39 ferry free by crossing the eight remaining fjords. The superstructure of the existing floating bridges is usually constructed from steel. In a marine environment these bridges are exposed to dynamic wave loads. As such, the current floating bridges suffer severe damage due to corrosion and fatigue. Using fiber reinforced polymer instead of steel could alleviate these phenomena and reduce maintenance costs. However, the lower stiffness could cause undesired vibrations in the floating bridge. Therefore a parametric model is developed to investigate the influence of design parameters on the dynamic response of a floating pontoon bridge.

A literature study is performed to find suitable concepts and techniques to develop the floating bridge model. The wave conditions around a floating bridge can be represented by a wave spectrum. A floating pontoon bridge can be schematized with rigid bodies, Euler-Bernoulli beam elements and linear springs and dashpots. The fluid-structure interaction is taken into account by including the added mass, hydrodynamic damping, hydrostatic stiffness and wave force transfer functions of the pontoons. These are computed by solving linear potential functions. A frequency domain approach is used to compute the dynamic response, because it is more convenient to include the hydrodynamic components than in a time domain analysis. This means that the floating bridge model transforms a wave spectrum into a response spectrum, which is used to obtain statistical information about the dynamic response at every node in every degree of freedom.

A parametric model of a floating pontoon bridge to predict the dynamic response is developed in Python. The hydrodynamic properties of the pontoons are computed by Diffrac and are used as input for the Python model. The Bergsøysund bridge is used as a reference case, because measurement data of this bridge's dynamic response is available and can be used for validation. To model the Bergsøysund bridge three important assumptions are made. First, only the governing wave direction is taken into account. Second, the curved alignment is assumed to be straight. Last, the continuous superstructure is modeled with separate beam elements which are connected through the pontoons.

The geometrical and structural properties of the Bergsøysund bridge are used to model its dynamic response. Wave conditions with a peak frequency at 2 rad/s are used. The results show that the response of the pontoons is governing compared to the response of the superstructure and that the dominant degree of freedom is sway. The fourth sway mode is the main contributor to this dynamic response. A comparison with measurement data shows that the produced response spectra are in good agreement with the measurements in terms of the peak locations. The magnitude deviates in the order of $1 \cdot 10^1$.

In the parametric study the influence of single design parameters on the dynamic response of a floating bridge is investigated independently. The results show that the length of the superstructure has the biggest influence on the dynamic response of the floating bridge. The structural damping of the superstructure and the distance between the pontoons which influences the hydrodynamic interaction have the smallest influence on the dynamic response of the floating bridge. In general, a reduction in stiffness in the superstructure leads to a lower overall frequency response function and thus to a lower dynamic response. Increasing the stiffness or reducing the mass of the bridge shifts the eigenfrequency of the fourth sway mode to a higher frequency and vice versa. Finally, when the damping is increased, the peaks in the frequency response function decrease and thereby the dynamic response in resonance reduces.

In conclusion, the dynamic response of a floating end-supported pontoon bridge is mainly influenced by the stiffness of the superstructure. A fiber reinforced polymer superstructure should be designed sufficiently stiff, especially in lateral direction, to keep the overall frequency response function low enough. Additionally, resonance peaks can be avoided by modifying the superstructure's stiffness and the dimensions of the pontoons.

Contents

List of symbols	ix
List of Latin symbols	ix
List of Greek symbols	x
List of abbreviations	xi
List of notations	xi
1 Introduction	1
1.1 Problem statement	3
1.2 Research objective and question	3
1.3 Scope & Approach	4
1.4 Outline	4
I Literature review	6
2 Floating bridges	7
2.1 Development of floating bridges	7
2.2 Fiber Reinforced Polymer	9
2.3 Design criteria of floating bridges	10
2.4 Coordinate system	11
2.5 Conclusion	11
3 Ocean waves	13
3.1 Description of ocean waves	13
3.2 Wave spectrum	14
3.3 Conclusion	16
4 Multibody dynamics of a floating bridge	17
4.1 Equations of motion	17
4.2 Frequency domain analysis	22
4.3 Finite Element Method: beam elements	26
4.4 Conclusion	27
5 Hydromechanics of a pontoon	29
5.1 Hydrostatics of a pontoon.	29
5.2 Hydrodynamics of a pontoon	30
5.3 Conclusion	32
6 Bergsøysund bridge	33
6.1 Location of the bridge.	33
6.2 Structural and geometrical parameters	34
6.3 Load cases	38
6.4 Measurement data	39
6.5 Conclusion	40
II Model development	42
7 Pontoon model	43
7.1 Pontoon model set-up	43
7.2 Assumptions of the pontoon model.	45

8 Floating bridge model	47
8.1 Model set-up	48
8.2 Three-dimensional model	51
8.3 Assumptions of the floating bridge model.	53
III Validation	56
9 Modeling results of the Bergsøysund bridge	57
9.1 Results pontoon model	57
9.2 Results floating bridge model	60
9.3 Conclusion	64
10 Validation	67
10.1 Validation of the pontoon model	67
10.2 Validation of the superstructure.	69
10.3 Validation measurement data.	70
10.4 Validation & discussion of the assumptions	71
10.5 Conclusion	72
IV Parametric study	74
11 Parametric study	75
11.1 Results	76
11.2 Conclusion	83
12 Applications for design	85
12.1 Assumptions for design	86
12.2 Design of the FRP alternative	87
12.3 Assessment method.	88
12.4 Results	89
12.5 Conclusion	90
V Conclusion	92
13 Conclusion, discussion and recommendations	93
13.1 Conclusion	93
13.2 Discussion	96
13.3 Recommendations	97
Bibliography	99
VI Appendices	103
A Bergsøysund bridge	105
B Structural dynamics	111
C Linear wave theory	115
D Potential flow theory	119
E Fiber reinforced polymers	127
F Model development	133
G FRP alternative	145

List of symbols

List of Latin symbols

Symbol	Description	Units
A	Surface area	m^2
A_{wl}	Submerged surface area	m^2
\overline{BM}	Distance between the center of buoyancy and the metacenter	m
$E_{\eta\eta}$	Wave energy density spectrum	$kg s^{-2} rad^{-1}$
E	Young's modulus	N/m^2
F	Force	N
F_d	Diffraction wave force	N
F_r	Hydrodynamic radiation force	N
F_s	Hydrostatic wave force	N
F_w	Froude-Krilov wave force	N
\overline{GM}	Distance between the center of gravity and the metacenter	m
$H_{1/3}$	Significant wave height	m
H_p	Height of the pontoon	m
$H_{\eta,F}$	Transfer function between wave elevation and wave force	kg/s^2
$H_{F,w}$	Transfer function between force and reponse	s^2/kg
$H_{k,j}$	Transfer function between quantities k and j	-
H_j	j^{th} wave height	m
H	Wave height	m
\mathbf{I}	Identity matrix	-
I	Second moment of area	m^4
K_p	Stiffness matrix of the pontoon	N/m
\overline{KB}	Distance between the bottom and the center of buoyancy	m
\overline{KG}	Distance between the bottom and the center of gravity	m
L_p	Length of the pontoon along the x axis	m
L_s	Length of the superstructure along the x axis	m
M_p	Mass matrix of the pontoon	kg
M_s	Mass of the superstructure	kg
M	Moment	Nm
N	Number of waves	-
P	Probability of exceedance	s^{-1}
Ψ	Time dependent part of the displacement equation	m
$S_{\eta\eta}$	Variance density spectrum of the wave elevation, or wave spectrum	$m^2 s / rad$
T	Wave period	s
T	Life time	y
T_0	Zero crossing wave period	s
V	Shear force	N
W	Space dependent part of the displacement equation	m
W_p	Width of the pontoon along the y axis	m
a_{kj}	Added mass in direction k due to displacement in direction j	kg
a_i	i^{th} amplitude of the surface elevation	m
a	Amplitude of the surface elevation	m
a	Multiplication factor of the standard deviation used in dynamic analysis	-
b_{kj}	Added damping in direction k due to displacement in direction j	Ns/m
c	Damping	Ns/m
c_{kj}	Hydrostatic stiffness in direction k due to displacement in direction j	N/m

Symbol	Description	Units
f	Force vector	N
g	Gravitational acceleration	m/s ²
k	Spring stiffness	N/m
k_w	Wave number	m ⁻¹
m	Mass	kg
m_n	Spectral moment	-
p	rotation around the x axis (roll)	rad
q	Rotation around the y axis (pitch)	rad
r	Rotation around the z axis (yaw)	rad
s_n	Characteristic exponent	-
t	Time	s
u	Displacement in the x direction (surge)	m
u_x	Particle velocity in x direction	m/s
u_y	Particle velocity in y direction	m/s
u_z	Particle velocity in z direction	m/s
v	Displacement in the y direction (sway)	m
w	Displacement in the z direction (heave)	m
x_h	Homogeneous solution	m
x_p	Particular solution	m

List of Greek symbols

Symbol	Description	Units
Φ	Velocity potential	m ² /s
α_w	Shape factor	-
α	Rayleigh damping constant	-
β_d	Reliability index	-
β_w	Reduction factor for deformation check	-
β	Rayleigh damping constant	-
$\epsilon_{\eta,F}$	Phase shift between the wave elevation and the wave force	rad
$\epsilon_{\eta,w}$	Phase shift between the wave elevation and the response of the structure	rad
ϵ_{η}	Random phase angle of the wave elevation	rad
$\epsilon_{F,\eta}$	Phase shift between the wave force and the wave elevation	rad
$\epsilon_{F,w}$	Phase shift between the wave force and the response of the structure	rad
$\epsilon_{w,F}$	Phase shift between the response of the structure and the radiation force	rad
ϵ	Phase difference	rad
η	Surface elevation	m
γ^r	Peak enhancement function	-
λ	Eigenvalue	-
μ_w	Mean value of heave	m
μ	Mean value	-
ω_i	i^{th} eigenfrequency	rad/s
ω	Angular frequency	rad/s
ω_0	Dominant radial frequency	rad/s
ω_n	Angular eigenfrequency	rad/s
ϕ	Rotational angle around the x axis	rad
ϕ_i	i^{th} eigenvector	-
ψ	Rotational angle around the z axis	rad
ρ	Density	kg/m ³
σ_w	Standard deviation of heave	m
σ	Standard deviation	-
∇	Submerged volume	m ³
ζ	Damping ratio	-

List of abbreviations

Symbol	Description
CFRP	Carbon Fibre Reinforced Polymer
CoG	Center of Gravity
DOF	Degree Of Freedom
EOM	Equation Of Motion
FE	Finite Element
FEM	Finite Element Method
FRF	Frequency Response Function
FRP	Fibre Reinforced Polymer
GFRP	Glass Fibre Reinforced Polymer
MDOF	Multiple Degree Of Freedom
RAO	Response Amplitude Operator
SLS	Serviceability Limit State
UD	Unidirectional
ULS	Ultimate Limit State

List of notations

Symbol	Description
\mathbf{X}	Matrix
x^*	Complex conjugate
\dot{x}	Derivative
\hat{x}	Amplitude
\bar{x}	Complex amplitude
\mathbf{x}	Vector

Introduction

The coastal highway E39 in Norway is part of the European trunk road system. In Norway this road runs from Trondheim to Kristiansand, a distance of 1100 km (figure 1.1). At the moment there are eight ferry connections in this route crossing wide and deep fjords. Because of these ferry connections the total travel time from Trondheim to Kristiansand is approximately 22 hours. The Norwegian government has initiated a research to develop the route into a more efficient corridor without ferry connections. Removing the ferry connections is expected to reduce the travel time by approximately 8 hours. The total costs of the project are estimated at 35 billion euros. The E39 project will study the possibilities and required technologies for the remaining fjord crossings.

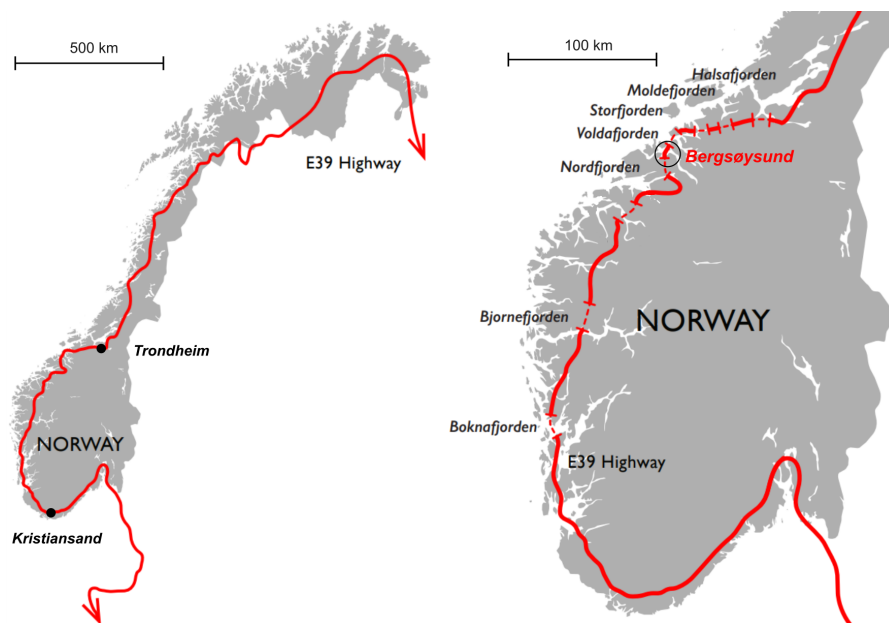


Figure 1.1: Coastal highway route E39 (Visser et al., 2017)

Suspension bridges and subsea tunnels are conventional solutions, but they are very expensive. An innovative solution is a submerged floating tunnel. However, this concept is still under development. One other alternative is already proven and used all over the world; floating bridges. Harsh environmental conditions introduce all kinds of dynamic loads such as waves, wind and currents on top of the traffic loads. As a result, fatigue and corrosion are major concerns in the design of these bridges.

A floating bridge becomes economically attractive compared to a conventional fixed bridge when the water depth increases. A floating bridge at a site with a water depth around 60 m is estimated to cost 3 to 5 times less than a fixed bridge according to W.F. Chen (2014). A floating bridge does not require a fixed foundation to support the dead weight and live loads, because these are compensated by the buoyancy force.

However, a mooring or structural system is required to preserve the longitudinal alignment and to restrain transverse displacements caused by environmental conditions.

Existing floating bridges are constructed from steel and concrete. The pontoons are often constructed with concrete and the superstructure usually consists of steel. The pontoons are generally simple floating structures with a rectangular box or cylindrical shape.

Different types of superstructures are possible such as a truss or girder structure (figure 1.2). In general, attention should be paid to fatigue, corrosion and brittle failure. Steel requires extensive maintenance against corrosion in a marine environment. The Bergsøysund bridge, one of the largest existing floating bridges, requires maintenance every twenty years to renovate the painting, which protects the steel against corrosion. The estimated costs of this maintenance procedure are 7,5 million euros (Ellevset, O., 2014a). On top of this, parts of the supports had to be replaced due to unexpected fatigue failure (Petersen et al., 2018).



(a) Truss superstructure, Bergsøysund bridge (Petersen et al., 2018).



(b) Girder superstructure, Nord-Hordland bridge (Dagrun Stokke, 2011).

Figure 1.2: Different types of steel superstructures.

A potential solution to account for these problems could be using fiber reinforced polymers (FRP) in the superstructure of a floating bridge. FRP is a composite consisting of fibers and a polymer resin (figure 1.3). One main advantage of this material is that the exact properties of an FRP structure depends on the arrangement of the elements and can be manipulated during fabrication. In general, FRP has advantages and drawbacks compared to other conventional construction materials. Especially the light weight, high durability and high fatigue resistance are advantageous properties for a floating bridge in a marine environment.

Main advantages of FRP

1. Light weight
2. High durability
3. Many potential shapes
4. Modifiable properties
5. High fatigue resistance
6. High chemical resistance

Main drawbacks of FRP

1. High material costs
2. Little experience in infrastructure
3. Complex details
4. Low stiffness
5. Complex modeling

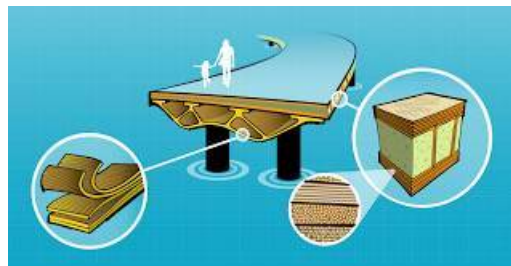


Figure 1.3: Schematization of a bridge with an FRP superstructure (Pavlovic, M., 2018).

1.1. Problem statement

Existing floating bridges show that a steel superstructure suffers severe damage due to corrosion in a marine environment (Ellevset, O., 2014a) and that fatigue damage is difficult to predict (Petersen et al., 2018).

Corrosion and fatigue problems drive the search for an alternative material choice. The use of FRP in the superstructure can solve the mentioned issues, because of its relatively long fatigue lifetime and high chemical resistance. However, the stiffness of FRP is lower than of steel. This might cause undesired vibrations in a floating bridge and limits the span between pontoons. Literature about the dynamic response of floating bridges became available in the past decades (Watanabe and Utsunomiya), (Yoneyama et al., 1997), (Kvåle and Øiseth, 2017). Additionally, a lot of research has been carried out into the use of FRP in civil infrastructure such as bridges (Rizkalla et al., 2006). However, to the knowledge of the author, no references are available about the effect of an FRP superstructure on the dynamic response of a floating bridge. Therefore it is desired to carry out research into the dynamic behaviour of a floating bridge with an FRP superstructure.

Research on the dynamic behaviour of floating bridges is currently mainly performed with Finite Element (FE) software, such as ABAQUS or DIANA FEA (Kvåle et al., 2016), and focuses mainly on one single detailed design instead of multiple alternatives. The composition of an FRP structure is very complex due to the varying properties of different laminates. It is therefore difficult to include this material in FE models. Furthermore, a FE model is usually not parametric. Many FE models with different geometries would be required to perform a parameter study. Hence, it is desirable to provide a parametric model to investigate the influence of different parameters on the dynamic behaviour of a floating bridge.

1.2. Research objective and question

A research objective is formulated to express the external aim of this thesis. To meet the objective, research questions are defined. The research questions represent the internal aim of the thesis.

1.2.1. Research objective

The objective of this research is to contribute to the knowledge about the potential of fiber reinforced polymer to enhance a design of a floating bridge.

1.2.2. Research question

Three main research questions are formulated to meet the research objective.

1. *How can the dynamic response of a floating end-supported pontoon bridge with a continuous superstructure be modeled?*
2. *Which parameters can be used to reduce the dynamic response of a floating end-supported pontoon bridge?*
3. *How would the differences between fiber reinforced polymer and steel affect the dynamic response of a floating end-supported pontoon bridge?*

1.2.3. Subquestions

To be able to answer the research questions, several sub-questions are formulated:

Literature review

- *What is an appropriate method to schematize a floating structure in order to model the dynamic response?*
- *Which solution technique is suitable to analyze the dynamic response of a multibody floating structure?*
- *How can the fluid-structure interaction between pontoons and waves be modeled?*
- *How can the interaction between the motions of the different pontoons be included in the model?*

Validation

- *Which degree(s) of freedom dominate(s) the dynamic response of the Bergsøysund bridge?*

- Which mode shape(s) of the Bergsøysund bridge dominate(s) the dynamic response at the governing degree of freedom?
- To what extent do the modeling results agree with measurements from the Bergsøysund bridge?

Parametric study

- Which geometrical and structural design parameters influence the dynamic response of a floating bridge?
- How do these parameters influence the dynamic response of a floating bridge?

1.3. Scope & Approach

- This thesis focuses on the technical aspects of floating pontoon bridges. Economical and durability aspects are mentioned, but will not be considered in detail.
- The scope of this research lies on the application of floating bridges in Norway. The combination of fjord formations and the desire to improve infrastructure, make Norway a relevant country to apply this technique. Therefore Norwegian environmental conditions are taken into account.
- This research focuses on floating end-supported separate pontoon bridges. This means that continuous pontoons bridges are not taken into account in this research. The latter type of floating bridge is not suited for Norwegian marine conditions, due to the significant wave loads. Furthermore, it means that mooring facilities are not taken into account. Norwegian fjords are often too deep for mooring facilities to become cost efficient.
- A truss bridge is the only type of bridge structure which is taken into account in the dynamic model. Truss bridges are economical to construct, because of the efficient use of material. The simple design of a truss structure allows to model it as a single beam element with generic structural properties. Although a truss bridge is the only bridge type that is taken into account in the model, still relevant results can be obtained to provide valuable conclusions for other bridge types such as girder and arch bridges.
- A parametric model is created to describe the dynamic response of a floating bridge. A floating bridge is schematized using rigid bodies, Euler Bernoulli beam elements, linear springs and linear dashpots.
- Only light weight concrete pontoons are used in the model, based on existing designs. The superstructure is modeled with steel or FRP properties.
- A frequency domain approach will be used to model the dynamic response of a floating bridge. The main reason for this is that it is more convenient to take the frequency dependent properties such as the added mass and hydrodynamic damping into account in a frequency domain approach compared to a time domain approach.
- Assessment of the dynamic response is based on serviceability limit state deflection criteria. These criteria are assumed to be governing for a floating end supported pontoon bridge with an FRP superstructure. Ultimate limit state criteria will only be evaluated in a case study.

1.4. Outline

First a literature review is presented where floating bridges are introduced and all required theory to develop a dynamic model of a floating bridge is explained. The theory is divided into three different chapters. Chapter 3 explains the basic principles of ocean waves, which constitutes the main excitation source of a floating bridge. Subsequently, chapter 4 explains the most important concepts of structural dynamics and finite element modeling. Finally, chapter 5 elaborates the hydromechanic behaviour of floating structures. Additionally, the case study of the Bergsøysund bridge is introduced.

In the second part, the model development is addressed. First, chapter 7 describes the hydrodynamic analysis of a pontoon. Subsequently, chapter 8 elaborates upon the development of the floating bridge model. Only the final model is presented here, but references are made to the other models in the appendices.

The third part describes the validation of the model. First the results of both the pontoon model and the floating bridge model are presented in chapter 9. The results are explained using physical principles and conclusions are drawn. Lastly, chapter 10 validates the pontoon model and the floating bridge model with results of research and measurement data.

Part four discusses the parameter study. The influence of different bridge spans, pontoon dimensions and truss designs in both steel and FRP is investigated. One design is described in detail to provide the relation between the developed model and an actual design. Finally, the conclusions, a discussion and recommendations are presented. The outline of this report is illustrated in figure 1.4.

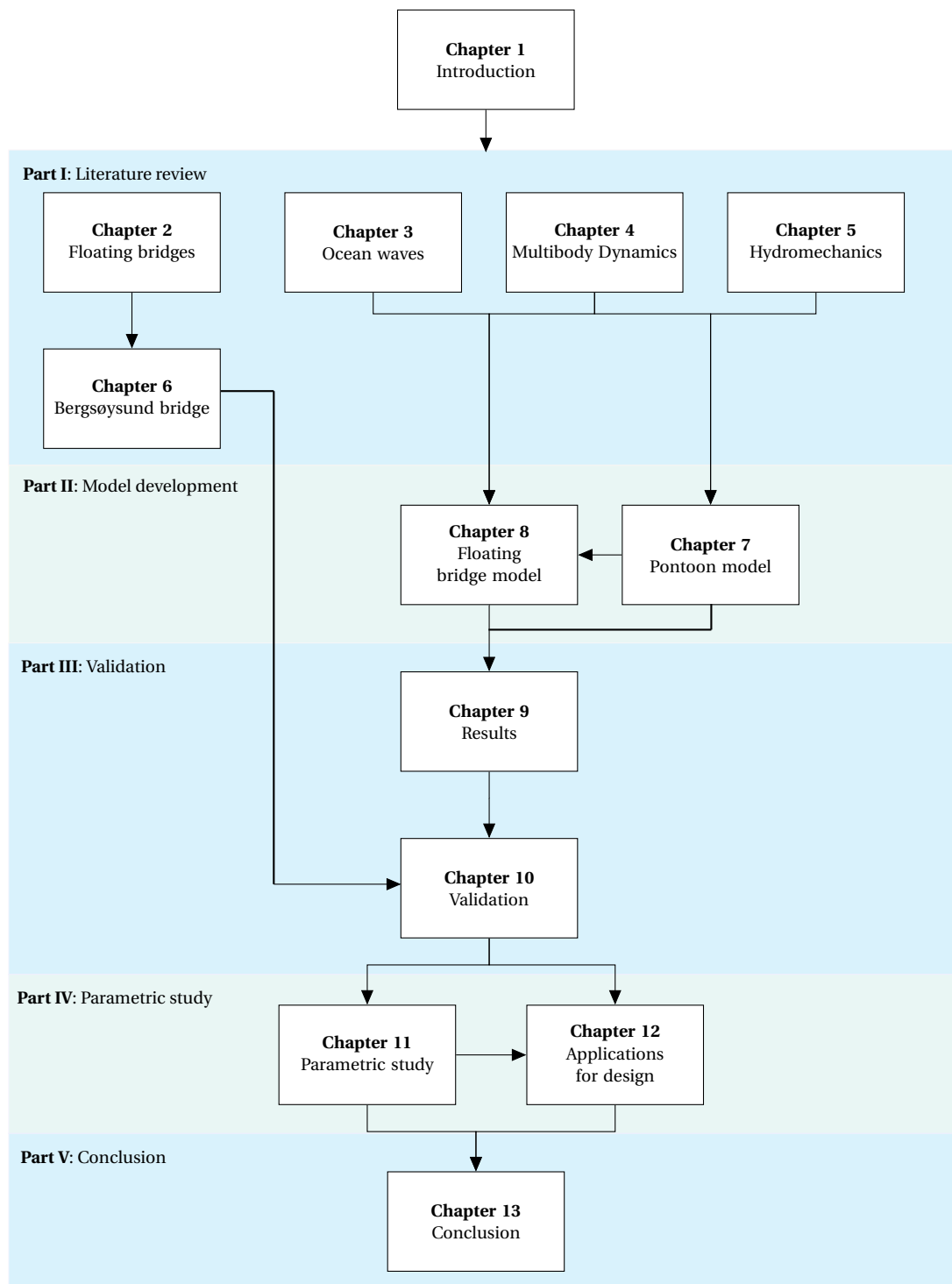


Figure 1.4: Outline of the report.

I

Literature review

2

Floating bridges

This chapter describes the state-of-the-art developments regarding floating bridges and FRP to put this research into perspective. Section 2.1 addresses the development of floating bridges. The most important challenges in the design of floating bridges and the used construction materials are discussed here. The material FRP will be elaborated upon in more detail in section 2.2. Subsequently, the design criteria of floating bridges are presented (section 2.3) and the coordinate system is explained (section 2.4).

2.1. Development of floating bridges

Floating bridges date back to ancient history and were mainly used for military purposes. The first floating bridges date back to 2000 BC and were most likely boat bridges (Watanabe and Utsunomiya). The first wooden pontoon bridge with a total length of 124 m was built in 1874 across the Mississippi River. In 1912, a steel floating bridge was constructed across the Golden Horn with a total length of 457 m. The first floating bridge using concrete pontoon girders appeared in 1940 in Washington with a length of 2018 m.

The most important design challenges of floating bridges are the environmental conditions: wave, wind, current and tidal conditions. These loads must be transferred either to the seabed or the abutments on land without resulting in unacceptable vibrations of the structure. With the knowledge on the hydrodynamic behaviour of floating structures increasing, designs have improved significantly in the last years. However, engineers still face many challenges in the design of floating bridges these days.

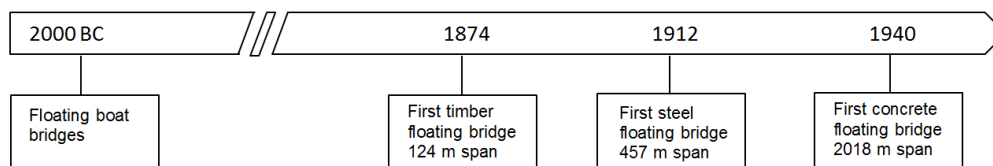
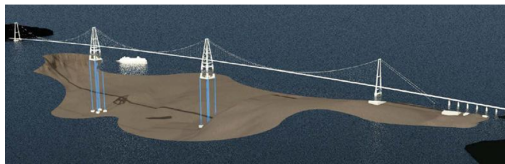


Figure 2.1: Timeline of the history of floating bridges.

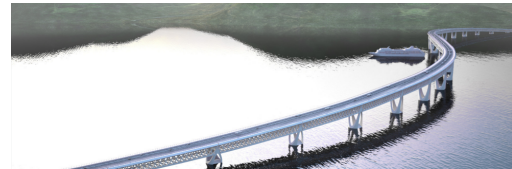
There are currently over 50 operational floating bridges, of which only six with a total span over a kilometer (Yip, 2015). The amount of research performed on the dynamic behaviour of these floating bridges is growing with the plans of the E39 in Norway. However, there is limited experimental data available. The only full scale measurements were obtained in an experiment at the Bergsøysund bridge (Figure 1.2a).

In 2013 feasibility studies to cross the Sognefjord and the Bjornafjord, with distances over 3 km, were published (figure 2.2). Techniques from floating structures in the offshore industry were introduced in these feasibility studies (Jakobsen, 2013).

In 2014 the Norwegian government initiated a R&D program at NTNU with 8 PhD studies researching different aspects of the technological challenges of the E39 project such as the dynamic behaviour of a floating Tension Leg Platform (TLP) suspension bridge and load identification of floating bridges (Petersen et al., 2017). In 2017 IV-consult presented a design of a floating bridge based on a spar system with a truss superstructure with enough freeboard to allow large vessels to pass (figure 2.2b).



(a) Crossing of the Bjornafjorden (Ellevset, O., 2014b).



(b) Crossing of the Sognjefjords (Visser et al., 2017).

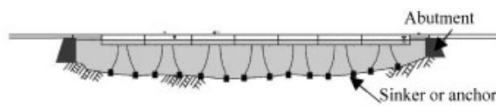
Figure 2.2: Artist impressions of feasibility studies of floating bridges.

2.1.1. Continuous and separate pontoon bridges

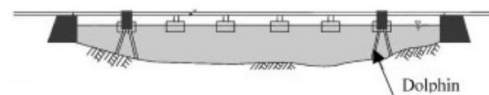
Pontoon is a general term for a floating structure, often with a simple cubical or cylindrical shape. Two main types of operational pontoon bridges exist today: continuous pontoon bridges (figure 2.3a) and separate pontoon bridges (figure 2.3b). The difference between these two types of bridges is whether there is a span between these pontoon to be crossed by a superstructure.

The lateral movements, caused by environmental loads, can be restricted by a stiff superstructure or through a mooring system. A continuous pontoon system has the advantage that a separate superstructure is not necessarily required. However, the costs of this type of bridge are usually higher due to the number of required pontoons. Another disadvantage of this type of floating bridge is that a larger part of the bridge is subjected to wave loads. Therefore this type of bridge is usually combined with horizontal support through mooring.

As such, separate pontoon bridges are often financially more attractive than continuous pontoon bridges. Separated pontoon bridges can be found in Norway crossing fjords. Continuous pontoon bridges are found in the US crossing calm rivers and lakes.



(a) Continuous pontoon bridge.



(b) Separate pontoon bridge.

Figure 2.3: Different types of floating bridges (Watanabe and Utsunomiya).

2.1.2. Navigability

A major challenge in the design of floating bridges is facilitating navigability for ships. Continuous pontoon bridges are impossible to pass for ships. For a separated pontoon bridge, the height of the fairway clearance is the major obstacle. Figure 2.4 shows two separated pontoon bridges allowing ships to pass. A part of the Nord-Hordland bridge exists of a fixed cable stayed bridge to reach the required clearance height. The Yumemai Bridge uses a swinging mechanism to rotate around its axis to allow ships to pass. These two types of floating bridges are currently the only types of operational floating bridges that allow large vessels to pass.



(a) Nord-Hordland bridge, partially fixed and partially floating (Stensvold, B. and Minoretta, A., 2014).



(b) Yumemai Bridge, with a floating movable part (KDC, 1999).

Figure 2.4: Separated pontoon bridges allowing navigation.

2.1.3. Potential floating bridge sites

The presence of fjords is the main reason that floating bridges are most relevant in Norway. Figure 1.1 shows the eight remaining ferry connections in the E39. All these locations are potential sites to construct a floating bridge, because of the combination of a span over a kilometer and a water depth over 500 m (Ellevset, 2012). Most of these sites are sheltered from waves from the open sea such as the Bergsøsund bridge. This means that the influence of swell waves is negligible and local wind waves dominate the wave conditions. Wave conditions in these eight fjords with a return period of 1 year have peak periods ranging from 3 s at the Bergsøsund bridge (Kvåle and Øiseth, 2017) to 6 s at the Bjørnafjorden (Jakobsen, 2017).

2.1.4. Materials

The most common construction materials used in a floating bridge are steel and concrete. In the past timber was also used, but currently pontoons are constructed with concrete and the superstructure consists of steel.

Concrete elements have proven to be suited for extreme environmental conditions in the offshore industry (Moe, 1997). One of the major advantages of concrete is its durability in water. The increase in the strength of concrete throughout the years was the main contributor to the developments of the material in floating structures.

Steel performs better in the superstructure, because in this part environmental loads cause large bending moments and displacements. The high strength and elasticity of steel are beneficial under these conditions.

FRP's light weight, high durability and high fatigue resistance are advantageous considering the design of a floating bridge. However, the properties of FRP depend on the arrangement of the elements, which makes it more complex. As such, there is a need to analyze this material in more detail.

2.2. Fiber Reinforced Polymer

FRP is a composite consisting of fibers and a polymer resin. The fibers determine the load bearing capacity of the structure, whereas the resin connects the fibers and determines the geometry of the structure. Furthermore, the resin transfers the loads between the fibers and enables them to work together. Therefore, the properties of an FRP structure depend completely on the type of fibers, type of polymer and the composition of the structure. The most common types of fiber are glass and carbon fibers. Glass fiber reinforced polymers (GFRP) is less expensive, but has also a lower strength and stiffness compared to carbon fiber reinforced polymers (CFRP).

Generally an FRP element exists of laminates. These laminates consist of different plies, layers with a specific thickness, fiber ratio and fiber orientation (figure 2.5). The fibers within a ply can be oriented in different directions. A distinction between plies is made based on this orientation. A ply with a single fiber orientation is called an UD-ply (Figure 2.5). The fiber volume percentage of an UD-ply can vary between 40 % to 70 %. The UD-ply is the type which is usually used in infrastructure.

Calculations with laminate structures are complex due to the variation of the properties of the elements in the structure. The most common method used to model FRP behaviour is the classical laminate theory, which is explained in section E.2. The most important advantages and drawbacks of FRP were already mentioned in section 1. The characteristics which are most important concerning the design of a floating bridge are elaborated in Appendix E.2.

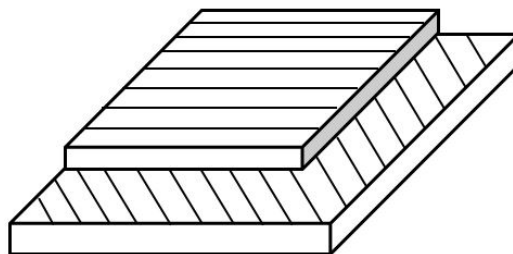


Figure 2.5: Structure of a laminate.

2.2.1. Failure mechanisms

According to CUR-aanbeveling 96 (2003) an FRP structure has to be assessed considering stability, stiffness, fatigue and strength. A stability assessment includes a buckling analysis in ultimate limit state (ULS). A stiffness analysis means that maximum deflections have to be assessed. Furthermore, a fatigue analysis must be performed according to CUR 2003. Lastly, the several types of internal forces have to be assessed to check the strength of an FRP structure and different failure mechanisms of the joints have to be assessed. The stiffness criteria is often governing in FRP structures due to the relatively low stiffness.

2.2.2. Developments of FRP in civil infrastructure

In the past few decades the use of FRP was mainly restricted to the aerospace and military industries because of high initial costs. However, prices dropped with improved production techniques and FRP started to become an attractive alternative construction material in the infrastructure industry. In past years, a lot of research is carried out into the use of fiber reinforced polymer lock gates, quay walls and bridge structures (Rizkalla et al., 2006). The first all-composite bridge superstructure was constructed in China in 1982. From that moment, FRP started to gain acceptance from civil engineers.

Hybrid bridge structures, with some FRP components, are becoming more popular these days. Bridge decks, girders and stay cables are typical components which are fabricated from FRP. However, all-composite bridge structures are still rare and spans remain in order of 10 to 50 meter. Nevertheless, feasibility studies show great potential (van IJsselmuijden, 2016) (Visser et al., 2017). Although research shows great perspectives, the lack of long term operational demonstration still withholds the development of FRP in the civil infrastructure (Potyrała, 2011).

2.3. Design criteria of floating bridges

The main distinction between a floating bridge and a fixed bridge is the induced motion due to the floating foundation. As a consequence, floating bridges are flexible structures allowing some deflections and accelerations. These deflections and accelerations can lead to an unacceptable level of discomfort to the users of the bridge. Therefore, on top of the regular design codes of fixed bridges (NEN-EN 1990, 2011) limitations are set regarding the accelerations (Hermans, 2014).

The design criteria of limited displacements and accelerations refer to a serviceability limit state (SLS). This implies that the limit state imposes a requirement considering the regular performance of the structure. Exceedance of the ultimate limit state would result in the failure of a structure, whereas exceeding the serviceability limit state refers to a condition beyond which service requirements cannot be fulfilled. The eurocode prescribes different reliability indexes β_d to assess these limit states. The principle of a reliability index is illustrated in figure 2.6. The reliability index of reversible serviceability limit states is 1,5 (NEN-EN 1990, 2011), which corresponds to a exceedance probability of a threshold value of $6,68 \cdot 10^{-2}$.

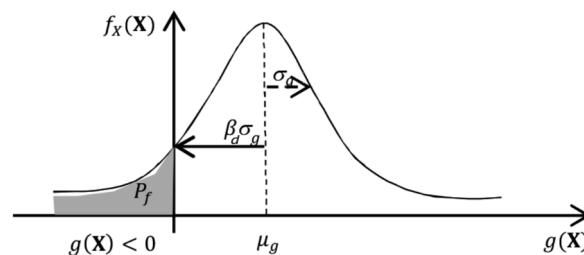


Figure 2.6: Reliability index beta (Corso, 2016).

The limitations of displacements and accelerations are based on NEN-EN 1990 (2011) and HB185 (2011). These guidelines present limitations considering deflections and accelerations in different directions (figure 2.7). The figure shows that deflections and accelerations in the longitudinal direction are not taken into account. A summary of the limitations is given in Table 2.1. Apart from these criteria, a floating bridge must satisfy the design codes for regular fixed bridges.

	Deflection (m)	Acceleration (m/s^2)	Rotation (rad)	Angular acceleration (rad/s^2)
Vertical plane	L/350	0,7	0,025	0,07
Lateral plane	L/350	0,5	0,03	0,05
Cross section	-	-	0,044	0,107

Table 2.1: Deflection and acceleration limits of floating bridges (Hermans, 2014).

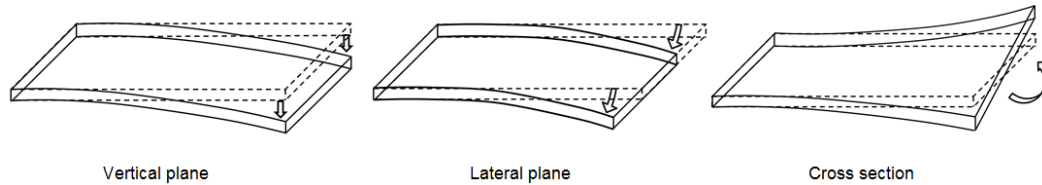


Figure 2.7: Illustration of the different planes in which deflections and accelerations must be limited.

2.4. Coordinate system

In this research a distinction is made between pontoons element and superstructure elements (figure 2.8). A local coordinate system is used as shown in figure 2.8. Translational motions of the pontoon along the x, y and z axis are called surge (u), sway (v) and heave (w) respectively. Rotational motions of the pontoon around the x, y and z axis are called roll (p), pitch (q) and yaw (r) respectively. Subscripts 1 to 6 are used for these motions in the same order. The displacements of the superstructure are indicated with the same symbols, but sometimes referred to differently. The translational displacements are often addressed with longitudinal displacement (u), lateral displacement (v) and vertical displacement (w). The rotational motions are often addressed with torsion (p), vertical rotation (q) and lateral rotation (r).

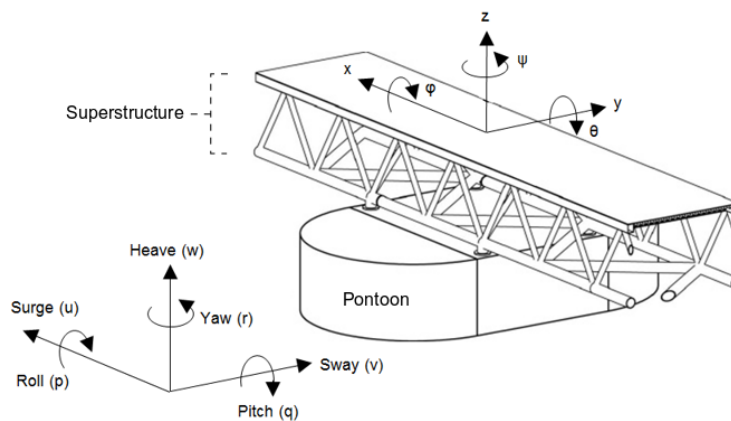


Figure 2.8: Definition of the coordinate system (Petersen et al., 2018).

2.5. Conclusion

The following conclusions are drawn based upon the literature review about floating bridges:

- The most important design criteria for FRP structures are generally the SLS criteria. In the case of a floating bridge these consist of deflection and acceleration criteria. The threshold values are presented in table 2.1. The design exceedance probability of these threshold values is $6,68 \cdot 10^{-2}$.
- The wave conditions with a return period of 1 year at the most relevant areas for floating bridges have peak wave periods ranging from 3 to 6 s and significant wave heights ranging from 0,5 tot 2 m. The governing wave direction is determined by the bathymetry of the fjord, but will most often be perpendicular to a floating bridge.
- The development of FRP in the civil engineering industry is mainly withhold by the lack of experience, rather than the properties of the material.

3

Ocean waves

Wave loads are assumed to be the governing dynamic load for a floating pontoon bridge. To understand the response of a floating structure due to wave loading, it is important to thoroughly comprehend the physics behind waves and to define a method to treat wave loading as a stochastic load. First, a general description of waves is presented in section 3.1 to explain the terminology. Subsequently, the principle of wave spectra is explained in section 3.2 and it is shown how this can be used to describe the sea surface as a stochastic process.

3.1. Description of ocean waves

It is important to make a distinction between a wave and the surface elevation. The surface elevation is the elevation of the water surface relative to a defined reference level in a time record. A wave can be described as the lineament of the surface elevation bounded by two following zero crossings. The time between two succeeding zero crossings is defined as the wave period.

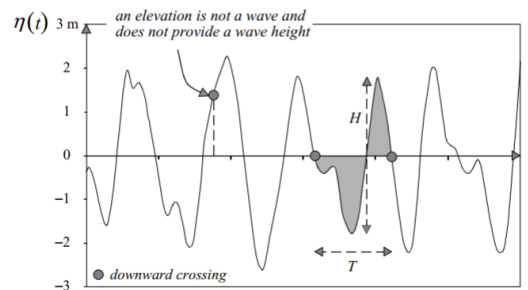


Figure 3.1: Visualization of several wave parameters (Holhuijsen, 2010).

The wave height is the vertical distance between the highest and lowest point of a wave. A frequently used version of the wave height is the significant wave height:

$$H_{1/3} = \frac{1}{N/3} \sum_{j=1}^{N/3} H_j \quad (3.1)$$

where:

H_j	=	j^{th} wave height	[m]
$H_{1/3}$	=	Significant wave height	[m]
N	=	Number of waves	[-]

Here j is the rank number of the wave heights in a wave record. Therefore, the significant wave height is the average wave height of the highest $1/3^{th}$ of the waves. Furthermore, a valuable statistical parameter to describe a wave record is the variance of the surface elevation. This is defined as the average of the squared surface elevation:

$$\overline{\eta^2} = \frac{1}{2} a^2 \quad (3.2)$$

where:

$$\begin{aligned} a &= \text{Amplitude of the surface elevation} \quad [\text{m}] \\ \eta &= \text{Surface elevation} \quad [\text{m}] \end{aligned}$$

The variance is a useful parameter when the random-phase/amplitude model is used. In this model a large number of harmonics is added to describe the surface elevation of a sea state. The variance of this sum is equal to the sum of the individual variances. The surface elevation of a propagating wave is often defined as:

$$\eta = \hat{\eta} e^{(k_w x - \omega t)} \quad (3.3)$$

where:

$$\begin{aligned} \omega &= \text{Angular frequency} \quad [\text{rad/s}] \\ k_w &= \text{Wave number} \quad [\text{m}^{-1}] \\ t &= \text{Time} \quad [\text{s}] \end{aligned}$$

3.2. Wave spectrum

Wave spectra are used to describe the sea surface as a stochastic process. The concept of these spectra is based on the random-phase/amplitude model, further discussed in Holhuijsen (2010). Using a fourier analysis, it is possible to determine the values of the amplitude a and the phase α for each frequency in a wave record. This principle is illustrated in figure 3.2. It is assumed that the values of the phases are uniformly distributed in the case of deep water (Holhuijsen, 2010). For many engineering purposes, this means that the influence of the random phase angle can be ignored. However, when the relative motion between floating structures is of interest, this is not the case. The influence of the random phase angle is further elaborated in chapter 4.

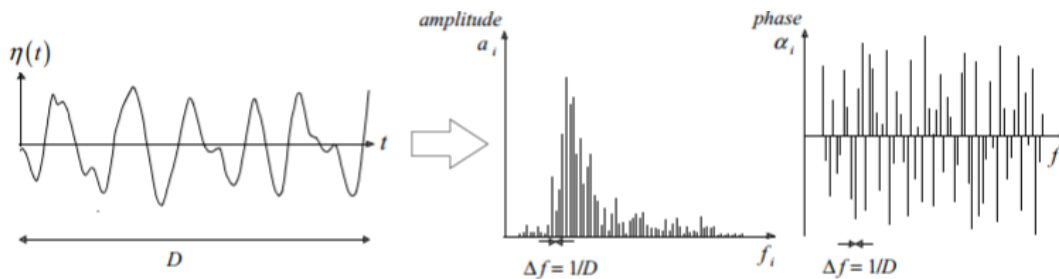


Figure 3.2: Visualization of the amplitude and phase spectrum of a surface elevation record (Holhuijsen, 2010).

Wave records of the same location would have a distinctive amplitude spectrum, so therefore this procedure should be repeated many times to find the average amplitude spectrum:

$$\bar{a}_i = \frac{1}{M} \sum_{m=1}^M a_{i,m} \quad (3.4)$$

where:

$$a_i = i^{th} \text{ amplitude of the surface elevation} \quad [\text{m}]$$

Here M is the number of amplitude spectra. However, it is more useful to use the variance of each wave component. An important advantage of using the variance is that it is linearly related to the wave energy of surface gravity waves. Hence, it is related to pressure variations and induced loads. A shortcoming of the variance spectrum $\frac{1}{2} \bar{a}_i^2$ is that it has discrete values for defined angular frequencies, whereas all frequencies are present in reality. To solve this problem, the variance value has to be distributed over the angular frequency interval $\Delta\omega$, resulting in a discontinuous variance density spectrum. Finally, to arrive at a continuous

spectrum, the limit of the angular frequency interval must be taken to zero. This procedure is summarized in figure 3.3.

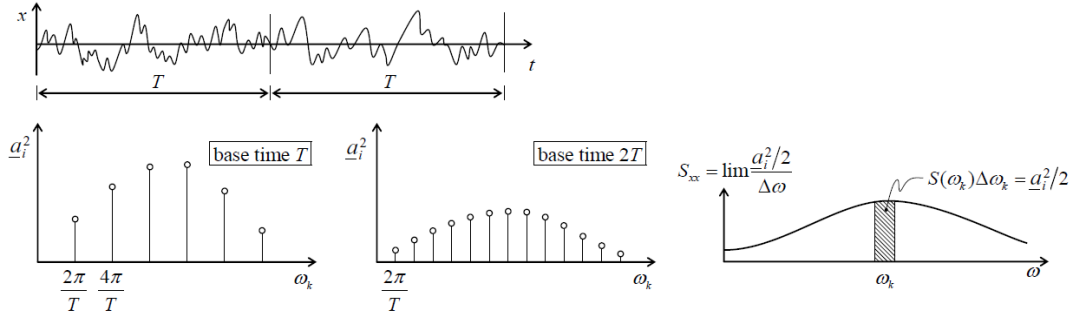


Figure 3.3: Process to transform the amplitude spectrum to the variance density spectrum (Vrouwenvelder, 2005).

The variance density can be defined as a function of the angular frequency $S_{\eta\eta}(\omega)$.

$$S_{\eta\eta}(\omega) = \lim_{\Delta\omega \rightarrow 0} \frac{1}{\Delta\omega} \frac{1}{2} \overline{a^2} \quad (3.5)$$

where:

$$S_{\eta\eta} = \text{Variance density spectrum of the wave elevation, or wave spectrum} \quad [\text{m}^2 \text{s} / \text{rad}]$$

When the variance density spectrum is multiplied by ρg , the energy density is obtained:

$$E_{\eta\eta}(\omega) = \rho g S_{\eta\eta}(\omega) \quad (3.6)$$

where:

$$\begin{aligned} E_{\eta\eta} &= \text{Wave energy density spectrum} \quad [\text{kg s}^{-2} \text{rad}^{-1}] \\ g &= \text{Gravitational acceleration} \quad [\text{m/s}^2] \\ \rho &= \text{Density} \quad [\text{kg/m}^3] \end{aligned}$$

This relation only holds for linear wave theory, which is a realistic assumption for wind generated waves. Now the variance density spectrum can be used to describe statistical phenomena of a wave field at a specific location and the energy density spectrum can describe the physical phenomena. It is important to realize that information of waves in all directions is included in these spectra. To arrive at a three dimensional spectrum, the horizontal dimension has to be included. The angle relative to the z-axis is used to add the horizontal dimension:

$$S_{\eta\eta}(\omega, \psi) = \lim_{\Delta\omega \rightarrow 0} \lim_{\Delta\psi \rightarrow 0} \frac{1}{\Delta\omega \Delta\psi} \frac{1}{2} \overline{a^2} \quad (3.7)$$

where:

$$\psi = \text{Rotational angle around the z axis} \quad [\text{rad}]$$

3.2.1. Statistical characteristics

The variance density spectrum can be used to obtain several statistical characteristics from a wave field. These statistical characteristics can be described by means of the moments of a spectrum, which is defined as:

$$m_n = \int_0^\infty \omega^n \cdot S_{\eta\eta}(\omega) d\omega \quad (3.8)$$

where:

$$m_n = \text{Spectral moment} \quad [-]$$

Table 3.1 gives a few useful statistical characteristics expressed in spectral moments. The individual values of wave heights are Rayleigh distributed according to Holhuijsen (2010). When the standard deviation is known, it is possible to determine the exceedance probability of a certain wave height.

Statistical characteristic	Expression
Variance $E(\eta^2)$	m_0
Standard deviation of the surface elevation σ_η	$\sqrt{m_0}$
Estimate of significant wave height H_{m_0}	$4\sqrt{m_0}$
Zero crossing period \bar{T}_0	$\sqrt{\frac{m_0}{m_2}}$

Table 3.1: Statistical characteristics expressed in spectral moments.

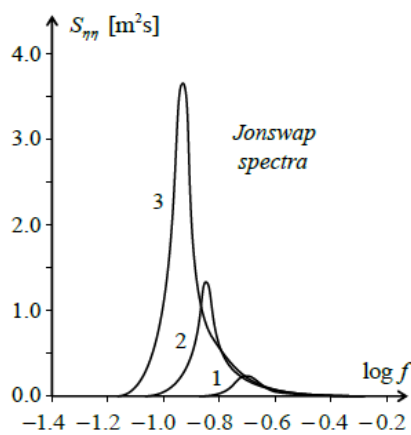
3.2.2. Jonswap spectrum

The previous sections explain the procedure to compute a variance density spectrum from wave records. Additionally, a wave spectrum can be approximated with general formulas which are derived from wave records. The most relevant wave spectrum for this research is the Jonswap spectrum, because it is used as industrial standard for applications in North Sea region (Holhuijsen, 2010). The Jonswap spectrum (figure 3.4a) is given by:

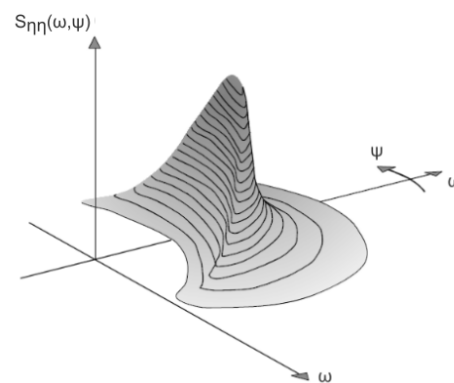
$$S_{\eta\eta}(\omega) = \alpha_w g^2 \omega^{-5} e^{(-1.25(\frac{\omega_0}{\omega})^4)} \gamma^r \quad (3.9)$$

where:

α_w	=	Shape factor	[-]
g	=	Gravitational acceleration	[m/s ²]
ω_0	=	Dominant radial frequency	[rad/s]
γ^r	=	Peak enhancement function	[-]



(a) Jonswap spectra with different input parameters (Vrouwenvelder, 2005).



(b) Three-dimensional variance density spectrum (Holhuijsen, 2010).

Figure 3.4: 2D and 3D representations of wave spectra.

3.3. Conclusion

The most important findings that are used in this research are:

- The variance density spectrum, or wave spectrum, can be used to describe wave conditions as a stochastic process. This spectrum contains statistical information about the wave heights and corresponding wave periods.
- The Jonswap spectrum is a suitable wave spectrum to approximate wave conditions in the Norwegian fjords.

4

Multibody dynamics of a floating bridge

The dynamic response of a structure such as a floating bridge is mainly covered in the field of structural dynamics. A floating bridge can be schematized as a series of floating bodies which are restrained by a continuous structure. Such a system is also called a multibody system. The theory of multibody dynamics considers the dynamic behavior of interconnected rigid and/or flexible bodies, each subjected to dynamic loads. The governing dynamic loads are addressed in chapter 3. This chapter elaborates upon the theory which is required to construct a multibody system and to analyze its dynamic response. Section 4.1 explains the fundamental concepts of structural dynamics. All elements which are used to build a floating bridge model are discussed here. Subsequently, section 4.2 shows how the dynamic response of such a model can be constructed. The frequency domain approach will be discussed in detail here. Finally, a technique to discretize a complex structure such as a floating bridge is introduced. Section 4.3 explains the FE method in detail which is used to model the superstructure of the bridge.

4.1. Equations of motion

First a single DOF system is introduced and the phenomenon of resonance is explained. This theory is expanded to multiple DOF systems and subsequently the dynamics of continuous systems are discussed.

4.1.1. Single degree of freedom system

An essential step of describing a dynamic system is knowing how to schematize a complex structure. The most fundamental dynamic system is a mass-spring rigid body system. A rigid body is a solid body which does not show deformations. In practice these mass-spring systems rarely occur, because there is always a certain amount of damping introduced that extracts energy from the system. As a consequence, dashpots are often included in a system. A simple system, such as the heave motion of a pontoon due to waves, can be modeled as a rigid body with a single DOF. Such a system is illustrated in figure 4.1. The equation of motion (EOM) of this system can simply be derived from Newton's second law:

$$F(t) + F_{spring}(t) + F_{dashpot}(t) = m\ddot{w}(t) \quad (4.1)$$

where:

m	=	Mass	[kg]
F	=	Force	[N]
w	=	Displacement in the z direction (heave)	[m]

This is often written as:

$$m\ddot{w} + c\dot{w} + kw = F \quad (4.2)$$

where:

c	=	Damping	[Ns/m]
k	=	Spring stiffness	[N/m]

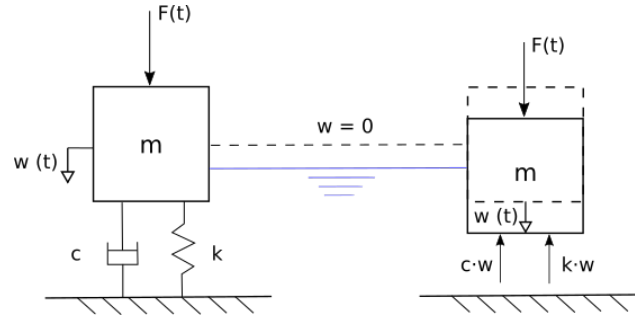


Figure 4.1: 1 DOF system with viscous damping.

The solution procedure of this single DOF system is elaborated in appendix B. The response of a single DOF damped system without external forcing is shown in figure 4.2. A single DOF system contains one eigenmode, which is motion in which the structure will vibrate when the system contains energy. In other words, when the system has an initial displacement or velocity, it will vibrate according to the eigenmode. This motion is also called the free vibration. The effect of the free vibration dampens out due to the dashpot. Without external forcing the system will stop vibrating when all energy is dissipated. In the presence of an external force, the response will eventually be dominated by this force when the free vibration is damped out. This response is defined as the steady state.

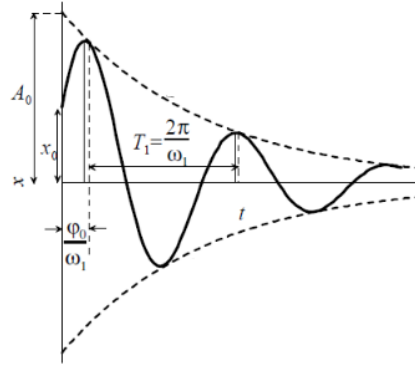


Figure 4.2: Free vibration of a viscous damped single degree of freedom system (Spijkers et al., 2006).

4.1.2. Resonance

An important phenomenon in the field of dynamics is resonance. Resonance occurs when the excitation frequency approaches the eigenfrequency of a system. Appendix B shows that the frequency of the free vibration is the eigenfrequency of the system. When the excitation frequency and the eigenfrequency are the same, the free vibration is continuously "pushed" by the excitation force, resulting in a growing response. Without damping, the response would grow to infinity (figure 4.3). The (undamped) eigenfrequency of the system can be found by solving the eigenproblem, as explained in Appendix B. For an undamped single DOF system, the eigenfrequency is calculated with:

$$\omega_n = \sqrt{\frac{k}{m}} \quad (4.3)$$

where:

$$\omega_n = \text{Angular eigenfrequency} \quad [\text{rad/s}]$$

The amount of resonance is determined by the amount of damping. The damping ratio is an often used parameter to describe the amount of damping and is defined as:

$$\zeta = \frac{c}{2m\omega_n} \quad (4.4)$$

where:

$$\zeta = \text{Damping ratio} \quad [-]$$

The undamped eigenfrequency can now be used to find the damped eigenfrequency, which is more accurate.

$$\omega_d = \omega_n \sqrt{1 - \zeta^2} \quad (4.5)$$

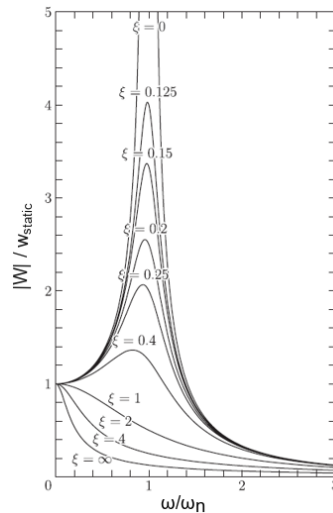


Figure 4.3: Dynamic amplification factor of a single DOF system with a varying amount of damping (Moan, 2017).

4.1.3. MDOFs systems: rigid bodies

Many structures can not be modeled with a single DOF system and should be described with a multiple degree of freedom (MDOF) system. A MDOF system can exist of multiple bodies describing a single DOF, one body describing multiple DOFs or multiple bodies describing multiple DOFs. For now the only element that is considered is a rigid body. When a structure is modeled using MDOFs, a system of ordinary differential equations represents the EOMs, which can conveniently be described in a matrix notation:

$$\mathbf{M}\ddot{\mathbf{w}} + \mathbf{C}\dot{\mathbf{w}} + \mathbf{K}\mathbf{w} = \mathbf{f} \quad (4.6)$$

where:

$$\mathbf{f} = \text{Force vector} \quad [\text{N}]$$

The mass, damping and stiffness matrices are all $n \times n$ matrices and the excitation force vector is a $n \times 1$ vector. The diagonal elements in these matrices describe the independent EOMs of every body in a specific DOF. This means that these elements are independent of the rest of the system. The off diagonal terms describe the relations between the different bodies or DOFs. The excitation force vector describes the force at every DOF.

A MDOF system contains exactly n eigenfrequencies. However, some of these eigenfrequencies can coincide at the same frequency, but correspond to a different mode shape. The eigenvalue problem (equation 4.7) must be solved to find the eigenvalues and eigenvectors of a system. The eigenvectors are used to compute the mode shapes of a dynamic system.

$$\det(\mathbf{K} - \mathbf{M}\omega_i^2)\boldsymbol{\phi}_i = 0 \quad (4.7)$$

where:

$$\omega_i = i^{\text{th}} \text{ eigenfrequency} \quad [\text{rad/s}]$$

$$\boldsymbol{\phi}_i = i^{\text{th}} \text{ eigenvector} \quad [-]$$

4.1.4. Structural damping

All structures possess a certain amount of damping related to the material and the structure. This is often referred to as structural damping. The exact amount of damping is often difficult to determine, but it is possible to make a good estimation using the mass and stiffness matrices of the structure. This is called the Rayleigh method. The damping matrix is found using (Spijkers et al., 2006):

$$\mathbf{C} = \alpha\mathbf{M} + \beta\mathbf{K} \quad (4.8)$$

where:

$$\begin{aligned} \alpha &= \text{Rayleigh damping constant} \quad [-] \\ \beta &= \text{Rayleigh damping constant} \quad [-] \end{aligned}$$

A major advantage of this method is that the damping matrix is proportional to the mass or stiffness matrix. This characteristic allows a calculation of the eigenfrequencies, including damping through the damping ratio. Equation 4.3 is used to calculate the undamped eigenfrequency.

4.1.5. Non-proportional damping

It is often assumed that a system is proportionally damped for practical engineering purposes. However, there are certain types of damping that can not assumed to be proportional. One of these types is hydrodynamic damping (Tisseur and Meerbergen, 2001). Hydrodynamic damping is damping which a floating structure experiences due to the influence of waves. This type of damping usually has a large influence on the dynamic system. Equation 4.5 is no longer valid now. This means that equation 4.7 must be reformulated:

$$(\mathbf{M}\lambda^2 + \mathbf{C}\lambda + \mathbf{K})\phi = 0 \quad (4.9)$$

In the case of equation 4.7, the eigenvalue problem is characterized as a standard eigenvalue problem, which results in real eigenvalues. With the introduction of the damping matrix, this problem becomes another type of quadratic eigenvalue problem (equation 4.9). The eigenvalues become complex now. In the case of a floating structure this quadratic eigenvalue problem must be solved to find more accurate eigenvalues of the system. An elegant method to reformulate this problem is to introduce the state space notation. This method reduces the problem to the standard eigenvalue problem (Lallement and Inman, 1995):

$$\mathbf{y} = \begin{bmatrix} \mathbf{y}_1 \\ \mathbf{y}_2 \end{bmatrix} = \begin{bmatrix} \phi \\ \lambda\phi \end{bmatrix} \quad (4.10)$$

where:

$$\lambda = \text{Eigenvalue} \quad [-]$$

The eigenvalue problem now becomes:

$$\lambda\mathbf{M}\mathbf{y}_2 + \mathbf{C}\mathbf{y}_2 + \mathbf{K}\mathbf{y}_1 = 0 \quad (4.11)$$

If the mass matrix is invertible this can be rewritten as:

$$(\lambda_i^2\mathbf{I} + \mathbf{M}^{-1}\mathbf{C}\lambda_i + \mathbf{M}^{-1}\mathbf{K})\phi_i = 0 \quad (4.12)$$

where:

$$\mathbf{I} = \text{Identity matrix} \quad [-]$$

Combining equations 4.10 and 4.12, the state space representation can be written as:

$$\lambda_i \begin{bmatrix} \mathbf{I} & \mathbf{0} \\ \mathbf{0} & \mathbf{I} \end{bmatrix} \begin{bmatrix} \phi_i \\ \lambda_i\phi_i \end{bmatrix} = \begin{bmatrix} \mathbf{0} & \mathbf{I} \\ -\mathbf{M}^{-1}\mathbf{K} & -\mathbf{M}^{-1}\mathbf{C} \end{bmatrix} \begin{bmatrix} \phi_i \\ \lambda_i\phi_i \end{bmatrix} = \mathbf{A} \begin{bmatrix} \phi_i \\ \lambda_i\phi_i \end{bmatrix} \quad (4.13)$$

which is again a standard eigenvalue problem. The only difference between equation 4.7 and equation 4.13 is that the complex eigenvalue problem has $2n$ eigenvalues. The eigenvalues come in conjugate pairs:

$$\begin{aligned} \lambda_i &= \alpha_i \pm i\beta_i \\ \omega_i &= \sqrt{\alpha_i^2 + \beta_i^2} \end{aligned} \quad (4.14)$$

4.1.6. Continuous structures: Euler-Bernoulli beam

The Euler-Bernoulli beam element is more suited than a rigid body to model the superstructure. The main reason for this is that the deformation in a rigid body is zero by definition. The superstructure is expected to deform and is therefore modeled with an Euler-Bernoulli beam element. Contrary to a rigid body, an Euler-Bernoulli beam is modeled as a continuous system with an infinite number of spatial nodes for each DOE. Figure 4.4 shows a beam subjected to a vertical load resulting in transverse motion. This vertical load varies both in space and time. The Euler-Bernoulli beam theory is adopted to solve this system. This theory states that the plane cross-section, which is initially perpendicular to the axis of the beam, remains plane and perpendicular to the neutral axis during vertical motion. According to this theory the following relation holds:

$$M = -EI \frac{\partial^2 w}{\partial x^2} \tag{4.15}$$

where:

M	=	Moment	[Nm]
E	=	Young's modulus	[N/m ²]
I	=	Second moment of area	[m ⁴]

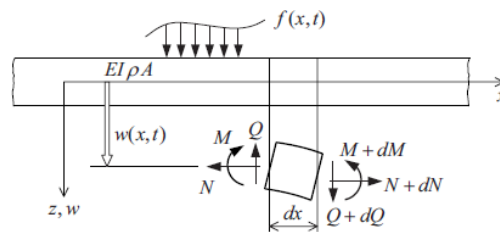


Figure 4.4: Conventions and forces of an Euler Bernoulli beam (Spijkers et al., 2006).

Again Newton's second law is adopted to find the EOMs. The derivation is elaborated in appendix B.2. The following EOMs of an Euler Bernoulli beam are found:

$$\rho A \frac{\partial^2 w}{\partial t^2} + \frac{\partial^2}{\partial x^2} EI \frac{\partial^2 w}{\partial x^2} = f(x, t) \tag{4.16}$$

where:

A	=	Surface area	[m ²]
ρ	=	Density	[kg/m ³]

The EOMs of a continuous system are space and time dependent. This means that the EOMs are partial differential equations instead of ordinary differential equations. Boundary conditions are now required to solve this system, because of the space dependency. A different solution procedure is required compared to ordinary differential equations. One of the most common solution procedures of a partial differential equation is called separation of variables. This procedure is explained in appendix B.2. The response of a beam element can be described with a summation of different mode shapes (figure 4.5) each corresponding to an eigenfrequency.

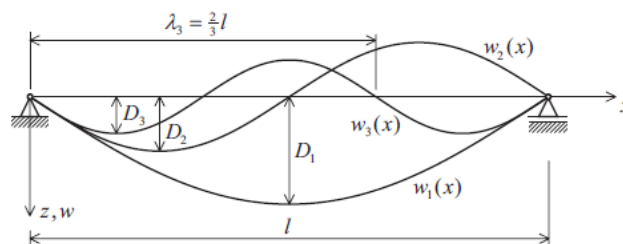


Figure 4.5: First three mode shapes of a simply supported euler bernoulli beam (Spijkers et al., 2006).

4.2. Frequency domain analysis

When the EOMs are derived, the response of a structure subjected to harmonic loading can be computed either in the time domain or in the frequency domain. These two domains are related to each other by means of Fourier integrals. Any time signal can be approximated by a summation of harmonics. This process is executed with the help of a Fourier transform. As such, a signal can be transformed from a time signal to a frequency signal and vice-versa.

EOMs can be solved directly in the time domain for arbitrary loads. Numerically this can be done for a discretized number of small time steps. At every time step the EOMs must be solved. Non-linear processes can be included in such an analysis. However, this technique requires a high amount of computational power compared to a frequency domain approach, because many calculations are performed. Furthermore, when the components of the EOMs consist of frequency dependent properties which are not constant, the EOMs have to be solved independently for every harmonic using a convolution technology (Cummins, 1962).

In case of a floating structure, the EOMs contain frequency depending terms, because the added mass, hydrodynamic damping and the excitation forces are functions of the frequency. Therefore it is a more convenient choice to analyze the motions of a floating structure in the frequency domain. A frequency spectrum represents the distribution of energy over different frequency bands. A time domain signal can be transformed into a frequency spectrum using a Fourier transform. This principle is schematized in figure 4.6.

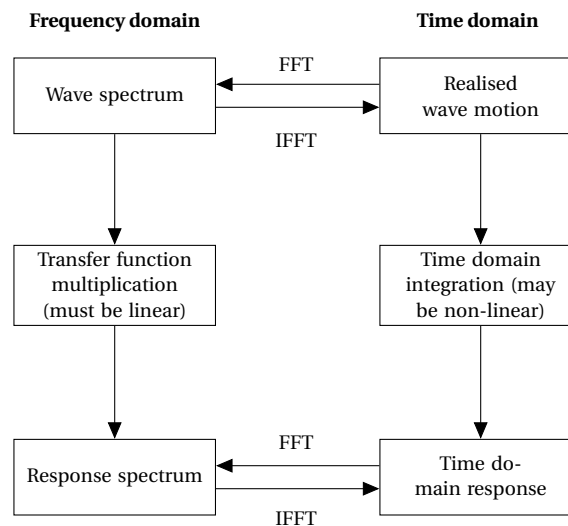


Figure 4.6: Flow scheme of different solutions techniques (Bergdahl, 2009).

One disadvantage of a response spectrum compared to a time trace of the response is that it is not possible to directly produce the response of a structure. A time domain approach accounts for initial conditions to compute this time trace of the response. A frequency domain approach does not require initial conditions. That means that the solution, the response spectrum, only contains information about the steady state response. This is sufficient for this research.

4.2.1. Transfer functions and response spectra

It is possible to transform the variance density spectrum into a wave-induced pressure or force spectrum. This transformation is performed with a transfer function. To use such a transfer function, it is required that the relationship between the variables can be considered as a linear system. This means that an amplification of the excitation results in an equal amplification of the response.

Linear wave theory provides such a relation between the surface elevation and the water pressure. The response of this system changes only in amplitude and phase. Therefore transfer functions of both the amplitude and the phase should be used to describe such a system completely. However, for now the amplitude response function is of main interest and is defined here:

$$|H_{k,j}(\omega)| = \frac{\hat{X}(\omega)}{\hat{x}(\omega)} \quad (4.17)$$

where:

$$H_{k,j} = \text{Transfer function between quantities k and j} \quad [-]$$

$\hat{X}(\omega)$ and $\hat{x}(\omega)$ are amplitudes with a linear relation. The transfer function is a $n \times n$ matrix for every discretized frequency relating two quantities. To describe a floating structure's dynamic response under the excitation of waves, two different transfer functions should be defined. First the wave elevation should be transformed into a wave force. Subsequently, the wave force must be transformed into the dynamic response of a floating structure. This first transfer function is called the wave force transfer function. Using this transfer function, the wave spectrum is transformed into a force spectrum:

$$S_{FF}(\omega, \psi) = [H_{\eta,F}(\omega, \psi)]^2 \cdot S_{\eta\eta}(\omega, \psi) \quad (4.18)$$

The transfer function is squared, because the variance density spectrum is originally obtained from the squared amplitudes of the surface elevations. A detailed explanation of this wave transfer function is presented in chapter 5. For now it is sufficient to know that this function represents the relation between the wave elevation and the wave force. The second transfer function is called the frequency response function (FRF). This transfer function can be derived assuming a standard solution to solve the equations of motion:

$$\begin{aligned} m\ddot{w} + c\dot{w} + kw &= F(t) \\ w(t) &= \hat{w} \cdot e^{i\omega t} \\ \dot{w}(t) &= \hat{w} \cdot i \cdot \omega \cdot e^{i\omega t} \\ \ddot{w}(t) &= -\hat{w} \cdot \omega^2 \cdot e^{i\omega t} \\ m \cdot -\hat{w} \cdot \omega^2 + c \cdot \hat{w} \cdot i \cdot \omega + k \cdot \hat{w} &= \hat{F} \\ \hat{w} &= \frac{1}{-m \cdot \omega^2 + c \cdot i \cdot \omega + k} \cdot \hat{F} \\ H_{F,w}(\omega) &= \frac{1}{m \cdot -\omega^2 + c \cdot i \cdot \omega + k} \end{aligned} \quad (4.19)$$

This equation shows that the denominator approaches zero at the eigenfrequencies. This means that the FRF shows peaks at these frequencies (figure 4.7). The equation also shows that these transfer functions become complex when damping is nonzero. The imaginary part of the transfer function is related to the phase shift between the force and the response.

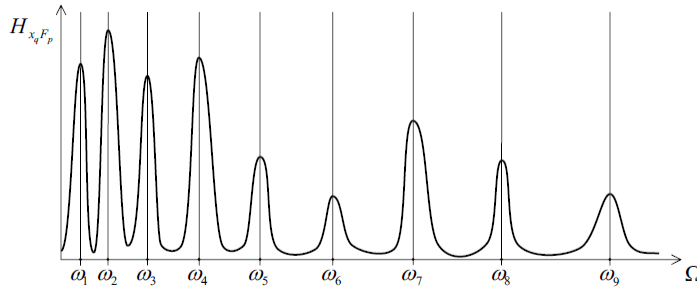


Figure 4.7: Frequency response function (Spijkers et al., 2006).

The response spectrum is now found using:

$$S_{ww}(\omega) = |H_{F,w}(\omega)|^2 \cdot S_{FF}(\omega) \quad (4.20)$$

The two transfer functions can be combined in a response amplitude operator. This principle is explained in appendix C.3. Furthermore, it is also possible to compute an acceleration response spectrum. the transfer function between the force and acceleration is calculated using:

$$H_{F,\ddot{w}}(\omega) = -\omega^2 \frac{1}{m \cdot -\omega^2 + c \cdot i \cdot \omega + k} \quad (4.21)$$

4.2.2. Relative response spectrum

A regular response spectrum is sufficient to evaluate the dynamic response of single body. However, when the relative response between for example two pontoons becomes of interest, a response spectrum on its own is inadequate. The reason for this is that the response spectrum not take the phase difference between bodies into account. Information about the phase difference is crucial when relative motions are predicted.

Relative motions are often important in the assessment of a multibody floating structure. Therefore the relative response spectrum should be constructed. Until now, the random phase angle was neglected. However, it can easily be integrated in the previous presented theory. According to the random phase model (Holhuijsen, 2010) a wave can be described as:

$$\eta = \hat{\eta} \cdot e^{-i\omega t} e^{i\epsilon_\eta} \quad (4.22)$$

where:

$$\epsilon_\eta = \text{Random phase angle of the wave elevation [rad]}$$

The random phase angle is uniformly distributed between 0 and π . The wave elevation can be transformed into a wave force using the wave transfer function. Because damping is present, this wave transfer function will also contain a phase shift between the wave elevation and the wave force:

$$F = \hat{F} \cdot e^{-i\omega t} e^{i(\epsilon_\eta + \epsilon_{\eta,F})} \quad (4.23)$$

where:

$$\epsilon_{\eta,F} = \text{Phase shift between the wave elevation and the wave force [rad]}$$

This phase shift is unique and depends on the shape of the structure, which is elaborated in chapter 5. For now it is sufficient to know that there is a unique phase shift between the random phase of the wave elevation and the wave force. Subsequently, the force is related to a response using the FRF. Also this transfer function goes along with a unique phase shift (figure 4.8).

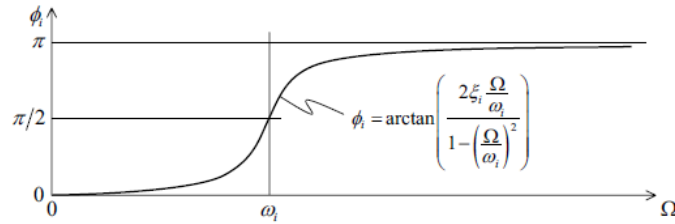


Figure 4.8: Angular phase displacement of the frequency response function (Spijkers et al., 2006).

This phase shift can be found with:

$$\epsilon_{F,w} = \tan^{-1} \left(\frac{\text{Im}(H_{F,w}(\omega))}{\text{Re}(H_{F,w}(\omega))} \right) \quad (4.24)$$

The total response of one DOF can be described with:

$$W = \hat{W} \cdot e^{-i\omega t} e^{i(\epsilon_\eta + \epsilon_{\eta,F} + \epsilon_{F,w})} \quad (4.25)$$

The question remains how this information is used to describe the relative motion. The relative motion between two connection floating structure can be described with:

$$\begin{aligned} W_\Delta &= W_1 - W_2 \\ W_\Delta &= \hat{W}_1 \cdot e^{-i\omega t} e^{i\epsilon_1} - \hat{W}_2 \cdot e^{-i\omega t} e^{i\epsilon_2} \end{aligned} \quad (4.26)$$

Although \hat{W}_1 and \hat{W}_2 may be equal, η_1 and η_2 are always different due to the influence of the random phase angle. It is clear that ΔW contains complex values. The amplitude of this relative motion is described by:

$$\hat{W}_\Delta = \sqrt{\text{Re}(W_\Delta)^2 + \text{Im}(W_\Delta)^2} \quad (4.27)$$

The amplitude of the relative motion can be used to plot the variance density spectrum of the relative response, also known as the relative response spectrum. Just as with a regular response spectrum, this spectrum can be used to obtain statistical information about the response.

4.2.3. Response spectrum analysis

A response spectrum contains valuable information regarding the response of a structure. Visually, the frequency bands that contain most energy can readily be determined. To predict the exceedance probability of specific values, the type of distribution must be known.

The following procedure must be followed to determine the distribution type from a response spectrum. First, time series have to be produced as shown in figure 4.6. A random phase, uniformly distributed, is assumed for incoming wave. Random phases need to be added to response spectrum because it is induced by incoming wave. Now arbitrary time series can be produced. Second, these can be discretized and presented in a histogram. Third, this data can be fitted with existing distributions types to determine the goodness of fit and obtain the corresponding statistical parameters. To find the extreme value distribution, the generalized extreme value distribution can be obtained from extremes computed with time series as explained in Vrijling and van Gelder (2002).

However, for a stationary Gaussian narrow-band process, an upper-bound approximation can be made instantly (Vrouwenvelder, 2005). A Rayleigh distribution is assumed here. The width of a spectrum can be expressed using the spectral moments:

$$q = \sqrt{1 - \frac{m_1^2}{m_0 m_2}} \quad (4.28)$$

A spectrum is said to be narrow banded when $q \ll 1$. This approximation is based on the assumption that the peak values of a narrow band spectrum (figure 4.9) are independent. This means that the probability of exceedance of a threshold value is given by:

$$P\{w(t) > W[0, T]\} \approx \sum_{i=1}^n P\{\hat{a}_i > W\} \quad (4.29)$$

where:

$$P = \text{Probability of exceedance} \quad [\text{s}^{-1}]$$

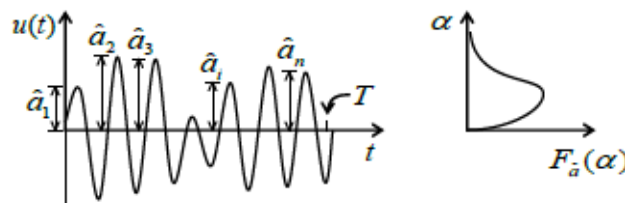


Figure 4.9: Peak values of a narrow band spectrum (Vrouwenvelder, 2005).

The upper bound approximation of the response exceeding with a probability P is now given by (Vrouwenvelder, 2005):

$$W = \mu_w + \sigma_w \sqrt{2 \ln \left(T \frac{\omega_0}{2\pi P} \right)} \quad (4.30)$$

where:

$$\begin{aligned} \mu_w &= \text{Mean value of heave} & [\text{m}] \\ \sigma_w &= \text{Standard deviation of heave} & [\text{m}] \\ T &= \text{Life time} & [\text{y}] \end{aligned}$$

4.3. Finite Element Method: beam elements

The superstructure of the floating bridge can be modeled with Euler-Bernoulli beam elements. To perform a dynamic analysis of a structure including a continuous system, it is convenient to discretize this system. A well known method to do this is the finite element method (FEM).

4.3.1. Discretized beam element

The EOMs of a continuous system are partial differential equations, because they contain spacial derivatives and time derivatives. Partial differential equations are generally difficult to solve and therefore it is convenient to transform them into homogeneous differential equations. In the case of an Euler Bernoulli beam, the first part of equation 4.31 is transformed into the second part by using the FEM.

$$\rho A \frac{\partial^2 w}{\partial t^2} + \frac{\partial^2}{\partial x^2} EI \frac{\partial^2 w}{\partial x^2} = 0 \quad \mathbf{M}\ddot{\mathbf{w}} + \mathbf{K}\mathbf{w} = 0 \quad (4.31)$$

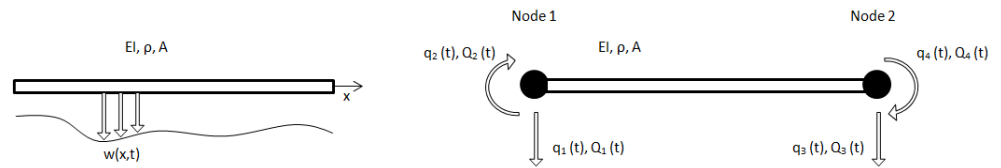


Figure 4.10: Continuous euler bernoulli beam and a discretized euler bernoulli beam.

4.3.2. Local mass and stiffness matrices

As the name already reveals, this method discretizes the continuous system into a finite number of elements. The most simple representation of a beam consists of a single element with two nodes (figure 4.10). The exact displacement is only determined in the nodes and the displacement in between these nodes is approximated. The nodes are characterized by a nodal coordinate $q(t)$ and a nodal force $Q(t)$. Just as the separation of variables technique, the FEM is based on the fact that an assumed equation for the displacement field must satisfy the boundary conditions of the system. The complete derivation of the local mass and stiffness matrices are presented in appendix B.4. For an Euler Bernoulli beam with only 2 DOFs per node, the local mass and stiffness matrix become:

$$\mathbf{M} = \frac{\rho AL}{420} \begin{bmatrix} 156 & 22L & 54 & -13L \\ 22L & 4L^2 & 13L & -3L^2 \\ 54 & 13L & 156 & -22L \\ -13L & -3L^2 & -22L & 4L^2 \end{bmatrix} \quad \mathbf{K} = \frac{EI}{L^3} \begin{bmatrix} 12 & 6L & -12 & 6L \\ 6L & 4L^2 & -6L & 2L^2 \\ -12 & -6L & 12 & -6L \\ 6L & 2L^2 & -6L & 4L^2 \end{bmatrix}$$

4.3.3. Global mass and stiffness matrices

In the computation of the global mass and stiffness matrices, the local matrices are added together. Figure 4.11 shows an example of a simply supported beam where 2 DOFs are included at every node.

When only two DOFs are included, the computation of global mass and stiffness matrices of two nodes is illustrated by the following matrices:

$$\mathbf{M} = \frac{\rho AL}{420} \begin{bmatrix} M_{11}^1 & M_{12}^1 & M_{13}^1 & M_{14}^1 & 0 & 0 \\ M_{21}^1 & M_{22}^1 & M_{23}^1 & M_{24}^1 & 0 & 0 \\ M_{31}^1 & M_{32}^1 & M_{33}^1 + M_{11}^2 & M_{34}^1 + M_{12}^2 & M_{13}^2 & M_{14}^2 \\ M_{41}^1 & M_{42}^1 & M_{43}^1 + M_{21}^2 & M_{44}^1 + M_{22}^2 & M_{23}^2 & M_{24}^2 \\ 0 & 0 & M_{31}^2 & M_{32}^2 & M_{33}^2 & M_{34}^2 \\ 0 & 0 & M_{41}^2 & M_{42}^2 & M_{43}^2 & M_{44}^2 \end{bmatrix}$$

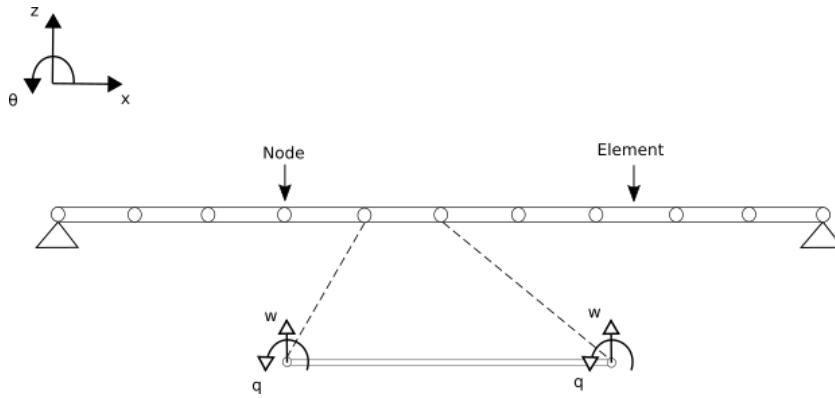


Figure 4.11: Elements and nodes of an Euler Bernoulli beam.

$$\mathbf{K} = \frac{EI}{L^3} \begin{bmatrix} K_{11}^1 & K_{12}^1 & K_{13}^1 & K_{14}^1 & 0 & 0 \\ K_{21}^1 & K_{22}^1 & K_{23}^1 & K_{24}^1 & 0 & 0 \\ K_{31}^1 & K_{32}^1 & K_{33}^1 + K_{11}^2 & K_{34}^1 + K_{12}^2 & K_{13}^2 & K_{14}^2 \\ K_{41}^1 & K_{42}^1 & K_{43}^1 + K_{21}^2 & K_{44}^1 + K_{22}^2 & K_{23}^2 & K_{24}^2 \\ 0 & 0 & K_{31}^2 & K_{32}^2 & K_{33}^2 & K_{34}^2 \\ 0 & 0 & K_{41}^2 & K_{42}^2 & K_{43}^2 & K_{44}^2 \end{bmatrix}$$

When the global mass and stiffness matrices are complete, the boundary conditions are added to complete the matrices. Otherwise the mass and stiffness matrices become singular matrices and the system is unsolvable. Certain information is always known at the boundaries. In the case of a simply supported beam, the vertical displacements and the bending moments are zero at the boundaries. Therefore the corresponding columns and rows of the mass and stiffness matrices can be erased and then the matrices are complete.

4.4. Conclusion

These conclusions contribute to the development of the floating bridge model:

- The pontoons can be modeled as rigid bodies, whereas the superstructure can be modeled with FE Euler-Bernoulli beams. The connections between these two component can be modeled using linear translational and rotational springs.
- A frequency domain analysis using wave force transfer functions and frequency response functions to convert a wave spectrum into a response spectrum is the most suited technique to analyze the response of a multibody floating structure.
- Damping can not be neglected in the computation of the eigenfrequencies, because hydrodynamic damping has a big influence on the eigenfrequencies. A state space method can be used to solve the quadratic eigenvalue problem to find the most accurate eigenfrequencies.
- It is possible to obtain information about the response between two different elements with the relative response spectrum. This spectrum can be found by subtracting the corresponding response spectra of the different elements. The phase difference is included in this process to account for the interaction.

5

Hydromechanics of a pontoon

The former two chapters describe the dynamic load (chapter 3) and the structural schematization (chapter 4) of a floating bridge model. This chapter will relate these two topics by considering the fluid-structure interaction, or hydromechanics. The hydromechanics of a floating structure such as a pontoon consists of a hydrostatic and a hydrodynamic part. First the hydrostatics of a pontoon are discussed in section 5.1. Subsequently, the hydrodynamic behaviour is explained thoroughly in section 5.2.

5.1. Hydrostatics of a pontoon

A structure is able to float when the buoyancy force is equal to the structure's weight (Equation 5.1). The buoyancy force is defined as the upward force that a structure experiences due to the displacement of fluid.

$$\rho \cdot g \cdot \nabla - m \cdot g = 0 \quad (5.1)$$

where:

$$\nabla = \text{Submerged volume} \quad [\text{m}^3]$$

The weight of the structure exerts a downward force from the centre of gravity G (CoG). The buoyancy force on the other hand, exerts an upward force from the center of buoyancy B . When the structure floats in perfect balance, these forces are aligned and no moment occurs.

In case of an excitation, the structure rotates around its CoG. The rotation around the x axis is defined as roll. Figure 5.1 illustrates an example of roll with an angle ϕ . It is clear that the shape of the submerged part of the structure changes. As a consequence, the center of buoyancy shifts to B_1 . The shift between B and B_1 is parallel to the line through the center of the immersed and submerged triangles.

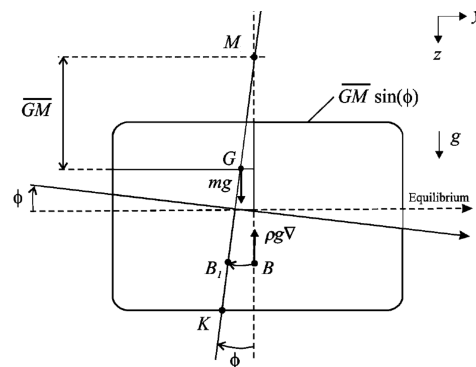


Figure 5.1: Schematization of the stability of a pontoon (Fossen, 2011).

The external roll moment M_h must be equaled by the righting moment M_s , which is caused by the buoyancy, to achieve an equilibrium:

$$M_s = \rho \cdot g \cdot \nabla \cdot \overline{GM} \sin(\phi) \quad (5.2)$$

where:

$$\overline{GM} = \text{Distance between the center of gravity and the metacenter} \quad [\text{m}]$$

\overline{GM} must be positive to guarantee stability. \overline{GM} can be determined with:

$$\overline{GM} = \overline{KB} + \overline{BM} - \overline{KG} \quad (5.3)$$

where:

$$\overline{KB} = \text{Distance between the bottom and the center of buoyancy} \quad [\text{m}]$$

$$\overline{BM} = \text{Distance between the center of buoyancy and the metacenter} \quad [\text{m}]$$

$$\overline{KG} = \text{Distance between the bottom and the center of gravity} \quad [\text{m}]$$

Finally, \overline{BM} can be found using:

$$\overline{BM} = \frac{I}{\nabla} \quad (5.4)$$

where:

$$I = \text{Second moment of area} \quad [\text{m}^4]$$

5.2. Hydrodynamics of a pontoon

Besides the static load of a fluid, the waves also exert a dynamic load on a floating pontoon. All forces on a rigid body in water can basically be divided into reaction forces and wave forces. The former are the forces that act on the rigid body due to the displacements of the rigid body. The latter are the forces that the waves exert on the rigid body. The forces acting on a rigid body in waves can be found by superposition of an oscillating rigid body in still water and a fixed rigid body in water with waves. This principle is illustrated in figure 5.2.

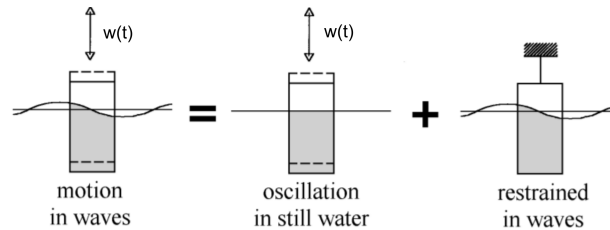


Figure 5.2: Principle of superposition of reaction and wave forces (Journée and Massie, 2002).

The whole procedure to determine the response of a floating structure under dynamic loading is presented in figure 5.3. Wave and wind data can be combined in a wave spectrum, explained in section 3. Design wave conditions can be obtained from the wave spectrum and fluid particle kinematics can be determined. This is explained in appendix C. Subsequently, the particle kinematics can be related to the wave-induced pressures and thus to forces acting on the floating structure. The hydrodynamic forces not only consist of wave forces, but also reaction forces of the structure due to motions. Therefore the response of the floating structure also influences the hydrodynamic forces. As such, this is an iterative process.

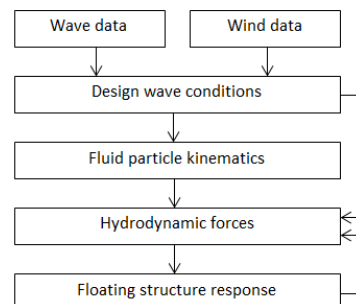


Figure 5.3: Overview of procedure to calculate dynamic responses of floating structures (Bergdahl, 2009).

A well known approach to compute the hydrodynamic loads on cylinders is the Morison equation (Morison et al., 1950). The Morison equation consists of a semi-empirical superposition of an inertial force and a viscous drag force. This approach assumes that the diffraction effects can be neglected, because the diameter of the floating body is much smaller than the wave lengths. This is not the case for the pontoons of a floating bridge. As such, it is preferable to apply another approach which takes diffraction into account.

A classical method to do this is using the potential flow theory. To be able to relate the fluid particle kinematics to wave-induced pressures, the kinematic equations, described in appendix C, together with the continuity equation, must be solved for specific boundary conditions. Appendix C elaborates upon the concept and the required assumptions to apply potential flow theory.

Due to the superposition principle, the motion response of a floating rigid body in an irregular wave field can be described in the form of equation 5.5.

$$\begin{aligned} w &= \hat{w} \cdot \cos(\omega t + \epsilon_{\eta,w}) = \text{Re} \left[\overline{w} \cdot e^{-i\omega t} \right] \\ \overline{w} &= \hat{w} \cdot e^{-i\epsilon_{\eta,w}} \end{aligned} \quad (5.5)$$

where:

$$\epsilon_{\eta,w} = \text{Phase shift between the wave elevation and the response of the structure} \quad [\text{rad}]$$

5.2.1. Hydromechanic forces

The hydromechanic forces consist of a reaction force and a wave force. The reaction force due to displacements of the structure consists of two components: a hydrostatic component (F_s) and a hydrodynamic component (F_r), the radiation force. The hydrostatic component is the force that the structures experiences during motion at infinitely low speed, meaning that the frequency approaches zero ($\omega \rightarrow 0$). An expression is given in Equation 5.6, where c_j is the hydrostatic stiffness in direction j. For heave this becomes:

$$F_{s,3} = -\rho \cdot g \cdot A_{wl} \cdot w = c_{33} \cdot w \quad (5.6)$$

where:

$$\begin{aligned} F_s &= \text{Hydrostatic wave force} & [\text{N}] \\ A_{wl} &= \text{Submerged surface area} & [\text{m}^2] \\ c_{kj} &= \text{Hydrostatic stiffness in direction k due to displacement in direction j} & [\text{N/m}] \end{aligned}$$

For floating structures the hydrostatic stiffness is present for heave, roll and pitch motions only. These hydrostatic components always exert a force in the same direction as the motion. All hydrostatic stiffness coefficients are given by:

$$\begin{aligned} c_{33} &= -\rho \cdot g \cdot A_{wl} \\ c_{44} &= \rho \cdot g \cdot \nabla \cdot \overline{GM}_x \\ c_{55} &= \rho \cdot g \cdot \nabla \cdot \overline{GM}_y \end{aligned} \quad (5.7)$$

The hydrodynamic component is the force that the structure experiences during motion which is not infinitely slow. This force is a summation of harmonics just as the motion, because linearity is assumed. It will be linearly dependent on the motion, but not necessarily in phase with the motion. Likewise, the motion of the structure is also not necessarily in phase with the wave elevation. The dynamic force and phase shifts are defined in equation 5.8.

$$\begin{aligned} F_{r,3} &= \hat{F}_{r,3} \cdot \cos(\omega t + \epsilon_{F,w} + \epsilon_{w,\eta}) \\ \epsilon_{F,\eta} &= \epsilon_{F,w} + \epsilon_{w,\eta} \end{aligned} \quad (5.8)$$

where:

$$\begin{aligned} F_r &= \text{Hydrodynamic radiation force} & [\text{N}] \\ \epsilon_{F,\eta} &= \text{Phase shift between the wave force and the wave elevation} & [\text{rad}] \\ \epsilon_{F,w} &= \text{Phase shift between the wave force and the response of the structure} & [\text{rad}] \\ \epsilon_{\eta,w} &= \text{Phase shift between the wave elevation and the response of the structure} & [\text{rad}] \end{aligned}$$

The radiation force consists of two parts; one part that is in phase with the acceleration and one part that is in phase with the velocity of the moving structure. These two parts can be characterized with respectively the added mass coefficient and the hydrodynamic damping coefficient. The added mass can be considered as a water mass moving along with vibrating structure and therefore contributing to the total mass of the structure. Hydrodynamic damping is associated with the process where new waves are created by the motion of the structure, which dissipates energy from the system.

The regular wave force consists of two components: Froude-Krilov-force F_w and diffraction force F_d . The Froude-Krilov force occurs due to the pressures in the fluid, assuming the fluid is not affected by the structure. The diffraction force occurs due to the pressure in the fluid that is disturbed by the structure. Substitution of the mentioned equations leaves the equations of motion (equation 5.9). It must be noted that this is an equation in the time domain for one specific frequency. A summary is presented in figure 5.4.

$$(m + a_3)\ddot{w} + b_3\dot{w} + c_3w = F_{w,3} + F_{d,3} \quad (5.9)$$

where:

$$\begin{aligned} F_w &= \text{Froude-Krilov wave force} \quad [\text{N}] \\ F_d &= \text{Diffraction wave force} \quad [\text{N}] \end{aligned}$$

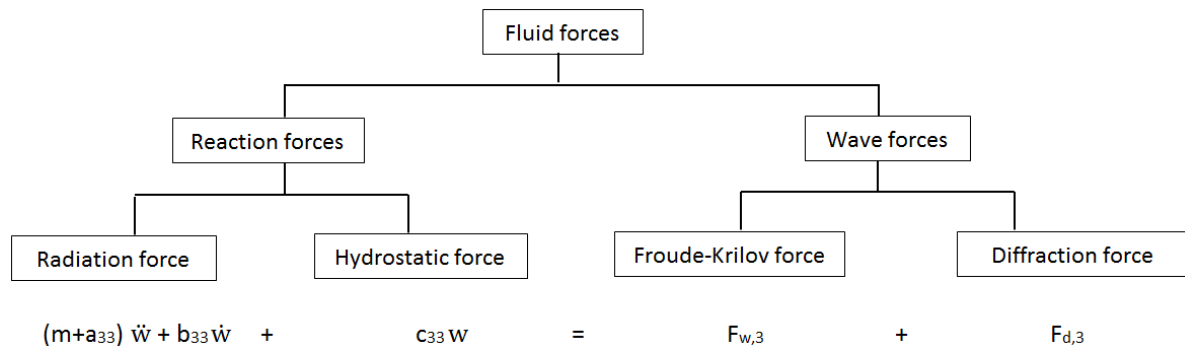


Figure 5.4: Overview of the different components of forces on a rigid body in water.

The question remains how the forces of Equation 5.9 are obtained. Equation D.24 shows that an expression has to be found for the added mass and damping coefficients to find expressions for the radiation forces. The potential flow theory can be used to find these coefficients. The derivation of these coefficients is presented in Appendix D. Furthermore, the other wave forces are derived and the solving procedure of potential functions is explained.

5.3. Conclusion

Several conclusions are drawn to be able to model the fluid-structure interaction between waves and pontoons:

- The Morison equation is not suitable to describe the dynamic wave forces on a floating pontoon, because diffraction can not be neglected for pontoons.
- The fluid-structure interaction between a pontoon and waves consists of reaction forces and wave forces. The former can be described with the added mass, hydrodynamic damping and hydrostatic stiffness. The latter is divided into a Froude-Krilov force and a diffraction force.
- These hydrodynamic components can be computed by solving linear potential functions with boundary conditions.

6

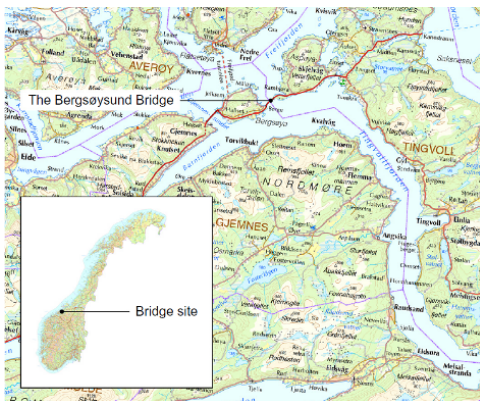
Bergsøysund bridge

The Bergsøysund bridge is used as a case study in this research. The availability of measurement data of accelerations and displacements of this bridge is unique in the case of floating bridges. Hence, these measurements will be used to validate the parametric model of a floating bridge. Therefore the geometry and the structural properties of the bridge must be known to use as input parameters. These parameters can be divided into three groups: parameters related to the pontoons, the superstructure and the connections.

First general information about the layout of the Bergsøysund bridge is presented. Subsequently, the structural and geometrical parameters required to model the bridge are given. Furthermore, relevant load conditions are stated and finally the available measurement data is presented.

6.1. Location of the bridge

The Bergsøysund bridge (figure 6.1b) is one of the two existing long-span end supported floating bridges in Norway. It is part of the E39 route (figure 6.1a). This bridge was opened in 1992 and spans 931 m with the support of seven floating pontoons.



(a) Overview of the location of the Bergsøysund bridge (Kvåle et al., 2017).



(b) Side view of the Bergsøysund bridge (Petersen et al., 2017).

Figure 6.1: Overview of the Bergsøysund bridge.

The floating bridge consists of concrete pontoons and a steel superstructure. The concrete that is used is light weight concrete to minimize the weight of the pontoons. The steel in the superstructure is S355 steel.

The layout of the Bergsøysund bridge is presented in figure 6.2. Rubber bearings are installed at the abutments to constrain the bridge vertically and horizontally. No mooring system is required due to these constraints, which is convenient with depths up to 300 m (figure 6.3). A steel rod is used on both ends to transfer the axial forces. Maintenance is carried out every twenty years to prevent failure due to corrosion. This procedure costs approximately 7,25 million euros and takes over a year (Ellevset, O., 2014a). More information about the maintenance is presented in appendix A.

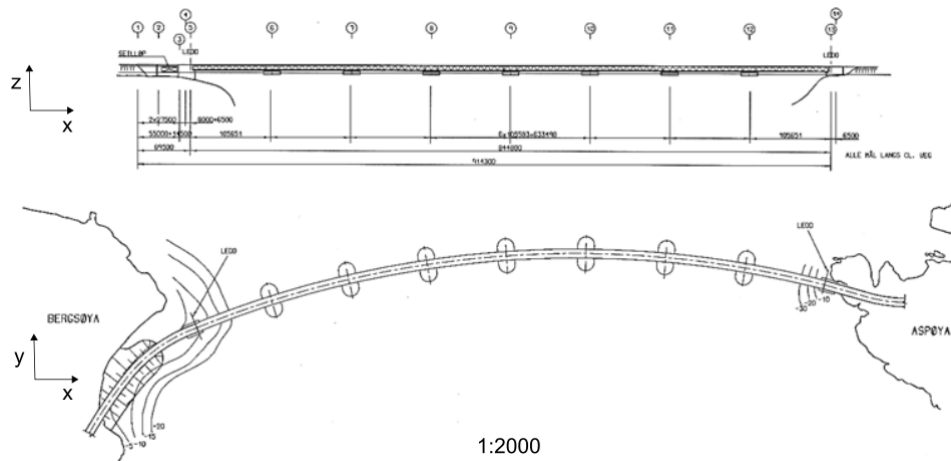


Figure 6.2: Overview of lay out of the Bergsøysund bridge (Statens vegvesen, 1991).

Figure 6.3 shows the depth profile of the soil at Bergsøysund bridge. It is clear that the top 300 meter consists of rock and from that point softer soils such as clay and sand appear. This is a typical depth profile at a fjord. Mooring is especially difficult in rock and therefore this is often avoided.

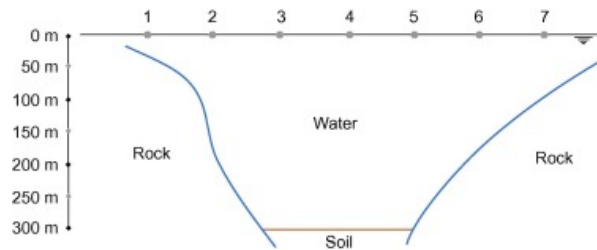


Figure 6.3: Depth profile of the Bergsøysund bridge (Kvåle et al., 2016).

6.2. Structural and geometrical parameters

Most geometrical parameters are obtained from the structural drawings of the Bergsøysund bridge (Statens vegvesen, 1991). Additionally, information from an existing FE model of the Bergsøysund bridge (Hermstad, 2013) is used to acquire the required parameters. The superstructure can be schematized according to figure 6.4. The cross section of the Bergsøysund bridge varies along the span of the bridge. Therefore a cross section with average dimensions is evaluated here. Furthermore, the dimensions of the two outer pontoons differ slightly from the middle five pontoons. The fourth pontoon, which is located in the middle of the bridge is evaluated here.

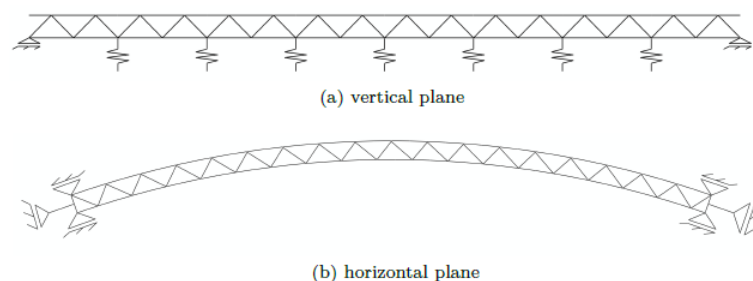
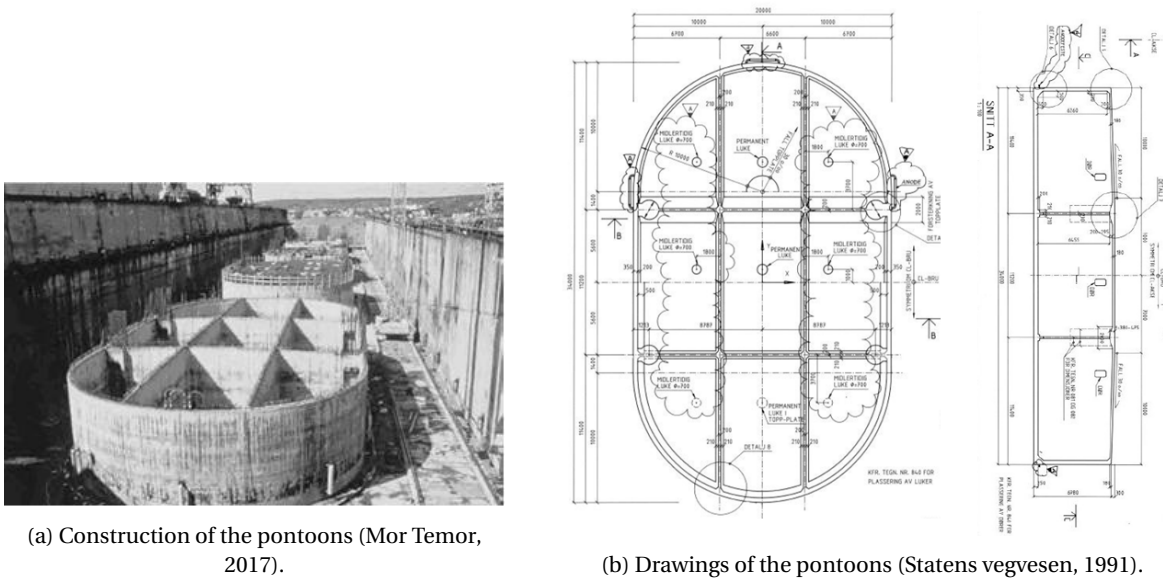


Figure 6.4: Schematized overview of the Bergsøysund bridge (Hermstad, 2013).

6.2.1. pontoons

A structural drawing and a picture of the construction of the pontoons of the Bergsøysund bridge are shown in figure 6.5. The dimensions of the five middle pontoons are presented in Table 6.1. Figure 6.5 shows that the pontoon consists of several compartments. Besides the structural benefits, this design prevents instability in case of leakage and is customary in the design of pontoons.



(a) Construction of the pontoons (Mor Temor, 2017).

(b) Drawings of the pontoons (Statens vegvesen, 1991).

Figure 6.5: Structural information about the Bergsøysund bridge.

Parameter	Value	Unit
Length (L_p)	34	m
Width (W_p)	20	m
Height (H_p)	6,07	m
Draft (D_p)	3,7	m
Density (ρ_p)	2000	kg/m^3
Mass (m_p)	1272540	kg
Mass moment of inertia (J_x)	$1,42 \cdot 10^8$	kgm^2
Mass moment of inertia (J_y)	$7,16 \cdot 10^7$	kgm^2
Mass moment of inertia (J_z)	$1,67 \cdot 10^8$	kgm^2

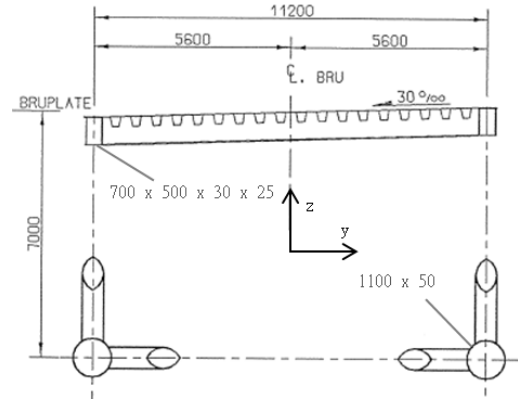
Table 6.1: Structural and geometrical parameters of the Bergsøysund bridge's pontoons.

6.2.2. Superstructure

A cross section of the superstructure with average dimensions is shown in figure 6.6. Figure 6.6b shows the structural drawing of this cross section and figure 6.6a is a picture of it. The dimensions of the superstructure's average cross section are presented in table 6.2. The second moments of area calculation is elaborated in appendix A.



(a) Picture of the cross section of the Bergsøysund bridge (Tidens Krav, 2017).



(b) Structural drawing of the cross section of the Bergsøysund bridge (Statens vegvesen, 1991).

Figure 6.6: Structural information about the Bergsøysund bridge.

Parameter	Value	Unit
Surface area (A_s)	0,557	m^2
Span Length (L_s)	110	m
Density (ρ_s)	7800	kg/m^3
Elasticity (E_s)	210000	MPa
Second moment of area (I_x)	11,7	m^4
Second moment of area (I_y)	5,85	m^4
Polar second moment of area (I_p)	15,1	m^4

Table 6.2: Structural and geometrical parameters of the Bergsøysund bridge's superstructure.

Additionally, research is carried out into the structural damping of the structure. Kvåle and Øiseth (2017) describes different methods to estimate the modal parameters of the structure. The damping ratios of the first 20 modes are identified. The first six modes contain about 5% of damping (figure 6.7).

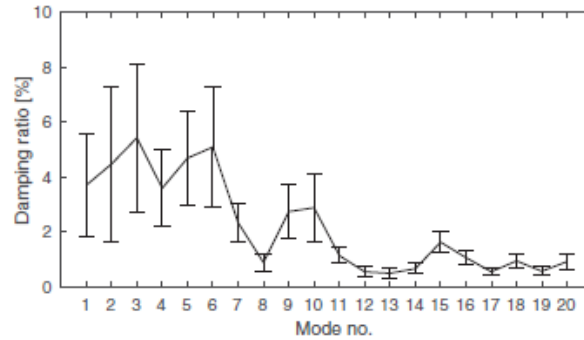


Figure 6.7: Estimated damping ratios of the Bergsøysund bridge (Kvåle and Øiseth, 2017).

6.2.3. Supports and joints

The Bergsøysund bridge has only fixed supports at the abutments. These supports consist of two parts that constrain the motion of the bridge (figure 6.8). Part one is a rod connecting the truss structure to a fixed concrete slab restricting movement in all directions. However, the main function of this connection is restraining the motion along the x-axis. Motions in the other directions are mainly restricted by rubber slabs. Nonetheless, the rubber slabs allow minor displacements in vertical direction to prevent extreme internal stresses due to tidal elevations. Additionally, rotations around the y and z axis are not restrained as well. Together the two

parts of the supports constrain all translations and the torsion of the bridge. An estimation of these spring constants is presented in table 6.3.

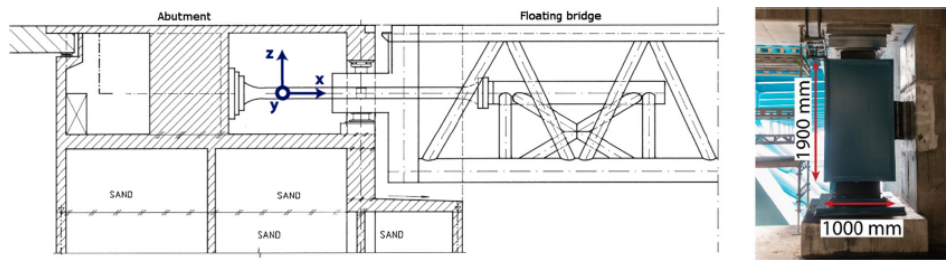


Figure 6.8: Land end support of the Bergsøysund bridge (Petersen and Øiseth, 2017).

The connections between the pontoons and the superstructure also influence the dynamic behaviour. Each pontoon is connected at four locations to the superstructure. A distinction is made between these four joints based on the type of connection. Every pontoon has two joints which are partly hinged (figure 6.10b) and two joints which are fixed (figure 6.10a). Figure 6.9 shows a schematic top view of the four connections between a pontoon and the superstructure. The corresponding table shows which connections are hinged (leddet lager) and which are fixed (fast lager).

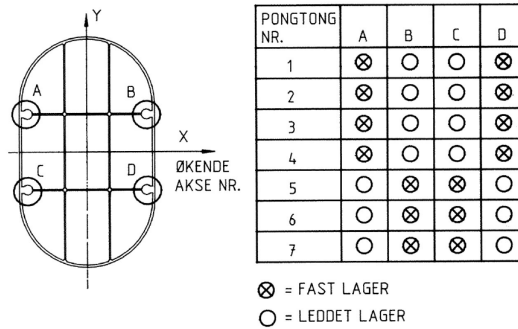


Figure 6.9: Connection between pontoons and superstructure (Statens vegvesen, 1991).

Figure 6.10 shows that the hinged (fast lager) joint is not hinged in all directions. In fact, there is only some rotation allowed around the y axis of the bridge. The fixed joint is completely fixed and does not allow any rotations.



(a) Non hinged connection.



(b) Hinged connection.

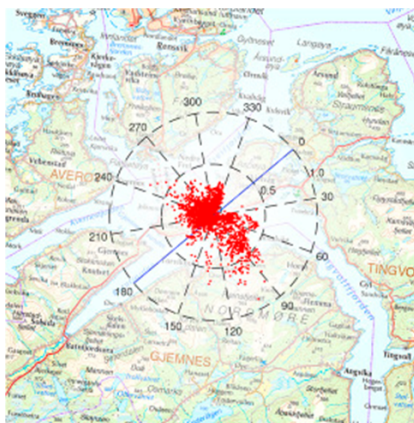
Figure 6.10: Types of connections between the pontoon and the superstructure. Photos by K.A. Kvåle

Parameter	Value	Unit
Support stiffness (K_x)	$1,41 \cdot 10^7$	N/m
Support stiffness (K_y)	$2,14 \cdot 10^8$	N/m
Support stiffness (K_z)	$1,30 \cdot 10^8$	N/m
Support stiffness (K_ϕ)	$2,09 \cdot 10^9$	Nm/rad
Joint stiffness (K_ϕ)	<i>unknown</i>	Nm/rad
Joint stiffness (K_θ)	<i>unknown</i>	Nm/rad
Joint stiffness (K_ψ)	<i>unknown</i>	Nm/rad

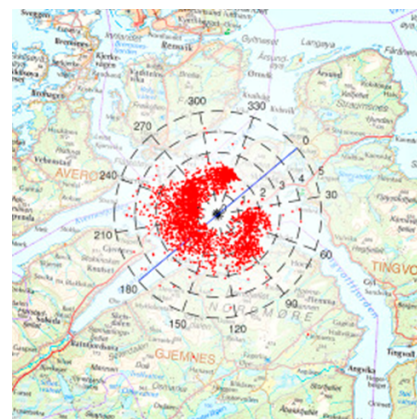
Table 6.3: Structural and geometrical parameters of the Bergsøysund bridge superstructure (Petersen et al., 2017).

6.3. Load cases

The loads effecting the dynamic behaviour of the Bergsøysund bridge are wave loads, wind loads, current loads and traffic loads. According to Petersen et al. (2018) the wave loads are the dominant source of the dynamic response of the Bergsøysund bridge. Kvåle and Øiseth (2017) states that in the case of the Bergsøysund bridge the direct effect of wind to the response of the structure is negligible compared to the influence of waves. The effect of traffic loads on the dynamic response can not be neglected. However, the effect of wave loads and traffic loads can be separated based on their frequency content. A non-dimensional traffic indicator is used to separate recordings influenced by waves and by traffic Kvåle and Øiseth (2017). Only measurements influenced by wave loading are used in this research. Measurements of the wave height and direction are shown in figure 6.11.



(a) Spatially averaged significant wave height [m].



(b) Spatially averaged peak period [s].

Figure 6.11: Measurements of the wave conditions at the Bergsøysund bridge (Kvåle and Øiseth, 2017).

Figure 6.11a shows that the largest significant wave heights originate from 60° to 120° , which is from the land side perpendicular to the bridge. In contrast, figure 6.11b shows that the peak periods are almost uniformly distributed.

Figure 6.12 shows three wave spectra of three different recordings. The measurement periods are 10 minutes, in contrary to usual measurements periods which are 30 minutes. This choice is based on the fact that wave conditions in fjords change faster than offshore. From figure 6.12 it becomes clear that the wave energy has its highest concentration between 0,3 and 0,5 Hz. This means that peak periods lie between 2 and 3,3 s, which implies that these waves are short local waves. This is another effect of the presence of the fjords which restrict the length of the fetch over which wind waves can develop.

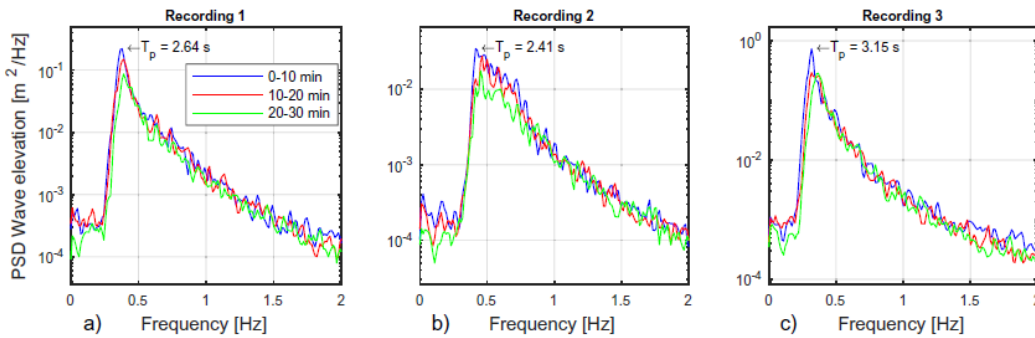


Figure 6.12: Wave spectra constructed with measurements. (Petersen et al., 2018).

6.4. Measurement data

A monitoring system was installed in February 2014 to collect measurement data on the Bergsøysund bridge for two years describing both the environmental conditions and the motions of the bridge. An overview of the measurement equipment is shown in appendix A. It is noticed here that the measurement equipment is connected to the superstructure. This means that the measurements which are meant to describe the motions of the pontoons, can show small deviations. To describe the motions of the pontoons exactly, the equipment should be installed exactly at the CoG.

Measurements like these are widespread available for conventional bridges or floating offshore structures. However, this measurement data is the only available dataset of a floating separate pontoon bridge. One characteristic set of measurements is presented here (figure 6.13). The rest of the measurement data is shown in appendix A.

Figure 6.13 shows five different variance response spectra which corresponds to the wave data of recording 3 (figure 6.12c). The top two plots describe the acceleration in vertical direction of the second pontoon and the lateral acceleration of the fifth pontoon respectively. The blue lines represent the data measured with accelerometers. The bottom three plots describe displacements of the middle pontoon in axial, lateral and vertical direction respectively. The blue line here represents the data measured with Global Navigation Satellite System (GNSS). This data is assumed to be less accurate than the accelerations. The red and green lines represent predictions of data and are not of interest here.

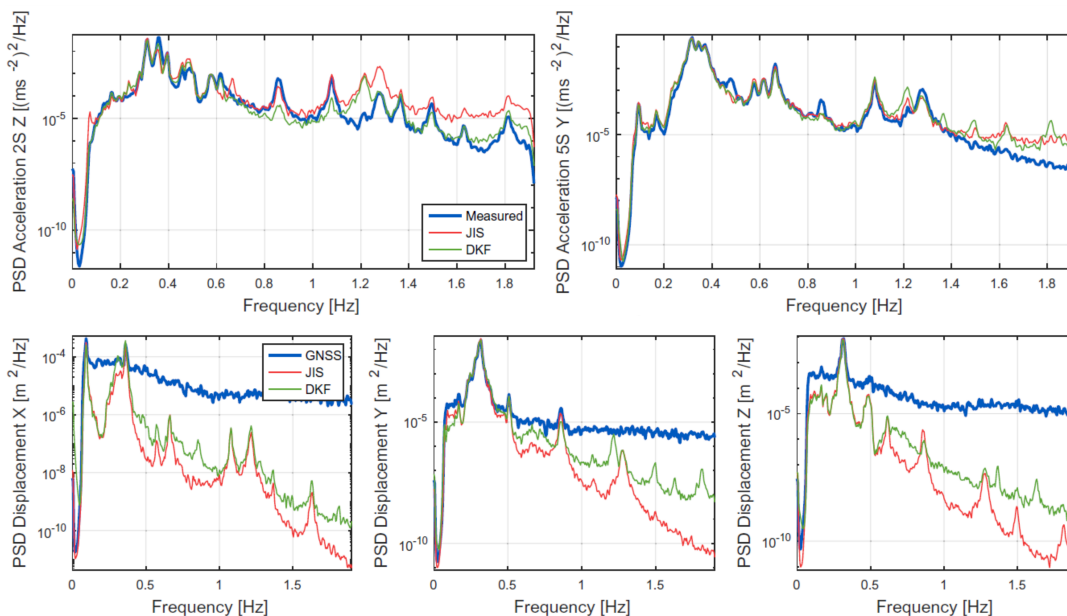


Figure 6.13: Displacement and acceleration measurements (Petersen et al., 2018).

The available data originates from different pontoons, which makes it difficult to compare the measurements. However, some important observations can be made to obtain information about the displacements and accelerations of the pontoons of a floating pontoon bridge. A comparison the response spectra of accelerations in vertical and lateral direction indicate that accelerations in sway show relatively higher peak values than the accelerations in heave. Furthermore, the displacements in the axial direction are negligible compared to the displacements in the lateral en vertical direction.

All other spectra show significant peaks around a frequency of 0,3 Hz. This coincides exactly with the peak which is visible in the variance wave spectrum of recording 3 (figure 6.12). This means that most wave energy is present around this frequency, which explains the peaks in the response spectrum. Therefore these peaks are not necessarily a sign of resonance and do not have to coincide with the eigenfrequencies of the system. The other peaks which are visible probably do coincide with eigenfrequencies but are relatively low due to the absence of excitation at those frequencies.

6.5. Conclusion

The literature review about the Bergsøysund bridge leads to the following conclusions:

- A lot of the structural properties of the Bergsøysund bridge are known. Additionally, measurements of the dynamic response are available. For these two reasons, this bridge is suitable to partly validate a parametric model which predicts the dynamic response of a floating bridge.
- The measurements of the Bergsøysund bridge show that the lateral (sway) and vertical (heave) motions are both DOFs showing a noticeable dynamic response. Sway is bigger than heave in these measurements. No conclusions can be made about the rotational DOFs, because measurements of rotations lacks in the data.
- The wave energy of the measured waves is concentrated between 1,5 and 3 rad/s with a wave peak frequency at 2,0 rad/s. This means that the peak wave period is 3,15 s.

II

Model development

7

Pontoon model

This chapter describes the approach which is used to model the floating behaviour of pontoons. Two different parts of the pontoon model are discussed: the structural pontoon model and the hydrodynamic pontoon model. Subsequently, the assumptions which are made to model the pontoon are discussed in section 7.2.

7.1. Pontoon model set-up

Two different pontoon models are developed: a structural model and a hydrodynamic model. The structural model is developed in Python and the hydrodynamic model is developed in Diffrac. The set-up of both models will be elaborated shortly.

7.1.1. Structural pontoon model

The structural pontoon model is a straightforward Python function to find the mass and stiffness matrix of a single pontoon based on its main dimensions and the assumptions mentioned in section 7.2. This model can be schematized with the following diagram:

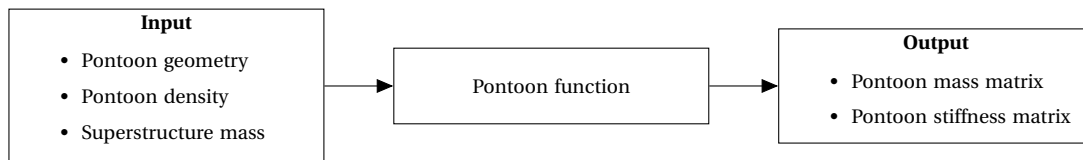


Figure 7.1: Flow scheme of the Python pontoon function.

Figure 7.1 shows that the dimensions and density of the pontoon and the superstructure's mass are required as input for the function. The mass of the pontoon can be calculated directly with these dimensions. With the mass of the different sections of the pontoon and the distance with respect to the CoG, the mass moments of inertia can be determined.

By adding the mass of the pontoon and the superstructure, the draft of the pontoon can be determined. Together with the geometry of the pontoon, the theory of section 5.1 is used to compute the hydrostatic properties of the pontoon and to assess hydrostatic stability.

Therefore, both the mass and stiffness matrices of the pontoon can be found using the structural pontoon model. Both of these matrices are 6 x 6 matrices containing values for every DOF.

7.1.2. Hydrodynamic pontoon model

A hydrodynamic pontoon model is developed using Diffrac. Diffrac is a numerical software package capable of modeling fluid-structure interaction by applying linearized potential theory. This theory is discussed in appendix D. The software is used to compute hydrodynamic properties of floating bodies in the frequency domain. A schematization of the model is presented in figure 7.2.

Figure 7.2 shows that the input parameters of the Diffrac model determine the discretization of both the frequency and the angle of incidence. The added mass, hydrodynamic damping and wave force transfer

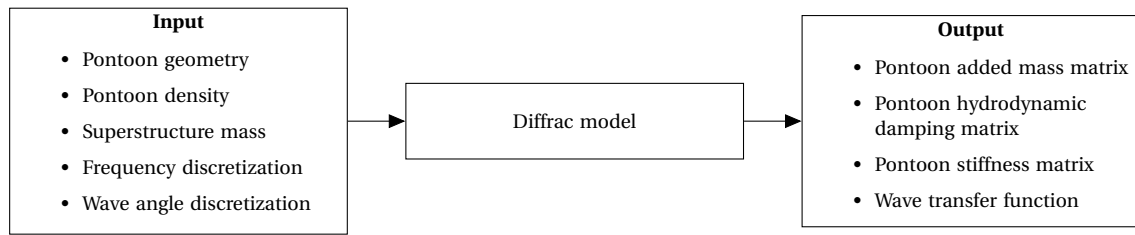


Figure 7.2: Flow scheme of the Diffrac pontoon model.

functions are all 6×6 matrices for every discretized frequency. The stiffness matrix is a 6×6 matrix analogous to the one computed by the Python function. A visualization of the input file of the pontoon is shown in figure 7.3. This figure shows that the surface of the pontoon is divided into multiple panels. The software solves the potential functions for every panel and combines these solutions to compute the hydrodynamic properties of the whole structure.

Another feature of Diffrac is to include multiple bodies to investigate interaction of the hydrodynamic behaviour. In this case, multiple pontoons are included in one file. With a distance of 110 meters between the pontoons, this interaction is negligible. However, in case of a shorter distance between two pontoons, this should be taken into account.

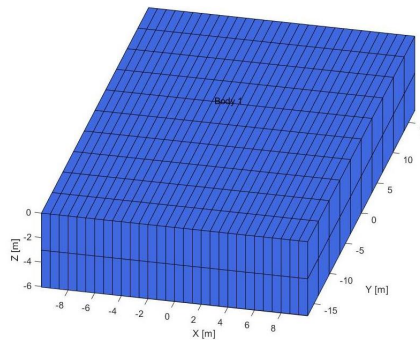


Figure 7.3: Pontoon modelled in diffrac.

7.1.3. Numerical input values

The following input values are used to model the dynamic response of the Bergsøysund bridge:

Parameter	Value	Unit
Pontoon		
Length (L_p)	20,0	m
Width (W_p)	34,0	m
Height (H_p)	6,07	m
Wall thickness (t_p)	0,25	m
Density (ρ_p)	2000	kg/m^3
Superstructure		
Surface area (A_s)	0,557	m^2
Span Length (L_s)	110	m
Density (ρ_s)	7800	kg/m^3
Discretization		
Frequency step ($\Delta\omega$)	0,025	rad/s
Frequency range ($[\omega_0.. \omega_n]$)	[0 .. 5]	rad/s
Wave direction step ($\Delta\psi$)	5	$^\circ$

Table 7.1: Input parameters of the model

7.2. Assumptions of the pontoon model

Several assumptions are made to model the floating behaviour of the pontoons. The validity of these assumptions must be checked in order for the model to be consistent with itself.

Wave spectrum

A Jonswap spectrum is assumed to represent the wave conditions. Kvåle and Øiseth (2017) states that the one parameter Pierson–Moskowitz spectrum is not able to represent the wave conditions around the Bergsøysund bridge correctly as it overestimates the peak periods. According to Holhuijsen (2010), the Jonswap spectrum is more suited for young sea states compared to the Pierson–Moskowitz spectrum. Due to the presence of the fjords, which limit the effective fetch length, this is the case at the Bergsøysund bridge.

Viscosity

Viscous effects such as viscous friction, flow separation or formation of vortices are not taken into account while determining the wave forces. The ratio between the wave height and the dimensions of the pontoon is small enough to neglect viscosity compared to inertia and gravitational effects (figure D.2a). This figure shows that around a ratio of 7, viscous effects become important. This is only the case for slender structures, which does not include pontoons. Therefore no drag force is taken into account. Subsequently, all assumptions required to allow the application of the potential theory are made. Flow is assumed to be homogeneous, continuous, incompressible and irrotational.

Rigid body

The pontoon is assumed to be infinitely stiff and is therefore treated as a rigid body. This is a realistic assumption, because the stiffness of the concrete pontoons is significantly higher than the bending stiffness of the superstructure.

Pontoon dimensions

The structure of a pontoon is schematized as a square box without internal walls. This means that the round shape at the edges is neglected and the mass moment of inertia will exceed reality slightly. A single wall thickness is assumed, where the bottom is twice the thickness of the other walls. The main reason for this simplification is to reduce the complexity of the hydrodynamic analysis. Using a square box for the pontoons enables easier scaling which is required for the parametric study.

Pontoon differences

From the seven pontoons in the Bergsøysund bridge, the outer two deviate slightly in dimensions from the other five. All pontoons are assigned the same dimensions in the model, so it is assumed that the outer two pontoons have the same dimensions as the rest.

Deep water

The pontoons of the floating bridge are assumed to be located in deep water ($d > 0,5L_w$). This is a valid assumption since the depth is 300 m and the measured wave lengths reach up to 15 m. The dispersion relation now reduces to: $\omega^2 = k_w g$.

Wave-body-current interaction

The effect of currents is not taken into account in the computation of the hydrodynamic properties. The current is assumed to only exert a static force on the pontoons.

8

Floating bridge model

The Bergsøysund bridge is shown in figure 8.1. Figure 8.2 is a schematization of this part of the bridge. In this schematization the different disciplines of theory which are required to model a floating bridge are indicated. The associated numbers refer to the sections where this theory is explained. This chapter explains how this theory is combined in a parametric model which is able to compute the dynamic response of a floating pontoon bridge.

First the general structure of the model is introduced in section 8.1. Four different models (figure 8.3) are constructed according to this general structure. These models increase gradually in complexity. This step-by-step method allows for simple test cases to validate the model. The most complex *Three-dimensional model* is discussed in detail in section 8.2. A detailed description of the simpler models, the *Rigid body model*, *Two pontoon plane frame model* and *Seven pontoon plane frame model* can be found in appendix F. For a thorough comprehension of the model development, it is recommended to study all these appendices. However, references are made in this chapter towards the important concepts which are introduced in those simpler models. Finally, the most important assumptions which are used to develop these models are summarized in section 8.3.



Figure 8.1: Picture of two pontoons of the Bergsøysund bridge.

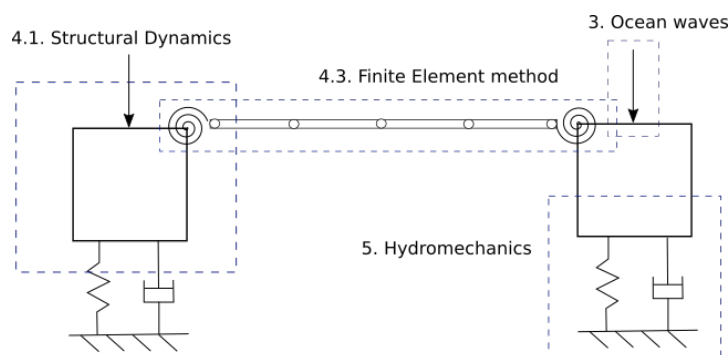


Figure 8.2: Schematization of a floating bridge with two pontoons.

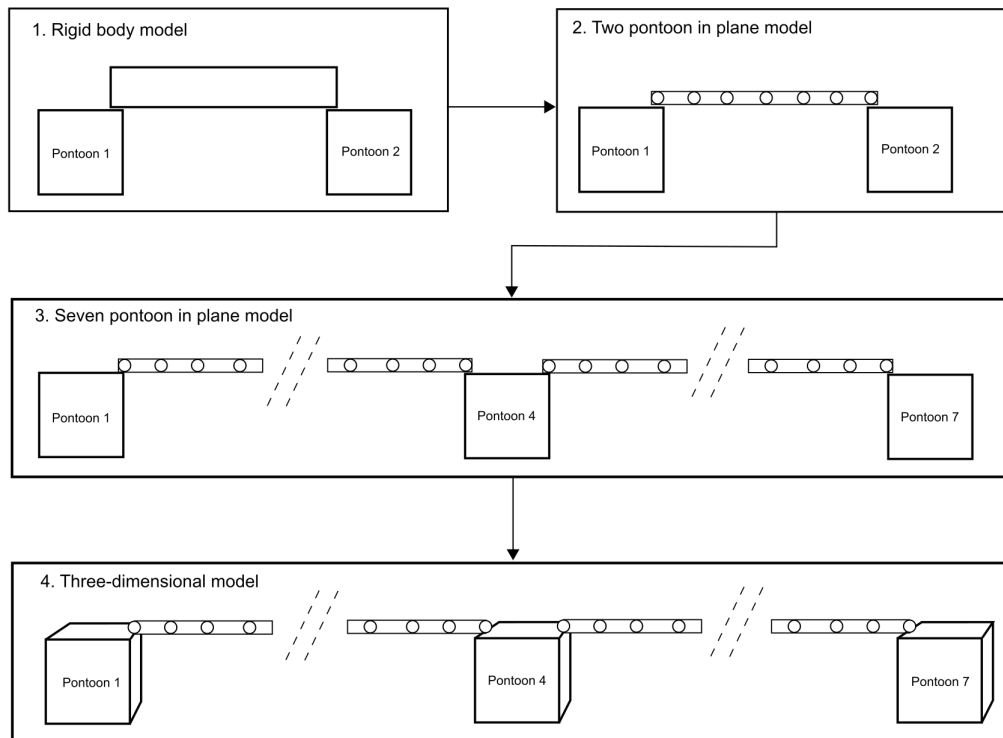


Figure 8.3: Overview of the different models.

Figure 8.3 shows the development from the most simple model to the most complex model. A summary of the properties of these models is given in table 8.1.

Model	Rigid body model	Two pontoon in plane model	Seven pontoon in plane model	Three-dimensional model
Documented section	Appendix E1	Appendix E2	Appendix E3	Section 8.2
Rigid bodies	✓	✓	✓	✓
Plane frame elements	×	✓	✓	✓
Number of pontoons	2	2	7	7
Types of DOFs	2	3	3	6
Total number DOFs	6	23	161	336
Damping included	×	✓	✓	✓

Table 8.1: Summary of the properties of the different models.

8.1. Model set-up

Chapter 7 explains the structural and hydrodynamic analysis of a floating pontoon. The *structural pontoon model* and the *hydrodynamic pontoon model* are basically two functions which are integrated into the floating bridge model. Figure 8.4 is a flow scheme of the complete floating bridge model. The pontoon function and Diffrac function are parts of this model.

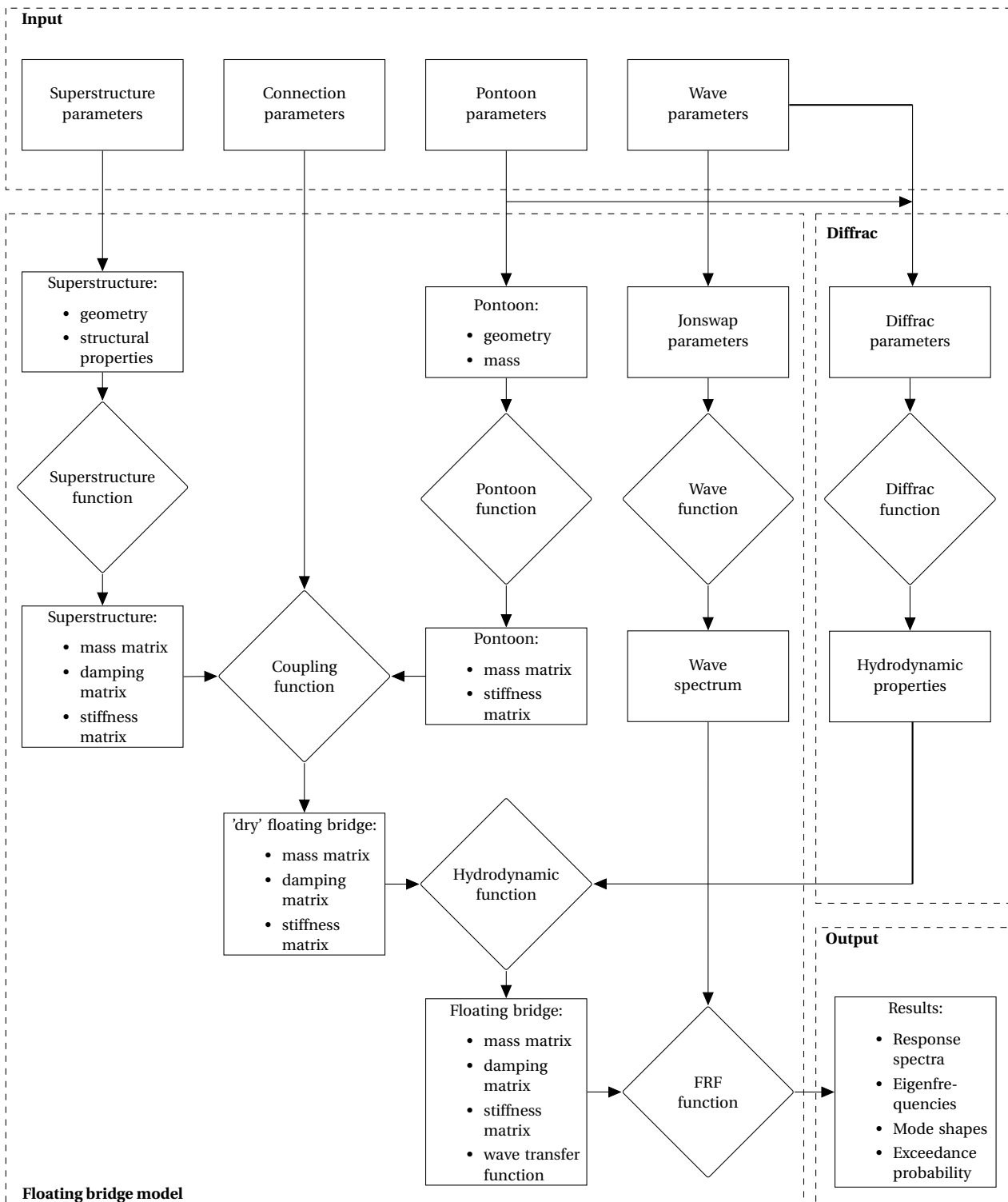


Figure 8.4: Set-up of the model.

Input parameters

The model requires a set of input parameters. The input parameters are divided into different categories (table 8.2). The pontoon parameters determine the geometry and density of all pontoons. The superstructure parameters represent the cross section of the floating bridge as well as the structural properties of the superstructure. The connection parameters describe the structural schematization of the bridge. Finally, the

wave conditions are determined by the wave parameters. Table 8.2 shows the numerical input values of the Bergsøysund bridge. Only the wave direction perpendicular to the floating bridge is used here.

Parameter	Value	Unit
Pontoon		
Length (L_p)	20	m
Width (W_p)	34	m
Height (H_p)	6.07	m
Wall thickness (t_p)	0.25	m
Density (ρ_p)	2000	kg/m ³
Superstructure		
Surface area (A_s)	0,593	m ²
Span Length (L_s)	110	m
Density (ρ_s)	7800	kg/m ³
Elasticity (E_s)	210000	MPa
Damping parameter (α)	0,005	-
Damping parameter (β)	0,005	-
Connection		
Connection rotational stiffness ($K_{c,\phi}$)	$3,0 \cdot 10^{10}$	Nm/rad
Connection rotational stiffness ($K_{c,\theta}$)	$1,5 \cdot 10^{11}$	Nm/rad
Connection rotational stiffness ($K_{c,\psi}$)	$3,0 \cdot 10^{11}$	Nm/rad
Support stiffness ($K_{s,x}$)	$5,90 \cdot 10^6$	Nm/rad
Support stiffness ($K_{s,y}$)	$2,14 \cdot 10^8$	Nm/rad
Support stiffness ($K_{s,z}$)	$1,30 \cdot 10^8$	Nm/rad
Support stiffness ($K_{s,\phi}$)	$2,09 \cdot 10^9$	Nm/rad
Wave conditions		
Wind speed (U_{10})	19	m/s
Fetch (F_J)	54	km
Peak enhancement parameter (γ_J)	3,3	-

Table 8.2: Input parameters of the model

Superstructure function

The superstructure function assembles the mass, damping and stiffness matrices of the superstructure based on FE theory. The structural properties, the number of nodes and included DOFs are variable.

Pontoon function

The pontoon function computes the mass and stiffness matrices of the pontoons. This process is explained in chapter 7. An example of this procedure is given in the *rigid body model* (appendix E.1).

Wave function

The wave function computes a Jonswap wave spectrum based on the wave parameters. A discretized frequency range from 0 to 5 rad/s is used here.

Diffrac function

The pontoon function computes the added mass, hydrodynamic damping and wave force transfer functions of the pontoons. This process is explained in more detail in chapter 7.

Coupling function

The coupling function connects the superstructure and the pontoons. Rotational springs are used to define the connection between these elements. Furthermore, boundary conditions are specified and imposed by this function. This process is explained in detail in section 8.2.

Hydrodynamic function

The hydrodynamic function adds the added mass and hydrodynamic damping matrices to the 'dry' floating bridge matrices. A frequency range from 0 to 5 rad/s is used here. For every discretized frequency, the added mass and hydrodynamic damping matrices are added to the system. This results in different mass and damping matrices for every discretized frequency. The stiffness matrix remains constant over the frequency range.

FRF function

First the wave force spectra are computed using the wave spectrum and the wave transfer function. The wave force spectrum represents the variance of the wave force for every frequency. Subsequently, the FRF is computed using equation 4.19. The wave force spectrum and the FRF both vary over the frequency. Finally, the response spectra are produced using the wave force spectra and the FRF. This whole process is illustrated in figure 8.5.

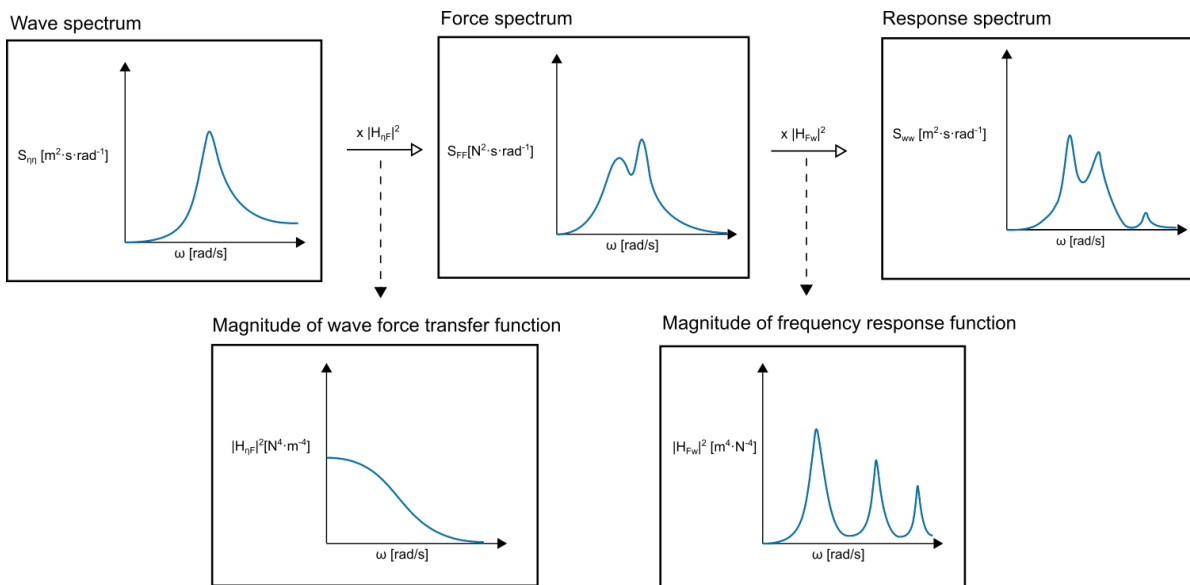


Figure 8.5: Summary of the modeling steps using transfer functions.

8.2. Three-dimensional model

The *Three-dimensional model* computes the dynamic response of a floating bridge which is excited by waves. The model consists of rigid bodies (pontoons) and Euler-Bernoulli elements (superstructure). These are coupled through rotational springs and rigid connections. These connections are explained in more detail in the *Two pontoon in plane model* (appendix E.2). The coupling between the superstructure is imposed with boundary conditions. Every node includes all six DOFs. This is illustrated in figure 8.6. The hydrodynamic damping and hydrostatic stiffness are schematized using linear dashpots and springs.

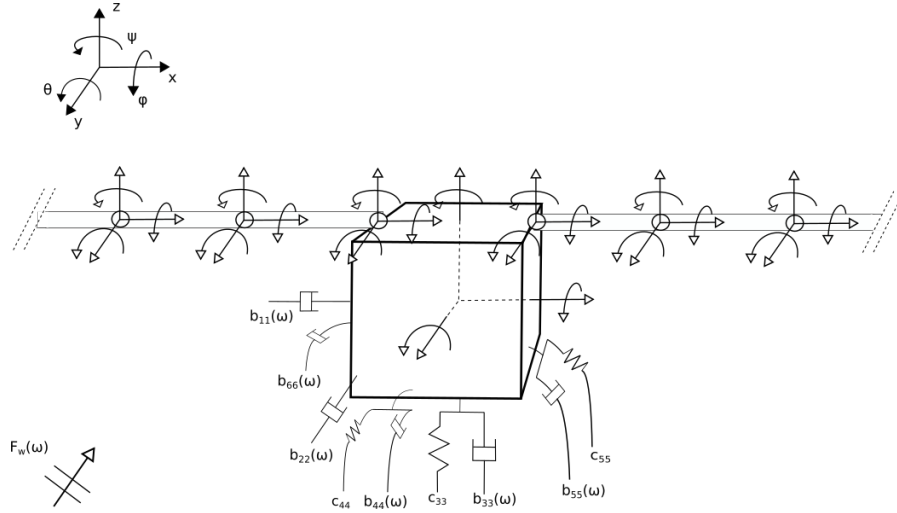


Figure 8.6: Schematization of the three-dimensional model.

The rotational springs which are used to model the connection between the superstructure and the pontoons are not included in figure 8.6 to keep the overview clear. Figure 8.7 shows these connections, but only for three DOFs. Figure 8.7 actually shows the *Seven pontoon in plane model*, which is elaborated in detail in appendix E3. However, *Three-dimensional model* only adds the DOFs sway, roll and yaw to this model. On both sides of the model, linear springs are used to model the abutments of the floating bridge.

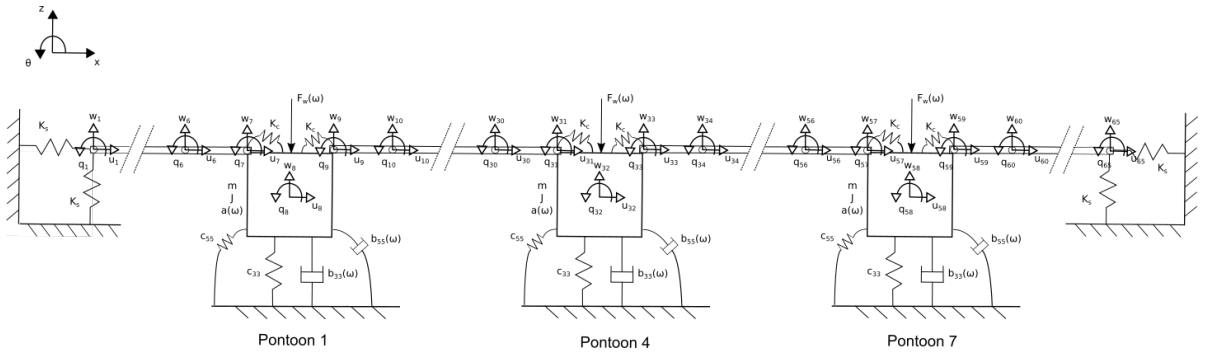


Figure 8.7: In plane model with seven pontoons

The connections between the pontoons and the superstructure are modeled rigidly and with rotational springs. The translations of the pontoon and the final node of the superstructure are connected rigidly, whereas the rotations are modeled through rotational springs. This can be described using boundary conditions. The master slave method (Felippa, 2004) is used to impose these boundary conditions. This essential procedure is explained in more detail in the simpler *Two pontoon in plane model* (appendix E2). The boundary conditions of the *Three-dimensional model* are:

$$\begin{aligned}
 u_{p+1} &= u_p - \frac{1}{2} H_p \cdot q_p \\
 v_{p+1} &= v_p - \frac{1}{2} W_p \cdot r_p \\
 w_{p+1} &= w_p + \frac{1}{2} L_p \cdot q_p \\
 u_{p-1} &= u_p - \frac{1}{2} H_p \cdot q_p \\
 v_{p-1} &= v_p + \frac{1}{2} W_p \cdot r_p \\
 w_{p-1} &= w_p - \frac{1}{2} L_p \cdot q_p
 \end{aligned} \tag{8.1}$$

Connections

The connections between the pontoons and the superstructure are modeled with linear rotational springs. The translational connection is assumed to be rigid. The flexibility of rotations can be modified by adjusting the spring stiffness.

Multiple plane frames

Multiple distinct plane frames are used to schematize the superstructure. Those plane frames are always connected to the corner of the pontoon. This assumption allows for some flexibility in the structural system of the bridge.

Single wave direction

Only a wave direction perpendicular to the superstructure is taken into account in the floating bridge model. The highest waves will originate from this direction and therefore this direction is assumed to be the dominant wave direction.

Bridge alignment

The alignment of the bridge is assumed to be straight in the model, where the actual alignment of the Bergsøysund bridge is curved. This is done to reduce the complexity of the parametric model.

Supports

The fixed supports on the abutments, consisting of longitudinal rods and rubber slabs are modeled with linear springs.

Cross section

The cross section of the superstructure is assumed to be uniform along the length. In the case of the Bergsøysund bridge, this cross section varies along the length. A cross section with average dimensions is chosen to represent the whole superstructure. Furthermore, the second moments of area are calculated using only the main structural elements of the superstructure. In a truss structure, the global structural system will determine the dynamic behaviour of the bridge as a whole.

Isotropic material

The material of the superstructure is assumed to behave isotropically. In the case of the Bergsøysund bridge this is a realistic assumption, because the superstructure consists of steel. In the case of an FRP superstructure, this is an important simplification. When the dynamic response is of interest, this assumption is probably realistic, because the average properties are of interest. However, when internal stresses become of interest, this assumption should be reconsidered.

Structural damping

The structural damping is assumed to be proportional and is modeled with Rayleigh damping. This assumption is often made when structural damping is modeled. This damping is probably relatively small compared to the hydrodynamic added damping.

Narrow banded spectrum

Peaks of a narrow-band process can be described using a Rayleigh distribution. This assumption is used to find an upper limit exceedance value with a given probability.

III

Validation

Modeling results of the Bergsøysund bridge

This is the first chapter of part III that describes the validation of the model. This chapter presents and explains the results of both the pontoon and the floating bridge model. The intention of this chapter is to present a thorough understanding of the underlying principles of the dynamic response of the Bergsøysund bridge. This knowledge is applied in the parametric study. First the results of the pontoon model are discussed in section 9.1. Subsequently, the results of the floating bridge model are presented in section 9.2.

9.1. Results pontoon model

The modeling results of the pontoon model using the input from table 7.1 are presented and evaluated here. In the evaluation of the results, the following three aspects are discussed:

- General description and discussion of the results
- Physical explanation of the results
- Effect of the results on the dynamic response

The results considering the translations and rotations are presented and discussed separately. The numerical values of the rotations will often exceed the numerical values of the translations significantly, because the translations are associated with forces and the rotations are associated with moments. It must therefore be noted that the scale of the plots considering translations and rotations are different.

9.1.1. Mass and stiffness matrices

The structural pontoon function computes the mass and hydrostatic stiffness matrices of the floating pontoons of the Bergsøysund bridge:

$$\mathbf{M}_p = \begin{bmatrix} 1,30 \cdot 10^6 & 0 & 0 & 0 & 0 & 0 \\ 0 & 1,30 \cdot 10^6 & 0 & 0 & 0 & 0 \\ 0 & 0 & 1,30 \cdot 10^6 & 0 & 0 & 0 \\ 0 & 0 & 0 & 3,82 \cdot 10^7 & 0 & 0 \\ 0 & 0 & 0 & 0 & 2,74 \cdot 10^7 & 0 \\ 0 & 0 & 0 & 0 & 0 & 5,11 \cdot 10^7 \end{bmatrix} \quad \mathbf{K}_p = \begin{bmatrix} 0 & 0 & 0 & 0 & 0 & 0 \\ 0 & 0 & 0 & 0 & 0 & 0 \\ 0 & 0 & 6,83 \cdot 10^6 & 0 & 0 & 0 \\ 0 & 0 & 0 & 6,45 \cdot 10^8 & 0 & 0 \\ 0 & 0 & 0 & 0 & 2,15 \cdot 10^8 & 0 \\ 0 & 0 & 0 & 0 & 0 & 0 \end{bmatrix}$$

The hydrostatic spring stiffness only exists in heave, roll and pitch. This makes sense, because the other DOFs experience no restoring force under a displacement. Therefore the total restoring spring stiffness is 0 in those directions. Of course, in a floating bridge model the superstructure provides stiffness in all DOFs.

Heave is the only translation experiencing a hydrostatic restoring force. Equation 5.7 shows that this restoring force increases when the surface area A_{wl} increases. The hydrostatic spring stiffness of the rotations is highest in roll direction. This means that this motion will experience the most resistance. Equation 5.7 shows that the only difference between the spring stiffness in roll and pitch is determined by the distance \overline{GM} . Equation 5.3 shows that a smaller \overline{KG} will increase the rotational springs stiffness in roll and pitch. This can be achieved by for example increasing the weight of the bottom. Furthermore, equation 5.7 shows that increasing the surface area A_{wl} also increases the rotational spring stiffness.

9.1.2. Added mass

The added mass is a part of the reaction force that is in phase with the acceleration. The structure experiences this force due to the relative motion of the structure with respect to the waves. Diffrac computes the added mass components of the pontoon. The diagonal of the added mass matrix of the Bergsøysund bridge pontoon model is plotted in figure 9.1. The "dry" mass and mass moments of inertia are plotted with dotted lines as a reference. The vertical dashed line represent the wave peak frequency. The translations and rotations are shown in respectively the left and right figure.

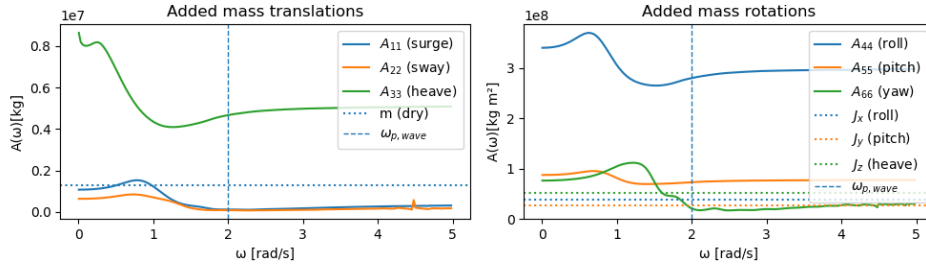


Figure 9.1: Added mass coefficients compared to the "dry" mass.

It is clear that the added mass is highly frequency dependent in the low frequency range and converges to a constant value in the higher frequency range for all components. Additionally, it turns out that, the added mass in all directions is in the same order of magnitude as the "dry" mass and mass moments of inertia or even larger. All added mass components in figure 9.1 show a somewhat similar shape. First the added mass grows to a peak between frequencies of approximately 0,3 and 1,3 rad/s. Subsequently, the graphs reach a minimum between 1 and 2 rad/s and finally the graphs convert to a constant value around 3 rad/s. General relations between the geometry of the structure and the added mass can be found for simple structures such as pontoons and are presented here. The wave peak frequency is indicated with the vertical dashed line.

Especially the added mass in heave direction is significantly higher than the "dry" mass compared to the other translations. This can be explained by a physical explanation of added mass. It can be interpreted as the mass of the water particles which needs to be accelerated in order to meet all the boundary conditions related to the fluid (Karlberg, 2014). The surface area "pushing" water away in heave is the largest of all translations.

For the rotational DOFs the individual mass moments of inertia are compared to the according added mass. The right plot of figure 9.1 shows that the added mass in roll is significantly higher than the "dry" mass moment of inertia. The high amount of added mass in roll is also explained by the amount of water particles which is "pushed" away. With the width-over-length ratio being bigger than 1, the added mass in roll will be larger than in pitch.

A higher mass results in a lower eigenfrequency according to equation 4.3. The high added mass components of heave and roll of the pontoon will therefore decrease the eigenfrequency of the modes associated to these motions. This is demonstrated in figure 9.2. This plot shows the variation of the eigenfrequencies on the vertical axis over the frequency on the horizontal axis. These eigenfrequencies are the theoretical eigenfrequencies of a single floating pontoon without any constraints of a superstructure. They are shown to illustrate the effect of the added mass on the eigenfrequencies. The solid lines represent the eigenfrequencies including the added mass and the dotted lines are the eigenfrequencies without the added mass. The eigenfrequencies including added mass fluctuate approximately 0,3 rad/s over the frequency range from 0 to 5 rad/s. It can be concluded that the dimensions of the pontoon have a significant influence on the added mass and therefore on the eigenfrequencies and the dynamic response of the pontoon.

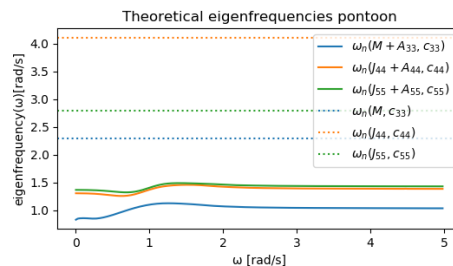


Figure 9.2: Effect of the added damping on the theoretical eigenfrequencies of a floating pontoon.

9.1.3. Hydrodynamic damping

The diagonal of the hydrodynamic damping matrix of the Bergsøysund bridge pontoon model is plotted in figure 9.3. The hydrodynamic damping is the part of the reaction force that is in phase with the velocity. The motion of the structure creates new waves, which dissipates energy. Again the translations and rotations are separated.

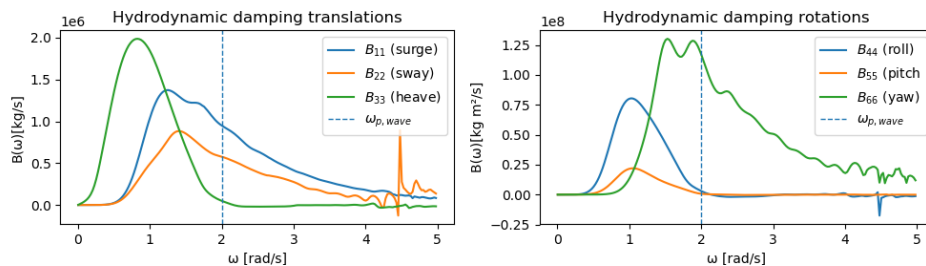


Figure 9.3: Hydrodynamic damping coefficients.

All hydrodynamic damping components of translations start at zero and increase to a different peak value at frequencies between 0,8 and 1,4 rad/s. The highest peak value is found in heave. Regarding the rotations, the yaw hydrodynamic damping is significantly higher than roll and pitch. A strange peak is noticeable for sway around 4,5 rad/s. This peak is caused by a numerical issue, but its influence on the dynamic response is negligible.

General relations can be found for the hydrodynamic damping of a simple structure such as a pontoon based on the physical interpretation of the hydrodynamic damping. The hydrodynamic damping dissipates energy from the system. Therefore, it makes sense that the hydrodynamic damping starts at zero, because the structure "follows" the wave motion when the wave length and period are infinitely large. The relative motion between the waves and the structure is zero and no waves are created to dissipate energy.

The magnitude of the peaks in hydrodynamic damping coefficients of the translations is caused by the surface area of the pontoon facing the waves. A larger surface area will generate more waves, which requires more energy.

The higher the damping in a direction, the lower the dynamic response in that direction will be. It can be concluded that the dimensions of the pontoon have a significant influence on the hydrodynamic damping and therefore on the dynamic response of the pontoon.

9.1.4. Wave force transfer function $H_{\eta F}$

The wave force transfer functions are plotted in figure 9.4. The transfer function $H_{\eta F}$ contains 6 x 1 vectors for every discretized frequency and every discretized angle of incidence. The presented results are based on incoming waves along the y axis, which is the governing wave direction in the case of the Bergsøysund bridge due to the bathymetry of the fjords.

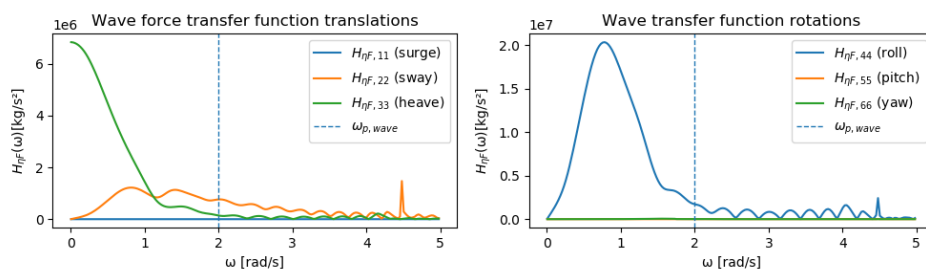


Figure 9.4: Transfer function between the wave spectrum and the force spectrum for a specific wave angle.

The wave force transfer function represents the relation between the wave elevation and the wave force which acts on the structure for every frequency. This wave force is divided into a positive Froude-Krilov force and a negative diffraction force. The Froude-Krilov force represents the pressure which the water particles exert on the structure. The wave force transfer functions of surge, pitch and yaw have negligible values, because

only waves in sway direction are taken into account. Either the waves are parallel to these motions (surge and pitch) or the waves forces balance each other out (yaw).

Regarding the translations, heave starts at a maximum and decreases fast until 1 rad/s. From here it converges slowly to 0. The sway wave force transfer function starts at zero and increases to a maximum value around 0,8 rad/s. From there it decreases with small oscillations. The transfer function of roll also starts at 0 and has a peak around 0,8 rad/s. Then it decreases fast to become almost 0 at a frequency of 1,6 rad/s. At the wave peak frequency the wave force transfer function is largest in sway direction.

The main difference between the heave and sway wave transfer functions is that long waves (low frequency) will excite heave more and short waves (high frequency) will excite sway more. This is caused by the fact that long waves contain more energy at a greater depth than short waves. The transfer of wave energy in heave occurs at the bottom of the pontoon. For sway this happens over the whole draft of the pontoon. A high wave transfer function will lead to a large force and consequently to a high dynamic response.

9.1.5. Phase shift between the wave elevation and wave force

The phase shift between the wave elevation and the wave force is plotted in figure 9.5. No general relations can be drawn from these phase shifts.

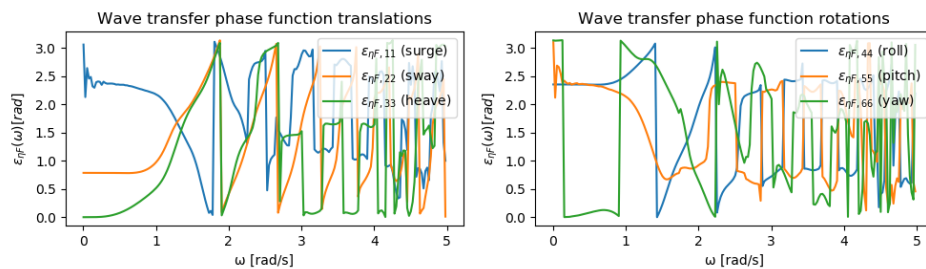


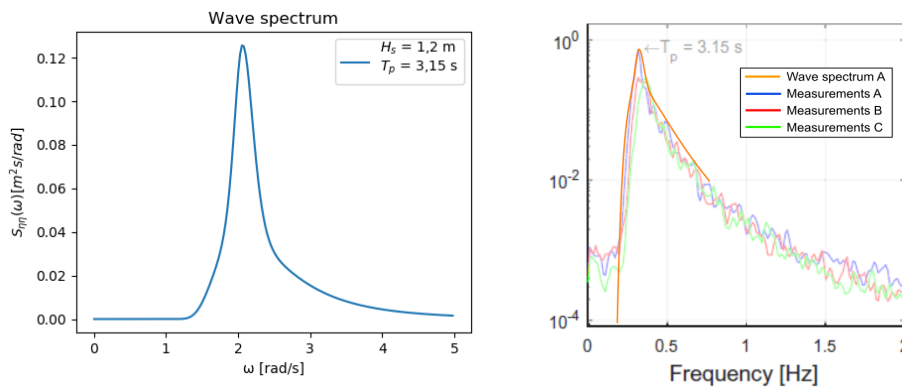
Figure 9.5: Phase shift between the wave elevation and the wave force for a specific wave angle.

9.2. Results floating bridge model

The floating bridge model computes the mass, damping and stiffness matrix of the entire floating bridge. This information is used to construct a FRF. Together with the wave force transfer function, this FRF can transform the wave spectrum into a response spectrum of a specific DOF at a specific node.

9.2.1. Wave forces

The wave spectrum representing the wave conditions at the Bergsøysund bridge is shown in figure 9.6a. In figure 9.6b this wave spectrum is compared to actual measurements at this location. The scale is logarithmic in this plot and only the wave conditions of measurement recording 3 are used in this case.



(a) Model results, normal scale.

(b) Model and measurements, logarithmic.

Figure 9.6: Wave spectrum representing the wave conditions measured at the Bergsøysund bridge.

The wave spectrum can be transformed into different wave force spectra using the wave force transfer functions presented in section 9.1. The wave force spectra of all DOFs are shown in figure 9.7. A logarithmic scale is used to be able to compare the force spectra of the different DOFs.

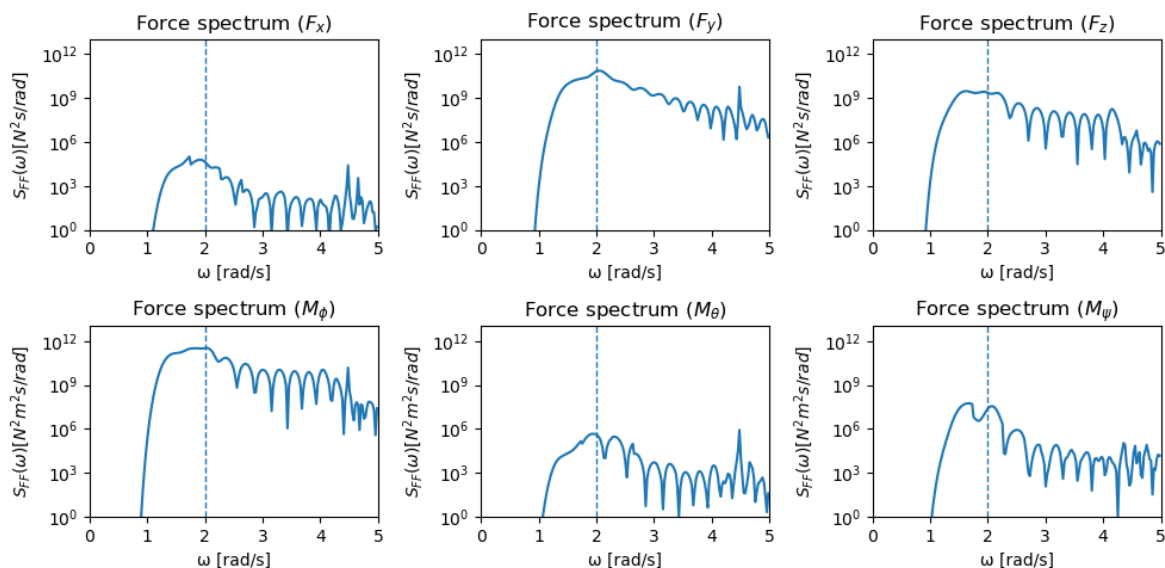


Figure 9.7: Force spectra representing the force input at a single pontoon.

All the wave force spectra reveal that most energy is concentrated around the wave peak frequency (vertical dashed line). However, it is also clearly visible that the shape of all force spectra differs because of the wave force transfer function. From the wave force spectra it can already be observed that the response will probably be dominated by vibrations with a frequency varying from 1 rad/s to 3 rad/s.

9.2.2. Pontoon response

Response spectra of both the pontoons and the middle nodes of the superstructure are computed. Only the response spectra of the pontoons are shown in this chapter. Appendix F.4 explains that the response of the pontoons is governing compared to the response of the superstructure.

The FRF is used to transform these wave force spectra into response spectra. A detailed explanation of this procedure is shown in appendix F. The pontoon's response spectra of all DOFs of the *Three-dimensional model* are presented in figure 9.8. 17 eigenfrequencies lie below a frequency of 5 rad/s and are included in these plots with the red vertical dashed lines. Because the model is symmetric, only the first four pontoons are presented in the plots. The response of the first pontoon will be identical to the last pontoon etc. The couples are included in the legends of the plots.

- Surge of the pontoons show clear narrow peaks 1,62 rad/s, 1,96 rad/s and 2,29 rad/s. The magnitude of these peaks are the lowest of all translations in the order of 10^{-6} .
- The sway response spectra are the highest in magnitude of all translations. Wide peaks are visible around 2,0 rad/s. The response spectra of the odd numbered pontoons are the largest in magnitude. The peaks are in the order of 10^{-2} .
- Response spectra of heave contain three narrow peaks at the same frequencies as the surge response spectra; at 1,62 rad/s, 1,96 rad/s and 2,29 rad/s. These peaks reach to a magnitude in the order of 10^{-3} .
- The roll response spectrum shows the highest peaks of all rotations. One clear narrow peak is visible at 1,81 rad/s with a magnitude in the order of 10^{-4} .
- The pitch response spectra of the pontoons shows peaks at the same frequencies as surge and heave. These peaks are in the order of 10^{-7} . This is the same as with the *seven pontoon in plane model*.
- Finally, the response spectra of yaw contain a wide peak at 2 rad/s with a magnitude in the order of 10^{-6} .

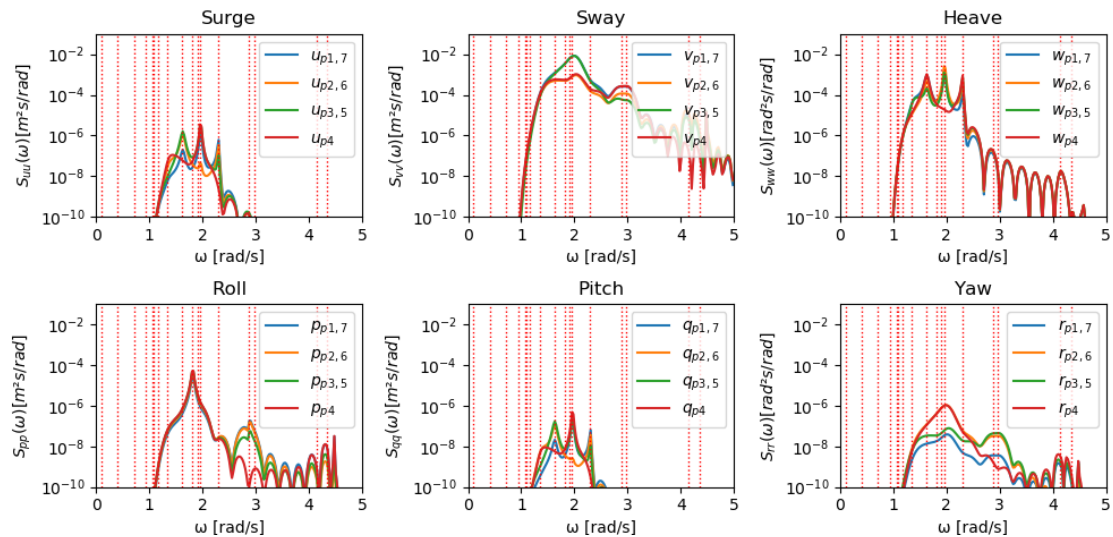


Figure 9.8: Reponse spectra of the pontoons of the 3d model.

The theoretical displacements with an exceedance probability of $6,68 \cdot 10^{-2}$ in a 100 year (equation 4.30) of the sway, heave and roll of all pontoons are summarized in table 9.1. Only these three DOFs are shown, because the amplitude of these motions is largest compared to the corresponding design criteria. This ratio is referred to as the unity check. A similar table of the accelerations is shown in appendix F4.

Pontoon	Sway [m]	$\frac{Sway}{Threshold}$	Heave [m]	$\frac{Heave}{Threshold}$	Roll [rad]	$\frac{Roll}{Threshold}$
1 & 7	0,19	0,60	0,05	0,16	0,0055	0,13
2 & 6	0,08	0,25	0,05	0,17	0,0065	0,15
3 & 5	0,19	0,60	0,04	0,14	0,0071	0,16
4	0,09	0,25	0,04	0,14	0,0073	0,17

Table 9.1: Displacement of sway, heave and roll of the pontoons with an exceedance probability of $6,68 \cdot 10^{-2}$ in a 100 year

Explanation of the pontoon responses

The wave force spectra (figure 9.7) and the FRF (figure 9.9) are used to explain the shape and magnitude of the response spectra corresponding to different DOFs. Sway appears to be the governing motion of the pontoons based on the ratio with the threshold values (table 9.1). This motion is therefore explained in more detail. The ratio between the lateral stiffness and the mass of the pontoons is in the order of 10^3 . Based on the theory explained in appendix C.3 it is concluded that the magnitude of the FRF is dominated by stiffness compared to the mass. At the resonance peaks, damping dominates the magnitude.

The peaks which are present in the FRF occur exactly at the eigenfrequencies of the system. These eigenfrequencies correspond to a specific mode shapes (figure 9.10). These mode shapes are used to explain the variation in the response spectra of the different pontoons.

- The narrow peaks of the surge spectra are mainly caused by and motion coupling with heave. In the heave response spectra peaks at the same frequencies are observed. Heave of the adjacent pontoons influences the surge of the middle pontoon, because both motions are coupled with pitch. The rotational spring at the connection between the pontoon and superstructure couples these motions.
- The sway response spectra of the pontoons are the largest in magnitude of all translations. Additionally, their unity check is largest of all motions. First of all, figure 9.7 shows that the force spectra of sway are highest in magnitude compared to the other translations. Additionally, the FRF of sway shows a wide peak around 2 rad/s (figure 9.9). The influence of the hydrodynamic damping (figure 9.3) at this frequency ensures that this peak remains smooth and wide compared to the first two narrow peaks.

The peak coincides with the fifth of blue dotted lines which represent the eigenfrequencies corresponding to the modes which excite sway. Thus, one would say that the fifth sway mode has a large influence

on the response spectra of the pontoons. However, the fourth blue dotted line also seems to lie within the frequency range where wave energy is concentrated. No peak is observed in the FRF at this frequency of 1,82 rad/s. This can be explained by looking at the mode shapes (figure 9.10). Although mode 10 is categorized as a mode that excites sway, it becomes clear from this figure that mode 11 dominates the sway response in this frequency range, because the amplitude of mode 11 is much higher than the amplitude of mode 10. The shape of mode 11 coincides with a theoretical fourth mode shape (figure B.2). Mode 11, or the fourth sway mode, also explains the difference in response between the pontoons. The odd numbered pontoons are clearly more excited than the even numbered pontoons.

- The three narrow peaks of the heave spectra coincide with the frequencies which correspond to modes 9, 12 and 13. This means that resonance occurs at the corresponding frequencies. These peaks can also clearly be observed in the FRF of heave (figure 9.9).
- The narrow peak of the roll spectra coincides with the frequency which corresponds to mode 10. Mainly roll is excited by this mode shape.
- The peaks of the pitch spectra are caused by motion coupling with the heave of the adjacent pontoons.
- The yaw spectra show a similar shape as the sway spectra. This is again caused by motion coupling through the rotational springs.

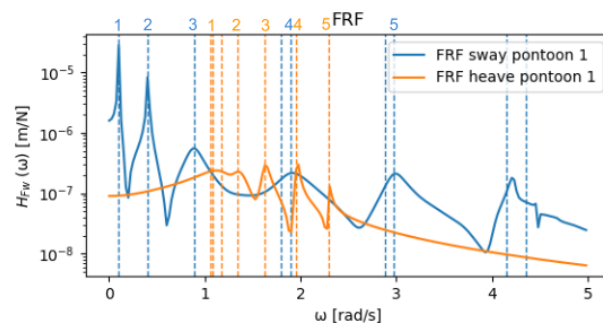


Figure 9.9: FRF components which represent the relation between the force and response in the sway and heave direction of pontoon 1.

When the complex eigenvalue problem is solved, the eigenvectors are obtained which represent the mode shapes of the system. The mode shapes corresponding to eigenfrequencies where wave energy is present are plotted in figure 9.10. The eigenfrequencies in the range between 0 rad/s and 5 rad/s are shown in table 9.2.

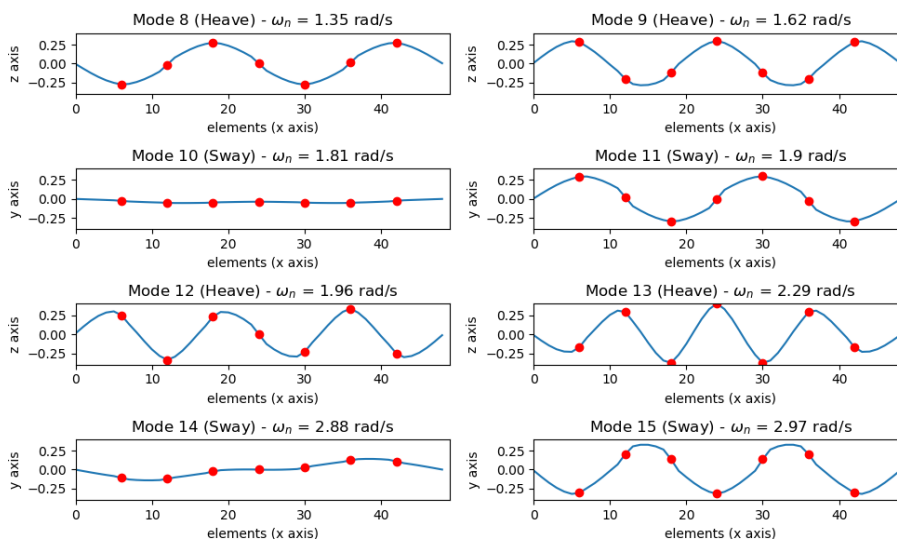


Figure 9.10: Mode shapes of mode 8 to mode 15.

Mode	Exciting DOFs	Components	ω_n [rad/s]
1	Sway	All	0,10
2	Sway	All	0,41
3	Surge	All	0,72
4	Sway	All	0,94
5	Heave	All	1,07
6	Heave/Surge	All	1,09
7	Heave	All	1,17
8	Heave	All	1,35
9	Heave	All	1,62
10	Sway/Roll	All	1,81
11	Sway	All	1,90
12	Heave	All	1,96
13	Heave	Pontoons	2,29
14	Sway	All	2,88
15	Sway/Roll	All	2,97
16	Sway	All	4,15
17	Sway/Roll	All	4,35

Table 9.2: Classification of the first 17 modes of the *three-dimensional model*.

9.3. Conclusion

The results of both models lead to several conclusions. These conclusions are separated per model. These conclusions contribute to the understanding of the Bergsøysund bridge's dynamic response and are used in the parametric study.

9.3.1. Conclusion pontoon model

Several general conclusions are drawn based upon the results of the hydrodynamic analysis of the pontoon and the theory of hydrodynamics. These conclusions contain general relations between the input parameters, the resulting eigenfrequencies and the dynamic response. They are valid for the frequency interval between 0 and 5 rad/s.

It is assumed that an increase in wave force leads to a higher dynamic response. Furthermore, the frequency range where the wave energy is concentrated is not taken into account here. Without any excitation source, the dynamic response will stay zero. Finally it is assumed that increasing the stiffness leads to an overall reduction in the FRF (equation 4.19).

- The hydrostatic stiffness in heave c_{33} increases when the surface area A_{wl} increases. This will increase the eigenfrequencies which correspond to the modes that excite heave. Additionally it will reduce the overall FRF associated to the modes that excite heave.
- The hydrostatic stiffnesses in roll c_{44} and pitch c_{55} will both increase when \overline{KG} decreases, and when the surface area A_{wl} increase. When c_{44} and pitch c_{55} are increased, the eigenfrequencies belonging to the modes where roll and pitch are excited will shift upwards.
- All added mass components increase when the corresponding surface areas displacing water increase. When for instance the surface area which displaces water in heave increases, the eigenfrequencies belonging to heave modes will shift to a lower frequency.
- All hydrodynamic damping components increase when the corresponding surface areas displacing water become larger. The dynamic response will be reduced due to a larger amount of damping. Furthermore, the eigenfrequencies will shift slightly.
- The wave force transfer function components become larger when the surface area perpendicular to the main wave direction increases. Consequently, a larger force excites the pontoon which generally increases the dynamic response.

9.3.2. Conclusion floating bridge model

The following conclusions are drawn based upon the results of all four models of the Bergsøysund bridge:

- Sway is the translation with the highest absolute response. Furthermore, sway results in the highest unity check of the deflection criteria. The theoretical amplitude of the pontoon's sway with an exceedance probability of $6,68 \cdot 10^{-2}$ in a 100 year is 0,19 m. This results in a unity check of 0,6.
- The magnitude of the pontoon's sway originates from a combination of the wave force spectrum with a large peak at 2,0 rad/s and the influence of the fourth sway mode (mode 11) at a frequency of 1,90 rad/s ($T = 3,31$ s). It is concluded that this mode dominates the dynamic response of the floating bridge. This mode and the adjacent sway modes are shown in figure 9.11.
- The odd numbered pontoons experience the largest sway excitation. This is caused by the shape of the fourth sway mode (mode 11). Furthermore, the response of all odd numbered pontoons is almost identical. The same goes for the even numbered pontoons. As long as the fourth sway mode is dominant for the dynamic behaviour, the dynamic response of the odd pontoons is governing.
- The ratio between the components of the stiffness matrix and mass matrix in sway direction are in the order of 10^3 . This means that the magnitude of the dynamic response in sway is dominated by the stiffness instead of the mass of the structure.
- The response of the pontoons exceeds the response of the adjacent parts of the superstructure when the wave sources are the only source of excitation. The superstructure tends to follow the motion of the pontoons. From now on only the pontoon motions are taken into account.

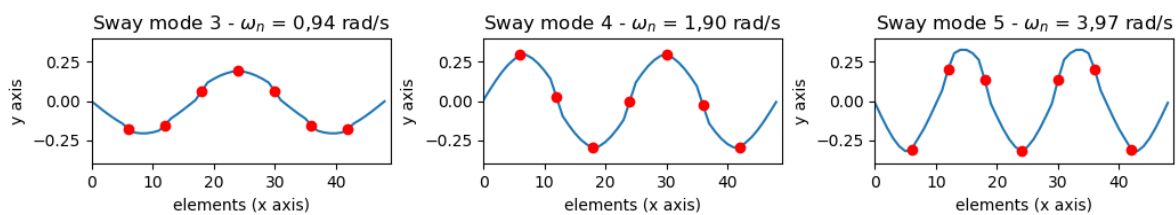


Figure 9.11: Sway mode 3, 4 and 5.

10

Validation

The floating bridge model must be validated before it can be used in a parametric study. This validation consists of three steps. First the results from the Diffrac model are verified using previous research on floating structures (section 10.1). Although the numerical software is already extensively validated, this verification is still required to prevent human errors. Hence, it is sufficient to show that the results are correct in order of magnitude and course over the frequency range.

Furthermore, the theoretical eigenfrequencies of an Euler-Bernoulli beam are used to validate the dynamic properties of the superstructure (section 10.2). Finally, the complete floating bridge model is validated in section 10.3 with the measurement data of the Bergsøysund bridge.

10.1. Validation of the pontoon model

The results of the Diffrac simulations are validated in two ways. A lot of research has already been carried out to predict hydrodynamic coefficients. Kolkman and Jongeling (2007) and Vugts (1971) both investigated hydrodynamic behaviour of floating structures in deep water. Therefore these researches are suitable for the validation of the Diffrac results.

10.1.1. Kolkman & Jongeling

Kolkman and Jongeling (2007) carried out experiments at Delft Hydraulics to investigate the dynamic behaviour of floating structures. With the measurements of these experiments, general formulas were derived to make an estimate of the added mass:

$$\begin{aligned} A_{11} &= 0,25 \rho \pi a^2 B \\ A_{33} &= 0,75 \rho \pi a^2 B \end{aligned} \quad (10.1)$$

These simple formulas can only be used to estimate the order magnitude of the added mass in heave and surge. A relation between the added mass and the frequency is absent in these formulas. Nevertheless, it can serve as a good starting point of a rough validation. Figure 10.1 shows that the ratio between the draft and length of the pontoon differs from the pontoons of the Bergsøysund bridge. Based on the length: $a = 10$. Based on the draft: $a = 3.7$. An average value of 6,85 is assumed.

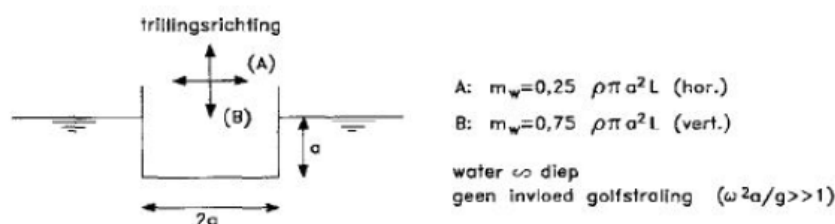


Figure 10.1: Derived formulas by Kolkman and Jongeling (2007) to make an estimate of the added mass.

Using the average a value and the parameters of table 7.1 results in:

$$\begin{aligned} A_{11} &= 0,128 \cdot 10^7 \text{ kg} \\ A_{33} &= 0,385 \cdot 10^7 \text{ kg} \end{aligned} \quad (10.2)$$

These values can readily be compared to figure 9.1. This shows that the results of Diffrac are in good agreement with the approximation of Kolkman and Jongeling (2007).

10.1.2. Vugts

Vugts (1971) published measurement data of experiments investigating the oscillations of pontoons with different dimensions. These measurements are frequency dependent and therefore better suited for a more detailed validation. The used cross section of the pontoon is shown in figure 10.2.

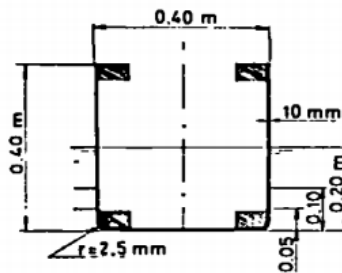


Figure 10.2: Cross section of the floating pontoon used in the experiments Vugts (1971).

The dimensions of the pontoons used in the model are modified to match the length over width ratio and the width over draft ratio used during the experiments. A pontoon with dimensions 100 times as large as the pontoon which is used in the experiments. The experiments uses 3 different ratios of width over draft ratio. The middle ratio, 4, is used to compare the experimental results to the modeling results.

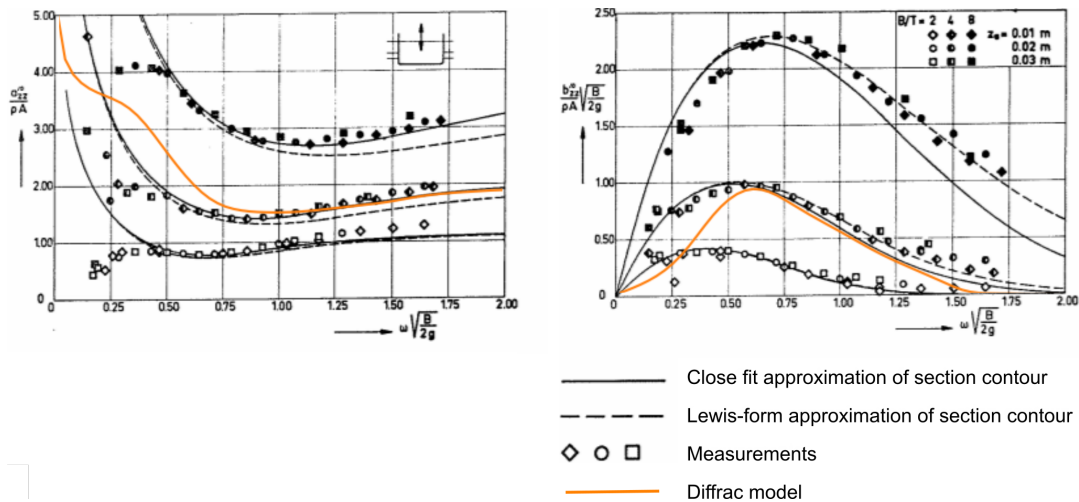


Figure 10.3: Added mass and hydrodynamic damping in heave according to Vugts (1971) (black lines) compared to diffrac results (orange lines).

Figure 10.3 shows that the Diffrac results are in very good agreement with the measurements. Both the added mass and the hydrodynamic damping show only a small deviation in the low frequency range. A possible explanation for this deviation could be that scaling ratios are not taken into account.

In the case of the added mass in heave, the measurements and modeling results are in very good agreement from a value of 0,75 on the x axis. For the hydrodynamic damping this is already the case from a value of 0,5 on the x-axis. Frequencies below these ranges are not important in this research, so it can be concluded that the results of the Diffrac model are accurate enough for the purpose of this research.

10.1.3. Wave force transfer function

The wave force transfer function is computed using the numerical software Diffrac. This software solves the linear potential functions and includes the diffraction force in this hydrodynamic analysis. A simplified method based on linear wave theory is proposed in appendix C. This method ignores the diffraction part. It is concluded that this is not a realistic assumption for wave conditions in fjords. However, it is a useful reference to compare with the output of Diffrac.

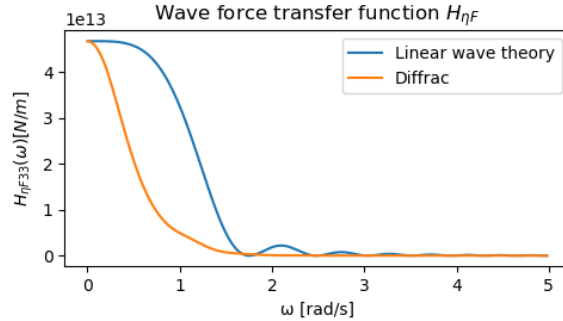


Figure 10.4: Transfer function between the wave spectrum and the force spectrum with and without diffraction.

Clearly, the results obtained with Diffrac show a lower force in the frequency range from 0 rad/s to 1,7 rad/s. This difference is explained by the diffraction force, which decreases the total wave force. The expectation that longer waves will diffract more than shorter waves is confirmed by the behaviour of the graphs. This qualitative relation is correctly taken into account by Diffrac. Furthermore, the magnitude of the wave force transfer function at 0 rad/s and 1,7 rad/s is the same. It is concluded that the diffraction force is qualitatively included correctly by Diffrac and that the results are in the correct order of magnitude.

10.2. Validation of the superstructure

The superstructure's validity is shown by comparing the eigenfrequencies of the *Two pontoon in plane model* with the theoretical eigenfrequencies of an Euler Bernoulli beam. The pontoon's hydrostatic stiffness is assumed to be infinitely large. As such, only the superstructure will be able to vibrate. The spring stiffness of the rotational spring will determine the type of support of the superstructure. Two different cases are used in this validation: a simply supported beam and a clamped beam (figure 10.5). Not only the first, but the first three eigenfrequencies are taken into account to improve the accuracy of the validation.

simply supported	simply supported			
			0.500	0.333 0.667
clamped	clamped			
			0.500	0.359 0.641

Figure 10.5: Theoretical eigenfrequency of a simply supported and clamped-clamped beam.

The results of this validation are presented in table 10.1. It appears that the difference between the theoretical eigenfrequencies and the modeled eigenfrequencies remains below 1%, which is sufficiently accurate.

Table 10.1: Validation of the superstructure based on theoretical eigenfrequencies of an Euler-Bernoulli beam.

eigenfrequencies	ω_1 [rad/s]	ω_2 [rad/s]	ω_3 [rad/s]
simply supported theoretical	13,716	54,889	123,536
simply supported model	13,716	54,904	123,922
delta	0,001%	0,026%	0,312%
clamped theoretical	31,127	85,739	168,143
clamped model	30,907	85,343	168,175
delta	0,706%	0,462%	0,019%

10.3. Validation measurement data

Measurement data of the Bergsøysund bridge is used to validate the floating bridge model. Due to a lack of the actual measurement data, only a visual comparison can be made. It is concluded in chapter 6 that the acceleration measurements are more accurate than the displacement measurements, so these are used here. The fifth pontoon's sway acceleration spectrum and the second pontoon's heave acceleration spectrum are compared with the modeling results of the corresponding pontoons. Figures 10.6 and 10.7 show both the measurements and the modeling results combined in one graph.

The scale in these graphs is logarithmic. Furthermore, the regular frequency (f) is used instead of the radial frequency (ω) to compare the measurements and the model correctly. The model only generates results for frequencies ranging from 0 to 5 rad/s, which is equal to 0,8 Hz. Hence, the results of the model only can be displayed on this interval. It is assumed that the measurements represent the motions at the CoG. Although this is not exactly true, for sway and heave it is expected to be relatively accurate, because motion coupling is minor for this motions.

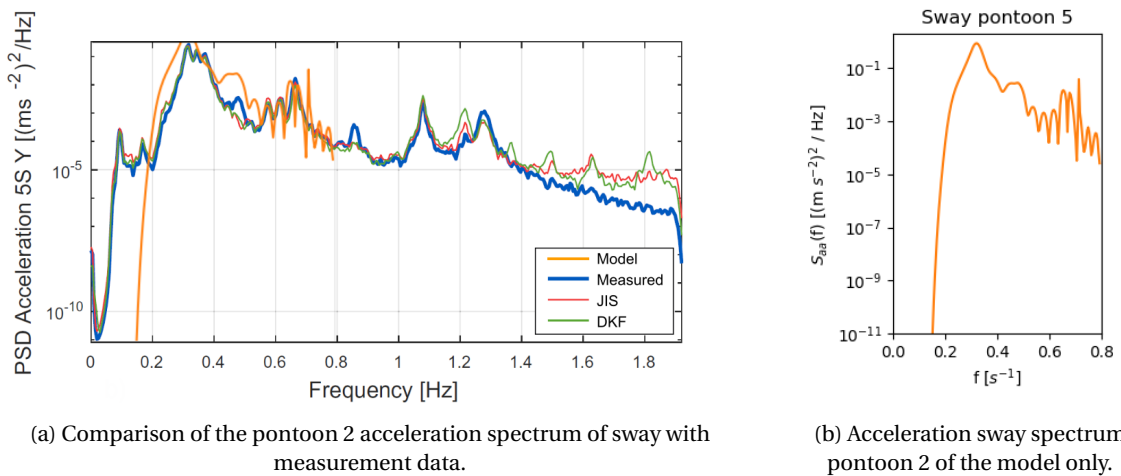


Figure 10.6: Comparison of the pontoon 2 acceleration spectrum of sway with measurement data (Petersen et al., 2018).

Figure 10.6 shows that the sway response spectra of the measurements and the model of the fifth pontoon's show great resemblance. Both spectra reach a peak at 0,32 Hz or 2,0 rad/s. The magnitude of the modeling results at this frequency is in the order $1 \cdot 10^1$ higher. On the interval between 0,3 and 0,8 Hz the graphs remain close to each other. The only clear deviation between the two graphs is found on the interval between 0 to 0,2 Hz. The measurement acceleration spectrum already starts increasing from 0,01 Hz, where the model acceleration spectrum starts increasing from 0,15 Hz. This can be explained by the fact that the wave spectrum which is used to model the dynamic response starts from 0,15 Hz.

Figure 10.7 shows that the response spectra of the measurements and the model of the second pontoon's heave accelerations also show great resemblance. The two peaks which are observed in the measurements at 0,30 and 0,35 Hz are present in the model at exactly the same frequency and with the same magnitude. One other peak is noticed in the modeling results at a frequency of 0,26 Hz. This peak is caused by the influence of mode 9 (figure 9.10), which is also identified by Petersen et al. (2018). On the interval between 0,4 and 0,8 Hz

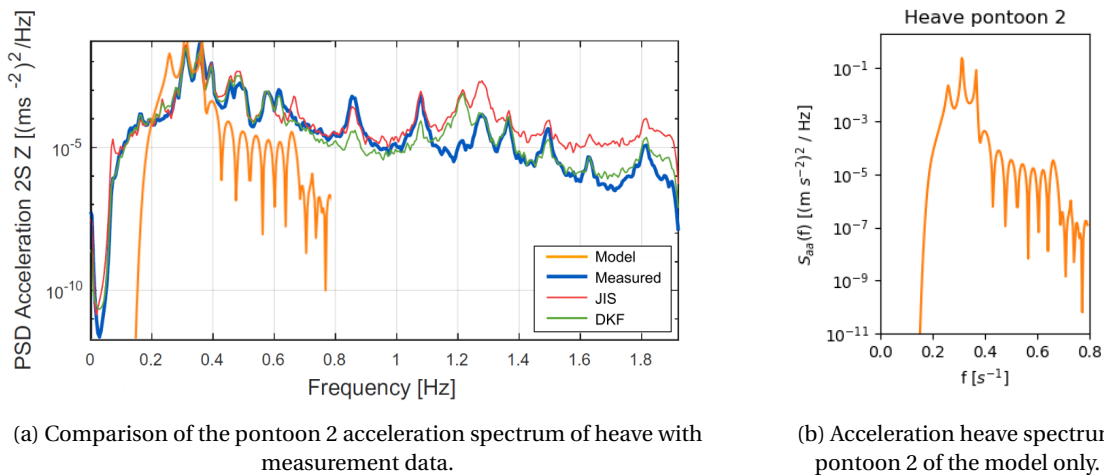


Figure 10.7: Comparison of the pontoon 2 acceleration spectrum of heave with measurement data.

the model deviates in the order of magnitude $1 \cdot 10^2$ from the measurements. Finally, the same explanation is valid as with the sway motion for the interval 0 - 0,15 Hz.

10.4. Validation & discussion of the assumptions

Several assumptions have been made to construct the pontoon model and the floating bridge model. Some of these assumptions can be validated with modeling results to see if the model is consistent with itself. Hence, the assumptions which are expected to have potential influence on the results of the model are validated if possible and otherwise their effect is discussed.

Pontoon dimensions

The pontoons are assumed to have square shape instead of a cylindrical shape. This assumption means that the surface area perpendicular to the main wave direction is larger than the actual pontoons. An increased surface area perpendicular to the wave direction will increase the dynamic response in sway direction, because a larger force is transferred.

Small angles of rotation

The maximum amplitude of the rotation angle is 0,0073 rad, or $0,42^\circ$ in roll direction. This means that the assumption of small rotational angles is a reasonable assumption.

Non-linear motions

Non linear effects are not included in the model. This means that only first order wave forces are taken into account. Especially the roll motion of ships is known to be effected significantly by non-linear effects such as viscous damping (Vugts, 1971). In the case of the pontoons, this motion coincides with the pitch motion of the pontoons. When this motions becomes important in the general response, attention should be paid to the potential influence of these non-linear effects.

Single wave direction

Only the wave direction perpendicular to the superstructure of the floating bridge is included in the floating bridge model. This results in dominant responses of sway, heave and roll. When inclined waves would have been added, response in pitch, surge and yaw would probably increase.

Alignment three-dimensional model

The curved alignment of the Bergsøysund bridge is not included in the floating bridge model. The dominant wave direction perpendicular to the superstructure would not reach all pontoons at the same angle anymore. The further the pontoons lay from the middle of the bridge, the larger the angle will be between the wave di-

rection and the sway direction of the pontoon. Therefore, a likely result of this assumption is that the model overestimates the sway response of the pontoons which lay at a distance from the middle pontoon.

Stiffness of the connections

No detailed information is available about the connections between the pontoons and the superstructure, which are represented by rotational springs. The stiffness of the supports at the abutments and the stiffness of the superstructure itself are used as reference values. However, this still leaves a large uncertainty in the estimation of the connection spring stiffness. When the estimated value is too small, less bending will occur in the superstructure and the pontoons are allowed to move more freely.

Narrow response spectra

The *upper limit approach* which is used to quantitatively express the response of the structure is based on the assumption that the response spectra are narrow banded. This allows the assumption that the response spectrum is rayleigh distributed. With this knowledge, the *upper limit approach* can be used as a good estimate of the upper limit response. Equation 4.28 is used to check whether the spectra are narrow banded. The q value indicates the narrowness of the spectrum, ranging from 0 (extremely narrow) to 1 (extremely wide). The sway response spectra result in the highest q values, but remain below 0,2. It is therefore concluded that the results of the *upper limit approach* are accurate enough for this research. However, the q values of the acceleration spectra exceed the 0,5. This means that the *upper limit approach* is not suitable to obtain quantitative results from the acceleration spectra.

10.5. Conclusion

The following conclusions are drawn based upon the different validations:

- The added mass and hydrodynamic damping coefficients of the pontoon that are computed with Difffrac are in good agreement with measurements obtained by Kolkman and Jongeling (2007) and Vugts (1971). It is concluded that the extensively validated software is correctly used to obtain the hydrodynamic properties of the pontoons.
- The wave force transfer function of the pontoon which is computed with Difffrac shows a correct relation with respect to the wave force transfer function which is computed using linear wave theory. Also the order of magnitude of these results coincide. It is concluded that Difffrac is correctly used to compute the wave force transfer function.
- Validation of the superstructure shows that the FE elements which are used in the superstructure have eigenfrequencies which show great resemblance to those of theoretical beam elements. It is concluded that the FE elements are correctly implemented in the floating bridge model.
- A comparison between the response spectra (heave and sway) from the model and the measurements shows a good resemblance. Especially the frequencies of peaks in the response spectra are accurately captured in the modeling results. However, some deviations occur in the magnitude of these peaks. Based on this validation it is concluded that the floating bridge model is accurate enough to investigate the influence of different parameters, but not accurate enough to assess the dynamic response of a structure for a detailed design.
- The *upper limit approach* appears not suitable to compute a quantitative acceleration from the acceleration spectra. This approach is only valid for narrow banded spectra, which the acceleration spectra are not. This means that the accelerations will not follow a Rayleigh distribution. It is recommended to investigate which distribution fits to the accelerations to be able to provide a better quantitative estimate.

IV

Parametric study

Parametric study

The influence of design parameters on the dynamic response is investigated in this chapter using a sensitivity study. The actual value of the selected parameters depends on the type of design and the materials that are used. The parametric study uses the input parameters and responses from the Bergsøysund bridge as a reference. A sensitivity analysis of these parameters is performed by increasing and decreasing them by 20 and 40%. The dimensions of the pontoon and the distance between the pontoons is only varied with 40%, because of the limited availability of Diffrac, which is required for the variation of these parameters.

The influence of the parameters will be expressed in percentiles of the Bergsøysund bridge's response. The selected parameters are shown in table 11.1. The associated ranges which are used in the parametric study and the properties which they influence are included as well. Figure 11.1 shows the selected parameters in a schematized overview.

Parameter	Symbol	Influences	Ranges [%]
Length of the superstructure	L_s	M_s, K_s	60 - 80 - 100 - 120 - 140
Elasticity modulus of the superstructure	E_s	K_s	60 - 80 - 100 - 120 - 140
Stiffness of the connection stiffness	K_c	K_s, K_p	60 - 80 - 100 - 120 - 140
Structural damping ratio	ζ	C_s	60 - 80 - 100 - 120 - 140
Length of the pontoon	L_p	$M_p, K_p, H_{\eta, F}$	60 - 100 - 140
Width of the pontoon	W_p	$M_p, K_p, H_{\eta, F}$	60 - 100 - 140
Distance between pontoons	Δ_p	$M_p, C_p, H_{\eta, F}$	20 - 60 - 100

Table 11.1: Selected parameters for the parametric study

Although several parameters are directly related to each other in a design, the influence of parameters will be investigated independently in this parametric study. When the potential influence on the dynamic response of all single design parameters is known, this knowledge can be applied in a design process. The relation between the parameters regarding design considerations is addressed in chapter 12.

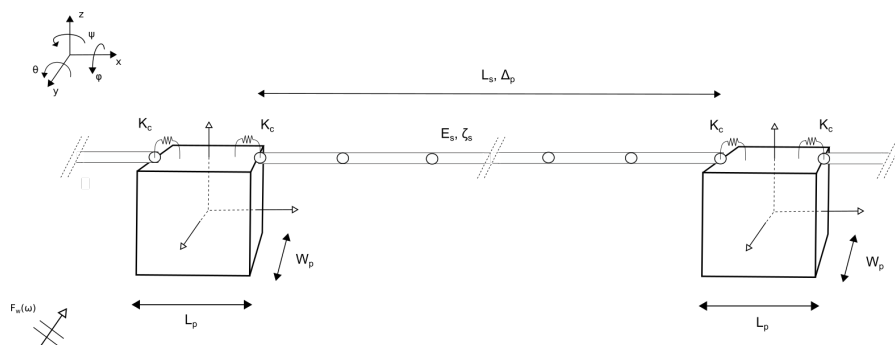


Figure 11.1: Schematization of the parameters used in the parametric study.

11.1. Results

First, a general distinction is made in the results of the parametric study between the odd and even numbered pontoons. This chapter mainly focuses on the results of the odd pontoons, because the results in chapter 9 have shown that the odd pontoons are governing. However, when the parameter variation yields governing even numbered pontoons, the results of these pontoons are elaborated in more detail as well. Pontoon 3 and 4 are chosen to represent the behaviour of the odd and even numbered pontoons respectively.

Quantitative results are computed using the *upper limit approach*. This yields insight in the magnitude of the parameters' influence on the dynamic response. Several conclusions can already be drawn based on these results. Additionally, a more detailed analysis of the effect on the dynamic response is performed to comprehend the influence of individual parameters better. In this analysis the focus lies on the effect that the parameters have on the eigenfrequency of the fourth sway mode, because this mode dominates the dynamic response in the given wave conditions.

Figure 11.2 shows the influence of the selected parameters on the dynamic response of pontoon 3. Three observations can readily be made from this graph:

- Varying the length of the superstructure has relatively the biggest influence on the dynamic response. Reducing the length of the superstructure by 40% even decreases the dynamic response by 48%.
- Changing the damping ratio and the distance between pontoons have relatively the smallest influence on the dynamic response. When the damping ratio is increased by 40%, the dynamic response only decreases by 1%. Reducing the distance between the pontoons by 40% only decreases the response by 0,03%.
- Increasing or decreasing all parameters with 20 or 40 % almost always reduces the dynamic response of pontoon 3.

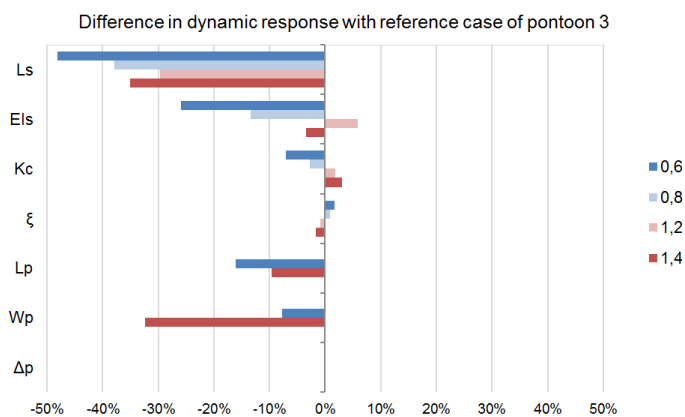


Figure 11.2: Sensitivity of design parameters on dynamic response of pontoon 3 compared to the reference case.

Figure 11.3 shows the influence of the selected parameters on the dynamic response of pontoon 4. It must be noted here that the scale has changed with respect to figure 11.2. As such, the two graphs should be compared with care. The fact that the influence of the selected parameters on the dynamic response is larger for pontoon 4 than for pontoon 3, is caused by the lower reference value of pontoon 4. Three observations can directly be made from the graph:

- A variation in the superstructure's length has relatively the most influence on the dynamic response. A 40% reduction of this length increases the dynamic response by 116%.
- Varying the connection stiffness, damping ratio and the distance between the pontoons has relatively the smallest effect on the dynamic response of all selected parameters. Decreasing the connection stiffness by 40% increases the dynamic response by 8%. Reducing the damping ratio by 40% increases the dynamic response by 1%. When the distance between the pontoons is reduced by 40%, the dynamic response only increases by 0,1%.
- Increasing or decreasing all parameters with 20 or 40 % almost always increases the dynamic response of pontoon 4.

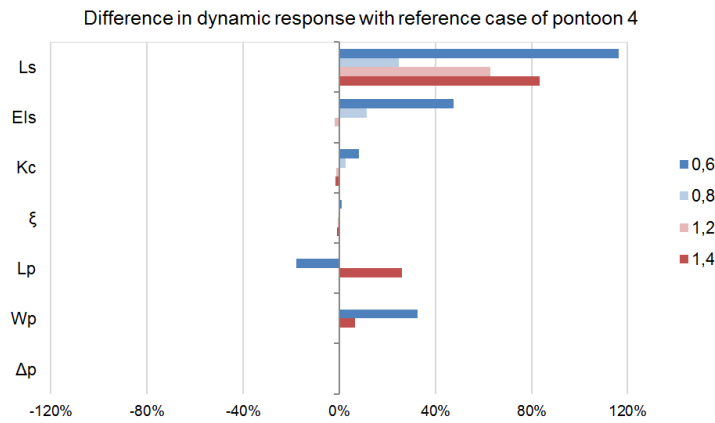


Figure 11.3: Sensitivity of design parameters on dynamic response of pontoon 4 compared to the reference case.

The results confirm the earlier drawn conclusion that sway of the pontoons is mostly influenced by the fourth sway mode. This mode excites mainly the odd numbered pontoons due to its mode shape. When the mass, damping or stiffness of the system changes, the eigenfrequency corresponding to this mode shifts. When this eigenfrequency shifts away from the wave peak frequency, the influence of the fourth sway mode reduces. Consequently, the dynamic response of the odd numbered pontoons reduces and the dynamic response of the even numbered pontoons becomes larger.

The effect that the variation of the parameters has on the eigenfrequency corresponding to the fourth sway mode and the potential amplification of the according dynamic response is analyzed in detail per parameter. The best way to analyze this effect is by comparing the different FRFs. However, the FRF is a $n \times n$ matrix containing the relation between the force input on every DOF and the response of every DOF. Only the effect of the component which relates the force in sway direction on the pontoon and the response in sway direction of the pontoon is investigated, because this component is dominant.

11.1.1. Length of the superstructure

The length of the superstructure is defined as the span between two pontoons. Only the superstructure is taken into account in the variation of this parameter. The influence of this distance on the hydrodynamic properties of the pontoons is ignored here and will be investigated individually as well. The length of the superstructure has a significant influence on the mass and the stiffness of the superstructure:

$$K \sim \frac{EI}{L_s^3}$$

$$M \sim \frac{A_s \rho_s L_s^2}{420}$$
(11.1)

This means that a reduction of 40% in length leads to a reduction of 64% in mass and an increase of 78% in stiffness and vice-versa. Apart from the abutments, the stiffness of the superstructure and the connections between the pontoons and the superstructure are the only constraints of the pontoons in sway direction. Hence, the relative influence of the length of the superstructure on this motion is expected to be large.

The result of the parametric study of the superstructure's length is presented in table 11.2. This table shows that the response of pontoon 4 even becomes the governing response with a 40% reduction of the length. Even a reduction of 20% of the superstructure's length causes the dynamic response of the odd and even numbered pontoons to be comparable.

Length superstructure	60%		80%		100%		120%		140%	
Response pontoon 1	0,17	-9,22%	0,14	-29,16%	0,19	0,17	-8,59%	0,18	-5,77%	
Response pontoon 2	0,16	99,5%	0,10	22,46%	0,08	0,11	38,53%	0,14	73,63%	
Response pontoon 3	0,10	-48,2%	0,11	-37,92%	0,19	0,13	-29,66%	0,12	-35,12%	
Response pontoon 4	0,20	116,19%	0,12	24,89%	0,09	0,15	62,86%	0,17	83,50%	

Table 11.2: Relative [%] and absolute [m] effect of the length of the superstructure on the dynamic response of the pontoons.

The FRFs of 60%, 100% and 140% length of the superstructure are plotted in figure 11.4. The eigenfrequencies of the fourth sway mode are indicated with the dotted lines. The large frequency shift is caused by both the increased stiffness and the reduced mass. The eigenfrequency shifts +1,74 rad/s in the case of a 60% length of the superstructure. This ensures that the fourth sway mode lies outside the frequency range where wave energy is concentrated at 2 rad/s. However, the eigenfrequency belonging to the third sway mode, indicated with a blue 3, also shifts up and lies exactly in the wave peak frequency. The peak of the blue line remains low at 2 rad/s, because the excitation of pontoon 3 by the third sway mode is small.

The opposite is true for the 140% length of the superstructure. Here the fourth mode of sway shifts -0,86 rad/s. However, now the fifth sway mode, indicated with a green 5, becomes important. The influence of this mode is small considering the response of pontoon 3. This is confirmed by the minor peak of the green line at 2 rad/s in figure 11.4. Nevertheless, pontoon 1 and 4 do show a significant response in this mode, which is in accordance with the mode shape (figure 9.11). Furthermore, the maximum value of the peaks corresponding to the fourth sway mode of all three cases is in the same order of magnitude.

As such, changing the length of the superstructure with 40% shifts the eigenfrequencies of the fourth sway mode beyond the region where wave energy is concentrated. This means that another pontoon becomes governing, but the magnitude of the governing response remains in the same order. Consequently, changing the length with 20% shifts the eigenfrequencies of the fourth sway mode just enough to lie outside the frequency range where wave energy is concentrated, but should not shift other sway modes into this area. This is confirmed by the results in table 11.2 that show a lower overall response for the 80% and 120% cases.

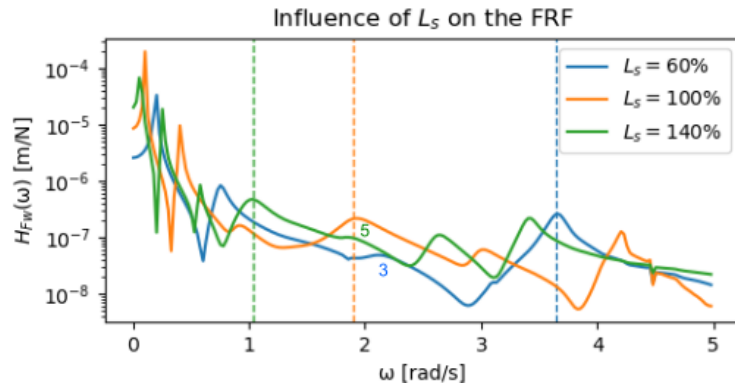


Figure 11.4: FRFs of varying the lengths of the superstructure.

11.1.2. Young's modulus of the superstructure

A Young's modulus can be assigned for every direction in the model. In this parametric study it is assumed that the Young's modulus remains equal in all directions. As such, it is treated as a single parameter. The bending stiffness of the superstructure is a function of the Young's modulus and the second moment of area. The Young's modulus has a linear relation with the bending stiffness of the superstructure:

$$K \sim \frac{EI}{L_s^3} \quad (11.2)$$

The results of the sensitivity study of the superstructure's Young's modulus are presented in table 11.2. This table shows that the governing response of the odd numbered pontoons decreases when the stiffness decreases. The response of the odd numbered pontoons increases comparably in absolute values. On the other hand, when the stiffness is increased, the governing response even increases for the 120% case.

Young's modulus	60%		80%		100%		120%		140%	
Response pontoon 1	0,17	-10,96%	0,17	-9,82%	0,19	0,20	5,08%	0,19	-3,24%	
Response pontoon 2	0,11	28,24%	0,09	5,92%	0,08	0,08	-0,26%	0,08	1,55%	
Response pontoon 3	0,14	-25,92%	0,16	-13,40%	0,19	0,20	5,91%	0,18	-3,44%	
Response pontoon 4	0,14	47,46%	0,10	11,47%	0,08	0,09	-2,04%	0,09	0,01%	

Table 11.3: Relative [%] and absolute [m] effect of the superstructure's Young's modulus on the dynamic response of the pontoons.

Figure 11.5 shows the FRFs of 60%, 100% and 140% Young's moduli of the superstructure. The eigenfrequency belonging to the fourth sway mode changes. Shifts of $-0,41$ rad/s and $+0,29$ rad/s are observed for the 60% and 140% cases respectively. The magnitude of all FRF peaks corresponding to the fourth sway mode remains the same. This is not the case for the first three modes, where an increasing stiffness leads to a reduced peak. One of the reasons that for the 60% Young's modulus' FRF the peak of the fourth sway mode remains in the same order of magnitude as the other FRFs, is that the hydrodynamic damping in the sway direction reaches a maximum at this frequency (figure 9.3).

A reduction of the Young's modulus with 40% and the consequential phase shift of the fourth sway mode are favorable for the overall dynamic response in this case. However, figure 11.5 does show reduced peaks and lower troughs in the FRF when the stiffness is increased. When the stiffness is increased enough to shift the fourth sway mode outside the range of the wave peak frequency, this leads to a smaller dynamic response than with a 40% reduction of the stiffness.

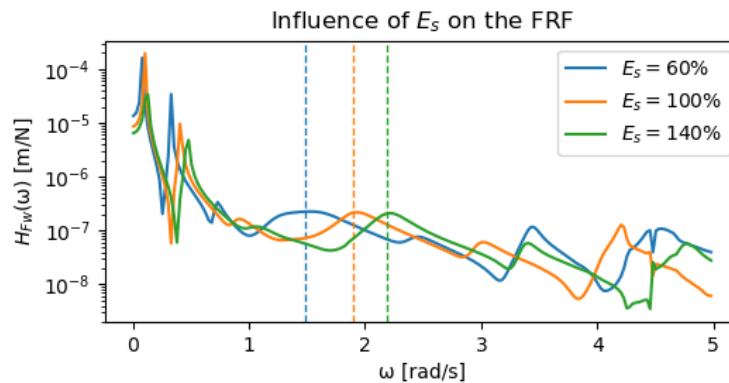


Figure 11.5: FRFs of varying the Young's modulus of the superstructure.

11.1.3. Stiffness of the connection springs

The connections between the pontoons and the superstructure are modeled rigidly with respect to all translations, but are modeled with rotational springs for the rotations. Thus, the stiffness of the connection springs is the stiffness of all three rotational springs which are used to model the resistance. This means that the stiffness of the connection springs influence the structural system of the floating bridge. With a relatively low spring stiffness, the connection will behave as if hinged. A relatively high spring stiffness will result in a clamped connection.

When the connections behave as hinges, the pontoons can freely translate and are less restrained by the bending stiffness of the superstructure. Thus, the stiffness of the connection springs determines to what extent the superstructure can constrain the motion of the pontoons through bending.

The results of the sensitivity study of the stiffness of the connections is presented in table 11.4. These results show that reducing the connection stiffness has a larger influence on the dynamic response than when the connection stiffness is increased.

Kc	60%		80%		100%		120%		140%	
Response pontoon 1	0,18	-4,83%	0,19	-2,03%	0,19	0,19	1,47%	0,20	2,47%	
Response pontoon 2	0,09	4,62%	0,08	1,51%	0,08	0,08	-0,42%	0,08	-0,64%	
Response pontoon 3	0,17	-7,02%	0,18	-2,75%	0,19	0,19	1,82%	0,19	3,02%	
Response pontoon 4	0,10	8,10%	0,09	2,58%	0,08	0,09	-1,12%	0,09	-1,68%	

Table 11.4: Relative [%] and absolute [m] effect of the stiffness of the connection springs between the superstructure and the pontoons on the dynamic response of the pontoons.

Figure 11.6 shows the FRFs of corresponding to the 60%, 100% and 140% connection stiffness values. Frequency shifts for the fourth sway mode of $-0,10$ rad/s and $+0,05$ rad/s are observed for the 60% and 140% cases respectively. Both frequency shifts are small, but the frequency shift belonging to the reduction in connection stiffness is double the shift of the increase in connection stiffness. This indicates that with the actual spring stiffness the connection already converges to a clamped connection. An increase in stiffness will not change the dynamic response that much anymore.

However, with an increased stiffness of the connections, the eigenfrequency belonging to the fourth sway mode does shift closer to the range where the wave energy is concentrated and therefore the dynamic response of the odd numbered pontoons increases.

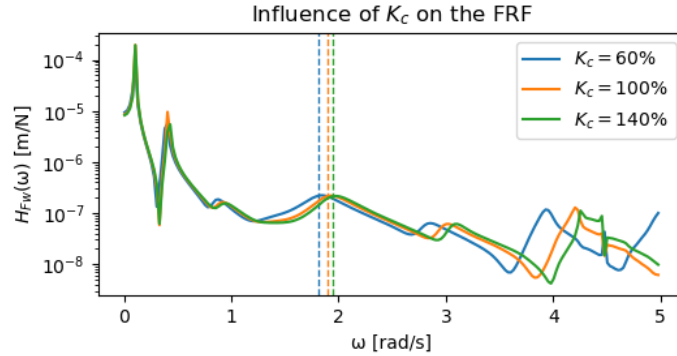


Figure 11.6: FRFs of varying the connection spring stiffness of the superstructure.

11.1.4. Structural damping

Structural damping and hydrodynamic damping are the only sources of damping in the model. The amount of damping determines to what extent the structure responds in resonance conditions. The results of the sensitivity study of the structural damping are presented in table 11.5. These results show that the effect of different amounts of structural damping on the dynamic response is minor.

Structural damping	60%		80%		100%	120%		140%	
Response pontoon 1	0,20	1,73%	0,19	0,85%	0,19	0,19	-0,83%	0,19	-1,64%
Response pontoon 2	0,08	0,70%	0,08	0,34%	0,08	0,08	-0,31%	0,08	-0,60%
Response pontoon 3	0,19	1,70%	0,19	0,84%	0,19	0,18	-0,82%	0,18	-1,63%
Response pontoon 4	0,09	0,98%	0,09	0,47%	0,08	0,09	-0,44%	0,09	-0,85%

Table 11.5: Relative [%] and absolute [m] effect of the structural damping in the superstructure on the dynamic response of the pontoons.

The FRFs of the 60%, 100% and 140% values of structural damping (figure 11.4) are used to explain the results of the parametric study. All these FRFs are almost identical, with small deviations in the peaks in the low and high frequency range. Furthermore, no shift is observed in the eigenfrequency belonging to the fourth sway mode. As such, the effect of a variation in the structural damping on dynamic response remains very small.

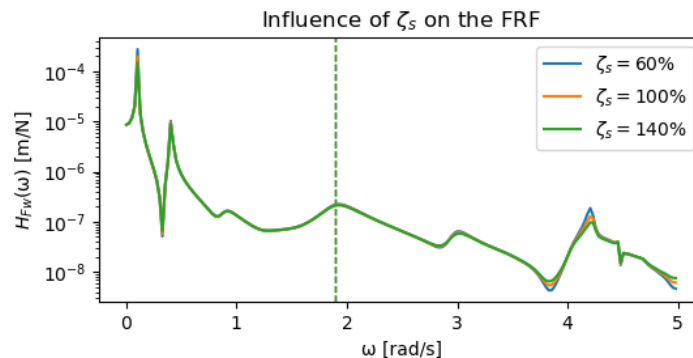


Figure 11.7: FRFs of varying the structural damping of the superstructure.

The fact that some smoothing of the FRFs occurs for an increased structural damping in the lower and higher frequency ranges is explained by the fact that the hydrodynamic damping is relatively low in these frequency ranges (figure 9.3). It can be concluded that the effect of the structural damping on the dynamic

response is minor due to the influence of the relatively large hydrodynamic damping in the frequency range where wave energy is concentrated.

11.1.5. Length of the pontoons

The length of the pontoon is defined as the side of the pontoon which lies parallel to the superstructure. The length of the pontoons linearly increases the surface area perpendicular to the sway direction. The submerged surface area of the pontoon has a linear relation with the added mass, hydrodynamic damping and the wave force transfer function in the corresponding direction. Additionally, the dry mass of the pontoon is also linearly related to the length of the pontoon. Summarized this means that the following properties have a linear relation with the length of the pontoons:

$$\begin{aligned}
 A_{22} &\sim L_p \\
 B_{22} &\sim L_p \\
 H_{\eta F,22} &\sim L_p \\
 M_p &\sim L_p
 \end{aligned}
 \tag{11.3}$$

The effect of different pontoon length's on the dynamic response is presented in table 11.6. Only a 60%, 100% and 140% value for the pontoon length is used here. The pontoons with a reduced length all show a decreased dynamic response, while increasing the pontoon's length only leads to a reduced dynamic response of the odd numbered pontoons.

Length pontoon	60%		100%	140%	
Response pontoon 1	0,16	-16,44%	0,19	0,18	-4,31%
Response pontoon 2	0,07	-16,73%	0,08	0,10	19,11%
Response pontoon 3	0,15	-16,15%	0,19	0,17	-9,57%
Response pontoon 4	0,08	-17,93%	0,09	0,12	25,69%

Table 11.6: Relative [%] and absolute [m] effect of the pontoon's length on the dynamic response of the pontoons.

Since the length of the pontoons influences both the properties of the structure as the magnitude of the wave load, both the FRFs and the wave force spectra are plotted in figure 11.8. The FRFs show that increasing the length decreases the eigenfrequency belonging to the fourth sway mode and vice versa for a reduced length. The frequency shifts are +0,31 rad/s and - 0,21 for the 60% and 140% cases respectively. This frequency shift can be explained by the change of mass. An increased mass leads to a decreased eigenfrequency.

Furthermore, the magnitude of the peaks decreases for an increased pontoon length. An increased hydrodynamic damping causes the smoothing of these peaks in the FRFs. Finally, the magnitude of the wave force spectrum increases for an increased pontoon length.

All together, an increased pontoon length will decrease the eigenfrequency belonging to the fourth sway mode. Additionally, it will reduce the magnitude of the according peak of the FRF and it will increase the magnitude of the wave force spectrum. This last aspect dominates the difference in the dynamic response.

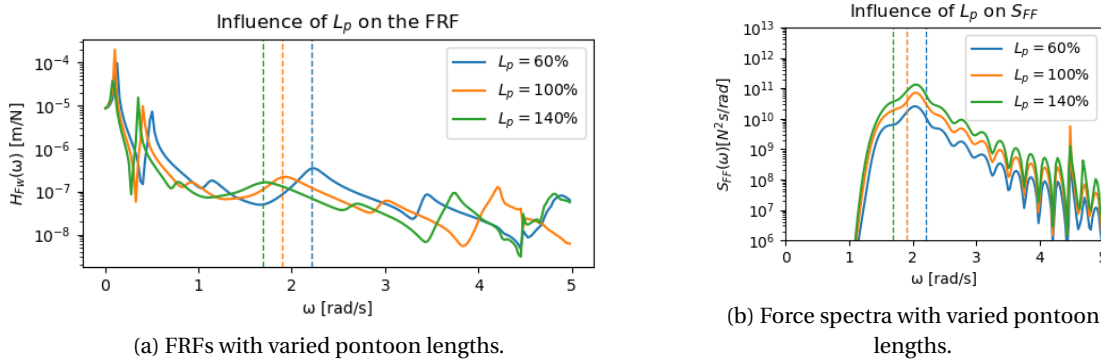


Figure 11.8: FRFs and force spectra of pontoon 3 in sway direction for different pontoon lengths.

11.1.6. Width of the pontoons

The width of the pontoon is defined as the side of the pontoon which lies perpendicular to the superstructure. The main influence of an increased width of the pontoons will be an increased mass. Increasing the width of a pontoon will not increase the surface area perpendicular to the sway direction. However, due to the diffraction, changing the width of a pontoon will affect the hydrodynamic properties in sway direction to some extent. The effect of different pontoon widths on the dynamic response is presented in table 11.7. Only a 60%, 100% and 140% value for the pontoon width are used here. Increasing the pontoon width by 40% reduces the dynamic response of the odd numbered pontoons more than that the dynamic response of the even numbered pontoons is increased. The reduction of 40% in the pontoon's width results in a little reduction of the dynamic response of the odd numbered pontoons, but increases the dynamic response of the even numbered pontoons significantly.

Width pontoon	60%		100%	140%	
Response pontoon 1	0,19	-2,99%	0,19	0,14	-25,43%
Response pontoon 2	0,11	31,95%	0,08	0,08	-3,46%
Response pontoon 3	0,17	-7,74%	0,19	0,12	-32,35%
Response pontoon 4	0,12	32,69%	0,09	0,10	6,54%

Table 11.7: Relative [%] and absolute [m] effect of the pontoon's width on the dynamic response of the pontoons.

Both the FRFs and the wave force spectra are plotted in figure 11.9. In contrast to the results of the length of the pontoon, the only clear observation here is the shift of the eigenfrequency corresponding to the fourth sway mode. Figure 11.9b shows that the wave force spectra are almost identical.

The magnitude of the peaks in figure 11.9a remains in the same order. The main contribution of the frequency shifts is the change in total mass of the pontoons. The frequency shifts of the eigenfrequency belonging to the fourth sway mode are +0,47 rad/s and - 0,31 rad/s for the 60% and 140% cases respectively. This also explains the large reduction of the dynamic response of pontoon 3 for the 140% case. The fourth sway mode is shifted completely outside the area were most of the wave energy is concentrated.

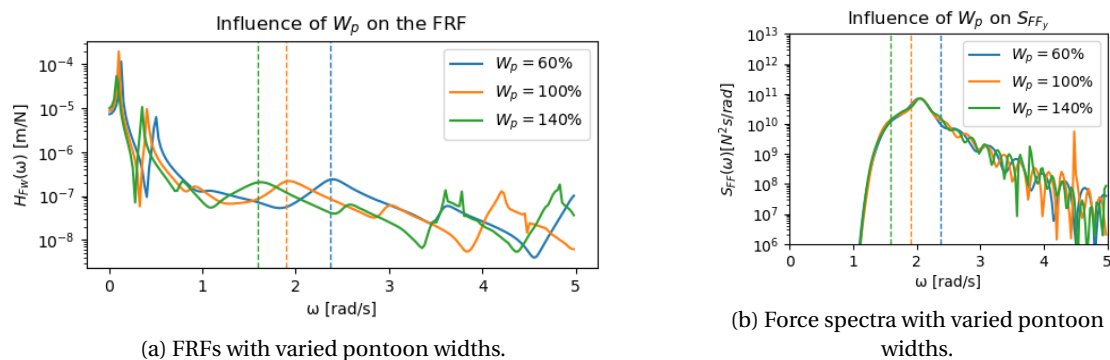


Figure 11.9: FRFs and force spectra of pontoon 3 in sway direction for different pontoon widths.

11.1.7. Distance between the pontoons

The distance between the pontoons determines to what extent the pontoons affect each others hydrodynamic properties. It was concluded that with a distance of 110 m between pontoons, this interaction is negligible. Therefore only relatively shorter distances are taken into account in this parametric study to investigate the effect of the distance between the pontoons. The results of this parametric study are shown in table 11.8. A reduction of 80% of the distance between the pontoons still has a negligible effect on the sway motion.

The effect of the distance between the pontoons on the hydrodynamic properties affecting the sway motion appears negligible when only the wave direction perpendicular to the superstructure is taken into account. However, the other DOFs are influenced significantly.

Width pontoon	20%		60%		100%
Response pontoon 1	0,19	-0,24%	0,19	0,03%	0,19
Response pontoon 2	0,08	0,12%	0,08	0,11	0,08
Response pontoon 3	0,18	-0,28%	0,19	0,03	0,18
Response pontoon 4	0,09	0,13%	0,09	0,10	0,09

Table 11.8: Relative [%] and absolute [m] effect of the distance between the pontoons on the dynamic response of the pontoons.

11.2. Conclusion

Several conclusions are drawn based on the results of the parametric study. These conclusions contribute to the prediction and explanation of the dynamic response of a floating bridge. However, it must be kept in mind that these conclusions assume that the dynamic response is dominated by the fourth sway mode and that the odd numbered pontoons have the governing response in sway direction.

- The variation of the length of the superstructure has relatively the biggest influence on the dynamic response of all selected parameters. A reduction of 40% leads to an increased stiffness of 78% and a decreased mass of 64% in the superstructure, which leads to a large shift in eigenfrequencies. The the eigenfrequency belonging to the third sway mode is shifted into the region where wave energy is concentrated and the original eigenfrequency belonging to the fourth sway mode is shifted away from this region.
- Increasing the superstructure's stiffness does not necessarily decrease the dynamic response. It increases the eigenfrequency belonging to the fourth sway mode, which in first instance has a negative impact on the dynamic response, because the eigenfrequency moves closer to the area where wave energy is concentrated. However, increasing the stiffness does contribute to an overall reduction of the FRF, so when resonance eigenfrequencies are avoided, it leads to a reduced dynamic response.
- The stiffness of the connections between the superstructure and the pontoons has a great influence on the structural behaviour of the floating bridge. Increasing the connection stiffness has a minor effect on the dynamic response and the eigenfrequency belonging to the fourth sway mode. Decreasing the connection stiffness on the other hand has a bigger effect on the dynamic response by decreasing the fourth sway mode's eigenfrequency. This eigenfrequency shifts almost twice as far for a 40% reduction in connection stiffness than for a 40% enlargement in connection stiffness. Additionally, decreasing the connection stiffness makes the connections behave more like hinges. This means that less bending in the superstructure occurs and that the constraints of the pontoons in sway direction reduce. A more detailed study into this phenomenon should be performed to draw accurate conclusions.
- The influence of the structural damping on the dynamic response of a floating bridge is minor. The main reason for this is that the hydrodynamic damping is relatively large compared to the structural damping in the frequency ranges where wave energy is concentrated.
- Reducing the length of the pontoons by 40% decreases the dynamic response of all pontoons. Although the fourth sway mode's peak in the FRF increases in magnitude, the resulting smaller wave forces lead to a reduced dynamic response. Increasing the length of the pontoons by 40% does shift the eigenfrequency belonging to the fourth sway mode further away from the wave energy, which leads to a small reduction of the dynamic response of the odd pontoons. However, the dynamic response of the even numbered pontoons is increased by this shift.
- Changing the width of the pontoons has less effect on the dynamic system in sway direction than changing the length. Only the increased mass effects this motion and can be used to decrease the influence of the fourth sway mode. Increasing this width proves to be an effective way to decrease the dynamic response of the odd pontoons.
- Decreasing the distance between two pontoons does not effect the sway motion of the pontoons as long as the wave direction perpendicular to the superstructure is the only wave direction which is taken into account.

A general overview of the influence of the dynamic properties on the FRF is shown in figure 11.10. First, a peak in the FRF can be shifted to a higher frequency range by increasing the stiffness of the superstructure or the connections or by reducing the mass of the pontoons. Second, the magnitude of the peaks can be reduced by increasing the hydrodynamic damping of the pontoons. Third, the overall magnitude of the FRF can be decreased by increasing the stiffness of the superstructure or the connections.

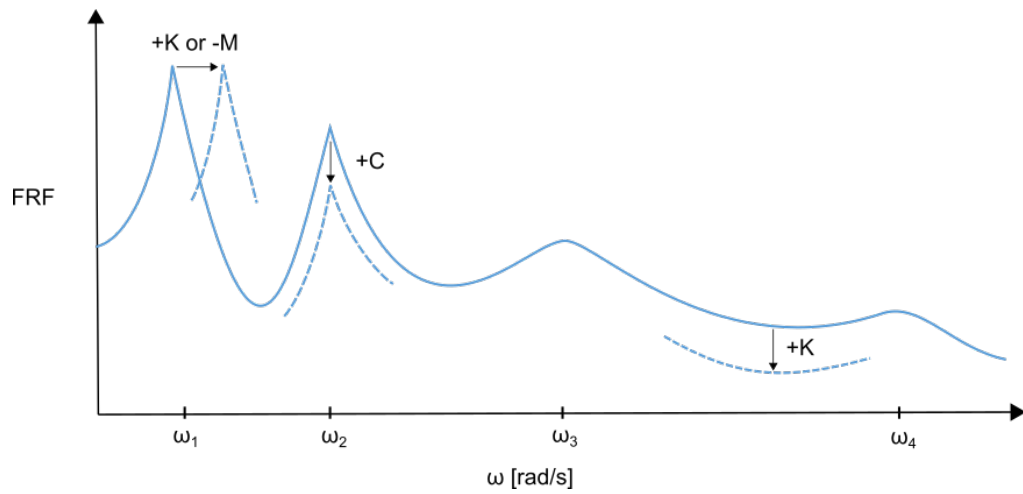


Figure 11.10: Influence of the mass, damping and stiffness on the frequency response function.

12

Applications for design

This chapter demonstrates the relation between the developed floating bridge model and the design process of a floating bridge. Figure 12.1 shows the integration of the model in a design cycle. Static loads and dynamic loads can be taken into account simultaneously to perform SLS and ULS checks. A case study of an FRP alternative to the Bergsøysund bridge is used to illustrate this concept in this chapter. It was concluded in chapter 10 that the floating bridge model is not suitable for detailed design calculations. It is therefore stressed that the quantitative results of this chapter should not be considered as accurate enough for such calculations. However, a comparison between a steel and FRP alternative can provide useful information about the differences in resonance ranges and the differences between the overall magnitude of the FRFs.

Several assumptions are made to design an FRP alternative and to perform SLS and ULS calculations. These assumptions are explained in section 12.1. The FRP alternative which is designed is presented in section 12.2. Subsequently, the FRP design and the Bergsøysund bridge are both assessed using deformation criteria (SLS) and strength and stability criteria (ULS). The assessment methods and results are presented in section 12.3. No design iterations are made. The purpose of this chapter is not to find an optimal design for the FRP alternative, but merely to demonstrate the relation between the dynamic model and the design procedure and to present preliminary conclusions about the feasibility of an FRP design as an alternative for the Bergsøysund bridge.

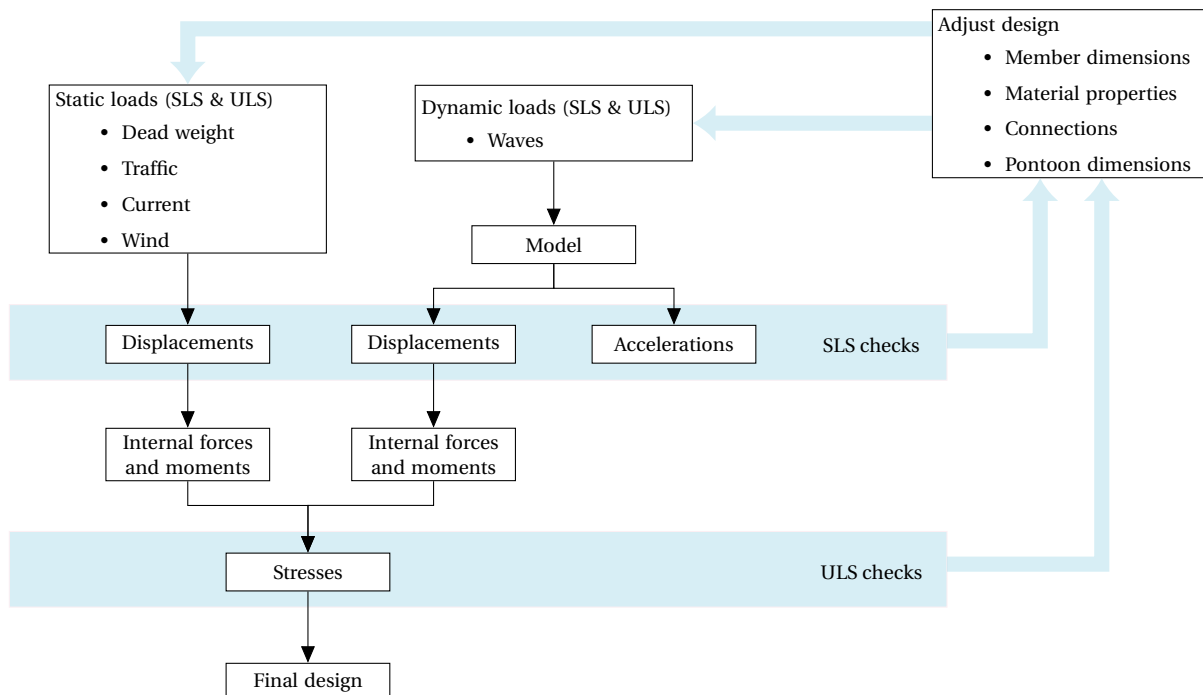


Figure 12.1: Integration of the floating bridge model in the design cycle of a floating bridge.

12.1. Assumptions for design

First general assumptions regarding the FRP alternative are mentioned. Subsequently, assumptions about the loads and the assessments method are discussed. Finally, several assumptions are made considering the structural design of the FRP alternative.

- The FRP alternative is based on the design of the Bergsøysund bridge. The environmental conditions, lay out and the type of superstructure (truss) are assumed to be the same. This means that the FRP design will also consist of seven pontoons crossed by eight parts of superstructure of 110 m. The clearance of the Bergsøysund bridge of 2,3 meters is also adopted as a requirement.
- A preliminary design of the superstructure is made using rules of thumb considering only strength and deflections. Dimensions of the superstructure are found by taking static traffic loads and the dead weight into account. These loads must be compensated by the buoyancy of the pontoons. Hence, with the clearance requirement in mind, this also determines the required pontoon dimensions. This method is explained in more detail in appendix G.1.

In the assessment of the FRP alternative and Bergsøysund bridge, more loads are taken into account:

Load	Type	Direction	Duration	Applies on	Value
Dead weight	Static	Z	Permanent	Pontoon & Superstructure	18,6 kN/m ³ or 76,5 kN/m ³
Traffic	Static	Z	Variable	Superstructure	21,2 kN/m ² or 600 kN
Wave	Dynamic	X, Y & Z	Variable	Pontoon	From model
Current	Static	Y	Variable	Pontoon	0,39 kN/m ²
Wind	Static	Y	Variable	Superstructure	0,05 kN/m ²

Table 12.1: Overview of the loads which are taken into account.

These loads are used to assess both the FRP alternative and the Bergsøysund bridge using SLS and ULS criteria. This assessment is based on the following assumptions:

- For SLS checks the values of loads which are presented in the table 12.1 are taken into account. Wave conditions with a 1-year return period (figure 12.2) are used to represent the serviceability wave loads. This wave spectrum has a significant wave height of 1 m and a peak period of 3,15 s. Appendix G.1 elaborates upon the derivation of these loads.
- The horizontal deflection is governing in these wave conditions. Therefore only this motion is taken into account in the SLS check.
- Safety factors are taken into account in the ULS assessment. In an ULS assessment a distinction is made between permanent loads, the main variable load and secondary variable loads. In this case the wave load is the main variable load. This is taken into account by using a wave spectrum which represents the wave conditions with a 100-y return period (figure 12.2). The significant wave height of these wave conditions is 2,5 m and the peak period is 5 s. NEN-EN 1990 (2011) states that permanent loads should be multiplied with a load factor of 1,35. Secondary load factors are multiplied with a partial load factor and safety factor which results in a total factor of 1,05.

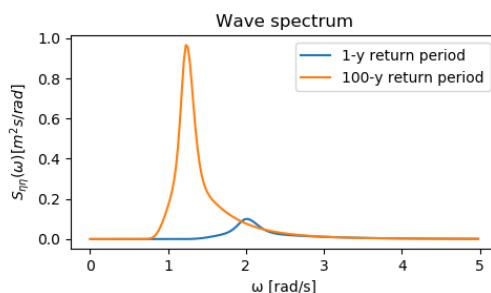


Figure 12.2: Wave spectra representing the wave conditions with a 1 year return period and a 100 year return period.

The following assumptions are made regarding the structural aspects of the design:

- The truss structure is assumed to be an ideal truss where no moments occur in the members of the structure. Only normal forces are taken into account in the members.
- The deck of the structure is assumed to be orthotropic. According to CUR-aanbeveling 96 (2003) the contribution of such a deck to the global stiffness of the cross section is 15% of the value calculated based on the surface area.
- The structural damping of the FRP alternative is assumed to be equal to the structural damping of the Bergsøysund bridge. Often the structural damping of FRP is higher, so this is a conservative approach. This choice is made, because it was concluded that structural damping has only a minor influence on the dynamic response of a floating bridge.
- The regular Young's modulus of FRP is divided by 1,1 to account for time related degradation. A value of 23,64 GPa is used.

12.2. Design of the FRP alternative

The type of cross section is shown in figure 12.3. The global dimensions are already indicated in this figure. Strength and stiffness checks are used to find the dimensions of all members. In the strength assessment it is checked whether tensile forces lead to stresses that exceed the stress limits. In the deflection assessment, the total deflection is determined and compared to the limit of $L/350$. This calculation is presented in appendix G. A unity check of 0,7 is approached for the governing failure mechanism in this preliminary design. The dimensions of the cross section that are found are listed in table 12.2. When the global and member dimensions of the FRP alternative are compared to the Bergsøysund bridge's dimensions (figure A.1), it is observed that the mainly the global dimensions are used to compensate for the the lower Young's modulus in the vertical plane. The member dimensions are comparable.

FRP110	Tension or compression	w [mm]	h [mm]	tf [mm]	tw [mm]
top chord	compression	1100	1100	30	30
bot. chord	tension	1100	1100	30	30
vertical	compression	400	400	20	20
diagonal	tension	500	500	20	20

Table 12.2: Dimensions of the FRP110 superstructure

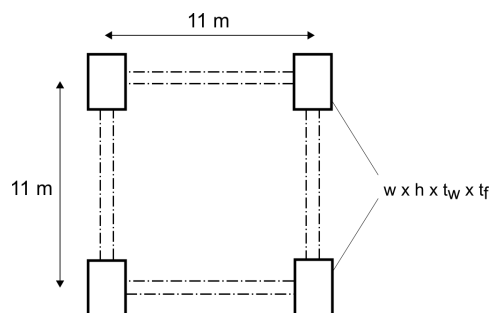


Figure 12.3: Cross section of the FRP alternative superstructure.

The dimensions of the superstructure are used to determine the total dead weight. With the total required buoyancy known, the dimensions of the pontoons can be determined. The requirement of a clearance height of 2,3 m leads to the dimensions which are presented in table 12.3. Only the stiffness of the connections remain left to be determined. The stiffness of the connections of the Bergsøysund bridge are used as a reference here. To maintain the same structural system, these reference stiffness values are reduced with the same ratio as the total stiffness of the superstructure reduces. All input parameters of the FRP alternative are presented in table 12.3 together with the input parameters of the Bergsøysund bridge.

Parameter	FRP alternative	Bergsøysund bridge	Unit
Pontoon			
Length (L_p)	15	20	m
Width (W_p)	26	34	m
Height (H_p)	6	6,07	m
Wall thickness (t_p)	0,20	0,25	m
Superstructure			
Surface area (A_s)	0,854	0,593	m^2
Density (ρ_s)	1900	7800	kg/m^3
Elasticity (E_s)	32630	210000	MPa
Second moment of area (I_y)	17,65	6,15	m^4
Second moment of area (I_z)	15,95	12,38	m^4
Second moment of area (I_p)	42,19	16,07	m^4
Damping parameter (α)	0,005	0,005	-
Damping parameter (β)	0,005	0,005	-
Connection			
Connection rotational stiffness ($K_{c,\phi}$)	$9,0 \cdot 10^9$	$3,0 \cdot 10^{10}$	Nm/rad
Connection rotational stiffness ($K_{c,\theta}$)	$4,5 \cdot 10^{10}$	$1,5 \cdot 10^{11}$	Nm/rad
Connection rotational stiffness ($K_{c,\psi}$)	$9,0 \cdot 10^{10}$	$3,0 \cdot 10^{11}$	Nm/rad
Support stiffness ($K_{s,x}$)	$5,9 \cdot 10^6$	$5,9 \cdot 10^6$	N/m
Support stiffness ($K_{s,y}$)	$2,1 \cdot 10^8$	$2,1 \cdot 10^8$	N/m
Support stiffness ($K_{s,z}$)	$1,3 \cdot 10^8$	$1,3 \cdot 10^8$	N/m
Support stiffness ($K_{s,\phi}$)	$2,1 \cdot 10^9$	$2,1 \cdot 10^9$	Nm/rad

Table 12.3: Input parameters of the model

12.3. Assessment method

Figure 12.1 shows an overview of the design cycle and the integration of the floating bridge model. In this cycle both SLS and ULS checks are mentioned. The only SLS check which is included here is the assessment of the deflection. The method to perform this SLS check consists of the following steps:

1. The wave spectrum which represents the wave conditions with a 1-year return period (figure 12.2) is used as input for the dynamic model.
2. The relative response spectrum of the governing translation is computed with the floating bridge model. It was concluded that sway of the pontoons is governing for the Bergsøysund bridge. As such, the governing relative translation is the biggest difference in sway between two pontoons (top left in figure 12.4). The relative displacement between pontoon 1 and pontoon 2 appears to be the governing displacement in this case and is therefore used in the assessment.
3. The random phase of the wave elevation is taken into account in this relative response spectrum. Consequently, every simulation will produce different relative response spectra. The relative response is obtained from each relative response spectrum with the *upper limit approach*. The results of 10 simulations are used to compute a single representative displacement. This procedure is explained in appendix G.
4. The computed displacement is divided through the deflection limit to calculate the unity check.

The same general steps are used in the ULS assessment with a few modifications and additional steps. Wave conditions with a 100-year return period are used now. Furthermore, besides sway also heave is included in this assessment. In contrast to the SLS assessment, the ULS assessment requires stresses instead of displacements to perform a strength and stability check. Therefore, the governing translations and rotations which are calculated according to step 3 will be used to find the internal stresses by:

4. The maximum relative translation between the pontoons and the maximum relative rotation of the connections are obtained from the relative response spectra. An overview of these degrees of freedom

in lateral direction is shown in figure 12.4. Each of these DOFs contribute to a moment in the superstructure. The rotations and the moment lines which are caused by these DOFs are indicated in figure 12.4. These two moment lines can be combined according to the superposition principle to find the envelope moment line caused by the wave load in and lateral and vertical direction.

5. The static loads in lateral and vertical direction are used to determine the moments in the superstructure between pontoon 1 and pontoon 2. This process is elaborated upon in appendix G.
6. The moments caused by the static and dynamic loads are combined to find the envelope. This moment is used to determine maximum member tension and compression forces by dividing through the height or width of the superstructure. Finally the stresses are determined by taking the surface area of the members into account.

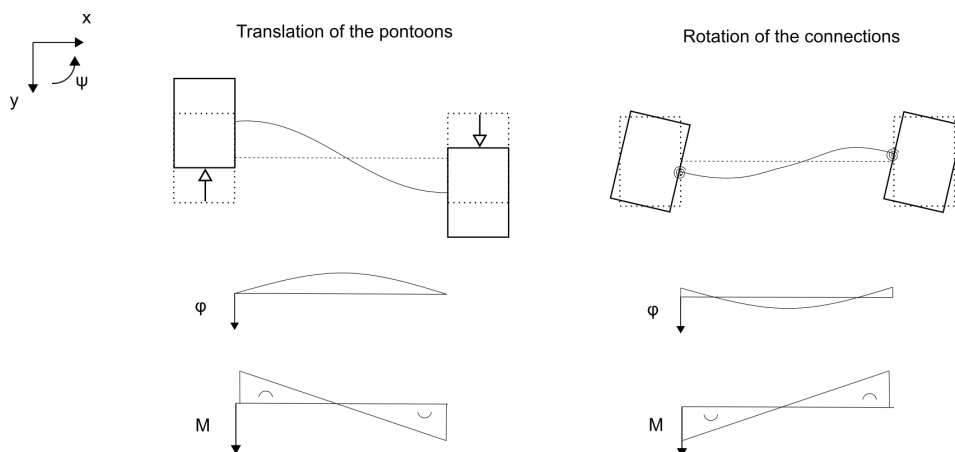


Figure 12.4: Moment lines caused by the wave loads.

12.4. Results

The result of the SLS and ULS assessments are presented in table 12.4. From this table it can be seen that the Bergsøysund bridge just meets the deflection and strength criteria. The FRP alternative does not meet the deflection criteria, but easily satisfies the strength criteria. Stability is no issue for both designs.

		Bergsøysund		FRP alternative	
		Horizontal	Vertical	Horizontal	Vertical
SLS	Deflection [m]	0,27	-	0,40	-
	Stiffness unity check	0,86	-	1,29	-
ULS	Max moment [kNm]	$1,32 \cdot 10^6$	$3,63 \cdot 10^5$	$1,71 \cdot 10^5$	$1,92 \cdot 10^5$
	Max tension stress [N/mm ²]	348,9	180,3	59,5	58,0
	Max compression stress [N/mm ²]	348,9	153,4	59,5	66,9
	Strength unity check	0,98	0,51	0,27	0,26
	Stability unity check	0,01	0,01	0,01	0,01

Table 12.4: Results of the SLS and ULS assessments of both the Bergsøysund bridge and the FRP alternative.

The hypothesis that the SLS deflection criteria is governing for a floating bridge with an FRP superstructure is confirmed by these results. For the Bergsøysund bridge the ULS strength criteria is governing. The difference between the dynamic response of the Bergsøysund bridge and the FRP alternative is relatively large. The FRFs (figure 12.5) of the pontoon's sway are compared to get more insight in this difference.

A shift of the peaks in the FRF towards the lower frequencies is expected based on the reduced stiffness of the superstructure. However, a reversed shift is expected because of the reduced mass of the superstructure and the pontoons. The relative difference in stiffness is larger and this is also confirmed by the FRFs. The peaks of the FRF corresponding to the FRP alternative are clearly shifted to lower frequencies compared to the Bergsøysund bridge's FRF.

Furthermore, almost the complete FRF of the FRP alternative exceeds the FRF of the Bergsøysund bridge in magnitude. This is also caused by the reduction in stiffness. Around the frequency of 2 rad/s, the peaks and troughs do not differ that much any more. The following design measures are expected to reduce the dynamic response:

- The stiffness of the superstructure can be increased in order to decrease the overall magnitude of the FRF. The preliminary design of the FRP alternative only compensated for the reduced Young's modulus in vertical direction by increasing the global dimensions. This can also be done in lateral direction. Additionally, this can shift the eigenfrequency belonging to the fifth sway mode out of the region where wave energy is concentrated.

Increasing the stiffness can either be achieved by using other fibers such as carbon fibers instead of glass fibers or by increasing the dimensions of the structure.

- The dimensions of the pontoons can be adjusted to decrease the surface area perpendicular to the sway direction. The total wave force acting on the pontoons will decrease hereby. This means that the length of the pontoons is reduced and the length is increased. Static stability must be taken into account in this optimization.
- Other design measures which can decrease the dynamic response in sway direction such as side moorings can be applied.

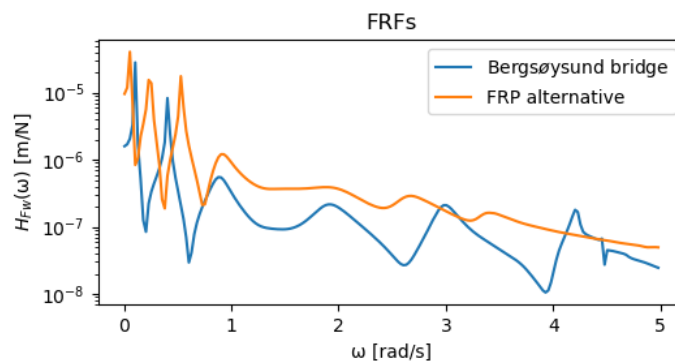


Figure 12.5: Sway FRFs of the Bergsøysund bridge and the FRP alternative.

12.5. Conclusion

The comparison between the dynamic response of the Bergsøysund bridge and the FRP alternative leads to the following conclusions:

- The case study of the FRP alternative confirms the expectation that the SLS criteria are the governing design criteria. The preliminary design of the FRP alternative satisfies all ULS criteria, but the dynamic response exceeds the deflection limit.
- The large reduction in the superstructure's stiffness of the FRP alternative increases the dynamic response significantly. The displacement which is exceeded with a probability of $6,68 \cdot 10^{-2}$ in 100 years is almost 1,5 times higher for the FRP alternative compared to the Bergsøysund bridge.
- The dynamic response of the FRP alternative can be reduced by:
 - Increasing the stiffness of the superstructure to reduce the influence of the fifth sway mode and to decrease the overall magnitude of the FRF. This can be achieved by using fibers with a larger stiffness or by changing the dimensions of the cross section.
 - Reducing the length of the pontoons in order to decrease the wave force acting on the pontoons.
- Based on these results an FRP alternative to the Bergsøysund bridge will be feasible when resonance is avoided and the lateral stiffness is sufficiently high.

V

Conclusion

13

Conclusion, discussion and recommendations

In this chapter the conclusions and recommendations of the complete research are presented. The research questions are answered in section 13.1. Subsequently, the effect of the assumptions on these conclusions are addressed in section 13.2. Finally, recommendations for further research are discussed in section 13.3.

13.1. Conclusion

Chapter 1 introduces the research questions of this research. These questions must be answered to fulfill the research objective: to contribute to the knowledge about the potential of fiber reinforced polymer to enhance a floating pontoon bridge design. The research questions are broken down into sub-questions in order to specify them. First these sub-questions are discussed to answer the research questions in the end.

Literature review

- *What is an appropriate method to schematize a floating bridge in order to model the dynamic response?*
The main elements of a floating bridge are the pontoons and the superstructure. The former are modeled using rigid bodies and the latter is modeled with Euler-Bernoulli beam elements. Boundary and interface conditions are modeled with linear translational and rotational springs and dashpots. The boundary and interface conditions are imposed using the master slave method.
- *Which solution technique is suitable to analyze the dynamic response of a floating bridge?*
A frequency domain approach is more suited than a time domain approach, because the frequency dependent hydrodynamic properties of a floating bridge can more easily be included in such an analysis. A wave spectrum is used to represent the wave conditions at a floating bridge. The developed model is used to transform such a wave spectrum into a response spectrum with transfer functions. These transfer functions depend on the geometrical and structural properties of the floating bridge. The response spectrum is used to derive statistical information about the steady state amplitude of the dynamic response of the floating bridge.
- *How can the fluid-structure interaction between pontoons and waves be modeled?*
The fluid-structure interaction between pontoons and waves can be divided into two components: reaction forces and wave forces. The former consist of the forces that the floating structure experiences due to the motion of the structure and can be expressed in added mass, hydrodynamic damping and hydrostatic stiffness. The wave forces consist of two forces which the waves exert on the structure: the Froude-Krilov force and the diffraction force. All these separate parts of the two force components can be found solving linear potential functions under the assumption of potential flow.
- *How can the interaction between the motions of the different pontoons be included in the model?*
First, wave interaction caused by the pontoons is included in the hydrodynamic analysis performed with Diffrac. As a result, the hydrodynamic properties of multiple pontoons are different from the hydrodynamic properties of a single pontoon. Second, it is possible to include the phase of the wave

elevation and the dynamic response of the structure by applying the relative response spectrum. The relative response spectrum contains information about the relative motion between two degrees of freedom. Statistical information about this motion can be obtained from the relative response spectrum.

Validation

- *Which degree(s) of freedom dominate(s) the dynamic response of the Bergsøysund bridge?*
Sway of the pontoons dominates the dynamic response of the the Bergsøysund bridge with respect to the deflection criteria. Furthermore, in absolute values sway also dominates the dynamic response compared to the other translations. The first reason for this is that the wave forces are largest in magnitude in this direction at a peak frequency of 2 rad/s. The second reason is that hydrostatic stiffness is absent in this direction, which means that the only constraint in this direction are the stiffness of the superstructure and the stiffness of the connections between the pontoons and the superstructure.
- *Which mode shape(s) of the Bergsøysund bridge dominate(s) the dynamic response at the governing degree of freedom?*
The mode shapes of the Bergsøysund bridge determine in which pattern and direction the structure vibrates under influence of wave loads in a perpendicular direction. The fourth sway mode is the main contributor to the dynamic sway response of the pontoons. The odd numbered pontoons are mainly excited under this mode shape and hence they show the largest dynamic response. The eigenfrequency which corresponds to the fourth sway mode is 1,90 rad/s. This explains the large influence of this mode shape, because the main wave energy is concentrated at 2,0 rad/s.
- *To what extent do the modeling results agree with measurements from the Bergsøysund bridge?*
The response spectra of sway and heave from the model and the measurements show a good resemblance. Especially the frequencies of peaks in the response spectra are accurately captured in the modeling results. However, some deviations occur in the order of magnitude of these peaks. Based on this validation it is concluded that the floating bridge model is accurate enough to investigate the influence of different parameters, but not accurate enough to assess the dynamic response of a structure for a detailed design.

Parametric study

- *Which geometrical and structural design parameters influence the dynamic sway response of a floating bridge?*
Of all design parameters the superstructure's length has the largest influence on the dynamic sway response. Additionally, the Young's modulus of the superstructure and the dimensions of the pontoons influence the dynamic sway response significantly. A change in the connection stiffness has a moderate effect on the dynamic sway response. Finally, the influence on the dynamic sway response of the structural damping of the superstructure and the distance between the pontoons is negligible.
- *How do these parameters influence the dynamic response of a floating bridge?*
When the mass of the total structure increases or the lateral stiffness direction decreases, the peaks in the frequency response function of sway which correspond to the eigenmodes will shift to a lower frequency. Vice-versa, increasing the lateral stiffness or reducing the mass shifts the peaks in the frequency response function to higher frequency ranges. Shifting eigenfrequencies of sway modes away from the peak wave frequency prevents resonance. Additionally, when the lateral stiffness is increased, the overall magnitude of the sway's frequency response function reduces. This will contribute to a reduced sway response of the pontoons.

Reducing the length of the superstructure leads to a large shift of the peaks in the frequency response function to a higher frequency range and vice-versa. A similar relation, but smaller in magnitude, applies to the Young's modulus and the second moment of area of the superstructure. Increasing the Young's modulus increases the frequency of these peaks. The connection stiffness mainly influences the structural system of the floating bridge and thereby the relative influence of the superstructure's bending stiffness on the dynamic sway response of the pontoons. When the connection stiffness is reduced, the connections will behave as if hinged. Hence, less bending occurs in the superstructure. This increases the dynamic sway response of the pontoons.

Increasing the dimensions of the pontoons is another effective measure to shift the peaks of the sway frequency response functions to a lower frequency range and vice-versa. This frequency shift is caused by the changed mass. Furthermore, when the length increases, the total wave force exciting the pontoons also becomes larger, which increases the dynamic response apart from the frequency response function.

Main research questions

1. *How can the dynamic response of a floating end-supported pontoon bridge with a continuous superstructure be modeled?*

Summarizing, the following concepts are used to model the dynamic response of a floating end-supported pontoon bridge with a continuous superstructure:

- A floating end-supported pontoon bridge can be schematized with:
 - Rigid bodies
 - Euler-Bernoulli beam elements
 - Linear springs
 - Linear dashpots
 - The fluid-structure interaction can be taken into account by including:
 - Added mass
 - Hydrodynamic damping
 - Hydrostatic stiffness
 - Wave force transfer functions
 - The dynamic response is computed with a frequency domain approach in which:
 - A wave spectrum is transformed into a response spectrum
 - Statistical information about the dynamic response is obtained from the response spectrum
2. *Which parameters can be used to reduce the dynamic response of a floating end-supported pontoon bridge?*

The most effective approach to reduce the dynamic response of a specific point on a floating end-supported pontoon bridge is to avoid resonance and to keep the overall magnitude of the frequency response function as low as possible. The former can be achieved by changing the stiffness of the superstructure or the dimensions of the pontoons. The latter can be accomplished by increasing the stiffness of the superstructure.

3. *How would the differences between fiber reinforced polymer and steel affect the dynamic response of a floating end-supported pontoon bridge?*

A fiber reinforced polymer superstructure will result in a lower mass and stiffness of the superstructure compared to a steel superstructure. Consequently, the dimensions of the pontoons will decrease. Mainly the reduced stiffness of the superstructure influences the dynamic response of the floating bridge. A higher overall magnitude of the frequency response function will increase the dynamic response and the eigenfrequencies belonging to sway modes will shift to a lower frequency. The latter means that higher order modes move closer to the peak wave frequency, which have wider peaks in the frequency response function and are thus more difficult to avoid. In general, the dynamic response will be larger when the superstructure of a floating bridge consists of fiber reinforced polymer instead of steel if the difference in bending stiffness is not accounted for in the design.

13.2. Discussion

This section describes the validity and the value of the conclusions presented previously. Several assumptions are used to model a floating bridge in this research. The influence of these assumptions and the input parameters on the modeling results are critically examined and related to the conclusions of this research.

13.2.1. Influence of the assumptions

The parametric model is based on several assumptions. All these assumptions will affect the modeling results to some extent. The effect of the most important assumptions is summarized here:

- The curved alignment of the Bergsøysund bridge is assumed to be straight in this research to limit the complexity of the model. However, it is expected that this curvature influences the dynamic response. First, the stiffness in the horizontal plane will change due to the curvature. When a curvature is introduced in the superstructure, the constraints of the pontoons in y direction no longer consist only of bending stiffness in lateral direction. According to the principle of vector decomposition, the influence of the lateral bending stiffness decreases, but the influence of the axial stiffness increases. However, since the stiffness in axial direction is larger than the stiffness in lateral direction, it is expected that the eigenfrequencies of sway increase a little and that the overall magnitude of the frequency response function of sway will decrease to some extent.

Second, the alignment of the pontoons changes. The wave loads will excite the pontoons under a different angle of incidence. Hence, the governing wave direction will not merely excite all pontoons in sway direction. Only the alignment of the middle pontoon remains the same. The larger the distance to the middle pontoon becomes, the larger the pontoon's angle becomes compared to the original position. Again following the principle of vector decomposition, the governing wave direction will excite sway and roll of these pontoons less, but will excite surge and pitch more. As such, the combination of these two aspects shows that neglecting the curvature of the superstructure leads to an overestimation of the sway response.

- The phase angle of the wave elevation is assumed to be independent and thus completely random in the computation of the relative response between two pontoons. When the distance between pontoons decreases, the dependency between the phase angles of the waves at two pontoons increases. Although the dependency between the phase angles is unknown, it can be argued that assuming them to be completely independent is probably a conservative assumption. The highest response will occur when the waves arrive exactly out of phase at two adjacent pontoons. The probability that this happens is higher when the phase angles are completely independent. Thus the dynamic sway response is probably overestimated, due to the assumption of independency between wave phase angles.
- The wave load is the only type of load which is taken into account as a dynamic load. The dynamic part of traffic, wind and current loads is assumed to be negligible compared to the dynamic wave load. However, this research shows that low frequency content, even with a small magnitude, can contribute significantly to the dynamic response of the pontoons and the superstructure of a floating bridge. Traffic loads are often transient and will therefore contain mainly energy in the high frequency range. Tidal currents have such a low frequency that this load is almost similar to a static load. Dynamic wind loads on the other hand do contain low frequency content and excite both the pontoons and the superstructure. The wind speed will be higher at a larger height. Hence, including the buffeting wind loads could result in a larger sway motion of mainly the superstructure and to some extent the pontoons.

13.2.2. Influence of the input parameters

The input parameters of the Bergsøysund bridge are used in this research to investigate the influence of design parameters on the dynamic response of a floating bridge. The chosen values of these input parameters determine the dynamic response. The parameters with a significant influence on the response are explained here:

- The spring stiffness of the connections between the pontoons and the superstructure contains a large uncertainty. The choice was made to model the superstructure with separate Euler-Bernoulli beam elements instead of one continuous beam element. The translations between the beam elements and the pontoons are rigidly connected. However, the rotations are connected through rotational springs.

Thus, these rotational springs represent the connection between the pontoon and two parts of the superstructure. The choice for the value of this input parameter contains a relatively large uncertainty, because no suitable reference is available. A higher spring stiffness would constrain the rotations of the superstructure more, but would hardly influence the sway of the pontoons. A lower springs stiffness would change the structural system of the bridge, because the influence of the superstructure's bending stiffness decreases. Hence, the pontoons would be allowed to move more freely without constraints.

- The wave conditions around the Bergsøysund bridge are used in this research. When the wave conditions approach open sea conditions and wave periods increase, the dynamic response of the pontoons in sway and heave would increase significantly. The sway response would increase because of the first two sway modes. Thus, the importance of the overall magnitude of the frequency response function would become of less importance. The first peaks in the frequency response function would dominate the dynamic response.
- Only a single wave direction is used as input for the dynamic loads. Based on the bathymetry it is concluded that this wave direction is the dominant wave direction. When other wave directions would be included, surge and pitch would be excited more. However, the effect on the sway motion of the pontoons is believed to remain minor.

13.2.3. Effect on the conclusions

The argumentation above shows that the assumptions of a straight alignment and the independency of the wave phase both lead to an overestimation of the pontoon's sway motion. Neglecting dynamic wind loads especially leads to an underestimation of the superstructure's sway. Based on these effects it is expected that the model overestimates the dynamic sway response of the pontoons. Furthermore, the model underestimates surge and pitch, but since the magnitude of these motions were negligible compared to sway, it is assumed that this has no effect on the conclusions. A conservative model will not affect the qualitative relations which are presented in the conclusions. However, the difference in the dynamic sway response of the pontoons between the steel and fiber reinforced polymer design is expected to reduce.

The discussion about the influence of the input parameters shows that a lower spring stiffness of the connection springs would result in a reduced influence of the superstructure's bending stiffness. This would affect the presented conclusions. The reduction of the pontoon's dynamic response which is expected when the superstructure's stiffness is increased, would become smaller. As such, the difference between the effect of a steel and fiber reinforced polymer superstructure on the dynamic response of a floating bridge would reduce.

Furthermore, it is shown that when wave conditions contain a significant low frequency component, the dynamic response of a floating bridge is dominated by the first two peaks of the frequency response function instead of its overall magnitude. This means that the influence of the superstructure's stiffness on the dynamic response would reduce. The differences between a steel and fiber reinforced polymer superstructure would become smaller.

13.3. Recommendations

This section presents an overview of recommendations for future research. These recommendations can be divided into three categories. First, the recommendations to improve the performance and accuracy of the current model are discussed. Subsequently, potential new extensions to investigate additional relevant aspects of a floating pontoon bridge are addressed. Finally, a recommendation is given about the use of fiber reinforced polymer in the superstructure of a floating bridge. For first two types of recommendations a short approach is suggested and the expected result is discussed.

13.3.1. Recommendations to improve the current model

- Section 13.2 shows that the uncertainty of the numerical value assigned to the connection springs stiffness has a big influence on the results of this research. It is recommended to perform a more detailed parametric study into the numerical value of these connection springs. Additionally, the possibility to model the superstructure as one continuous beam element should be investigated to compare the dynamic response of the different options.
- A more extensive validation is required to determine the actual accuracy of the model. The validation in this research is based on visual comparison between acceleration spectra. The actual measurement

data are not available at this time. A better validation would consist of a comparison with the actual measurement data. Additionally, measurements obtained in different wave conditions are preferable to check the validity of the model.

- In this research a quantitative estimate of the response of the floating bridge is obtained from the response spectra using the *upper limit approach*. This method relates the surface area of the response spectrum to a response which is exceeded with a probability P in a period T . However, this estimate contains some uncertainty, because it assumes that the peak values of a narrow band process are completely independent, which is not completely true. It was therefore concluded that this model is not applicable for detailed design calculations. Furthermore, this approach appeared not applicable to assess a quantitative acceleration from the acceleration spectrum.

To provide a better assessment of the dynamic response, time series can be produced from the response spectrum. With the addition of random phase angles, this can be used to construct histograms of the dynamic response. A distribution can be fitted to these histograms which will give a more accurate representation of the dynamic response.

- A frequency domain approach is used in this research, because the frequency dependency of the hydrodynamic properties of the pontoons is more easily included. In a frequency domain analysis non-linear effects such as non-potential damping can not be taken into account. It is therefore advised to examine the influence of these non-linear effects. For instance, it is widely known that the pitch motion of the pontoons, which coincides with the roll motion of a ship, is influenced by viscous damping. When the relative influence of these non linear effects becomes large for the motions of interest, it is recommended to take this in some way into account.

13.3.2. Recommendations for future applications of the model

- Only an end-supported pontoon bridge is currently included in the model. In such a structure the only way to constrain the sway motion of the pontoons is through the superstructure. It is recommended to extend the model to be able to apply different solutions to constrain motions of the pontoons. For instance, side moorings can be added by including extra translational springs at the pontoons. Next to that, tension cables, connected between two pontoons, could be used to constrain the relative motion between two pontoons. These can also be added with translational springs.
- The only type of superstructure which is incorporated in the model is a truss structure. The main reasons for this are that a truss structure is an efficient design, it is easy to model and the superstructure of the Bergsøysund bridge also is truss. However, when distances of 110 m and larger are spanned, a fiber reinforced polymer superstructure would probably be an arch structure. For this reason, it would be interesting to include arch structures in the model. However, it is not possible to represent an arch superstructure with only one beam element. At least two interconnected beam elements are required to model the structural properties of arch bridges.
- It is advised to use Timoshenko beam elements instead of Euler-Bernoulli beam elements. A Timoshenko beam element is able to account for shear deformations, which are more relevant in the case of an arch bridge.
- When the accuracy of the dynamic response is increased, it becomes interesting to look at economic aspects in the comparison between a steel and fiber reinforced polymer superstructure. First quantities of material can easily be compared in terms of costs. Furthermore, fabrication and durability are interesting aspects to take into account.

13.3.3. Recommendation about the use of fiber reinforced polymer in a floating bridge

This study shows that the dynamic response of a floating end-supported pontoon bridge is mainly determined by the stiffness of the superstructure. The reduction in stiffness caused by the Young's modulus of fiber reinforced polymer must be accounted for in the design to keep the dynamic sway response within acceptable limits. It is possible to achieve this by increasing the width of the superstructure. Additionally, other solutions to constrain the sway motion such as side moorings can be used to account for the reduced stiffness. Based on these findings it is feasible to construct the superstructure by fiber reinforced polymers. Therefore, it is recommended to improve the accuracy of the model to investigate the competitiveness of a fiber reinforced polymer superstructure compared to steel.

Bibliography

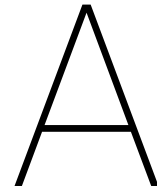
- Bergdahl, L. (2009). *Wave-Induced Loads and Ship Motions*. Chalmers university of technology.
- Bureau Veritas (2015). *Classification of Mooring Systems for Permanent and Mobile Offshore Units*.
- Corso, L. L. (2016). Reliability based design optimization using a genetic algorithm: application to bonded thin films areas of copper/polypropylene. *Ingeniare. Rev. chil. ing.*
- Cummins, W. E. (1962). The impuls response function and ship motions. Technical report, David Taylor Model Basin.
- CUR-aanbeveling 96 (2003). *Vezelversterkte kunststoffen in civiele draagconstructies*. Aeneas Media.
- Dagrun Stokke (2011). Meir enn 60 millionar har passert over brua. *Nordhordland*.
- Edmondson, B. (2017). Collision resistance of frp lock gates. Master's thesis, TU Delft.
- Ellevset, O. (2012). Project overview coastal highway route e39. Technical report, Statens vegvesen.
- Ellevset, O. (2014a). Teknologidagene 2014. https://www.vegvesen.no/_attachment/704759/binary/989366?fast_title=St_C3_A5lbruer+i+100+_C3_A5r.pdf. Accessed: 2017-10-10.
- Ellevset, O. (2014b). Teknologidagene 2014. https://www.vegvesen.no/_attachment/706838/binary/995297?fast_title=Prosjeker+med+teknologisk+gjennombrudd+%E2%80%93-bruer+og+%C2%ABplussveger%C2%BB.pdf. Accessed: 2017-10-10.
- Felippa, C. A. (2004). *Introduction to Finite Element Methods*. University of Colorado.
- Flore, D. and Wegener, K. (2015). Modelling the Mean Stress Effect on Fatigue Life of Fibre Reinforced Plastics. *International Journal of Fatigue*.
- Fossen, T. I. (2011). *Handbook of Marine Craft Hydrodynamics and Motion Control*. John Wiley & Sons.
- HB185 (2011). *Bruprojektering Eurokodeutgave*. Statens vegvesen.
- Hermans, R. (2014). Buoyancy aided Crossing for Bridging Extreme Widths. Master's thesis, TU Delft.
- Hermstad, S. M. (2013). Dynamic Analysis of the Bergsøysund Bridge in the Time Domain. Master's thesis, NTNU.
- Holhuijsen, L. H. (2010). *Waves in Oceanic and Coastal Waters*. Cambridge University.
- Jakobsen, S. E. (2013). Sognefjorden feasibility study of floating bridge. Technical report, Aas-Jakobsen, Johs Holt As, COWI, SKANSKA.
- Jakobsen, S. E. (2017). Design Basis Bjørnafjorden. Technical report, Stagens vegvesen.
- Journée, J. and Massie, W. (2002). *Offshore Hydromechanics*. VSSD.
- Karlberg, D. (2014). The effect of three-dimensionality on the radiation forces of surface piercing bodies. Master's thesis, Aalto University.
- KDC (1999). Movable floating bridge. http://kansai-design.co.jp/en/project/project01_002.html. Accessed: 2018-05-03.
- Kolkman, P. A. and Jongeling, T. H. G. (2007). *Dynamic behaviour of hydraulic structures*. Delft Hydraulics.
- Kvåle, K. A. and Øiseth, O. (2017). Structural monitoring of an end-supported pontoon bridge. *Marine Structures*.

- Kvåle, K. A., Øiseth, O., and Rønnquist, A. (2017). Operational modal analysis of an end-supported pontoon bridge. *Engineering Structures*.
- Kvåle, K. A., Øiseth, O., and Sigbjörnsson, R. (2016). Modelling the stochastic dynamic behaviour of a pontoon bridge: A case study. *Computers and structures*.
- Lallement, G. and Inman, D. J. (1995). A tutorial on complex eigenvalues. *13th International Modal Analysis Conference*.
- Le Mehaute, B. (1976). *An introduction to hydrodynamics and water waves*. Springer verslag.
- Marin (2014). Difffrac user guide. Technical report, Marin.
- Moan, N. (2017). *Stochastic Dynamics of Marine Structures*. Cambridge University.
- Moe, G. (1997). Design philosophy of floating bridges with emphasis on ways to ensure long life. *Journal of Marine Science and Technology*.
- Mor Temor (2017). Norway floating bridge. <http://eng.mortemor.com/index.php/articles/index/norway-floating-bridge/>. Accessed: 2018-02-03.
- Morison, J., Johnson, J., and Schaaf, S. (1950). 'The Force Exerted by Surface Waves on Piles. *Journal of Petroleum technology*.
- NEN-EN 1990 (2011). *Grondslagen van het constructief ontwerp*. NEN.
- Nijssen, R. (2013). *Basiskennis van composieten*. Hogeschool Inholland.
- Pavlovic, M. (2018). Fiber reinforced polymer composites in structural engineering. <https://online-learning.tudelft.nl/courses/frp-composites-in-structural-engineering/>. Accessed: 2018-05-03.
- Petersen, Ø., Øiseth, O., Nord, T., and Lourens, E. (2018). Estimation of the full-field dynamic response of a floating bridge using Kalman-type filtering algorithms. *Mechanical Systems and Signal Processing*.
- Petersen, Ø. W., Øiseth, O., Nord, T. S., and Lourens, E.-m. (2017). Model-Based Estimation of Hydrodynamic Forces on the Bergsoysund Bridge. *Dynamics of Civil Structures*.
- Petersen, W. and Øiseth, O. (2017). Sensitivity-based finite element model updating of a pontoon bridge. *Engineering Structures*.
- Potyrala, P. B. (2011). *Use of Fibre Reinforced Polymer Composites in Bridge Construction. State of the Art in Hybrid and All-Composite Structures*. Universitat politechnica de Catalunya.
- Rizkalla, S., Dawood, M., and Shahawy, M. (2006). FRP for Transportation and Civil Engineering Infrastructure: Reality and Vision. *Transportation research E-circular*.
- Smulders, J. (2014). Dynamics assessment of the bolivar roads navigational barge gate barrier. Master's thesis, TU Delft.
- Spijkers, J., Vrouwenvelder, A., and Klaver, E. (2006). *Dynamics of Structures Part 1 Vibration of Structures*. VSSD.
- Statens vegvesen (1991). Stålkonstruksjoner Bergsøysund.
- Stensvold, B. and Minoretti, A. (2014). Long span bridge in norway. *International Seminar on Long Span Bridge Construction, Maintenance and Disaster Resistance Techniques*.
- Tidens Krav (2017). En doktorgrad for bergsøysundbrua. <https://www.tk.no/nyheter/kristiansund/lordag/en-doktorgrad-for-bergsøysundbrua/f/5-51-283168>. Accessed: 2018-02-03.
- Tisseur, F. and Meerbergen, K. (2001). The Quadratic Eigenvalue Problem. *SIAM Review*.
- van Ijsselmuiden, K. (2016). Sognefjord haalbaarheidsstudie voor een hangbrug in vvk met een overspanning van 3,7 km. *Tijdschrift bruggen*.

- Visser, W., Amico, F., Torsing, R., Top, R., Oosterman, K., Bhattafcharya, A., Bijlaard, F., and Yip, C. (2017). Long span buoyancy bridge. *Proceedings of Eurosteel 2017*.
- Vrijling, J. K. and van Gelder, P. H. A. J. M. (2002). *Probabilistic design in hydraulic engineering*. VSSD.
- Vrouwenvelder, T. (2005). *Random Vibrations*. VSSD.
- Vugts, J. (1971). The hydrodynamic forces and ship motions in oblique waves. Technical report, TNO.
- Watanabe, E. and Utsunomiya, T. Analysis and design of floating bridges. *Progress in Structural Engineering and Materials*.
- W.F. Chen, L. D. (2014). *Bridge Engineering Handbook 2nd Edition, Fundamentals*. CRC Press.
- Yip, C. M. (2015). Long span buoyancy bridge with submerged cable anchoring. Master's thesis, TU Delft.
- Yoneyama, H., Shiraishi, S., and Ishimi, G. (1997). Model experiments on characteristics of motions of continuous pontoon type and separate support type elastic floating bodies in waves. *Proceedings of civil engineering in the ocean*.

VI

Appendices



Bergsøysund bridge

This appendix presents detailed information about the Bergsøysund bridge. First, the second moments of area are calculated from an average cross section of the Bergsøysund bridge. Subsequently, the measurement equipment is shown and several measurements are presented. Finally, picture of the corrosion process at the Bergsøysund bridge are shown.

A.1. Structural parameters

The selected cross section can be divided into three main parts: tubes, beams and the deck structure. The two main tubes and two main beams are regular structural elements. Their dimensions are presented in figure A.1 and in table A.1. In contrast, the deck structure is complex and not easily modeled as a uniform component. Hermstad (2013) used the software Cross-X to model this deck structure as a uniform beam element. The results of this analysis are used here.

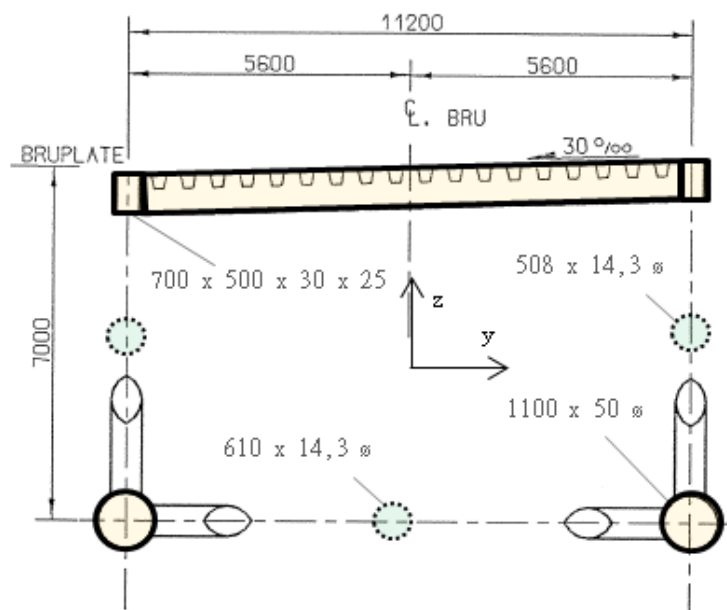


Figure A.1: Cross section of the Bergsøysund bridge (Statens vegvesen, 1991).

Component	Height [m]	Width [m]	Thickness _z [m]	Thickness _y [m]	Total surface area [m ²]
Tube (2)	1,1	1,1	0,05	0,05	0,169
Beam (2)	0,7	0,5	0,03	0,025	0,124
Horizontal diagonal (1)	0,61	0,61	0,014	0,014	0,014
Vertical diagonal (2)	0,508	0,508	0,014	0,014	0,023
Deck (1)					0,264
Total					0,593

Table A.1: Dimensions of individual segments of the cross section.

The second moment of area relative to the center of gravity is calculated with:

$$I_{z'} = I_z + A \cdot d^2 \quad (\text{A.1})$$

where $I_{z'}$ is the second moment of area relative to the center of gravity, I_z is the second moment of area of a component around its own center of gravity, A is the surface area and d is the distance between the centers of gravity of an element and the cross section. The second moments of area of the three main parts are presented below. The second moments of area around the z, y and x axis are presented in tables A.2, A.3 and A.4 respectively. The diagonals (green in figure A.1) are only taken into account when they are assumed to experience bending moment. The horizontal diagonal is only taken into account considering I_y and I_x . The vertical diagonals are only taken into account considering I_z and I_x .

Component	I_z [m ⁴]	Steiner [m ⁴]	$I_{z'}$ [m ⁴]
Tube (2)	0,0244	5,30	5,32
Beam (2)	0,00486	3,89	3,89
Deck (1)	2,45	0	2,45
Vertical diagonal (2)	0,0007	0,706	0,706
Total			12,4

Table A.2: Second moment of area (I_z) of the selected cross section.

Component	I_y [m ⁴]	Steiner [m ⁴]	$I_{y'}$ [m ⁴]
Tube (2)	0,0244	4,53	4,55
Beam (2)	0,0089	0,411	0,420
Deck (1)	0,000331	0,874	0,874
Horizontal diagonal (1)	0,0006	0,341	0,342
Total			6,15

Table A.3: Second moment of area (I_y) of the selected cross section.

Component	I_x [m ⁴]	Steiner [m ⁴]	$I_{x'}$ [m ⁴]
Tube (2)	0,0488	9,83	9,88
Beam (2)	0,00689	4,30	4,31
Deck (1)	0,00345	0,874	0,877
Vertical diagonal (2)	0,001	0,706	0,706
Horizontal diagonal (1)	0,001	0,341	0,342
Total			16,1

Table A.4: Second moment of area (I_p) of the selected cross section.

A.2. Measurement equipment

Accelerations of the bridge structure, wave elevations and wind speeds were monitored in the measurement period. Figure A.3 shows the different types of equipment which were used to perform the measurements and Figure A.2 indicates the locations where these measurement equipment was installed. Usually when measurements are performed regarding wave action, periods of at least 30 minutes are used to extract information. In this case periods of only 10 minutes were used, due to the fast changing wave conditions (Kvåle and Øiseth, 2017). One general disadvantage of short wave measurement periods is that they will likely overestimate the variance, because of the limited number of measured waves. However, in this case it was assumed that waves have relatively short wave periods and therefore enough waves would be measured in this period.

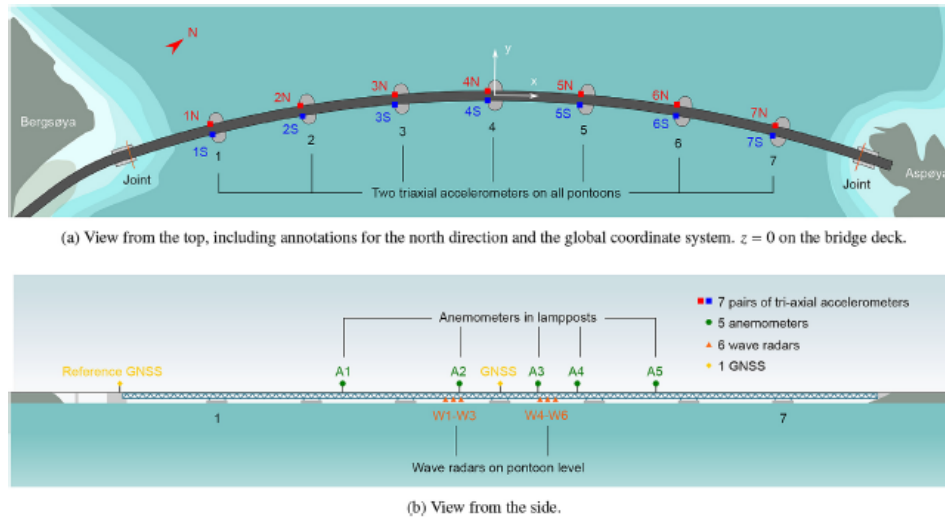


Figure A.2: Locations of measurement instruments at the Bergsøysund bridge (Kvåle et al., 2017).



Figure A.3: Measurement equipment used at the Bergsøysund bridge (Kvåle and Øiseth, 2017).

A.3. Measurement data

Different papers containing results of the measurements were published in the past few years (Kvåle and Øiseth, 2017). However, only one dataset contains useable information, because the information about the wave conditions and the dynamic response is published. The following figures present these measurements.

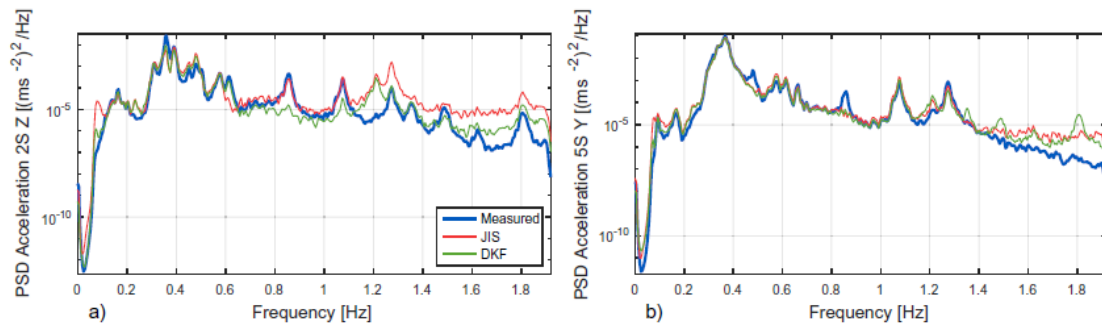


Figure A.4: Response spectra of the acceleration measurements of recording 1 (Petersen et al., 2018).

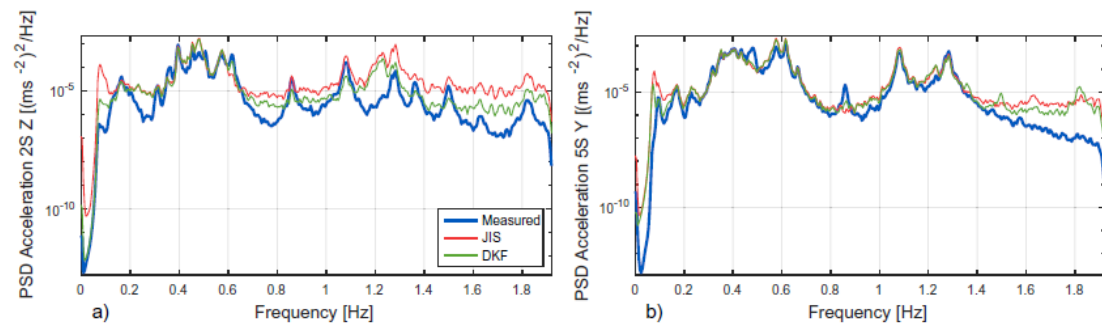


Figure A.5: Response spectra of the acceleration measurements of recording 2 (Petersen et al., 2018).

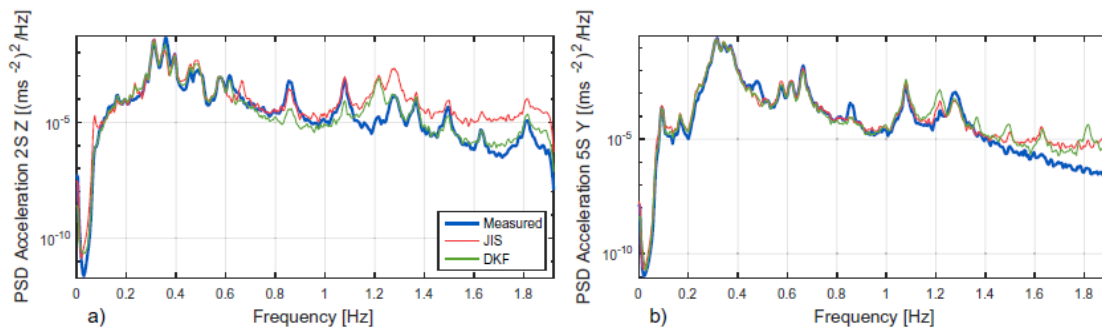


Figure A.6: Response spectra of the acceleration measurements of recording 3 (Petersen et al., 2018).

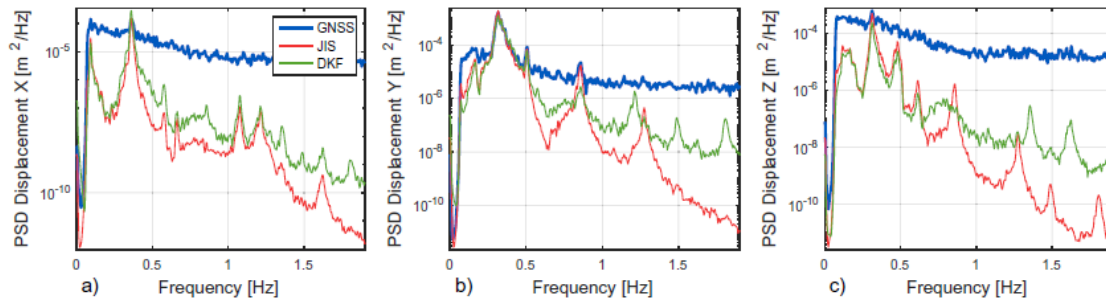


Figure A.7: Response spectra of the displacement measurements of recording 1 (Petersen et al., 2018).

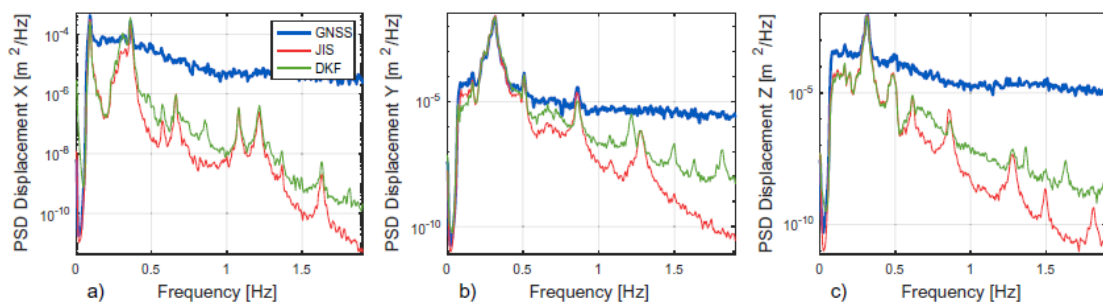


Figure A.8: Response spectra of the displacement measurements of recording 3 (Petersen et al., 2018).

A.4. Maintenance at the Bergsøysund bridge

The following figures illustrate the wave action at the Bergsøysund bridge which causes salt to stick to the superstructure. Eventually this leads to corrosion.



(a) Wave action at the Bergsøysund bridge.



(b) Wave action at the Bergsøysund bridge.

Figure A.9: Wave action at the Bergsøysund bridge (Ellevset, O., 2014a).



(a) Salt on the superstructure.



(b) Corrosion damage.

Figure A.10: Corrosion at the Bergsøysund bridge (Ellevset, O., 2014a).



(a) Maintenance at the Bergsøysund bridge.



(b) Maintenance at the Bergsøysund bridge.

Figure A.11: Maintenance at the Bergsøysund bridge (Ellevset, O., 2014a).

B

Structural dynamics

This appendix contains several derivations of equations and concepts which are used in the main report. The solution procedure of a single DOF system is explained. Subsequently, the derivation of the EOMs of an Euler-Bernoulli beam are presented. The separation of variables technique which is used to solve a continuous system is presented next. Furthermore, a derivation of the FEM is shown.

B.1. 1 DOF pontoon system

The equation of motion of a 1DOF spring-mass-dashpot system is given by:

$$m\ddot{x} + c\dot{x} + kx = F_w(t) \quad (\text{B.1})$$

Dividing through m simplifies the differential equation:

$$\ddot{x} + 2n\dot{x} + \omega_n^2 x = F(t) \quad (\text{B.2})$$

Here $2n = c/m$, where n is a measure for the viscous damping and $\omega_n = \sqrt{\frac{k}{m}}$, where ω_n is the natural frequency of the undamped system. First a solution must be found for the free vibrations. In this case $F_w(t)$, the force term, becomes 0 and this equations reduces to a simple second order ordinary differential equation. This system can now be solved when two initial conditions are known. The general solution has to satisfy both the equation of motion and the initial conditions and can be written as:

$$x_h(t) = \sum_{n=1}^2 X_n \cdot e^{s_n t} \quad (\text{B.3})$$
$$s_n = -n \pm \sqrt{n^2 - \omega_n^2}$$

where:

x_h	=	Homogeneous solution	[m]
s_n	=	Characteristic exponent	[-]

where s_n is the characteristic component. This solution is called the homogeneous solution. Subsequently, assuming that the excitation force is sinusoidal, the particular solution can be found in the form:

$$x_p(t) = \text{Re}(\hat{X} \cdot e^{i\omega t}) \quad (\text{B.4})$$

where:

x_p	=	Particular solution	[m]
-------	---	---------------------	-----

where \hat{X} is a constant. This solution is substituted into the EOM to determine the constant. The particular solution is also known as the steady state response and is independent of the initial conditions. The general solution now becomes:

$$x(t) = x_h(t) + x_p(t) \quad (\text{B.5})$$

This equation is substituted into both the EOM and the initial conditions to solve the remaining unknown constants.

Furthermore, when the assumed solution of Equation B.4 is substituted into the EOMs, the following result is obtained if the damping and forcing term are not taken into account:

$$\begin{aligned} -\omega^2 m \cdot e^{i\omega t} + k \cdot e^{i\omega t} &= 0 \\ -\omega^2 m + k &= 0 \end{aligned} \quad (\text{B.6})$$

This is called the eigenvalue problem and has to be solved to find the eigenfrequencies of the system.

B.2. Continuous systems: equations of motions of an Euler-Bernoulli beam

The derivation of a system with infinite spatial coordinates is presented here. Newton's second law is adopted to find the EOMs of an Euler-Bernoulli beam.

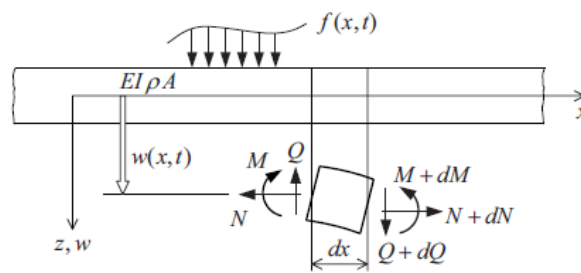


Figure B.1: Conventions and forces of an Euler-Bernoulli beam (Spijkers et al., 2006).

From figure B.1 the following can be deduced:

$$\rho A \Delta x \frac{\partial^2 w}{\partial t^2} = -V(x) + V(x + \Delta x) + q_1 \Delta x \quad (\text{B.7})$$

where:

$$V = \text{Shear force [N]}$$

Using a Taylor expansion this can be simplified to:

$$\rho A \frac{\partial^2 w}{\partial t^2} = \frac{\partial V}{\partial x} + q_1 \quad (\text{B.8})$$

Using the fact that the shear force equals the spatial derivative of the moment and substituting equation 4.15 into this, the EOM of a bending beam are defined:

$$\rho A \frac{\partial^2 w}{\partial t^2} + \frac{\partial^2}{\partial x^2} EI \frac{\partial^2 w}{\partial x^2} = q_1 \quad (\text{B.9})$$

B.3. Separation of variables

Separation of variables is used to solve a continuous system. Additional to the initial conditions, boundary conditions are now required to solve this system. The number of required boundary conditions depends on the system and is always equal to the order of the spatial derivative in the EOMs. One way to solve this system analytically is to apply separation of variables. A solution in the following form is searched for:

$$w(x,t) = W(x)\Psi(t) \quad (\text{B.10})$$

where:

$$\begin{aligned} W &= \text{Space dependent part of the displacement equation [m]} \\ \Psi &= \text{Time dependent part of the displacement equation [m]} \end{aligned}$$

Substitution of this equation in the EOM and subsequently dividing through $W\Psi$ results in:

$$\frac{1}{\Psi} \frac{\partial^2 \Psi}{\partial t^2} + a^2 \frac{1}{W} \frac{\partial^4 W}{\partial x^4} = 0 \tag{B.11}$$

where a^2 is equal to $\frac{EI}{\rho A}$. This equation can only be satisfied when both the time dependent and the space dependent part are equal to a constant:

$$\begin{aligned} \frac{1}{\Psi} \frac{d^2 \Psi}{dt^2} &= -\omega^2 \\ a^2 \frac{1}{W} \frac{d^4 W}{dx^4} &= \omega^2 \end{aligned} \tag{B.12}$$

The space dependent differential equation can be described as the eigenvalue problem:

$$\frac{d^4 W(x)}{dx^4} - \beta^4 W(x) = 0 \tag{B.13}$$

where β^4 is equal to $\frac{\omega^2}{a^2}$. The general solutions of this equation becomes:

$$W(x) = \sum_{n=1}^4 \tilde{C}_n \cdot e^{s_n x} \tag{B.14}$$

This leaves 5 unknowns, namely the four constants, \tilde{C}_n , and β , which includes the unknown frequency. Only four of these can be solved by substituting the general solution into the boundary conditions. Three of the constants can be found and the eigenfrequencies can be determined. The free vibration of a beam having infinite eigenfrequencies is a summation of the corresponding mode shapes:

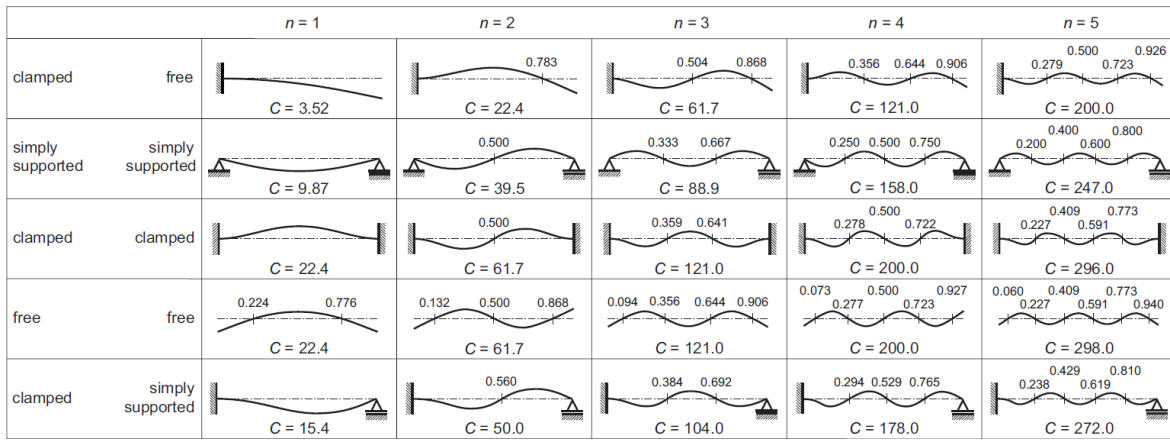


Figure B.2: Theoretical mode shapes of beams with different boundary conditions (Spijkers et al., 2006).

Subsequently, the complete general solution can be substituted into the initial conditions to determine the constants A and B .

B.4. FEM

The FEM is another technique to solve a system with infinite spacial coordinates. Just as the separation of variables technique, the FEM is based on the fact that an assumed equation for the displacement field (Equation B.15) must satisfy the boundary conditions of the system (Equation B.16).

$$w(x, t) = a_0 + a_1 x + a_2 x^2 + a_3 x^3 \tag{B.15}$$

The boundary conditions of this simple beam element are given by:

$$\begin{aligned}
w(0, t) &= q_1(t) \\
\left. \frac{\partial w}{\partial x} \right|_{x=0} &= q_2(t) \\
w(L, t) &= q_3(t) \\
\left. \frac{\partial w}{\partial x} \right|_{x=L} &= q_4(t)
\end{aligned} \tag{B.16}$$

Substitution of these four boundary conditions in Equation B.15 solves the constants in this equation. This can be represented in matrix form:

$$w(x, t) = \begin{bmatrix} 1 - 3\left(\frac{x}{L}\right)^2 + 2\left(\frac{x}{L}\right)^3 & x - 2L\left(\frac{x}{L}\right)^2 + L\left(\frac{x}{L}\right)^3 & 3\left(\frac{x}{L}\right)^2 - 2\left(\frac{x}{L}\right)^3 & -L\left(\frac{x}{L}\right)^2 + L\left(\frac{x}{L}\right)^3 \end{bmatrix} \begin{bmatrix} q_1 \\ q_2 \\ q_3 \\ q_4 \end{bmatrix}$$

In general terms this can be rewritten as:

$$w(x, t) = \Phi^T(x) \cdot \mathbf{q}(t) \tag{B.17}$$

where Φ is defined as the vector containing the shape functions of the element and \mathbf{q} is the vector containing the nodal coordinates. The relation between the mass and stiffness matrices and these vectors can now be derived via the principle of energy. Assuming that ρ and A are constant, the kinetic energy and strain energy are defined as:

$$\begin{aligned}
T &= \frac{1}{2} \dot{\mathbf{q}}^T \cdot \mathbf{M} \cdot \dot{\mathbf{q}} & U &= \frac{1}{2} \mathbf{q}^T \cdot \mathbf{K} \cdot \mathbf{q} \\
T &= \frac{1}{2} \rho A \int_0^L \dot{w}^2 dx & U &= \frac{1}{2} EI \int_0^L \dot{w}_{xx}^2 dx
\end{aligned} \tag{B.18}$$

Substituting equation B.17 into these equations gives an expression for the mass and stiffness matrices:

$$\mathbf{M} = \rho A \int_0^L \Phi \cdot \Phi^T dx \qquad \mathbf{K} = EI \int_0^L \Phi_{xx} \cdot \Phi_{xx}^T dx \tag{B.19}$$

Using the linear shape functions derived above finally provides the following local mass and stiffness matrices:

$$\mathbf{M} = \frac{\rho AL}{420} \begin{bmatrix} 156 & 22L & 54 & -13L \\ 22L & 4L^2 & 13L & -3L^2 \\ 54 & 13L & 156 & -22L \\ -13L & -3L^2 & -22L & 4L^2 \end{bmatrix} \qquad \mathbf{K} = \frac{EI}{L^3} \begin{bmatrix} 12 & 6L & -12 & 6L \\ 6L & 4L^2 & -6L & 2L^2 \\ -12 & -6L & 12 & -6L \\ 6L & 2L^2 & -6L & 4L^2 \end{bmatrix}$$

C

Linear wave theory

This appendix presents additional information about linear wave theory. A derivation of a simplified wave force transfer function is shown. Subsequently, the concept of a response amplitude operator is explained.

C.1. Linear wave theory

Linear wave theory provides relations to describe physical characteristics of wind waves. First a simplified wave force is derived using linear wave theory. Additionally the more complex linear potential theory is elaborated in appendix D. Linear wave theory makes use of the assumption that gravitation is the only external force which is considered. The derivation of the equations can be found in Holhuijsen (2010). A direct relation between the wave elevation and the wave induced pressure is presented. This relation is visualized in figure C.1.

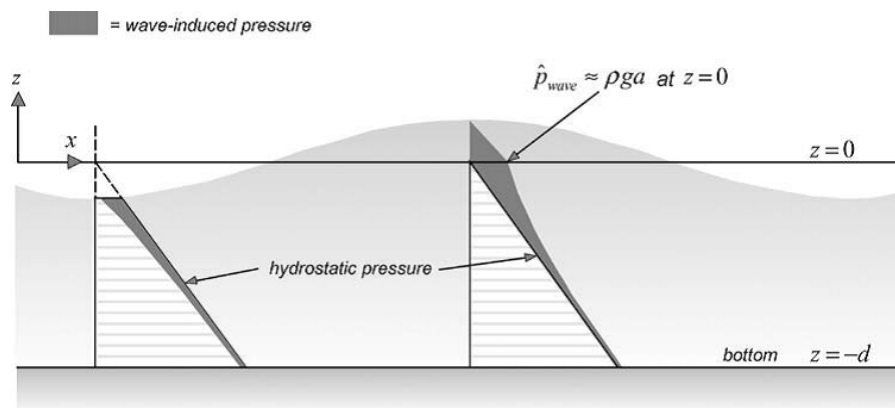


Figure C.1: Pressure according to linear wave theory (Holhuijsen, 2010).

With the relation between the wave amplitude and wave pressure, a transfer function can be derived to compute wave forces from wave amplitudes:

$$H_{\eta,F}(\omega) = \rho g \cdot \frac{2g}{\omega^2} \sin\left(\frac{\omega^2 W_p}{2g}\right) L_p \quad (C.1)$$

where:

$H_{\eta,F}$	=	Transfer function between wave elevation and wave force	[kg/s ²]
L_p	=	Length of the pontoon along the x axis	[m]
W_p	=	Width of the pontoon along the y axis	[m]

The complete derivation of this transfer function is presented in section C.2. The concept of a transfer function is further elaborated in section 4.2.1.

It is important to realize that this transfer function neglects diffraction effects. This is not realistic when the dynamic behaviour of a floating bridge is modeled. Although Journée and Massie (2002) states that the diffraction part of the wave force is very small for low frequency components (long waves), this can not readily be assumed for floating bridges. The bathymetry in Norwegian fjords limits the effective fetch and hence the wave lengths. Therefore, the diffraction part of the wave force should be taken into account for a more realistic approximation.

C.2. Simplified wave force transfer function

If only the radiation force is taken into account, a transfer function between the wave spectrum and the force spectrum can be derived easily:

$$F_{33} = \tilde{\eta} \rho g \cdot \frac{\cosh(k_w(d-z))}{\cosh(k_w d)} \int_{-\frac{1}{2}W_p}^{\frac{1}{2}W_p} \sin(\omega t - k_w x) dx \quad (\text{C.2})$$

In deep water this reduces to:

$$F_{33} = \tilde{\eta} \rho g \cdot \int_{-\frac{1}{2}W_p}^{\frac{1}{2}W_p} \sin(\omega t - k_w x) dx \quad (\text{C.3})$$

Solving the integral with respect to space, this becomes a function depending of the wave elevation $\eta(t)$:

$$F_{33} = \rho g \cdot \frac{2}{k_w} \sin\left(\frac{k_w W_p}{2}\right) \eta(t) \quad (\text{C.4})$$

The transfer function $H_{F\eta,33}$ can be extracted from this equation:

$$H(\omega) = \rho g \cdot \frac{2g}{\omega^2} \sin\left(\frac{\omega^2 W_p}{2g}\right) \quad (\text{C.5})$$

An overview of this transfer function for heave is given in Figure C.2.

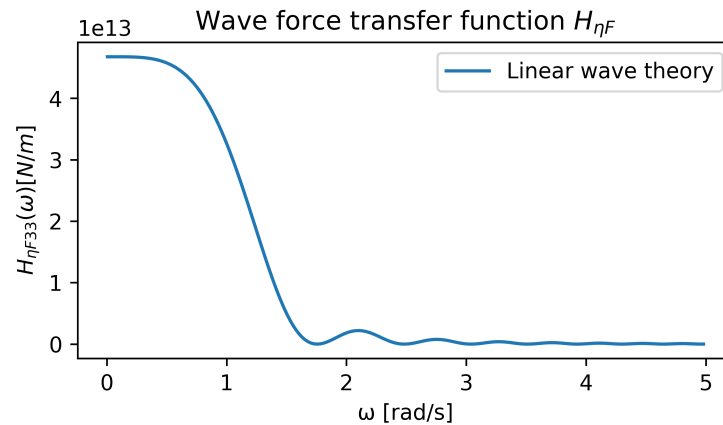


Figure C.2: Transfer function between the wave spectrum and the force spectrum without taking the diffraction force into account.

C.3. Response amplitude operator

The response amplitude operator (RAO) is a function which represent the relation between the wave spectrum and the response spectrum. This means that both the wave force transfer function and the FRF are included in the RAO:

$$RAO = [H_{F,w}(\omega) \cdot H_{F,w}^*(\omega)] \cdot [H_{\eta,F}(\omega)]^2 \tag{C.6}$$

H^* indicates the complex conjugate of matrix H, because this matrix contains complex values. Figure C.3 illustrates the principle of a RAO.

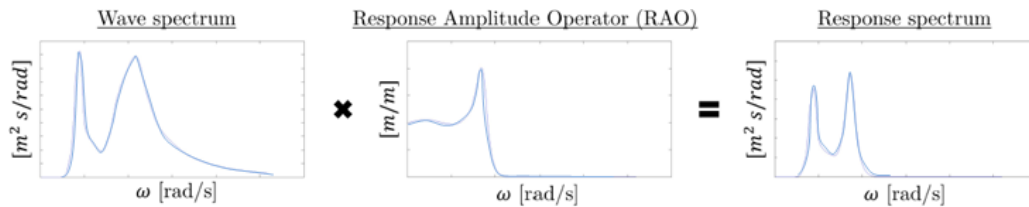


Figure C.3: Transfer function (Smulders, 2014).

Figure C.4 shows a theoretical RAO function of the heave motion and distinguishes three different frequency ranges:

1. The low frequency area ($\omega^2 \ll \frac{k}{m}$). In this region the response is dominated by the stiffness terms of the floating structure. The structure tends to follow the waves around the lowest frequencies. Here the force can be assumed to be almost static and therefore the RAO of heave always starts at 1.
2. The resonance area ($\omega^2 \approx \frac{k}{m}$). In this region the response is dominated by the damping terms. The amount of damping determines the magnitude of the resonance. Furthermore, a phase shift of $-\pi$ occurs exactly at the resonance frequency.
3. The high frequency area ($\omega^2 \gg \frac{k}{m}$). In this region the response is dominated by the inertial terms. Here the influence of waves decreases on the dynamic response, because several crests and troughs appear over the width of the structure.

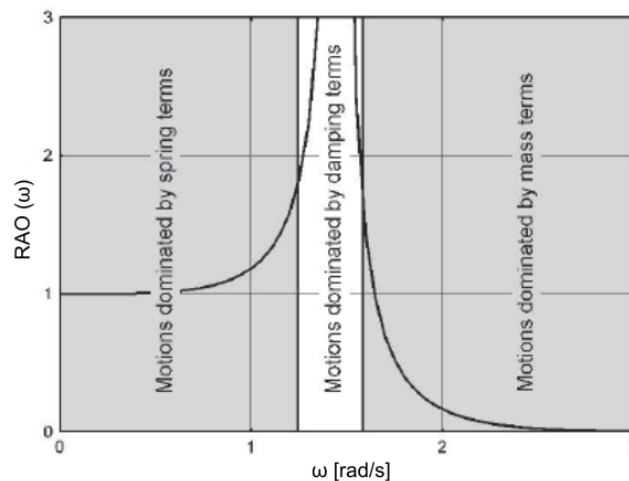
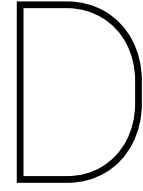


Figure C.4: Different frequency ranges of a RAO (Journée and Massie, 2002).



Potential flow theory

In this appendix additional information is presented about the principles of potential flow. The most important assumptions are explained. Derivations of the radiation potential, the radiation force and the wave excitation potential are given. Finally, the solving procedure of a potential function is briefly explained.

D.1. Potential flow

Potential flow is a method which is applied in linear wave theory to explain the motions of gravity waves at the surface. The linearized momentum balance relates the fluid particle kinematics to wave-induced pressures. The origin of these equations is based on linear wave theory and is explained in Holhuijsen (2010). This relation is given by:

$$\begin{aligned}\frac{\partial u_x}{\partial t} &= -\frac{1}{\rho} \frac{\partial p}{\partial x} \\ \frac{\partial u_y}{\partial t} &= -\frac{1}{\rho} \frac{\partial p}{\partial y} \\ \frac{\partial u_z}{\partial t} &= -\frac{1}{\rho} \frac{\partial p}{\partial z} - g\end{aligned}\tag{D.1}$$

where:

$$\begin{aligned}u_x &= \text{Particle velocity in x direction} \quad [\text{m/s}] \\ u_y &= \text{Particle velocity in y direction} \quad [\text{m/s}] \\ u_z &= \text{Particle velocity in z direction} \quad [\text{m/s}]\end{aligned}$$

The velocity potential is a scalar function $\Phi = \Phi(x, y, z, t)$, which is defined as a function of which the spatial derivatives equal the particle flow velocities:

$$\begin{aligned}u_x &= \frac{\partial \Phi}{\partial x} \\ u_y &= \frac{\partial \Phi}{\partial y} \\ u_z &= \frac{\partial \Phi}{\partial z}\end{aligned}\tag{D.2}$$

The potential value between A and B is visualized in Figure D.1 and is defined as:

$$\Delta\Phi_{A \rightarrow B} = \int_A^B \mathbf{v} \cdot d\mathbf{s} = \int_A^B (\dot{u}_x \cdot dx + \dot{u}_y \cdot dy + \dot{u}_z \cdot dz) = \int_A^B \left(\frac{\partial \Phi}{\partial x} dx + \frac{\partial \Phi}{\partial y} dy + \frac{\partial \Phi}{\partial z} dz \right)\tag{D.3}$$

D.2. Assumptions

The following assumptions are made to allow the use of the potential theory and the superposition principle:

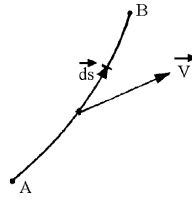


Figure D.1: Principle of the potential theory (Journée and Massie, 2002).

- Flow is homogeneous
- Flow is continuous
- Flow is non-viscous
- Fluids are incompressible ($\nabla^2 \Phi = 0$)
- Flow is irrotational ($\nabla \times \mathbf{v} = 0$)

These assumptions are made based on the results of previous research on deep water. Floating bridges are usually only feasible in areas with a large water depth, so deep water is assumed in this case. Figure D.2a indicates in the case of deep water waves, linear wave theory can be assumed. This allows the use of the superposition principle. Furthermore, forces on a non moving structure in a wave environment are dominated by gravity forces instead of viscous forces according to Journée and Massie (2002).

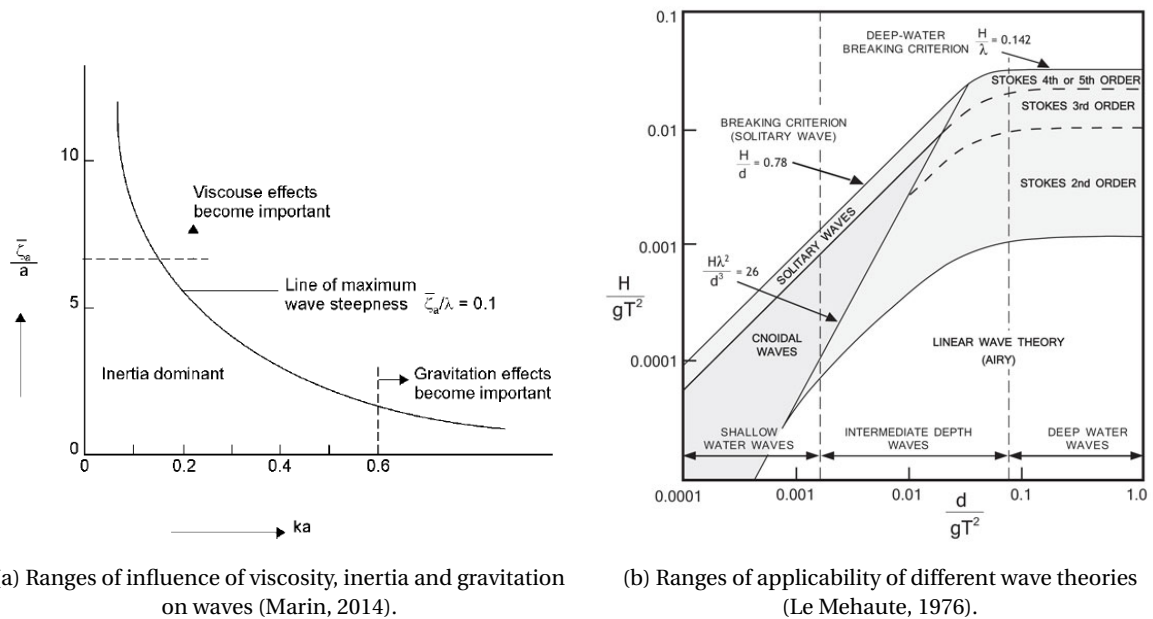


Figure D.2: Applicability ranges for linear wave theory

Additionally, Journée and Massie (2002) states that if flow is assumed to be inviscid, or irrotational, the following holds:

$$\nabla \times \mathbf{V} = 0 \quad (\text{D.4})$$

where ∇ is the curl or the gradient and \mathbf{V} is the velocity vector. If the curl of a vector is zero, the vector has to be the gradient of a scalar function. This means that:

$$\mathbf{V} = \nabla \times \Phi \quad (\text{D.5})$$

D.3. Radiation potential

All forces mentioned in section 5, except for the hydrostatic reaction force, are related to fluid dynamics around the structure. Under the assumptions of irrotational and non-viscous flow it is allowed to use the potential flow theory. This means that the fluid can only exert a force perpendicular to the structure. The potential that is involved in the radiation force (F_r), is called the radiation potential (Φ_r). Like the force, this potential is depending on the motion of the structure (equation D.6). It is convenient to express these terms in a complex form.

$$\begin{aligned}\Phi_r &= \hat{\Phi}_r \cdot \cos(\omega t + \epsilon_{\Phi_r, w} + \epsilon_{\eta, w}) = Re \left[\hat{\Phi}_r \cdot e^{-i\epsilon_{\Phi_r, w}} \cdot e^{-i\epsilon_{\eta, w}} \cdot e^{-i\omega t} \right] \\ &= Re \left[\hat{\Phi}_r \cdot e^{-i\epsilon_{\eta, w}} \cdot e^{-i\omega t} \right]\end{aligned}\quad (D.6)$$

The total radiation potential can be described in the same way as the superposition of the motions of the structure. Therefore the radiation potential is defined as the sum of the radiation potentials in all 6 DOFs.

$$\Phi_r = \sum_{j=1}^6 \Phi_{r,j} \quad (D.7)$$

Transfer functions are often used to perform calculations with a system of equations in dynamics. The term $\frac{\hat{\Phi}_{r,j,a}}{\zeta_{j,a}}$ in Equation D.8 can be described as a transfer function that relates the radiation potential to the motion. However, it is more convenient to use a transfer function that relates the radiation potential to the velocity: ϕ_r .

$$\Phi_r(x, y, z, t) = \sum_{j=1}^6 Re \left[\frac{\hat{\Phi}_{r,j}}{\hat{w}_j} \cdot \hat{w}_j \cdot e^{-i\omega t} \right] = \Phi_r(x, y, z, t) = \sum_{j=1}^6 \phi_{r,j}(x, y, z) \cdot v_j(t) \quad (D.8)$$

In this equation v_j is the oscillatory velocity. Now the time and space dependent parts are completely separated.

$$v_j = Re \left[-i\omega \hat{w}_j \cdot e^{-i\omega t} \right] \quad (D.9)$$

$$\phi_{r,j} = Re \left[\frac{\hat{\Phi}_{r,j}}{-i\omega \hat{w}_j} \right] \quad (D.10)$$

Now it is possible to write the normal velocity on the surface of the structure as:

$$\frac{\partial \Phi_r}{\partial z_k} = \sum_{j=1}^6 \frac{\partial \phi_j}{\partial z_k} \cdot v_j \quad (D.11)$$

The relation between the radiation force and the radiation potential is given in Equations D.12 and D.13. The radiation force is found by integrating over the submerged area where the pressure acts perpendicular to the structure. A second subscript k is introduced to indicate the direction of the hydrodynamic force due to the radiation potential in the direction j .

$$F_{r,k,j} = \int \int_s \left(-p_{r,j} \cdot z_k \right) dS \quad (D.12)$$

$$p = -\rho \cdot \frac{\partial \Phi_{r,j}}{\partial t} \quad (D.13)$$

Combining these equations yields:

$$F_{r,k,j} = \int \int_s \left(\rho \cdot \frac{\partial \Phi_{r,j}}{\partial t} \cdot z_k \right) dS \quad (D.14)$$

$$F_{r,k,j} = \int \int_s \left(\rho \cdot \frac{\partial v_j}{\partial t} \cdot \phi_{r,j} \cdot z_k \right) dS \quad (D.15)$$

As shown in Equation D.23 the radiation force can be expressed in the added mass and damping coefficient. Equations D.16 and D.17 express Equations 5.8 and D.23 in a complex notation for all DOFs.

$$F_{r,k,j} = \text{Re} \left[\hat{F}_{r,k,j} \cdot e^{-i\epsilon_{w_j,\eta}} \cdot e^{-i\omega t} \right] \quad (\text{D.16})$$

$$\text{Re} \left[\frac{\hat{F}_{r,k,j}}{\hat{w}_j} \cdot \hat{w}_j \cdot e^{-i\omega t} \right] = -a_{kj} \cdot \text{Re} \left[(-i\omega)^2 \cdot \hat{w}_j \cdot e^{-i\omega t} \right] - b_{kj} \cdot \text{Re} \left[(-i\omega) \cdot \hat{w}_j \cdot e^{-i\omega t} \right] \quad (\text{D.17})$$

Combining Equations D.15, D.16 and D.15 results in:

$$\rho \int \int_s \left(-v_j \cdot i\omega \cdot \phi_{r,j} \cdot z_k \right) dS = -a_{kj} \cdot \text{Re} \left[(-i\omega)^2 \cdot \hat{w}_j \cdot e^{-i\omega t} \right] - b_{kj} \cdot \text{Re} \left[(-i\omega) \cdot \hat{w}_j \cdot e^{-i\omega t} \right] \quad (\text{D.18})$$

Finally after eliminating $\hat{w}_j \cdot e^{-i\omega t}$ this yields:

$$\int \int_s \left(-\rho \cdot \phi_{r,j} \cdot \omega^2 \cdot z_k \right) = a_{kj} \cdot \omega^2 + b_{kj} \cdot i\omega \quad (\text{D.19})$$

An expressions for the added mass and damping coefficients (Equation D.20) is now found, which is independent of time:

$$\begin{aligned} a_{kj} &= \text{Re} \left[\int \int_s \left(-\rho \cdot \phi_{r,j} \cdot n_k \right) dS \right] \\ b_{kj} &= \text{Im} \left[\int \int_s \left(-\rho \cdot \phi_{r,j} \cdot \omega \cdot n_k \right) dS \right] \end{aligned} \quad (\text{D.20})$$

In a similar way an expression for the moment that a structure experiences due to reaction force can be derived.

$$M_{r,k,j} = \int \int_s \left(-p_{r,k,j} \cdot (r \times z)_k \right) dS = -a_{k+3j} \text{Re} \left[-\omega^2 \hat{w}_j \cdot e^{-i\omega t} \right] - b_{k+3j} \text{Re} \left[(-i\omega) \hat{w}_j \cdot e^{-i\omega t} \right] \quad (\text{D.21})$$

D.3.1. Radiation force

Using the radiation potential, the radiation force can be found.

$$\begin{aligned} F_r &= \hat{F}_r \cdot \cos \left(\omega t + \epsilon_{F_r,w} + \epsilon_{\eta,w} \right) \\ \epsilon_{\eta,F_r} &= \epsilon_{F_r,w} + \epsilon_{\eta,w} \end{aligned} \quad (\text{D.22})$$

where:

F_r	=	Hydrodynamic radiation force	[N]
$\epsilon_{\eta,F}$	=	Phase shift between the wave elevation and the wave force	[rad]
$\epsilon_{\eta,w}$	=	Phase shift between the wave elevation and the response of the structure	[rad]
$\epsilon_{w,F}$	=	Phase shift between the response of the structure and the radiation force	[rad]

Using goniometrics (Equations D.23 and D.24) this can be rewritten to find the added mass coefficient and the hydrodynamic damping coefficient. The added mass can be considered as a water mass moving along with vibrating structure and therefore contributing to the total mass of the structure. The added mass moves in phase with the acceleration of the structure. Hydrodynamic damping is associated with the process where new waves are created by the motion of the structure, which dissipate energy from the system. The hydrodynamic damping moves in phase with the velocity of the structure.

$$\begin{aligned} F_r &= -\frac{\hat{F}_r}{\hat{w} \cdot \omega^2} \cdot \cos \left(\epsilon_{F_r,w} \right) \cdot \hat{w} \cdot \omega^2 \cos \left(\omega t + \epsilon_{\eta,w} + \pi \right) - \\ &\frac{\hat{F}_r}{\hat{w} \cdot \omega} \cdot \sin \left(\epsilon_{F_r,w} \right) \cdot \hat{w} \cdot \omega \cdot \cos \left(\omega t + \epsilon_{\eta,w} + \frac{\pi}{2} \right) \end{aligned} \quad (\text{D.23})$$

$$\begin{aligned}
F_r &= -a_{33} \cdot \ddot{w} - b_{33} \cdot \dot{w} \\
a_{33} &= \frac{\hat{F}_r}{\omega^2 \cdot \dot{w}} \cdot \cos(\epsilon_{F_r, w}) \\
b_{33} &= \frac{\hat{F}_r}{\omega \cdot \dot{w}} \cdot \sin(\epsilon_{F_r, w})
\end{aligned} \tag{D.24}$$

where:

$$\begin{aligned}
a_{kj} &= \text{Added mass in direction } k \text{ due to displacement in direction } j & [\text{kg}] \\
b_{kj} &= \text{Added damping in direction } k \text{ due to displacement in direction } j & [\text{Ns/m}]
\end{aligned}$$

D.3.2. Motion coupling

The heave motion is used in section D.3 to demonstrate the hydrodynamics of a rigid body. However, motions in all DOFs will influence different hydrodynamic reaction force components. Under the assumption of linearization it is allowed to consider the motion in any point P on the structure to be a superposition of the motions in all DOFs. Therefore the motions of an arbitrary point P can be described with:

$$\begin{bmatrix} u_P(t) \\ v_P(t) \\ w_P(t) \end{bmatrix} = \begin{bmatrix} u(t) \\ v(t) \\ w(t) \end{bmatrix} + \begin{bmatrix} 0 & r(t) & q(t) \\ r(t) & 0 & p(t) \\ q(t) & p(t) & 0 \end{bmatrix} \cdot \begin{bmatrix} x_{bP} \\ y_{bP} \\ z_{bP} \end{bmatrix}$$

Using the cross product instead of the dot product, this can be simplified to:

$$\begin{bmatrix} u_P(t) \\ v_P(t) \\ w_P(t) \end{bmatrix} = \begin{bmatrix} u(t) \\ v(t) \\ w(t) \end{bmatrix} + \begin{bmatrix} p(t) \\ q(t) \\ r(t) \end{bmatrix} \times \begin{bmatrix} x_{bP} \\ y_{bP} \\ z_{bP} \end{bmatrix}$$

D.4. Wave excitation force potential

Again the potential theory is used to find an expression for the wave excitation force. As mentioned before, this force consists of two components: the undisturbed wave force and the diffraction force. First the undisturbed wave force is discussed. Equation D.25 gives an expression for the potential in complex notation.

$$\Phi_w(x, y, z, t) = \frac{\hat{\eta}g}{\omega} e^{kz} \cdot \sin(kx \cos(\mu) + ky \sin(\mu) - \omega t) = -Re \left[\frac{\hat{\eta}g}{\omega} e^{kz} \cdot e^{i(kx \cos(\mu) + ky \sin(\mu) - \omega t)} \right] \tag{D.25}$$

The wave number k relates to the radial frequency through the dispersion equation (Equation D.26). Here $kx \cos(\mu) + ky \sin(\mu)$ presents the phase shift between the local wave elevation and the wave elevation in the center of gravity. μ is the angle between the incident waves and the x-axis.

$$\omega^2 = k \cdot g \cdot \tanh(k \cdot d) \tag{D.26}$$

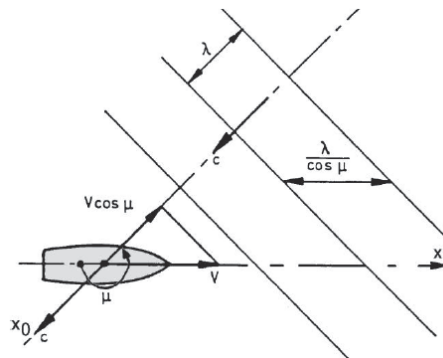


Figure D.3: Illustration of angle μ (Journée and Massie, 2002).

Separation of variables is performed to isolate the space dependent part and the time dependent part (Equation D.27). The space dependent part can be interpreted as a transfer function, while the time dependent part is the velocity of the surface elevation at the origin of the axes system ($\dot{\eta}_0$).

$$\begin{aligned}\Phi_w(x, y, z, t) &= -Re \left[i \frac{g}{-\omega^2} e^{kz} \cdot e^{i(kx \cos(\mu) + ky \sin(\mu))} \cdot -i\omega \hat{\eta} e^{-i\omega t} \right] = Re \left[\frac{g}{\omega^2} e^{kz} \cdot e^{i(kx \cos(\mu) + ky \sin(\mu))} \cdot \dot{\eta}_0 \right] \\ &= Re \left[\phi_0(x, y, z) \cdot \dot{\eta}_0(t) \right]\end{aligned}\quad (D.27)$$

An expression for the diffracted wave potential can be derived in a similar way when it is assumed that it is linearly related to the incoming wave.

$$\Phi_d(x, y, z, t) = Re \left[\phi_7(x, y, z) \cdot \dot{\eta}_0(t) \right] \quad (D.28)$$

Finally, the forces are found in a similar way as with the radiation force:

$$F_{wkj} + F_{dkj} = \int \int_s \left(\rho \cdot \left(\frac{\partial \Phi_{wj}}{\partial t} + \frac{\partial \Phi_{dj}}{\partial t} \right) \cdot n_k \right) dS \quad (D.29)$$

D.5. Requirements and boundary conditions

To solve the potential functions, the Laplace equation has to be fulfilled:

$$\frac{\partial^2 \Phi}{\partial x^2} + \frac{\partial^2 \Phi}{\partial y^2} + \frac{\partial^2 \Phi}{\partial z^2} = 0 \quad (D.30)$$

The following boundary conditions are required to do this:

Seabed boundary condition:

$$\frac{\partial \Phi}{\partial z} = 0 \quad z = -h \quad (D.31)$$

Free surface boundary condition:

$$g \frac{\partial \Phi}{\partial z} + \frac{\partial^2 \Phi}{\partial t^2} = 0 \quad z = \eta \quad (D.32)$$

Kinematic boundary condition on the oscillating body surface:

$$g \frac{\partial \Phi}{\partial z} = \mathbf{v} \cdot \mathbf{z} \quad (D.33)$$

Radiation Condition:

$$\lim_{R \rightarrow \infty} \Phi = 0 \quad (D.34)$$

Symmetric condition:

$$\begin{aligned}\Phi_2(-x, y) &= -\Phi_2(+x, y) \\ \Phi_3(-x, y) &= +\Phi_3(+x, y) \\ \Phi_4(-x, y) &= -\Phi_4(+x, y)\end{aligned}\quad (D.35)$$

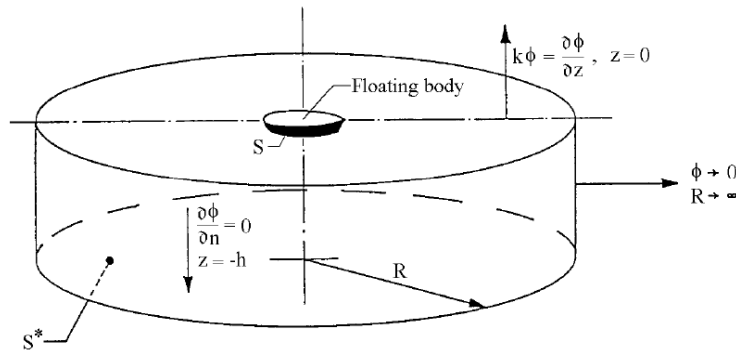


Figure D.4: Boundary conditions (Journée and Massie, 2002).

D.6. Solving a potential function

First a potential function will be evaluated in a 2D situation without a structure. A wave in a 2D plane can be described with a function of both time and space (Equation 3.3). Thus it can be assumed that the potential function can be described as a product of three functions:

$$\Phi = X(x)Z(z)T(t) \tag{D.36}$$

Here $X(x)$ is the space dependent part as a function of x , $Z(z)$ is the space dependent part as a function of z and $T(t)$ is the time dependent part as a function of t . The simplified Laplace equation now becomes:

$$\frac{\partial^2 \Phi}{\partial x^2} + \frac{\partial^2 \Phi}{\partial z^2} = [X''(x)Z(z) + X(x)Z''(z)]T(t) = 0 \tag{D.37}$$

Applying separation of variables, this equation can be reduced to two simple second order ordinary differential equations:

$$\begin{aligned} X'' + k_w^2 X &= 0 \\ Z'' - k_w^2 Z &= 0 \end{aligned} \tag{D.38}$$

The following solutions can be assumed for these differential equations:

$$\begin{aligned} X(x) &= A \cdot e^{ik_w x} + B \cdot e^{-ik_w x} \\ Z(z) &= C \cdot e^{ik_w z} + D \cdot e^{-ik_w z} \end{aligned} \tag{D.39}$$

The function T is similar to the complex waveform (Equation 3.3 and therefore defined as $e^{-i\omega t}$. The constants A, B, C and D can be solved with the mentioned boundary conditions. Equation 3.3 shows a wave progressing to the right, which means that B must be zero. If A is set to 1, combining it with C and D yields:

$$\Phi = (C \cdot e^{k_w z} + D \cdot e^{-k_w z}) e^{i(k_w x - \omega t)} \tag{D.40}$$

Constants C and D can be found using the free surface and the bottom boundary condition:

$$\frac{\partial \Phi}{\partial z} = k(C \cdot e^{-k_w h} - D \cdot e^{k_w h}) e^{i(k_w x - \omega t)} = 0 \tag{D.41}$$

To find a unique solutions of this equation, the following must be true:

$$\begin{aligned} C \cdot e^{-k_w h} - D \cdot e^{k_w h} &= 0 \\ C &= D \cdot e^{2k_w h} \end{aligned} \tag{D.42}$$

Now using free surface boundary condition an expression for the potential function can be found:

$$X(x)Z(z)\ddot{T}(t) + gX(x)Z'(z)T(t) = 0 \tag{D.43}$$

After eliminating $X(x)$, this can be reduced to:

$$2D \cdot e^{k_w h} \cosh(z+h) \cdot (-\omega^2 e^{-i\omega t}) + 2gk_w D \cdot e^{k_w h} \sinh(z+h) \cdot e^{-i\omega t} = 0 \quad (\text{D.44})$$

Now the expression of the potential function becomes:

$$\Phi = -i \frac{\hat{\eta} g}{\omega} \frac{\cosh(k_w(z+h))}{\cosh(k_w h)} e^{i(k_w x - \omega t)} \quad (\text{D.45})$$

In deep water, where $\tanh(k_w d) \rightarrow 1$, this reduces to:

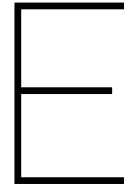
$$\Phi = -i \frac{\hat{\eta} \omega}{k_w} e^{k_w z} \cdot e^{i(k_w x - \omega t)} \quad (\text{D.46})$$

In 3D, including the x,y and z axis, this expands to the incoming wave potential:

$$\Phi_w = i \frac{\hat{\eta} \omega}{k_w} e^{k_w z} \cdot e^{i(k(\cos(\mu)) + (\sin(\mu))y)} \cdot e^{-i\omega t} \quad (\text{D.47})$$

To solve all required potential functions regarding a 3D structure requires complex volume integrals. To avoid these complex integrals, Green's second integral can be used to transform the volume integral into a more convenient surface integral.

$$\int_V \int \int (\phi_j \cdot \nabla^2 \phi_k - \phi_k \cdot \nabla^2 \phi_j) dV = \int_S \int (\phi_j \frac{\partial \phi_k}{\partial n} - \phi_k \frac{\partial \phi_j}{\partial n}) dS \quad (\text{D.48})$$



Fiber reinforced polymers

This appendix elaborates upon the material FRP. General properties which are used in the main report are presented and a derivation of the classical laminate theory is presented. This latter part is mainly included to provide a method to work out the internal stresses in the FRP superstructure.

E.1. Properties of fiber reinforced polymers

High strength-to-weight ratio

FRPs feature a high tensile strength compared to other traditional construction materials. The strength properties of two different laminates consisting of UD-ply are given in Table E.1. The plies of the quasi-isotropic laminate are equally distributed in all directions. 55 % of the plies of the anisotropic laminate are oriented in the 0° . The rest is equally distributed over the other three directions.

Strength properties	Quasi-isotropic laminate 50 %	anisotropic laminate 50 %
σ_{1tR} (MPa)	223	310
σ_{1cR} (MPa)	223	310
σ_{2tR} (MPa)	223	191
σ_{2cR} (MPa)	223	191
τ_{12R} (MPa)	168	134

Table E.1: Characteristic strength properties of two laminates with UD-ply with a fiber volume of 50 % (CUR-aanbeveling 96, 2003).

High durability

FRPs possess a considerably higher resistance to corrosion, chemical reagents and aggressive media compared to traditional construction materials. It is often assumed that these processes do not lead to required maintenance for an FRP structure.

High fatigue resistance

Fatigue resistance of FRP is considered high compared to traditional construction materials. However, it has to be taken into account that the stiffness of FRP gradually decreases due to fatigue. One way to model fatigue is based on S-N curves (Figure E.1). These curves present the correlation between the number of cycles to failure and applied stresses. The S-N curve of FRP usually does not show a fatigue limit. The correlation can be expressed with the following formula:

$$N_f = N_D \cdot \left(\frac{\sigma_a}{\sigma_D} \right)^{-k} \quad (\text{E.1})$$

where N_f is the number of cycles to failure, N_D is the number of cycles indicated in Figure E.1, k is the steepness of the curve, σ_a is the applied stress amplitude and σ_D is the endurance limit. The slope factor k is usually higher in the case of FRP, 9 to 10, compared to steel, 5 (CUR-aanbeveling 96, 2003). This means that when applied stress decreases, the number of cycles to failure increases more than in the case of steel.

Of course, this also works the other way around, but it is often accepted as a positive characteristic (Nijssen, 2013).

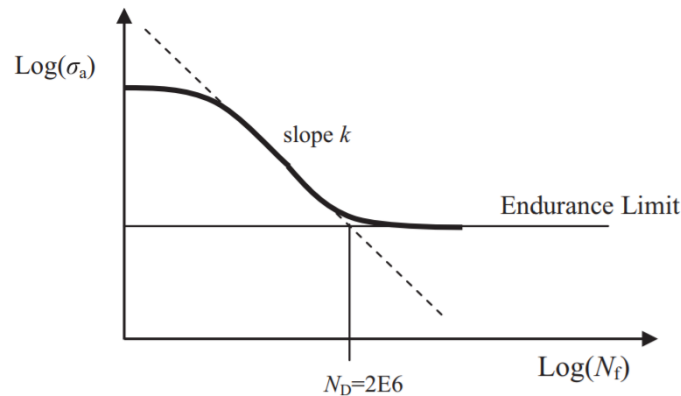


Figure E.1: General S-N curve of FRP (Flore and Wegener, 2015).

Low stiffness-to-weight ratio

GFRP feature a low stiffness compared to other traditional construction materials. It is important to keep this in mind in the design process, because displacement requirements are often governing in the design of an FRP structure. Table E.2 presents the stiffness properties of an UD-ply for the possible fiber volume percentages. Interpolation can be used in case of a percentage between these values.

Fiber volume	E_1 (GPa)	E_2 (GPa)	G_{12} (GPa)	ν_{12}
40 (%)	30,8	8,9	2,8	0,3
45 (%)	34,3	10,0	3,1	0,29
50 (%)	37,7	11,3	3,5	0,29
55 (%)	41,1	12,8	3,9	0,28
60 (%)	44,6	14,6	4,5	0,27
65 (%)	48,0	16,7	5,1	0,27
70 (%)	51,4	19,3	6,0	0,26

Table E.2: Nominal values of stiffness properties of an UD-ply. These values, except for ν_{12} , have to be multiplied with a reduction factor 0,97 (CUR-aanbeveling 96, 2003).

E.1.1. Failure mechanisms

The following types of internal forces have to be checked in the assessment of an FRP structure:

- Tensile stress in the direction of the fibers
- Compression in the direction of the fibers
- Tensile stress perpendicular to the fibers
- Compression perpendicular to the fibers
- Shear stress between the two directions
- Inter laminar shear stresses

The maximum strain until failure is assumed to be 1,2 %.

E.2. Classical laminate theory

One method to determine the global properties of FRP is classical laminate theory. The global properties of a laminate are deduced from the properties of multiple plies. In this theory the properties of plies and thus the laminate are expressed in a matrix form, to be able to use it in calculations. This theory is often included in FE software to be able to model FRP behaviour. The following characteristics are required to use classical laminate theory:

E_{11}	Young's modulus in fiber direction.
E_{22}	Young's modulus perpendicular to fiber direction
G_{12}	Shear modulus
ν_{12}, ν_{21}	Poisson's ratio
t	Ply thickness
θ	Fiber angle to global axis

Table E.3: Required characteristics to use classical laminate theory

To be able to use the classical laminate theory, the following assumptions have to be made:

- Euler Bernoulli beam theory is valid, assuming cross-sections to be perpendicular to the center line and thus neglecting shear deformations.
- Single plies have fibers in only one direction.
- Slip between plies is neglected.
- Plies are thin enough to neglect forces perpendicular to their plane

The classical laminate theory is based on Hooke's law, $\sigma = E \cdot \epsilon$. However, a ply is anisotropic, so in 3D Hooke's law is given as:

$$\sigma_{ij} = E_{ijkl} \cdot \epsilon_{kl} \quad (i, j, k, l = 1, 2, 3) \quad (\text{E.2})$$

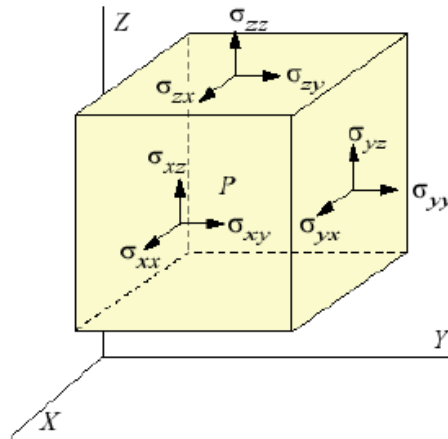


Figure E.2: Stress orientation of a 3D element (Edmondson, 2017).

Figure E.2 illustrates the orientation of the stresses in 3D. These nine stresses correspond to nine strains and therefore the stiffness matrix \mathbf{Q} becomes a 9x9 matrix. However, the conservation of angular momentum shows that $\sigma_{ij} = \sigma_{ji}$ and therefore \mathbf{Q} can be reduced to a 6x6 matrix:

$$\begin{bmatrix} \sigma_{11} \\ \sigma_{22} \\ \sigma_{33} \\ \sigma_{23} \\ \sigma_{31} \\ \sigma_{12} \end{bmatrix} = \begin{bmatrix} Q_{11} & Q_{12} & Q_{13} & 0 & 0 & 0 \\ Q_{21} & Q_{22} & Q_{23} & 0 & 0 & 0 \\ Q_{31} & Q_{32} & Q_{33} & 0 & 0 & 0 \\ 0 & 0 & 0 & Q_{44} & 0 & 0 \\ 0 & 0 & 0 & 0 & Q_{55} & 0 \\ 0 & 0 & 0 & 0 & 0 & Q_{66} \end{bmatrix} \cdot \begin{bmatrix} \epsilon_{11} \\ \epsilon_{22} \\ \epsilon_{33} \\ \epsilon_{23} \\ \epsilon_{31} \\ \epsilon_{12} \end{bmatrix}$$

All the zeros in this matrix can be explained by the absence of coupling between normal stresses and shearing angles. Furthermore, the assumptions of thin planes and no slip between plies reduce the matrix to:

$$\begin{bmatrix} \sigma_{11} \\ \sigma_{22} \\ \sigma_{12} \end{bmatrix} = \begin{bmatrix} Q_{11} & Q_{12} & 0 \\ Q_{21} & Q_{22} & 0 \\ 0 & 0 & Q_{66} \end{bmatrix} \cdot \begin{bmatrix} \epsilon_{11} \\ \epsilon_{22} \\ \epsilon_{12} \end{bmatrix}$$

where the individual values of this matrix are defined as:

$$\begin{aligned} Q_{11} &= \frac{E_{11}}{1 - \nu_{12}\nu_{21}} \\ Q_{22} &= \frac{E_{22}}{1 - \nu_{12}\nu_{21}} \\ Q_{12} &= \frac{\nu_{12}E_{22}}{1 - \nu_{12}\nu_{21}} \\ Q_{66} &= G_{12} \end{aligned} \quad (E.3)$$

With the above relations it is possible to determine the stress and strain of a ply in fiber direction. However, one of the characteristics of laminate is that plies have a different fiber orientation. A transformation matrix \mathbf{T} expressed in angle θ to include the fiber orientation of a ply. The matrix \mathbf{T} is defined as:

$$[T] = \begin{bmatrix} \cos^2(\theta) & \sin^2(\theta) & 2\sin(\theta)\cos(\theta) \\ \sin^2(\theta) & \cos^2(\theta) & -2\sin(\theta)\cos(\theta) \\ -\sin(\theta)\cos(\theta) & \sin(\theta)\cos(\theta) & \cos^2(\theta) - \sin^2(\theta) \end{bmatrix}$$

Now the relation between the stresses and strains is defined as followed:

$$\begin{bmatrix} \sigma_{xx} \\ \sigma_{yy} \\ \sigma_{xy} \end{bmatrix} = [T]^{-1} \cdot [Q] \cdot [T] \cdot \begin{bmatrix} \epsilon_{xx} \\ \epsilon_{yy} \\ \epsilon_{xy} \end{bmatrix}$$

Subsequently, with a relation for the stress and strain in a ply, the properties of a laminate can be determined. A definition for displacements of a laminate subjected to bending is required. It must be noted that the displacement is not equal on a plane perpendicular to the central axis. This displacement yields:

$$u = u_0 - z \frac{\partial w_0}{\partial x} \quad (E.4)$$

where u and u_0 are the displacement and initial displacement respectively in x direction and $\frac{\partial w_0}{\partial x}$ is the rotation angle in the z direction. This results in the following relation of the strains:

$$\begin{aligned} \epsilon_{xx} &= \frac{\partial u}{\partial x} = \frac{\partial u_0}{\partial x} - z \frac{\partial^2 w_0}{\partial x^2} \\ \epsilon_{yy} &= \frac{\partial v}{\partial y} = \frac{\partial v_0}{\partial y} - z \frac{\partial^2 w_0}{\partial y^2} \\ \epsilon_{xy} &= \frac{\partial u}{\partial y} + \frac{\partial v}{\partial x} = \frac{\partial u_0}{\partial y} - \frac{\partial v_0}{\partial x} - 2z \frac{\partial^2 w_0}{\partial x \partial y} \end{aligned} \quad (E.5)$$

To be able to use a matrix notation, the following relations are defined:

$$\begin{bmatrix} \epsilon_{xx}^0 \\ \epsilon_{yy}^0 \\ \epsilon_{xy}^0 \end{bmatrix} = \begin{bmatrix} \frac{\partial u_0}{\partial x} \\ \frac{\partial v_0}{\partial y} \\ \frac{\partial u_0}{\partial y} + \frac{\partial v_0}{\partial x} \end{bmatrix} \quad \text{and} \quad \begin{bmatrix} \kappa_{xx} \\ \kappa_{yy} \\ \kappa_{xy} \end{bmatrix} = - \begin{bmatrix} \frac{\partial^2 w_0}{\partial x^2} \\ \frac{\partial^2 w_0}{\partial y^2} \\ 2 \frac{\partial^2 w_0}{\partial x \partial y} \end{bmatrix}$$

where ϵ^0 is the vector that represents the displacement in the central axis. Furthermore, κ is the curvature vector. With these vectors a strain vector can be computed. This relation shows that the strain is linearly distributed over the height of a laminate:

$$\begin{bmatrix} \epsilon_{xx} \\ \epsilon_{yy} \\ \epsilon_{xy} \end{bmatrix} = \begin{bmatrix} \epsilon_{xx}^0 \\ \epsilon_{yy}^0 \\ \epsilon_{xy}^0 \end{bmatrix} + z \begin{bmatrix} \kappa_{xx} \\ \kappa_{yy} \\ \kappa_{xy} \end{bmatrix}$$

This means that the stress can be found with:

$$\begin{bmatrix} \sigma_{xx} \\ \sigma_{yy} \\ \sigma_{xy} \end{bmatrix} = [T]^{-1} \cdot [Q] \cdot [T] \cdot \begin{bmatrix} \epsilon_{xx}^0 \\ \epsilon_{yy}^0 \\ \epsilon_{xy}^0 \end{bmatrix} + z [T]^{-1} \cdot [Q] \cdot [T] \cdot \begin{bmatrix} \kappa_{xx} \\ \kappa_{yy} \\ \kappa_{xy} \end{bmatrix}$$

This relation reveals that the stress does not vary linearly over the height of a laminate. The change of θ between the plies leads to a jump in the stress distribution. These discontinuities will cause interface shear between the plies. To avoid these discontinuities in the modeling of a laminate, a simpler method can be used. The stresses are converted to normal forces and moments through a summation of the stresses over the height of a ply. For a single ply this becomes:

$$\begin{aligned} N_{xx} &= \int_{-h/2}^{h/2} \sigma_{xx} dz & M_{xx} &= \int_{-h/2}^{h/2} \sigma_{xx} z dz \\ N_{yy} &= \int_{-h/2}^{h/2} \sigma_{yy} dz & M_{yy} &= \int_{-h/2}^{h/2} \sigma_{yy} z dz \\ N_{xy} &= \int_{-h/2}^{h/2} \sigma_{xy} dz & M_{xy} &= \int_{-h/2}^{h/2} \sigma_{xy} z dz \end{aligned} \quad (E.6)$$

Including multiple plies and introducing a matrix notation gives the following relation regarding normal forces:

$$\begin{bmatrix} N_{xx} \\ N_{yy} \\ N_{xy} \end{bmatrix} = \sum_{k=1}^n \left[\int_{h_{k-1}}^{h_k} [T_{ij}]^{-1} \cdot [Q_{ij}] \cdot [T_{ij}] \begin{bmatrix} \epsilon_{xx}^0 \\ \epsilon_{yy}^0 \\ \epsilon_{xy}^0 \end{bmatrix} dz + \int_{h_{k-1}}^{h_k} [T_{ij}]^{-1} \cdot [Q_{ij}] \cdot [T_{ij}] \begin{bmatrix} \kappa_{xx} \\ \kappa_{yy} \\ \kappa_{xy} \end{bmatrix} z dz \right]$$

where h_k is the height of specific ply and n is the number of plies. A comparable relation is found to express the moments:

$$\begin{bmatrix} M_{xx} \\ M_{yy} \\ M_{xy} \end{bmatrix} = \sum_{k=1}^n \left[\int_{h_{k-1}}^{h_k} [T_{ij}]^{-1} \cdot [Q_{ij}] \cdot [T_{ij}] \begin{bmatrix} \epsilon_{xx}^0 \\ \epsilon_{yy}^0 \\ \epsilon_{xy}^0 \end{bmatrix} z dz + \int_{h_{k-1}}^{h_k} [T_{ij}]^{-1} \cdot [Q_{ij}] \cdot [T_{ij}] \begin{bmatrix} \kappa_{xx} \\ \kappa_{yy} \\ \kappa_{xy} \end{bmatrix} z^2 dz \right]$$

To make these expressions more workable, coefficients A_{ij} , B_{ij} and D_{ij} are introduced, which are related to the axial stiffness matrix, the coupling matrix and the binding stiffness matrix respectively. These coefficients are defined as:

$$\begin{aligned} A_{ij} &= \sum_{k=1}^n (T_{ij}^{-1} Q_{ij} T_{ij})_k \cdot (h_k - h_{k-1}) \\ B_{ij} &= \frac{1}{2} \sum_{k=1}^n (T_{ij}^{-1} Q_{ij} T_{ij})_k \cdot (h_k^2 - h_{k-1}^2) \\ D_{ij} &= \frac{1}{3} \sum_{k=1}^n (T_{ij}^{-1} Q_{ij} T_{ij})_k \cdot (h_k^3 - h_{k-1}^3) \end{aligned} \quad (E.7)$$

With these equations a complete relationship for the internal forces of the laminate is found:

$$\begin{bmatrix} N_{xx} \\ N_{yy} \\ N_{xy} \\ M_{xx} \\ M_{yy} \\ M_{xy} \end{bmatrix} = \begin{bmatrix} A_{11} & A_{12} & A_{16} & B_{11} & B_{12} & B_{16} \\ A_{12} & A_{22} & A_{26} & B_{12} & B_{22} & B_{26} \\ A_{16} & A_{26} & A_{66} & B_{16} & B_{26} & B_{66} \\ B_{11} & B_{12} & B_{16} & D_{11} & D_{12} & D_{16} \\ B_{12} & B_{22} & B_{26} & D_{12} & D_{22} & D_{26} \\ B_{16} & B_{26} & B_{66} & D_{16} & D_{26} & D_{66} \end{bmatrix} \begin{bmatrix} \epsilon_{xx}^0 \\ \epsilon_{yy}^0 \\ \epsilon_{xy}^0 \\ \kappa_{xx} \\ \kappa_{yy} \\ \kappa_{xy} \end{bmatrix}$$

Or simplified:

$$\begin{bmatrix} N \\ M \end{bmatrix} = \begin{bmatrix} A & B \\ B & D \end{bmatrix} \begin{bmatrix} \epsilon^0 \\ \kappa \end{bmatrix}$$

The ABD matrix contains many components, but simplifications can be made in specific situations. In case of a symmetrical laminate, which is often the case, the **B** matrix becomes zero, because there is no coupling. If the laminate is orthotropic, so normal forces do not effect shear angles, A_{16} and A_{26} become 0. An overview of multiple situations where simplifications are possible is presented in Figure E.3.

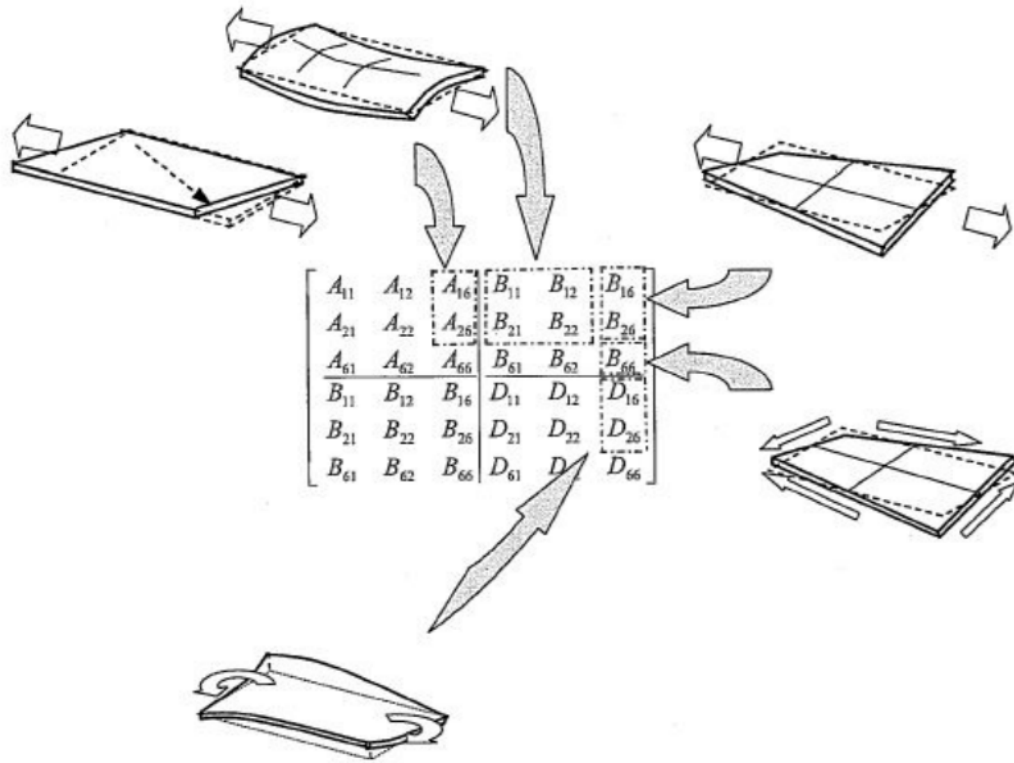
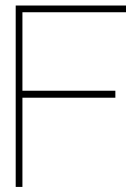


Figure E.3: Scenarios where components of the ABD matrix become 0 (CUR-aanbeveling 96, 2003).



Model development

This appendix presents the *Rigid body model*, *Two pontoon in plane model* and the *Seven pontoon in plane model*. Furthermore, additional results of the *Three dimensional model* are included. Finally, the results of a mesh sensitivity analysis are presented.

F.1. Rigid body model

The most simple floating bridge model consists of three rigid bodies representing two pontoons with a superstructure in between. This means that the superstructure is assumed to be infinitely stiff. A visualization of this model is shown in figure F.1. Only the heave and pitch motions of all rigid bodies are included in this model. Furthermore, damping is neglected here.

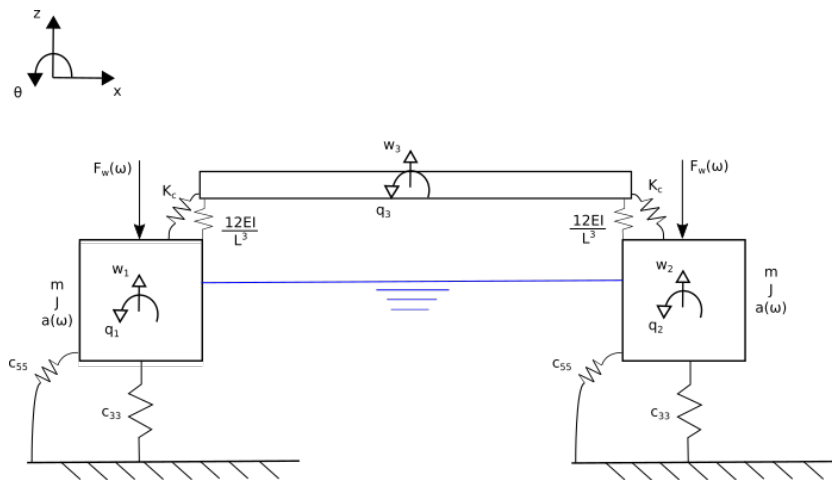


Figure F.1: Simplified 6 DOF floating bridge without damping.

The mass and the added mass of the pontoon are obtained from the pontoon model. The EOMs of this system are given by:

$$\begin{bmatrix}
 m_p + A_{33} & 0 & 0 & 0 & 0 & 0 \\
 0 & J_p + A_{55} & 0 & 0 & 0 & 0 \\
 0 & 0 & m_p + A_{33} & 0 & 0 & 0 \\
 0 & 0 & 0 & J_p + A_{55} & 0 & 0 \\
 0 & 0 & 0 & 0 & m_{bridge} & 0 \\
 0 & 0 & 0 & 0 & 0 & J_{bridge}
 \end{bmatrix}
 \begin{bmatrix}
 \ddot{w}_1 \\
 \ddot{q}_1 \\
 \ddot{w}_2 \\
 \ddot{q}_2 \\
 \ddot{w}_3 \\
 \ddot{q}_3
 \end{bmatrix}
 +$$

$$\begin{bmatrix}
 c_{33} + \frac{12EI}{L_b^3} & \frac{1}{2}L_p \frac{12EI}{L_b^3} & 0 & 0 & -\frac{12EI}{L_b^3} & \frac{1}{2}L_b \frac{12EI}{L_b^3} \\
 \frac{1}{2}L_p \frac{12EI}{L_b^3} & \frac{1}{4}L_p^2 \frac{12EI}{L_b^3} + k_c + c_{55} & 0 & 0 & -\frac{1}{2} \frac{12EI}{L_b^3} & \frac{1}{4}L_p L_b \frac{12EI}{L_b^3} - k_c \\
 0 & 0 & c_{33} + \frac{12EI}{L_b^3} & -\frac{1}{2}L_p \frac{12EI}{L_b^3} & -\frac{12EI}{L_b^3} & -\frac{1}{2}L_b \frac{12EI}{L_b^3} \\
 0 & 0 & -\frac{1}{2}L_p \frac{12EI}{L_b^3} & \frac{1}{4}L_p^2 \frac{12EI}{L_b^3} + k_r + c_{55} & \frac{1}{2}L_p \frac{12EI}{L_b^3} & \frac{1}{4}L_p L_b \frac{12EI}{L_b^3} - k_r \\
 -\frac{12EI}{L_b^3} & -\frac{1}{2}L_p \frac{12EI}{L_b^3} & -\frac{12EI}{L_b^3} & \frac{1}{2}L_p \frac{12EI}{L_b^3} & 2\frac{12EI}{L_b^3} & 0 \\
 \frac{1}{2}L_b \frac{12EI}{L_b^3} & -k_c + \frac{1}{4}L_p L_b \frac{12EI}{L_b^3} & -\frac{1}{2}L_b \frac{12EI}{L_b^3} & -k_r + \frac{1}{4}L_p L_b \frac{12EI}{L_b^3} & 0 & 2k_c + \frac{1}{2}L_b^2 \frac{12EI}{L_b^3}
 \end{bmatrix}
 \begin{bmatrix}
 w_1 \\
 q_1 \\
 w_2 \\
 q_2 \\
 w_3 \\
 q_3
 \end{bmatrix}
 =
 \begin{bmatrix}
 F_{wave} \\
 M_{wave} \\
 F_{wave} \\
 M_{wave} \\
 0 \\
 0
 \end{bmatrix}$$

The hydrodynamic stiffness components (c_{33} and c_{55}) model the floating behaviour of the pontoons. The superstructure is connected to the pontoons through vertical springs and rotational springs. The vertical springs model the elastic behaviour of a superstructure with an elasticity modulus. The spring stiffness is derived from structural mechanics (figure F2). The rotational spring models the connection between the superstructure and the pontoons.

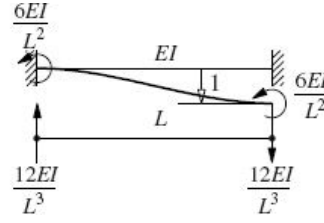


Figure F2: "Vergeet me nietjes" of structural mechanics.

Furthermore, all components of the matrix $\mathbf{H}_{wF} \mathbf{H}_{wF}^*$ of the rigid body model are plotted in figure F3. The relevant eigenfrequencies within the presented range of frequencies are indicated with a dashed red line. Two eigenfrequencies are present at a frequency of 1,1 rad/s. It is noted that because this model exists of 6 DOFs, this system contains an equal number of eigenfrequencies. However, the other eigenfrequencies just fall out of the frequency range that is presented here.

All FRFs show peaks at the resonance frequencies and the translations of the pontoon are the largest in magnitude. Theoretically, these peaks should go to infinity, due to the absence of damping. However, because of the frequency distretization, the exact resonance frequency is not present in the FRF.

Furthermore, some frequency absorption is visible for the rotations of the pontoons. Finally, it can be concluded that the structure is symmetrical, because the first two plots are identical to the third and forth.

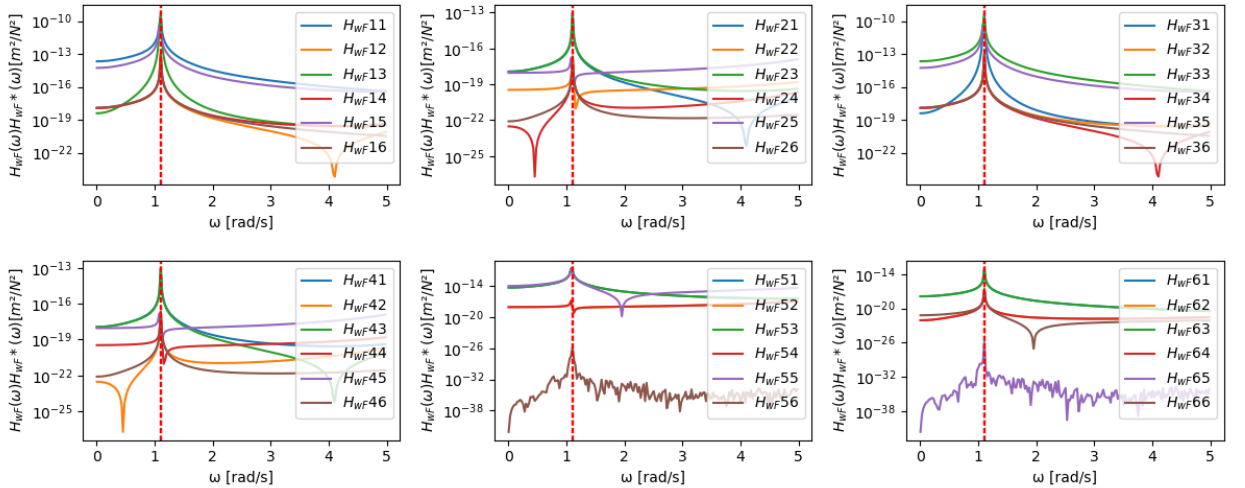


Figure F3: Transfer functions between wave force and reponse.

The added mass varies with the frequency. Every discretized frequency therefore contains different eigenfrequencies. The variation of the first two eigenfrequencies is shown in figure F4. An inversely proportional

relation with the added mass is clearly visible. A reduction in the added mass leads to a growth of the eigenfrequency.

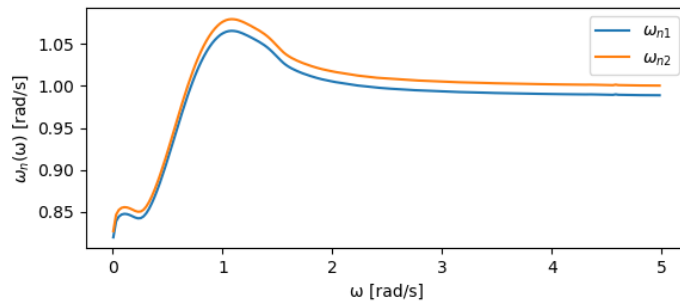


Figure E4: First and second frequency dependent eigenfrequencies of the rigid body model.

Figure E5 shows the response spectra which are computed using $|\mathbf{H}_{\omega F}|^2 \mathbf{S}_{FF}$. The bottom two plots in figure E5 show the same graphs, but are zoomed in to clarify the results. When the blue curve is not visible, it means that the orange curve lies exactly on top of it.

Equation 4.30 is used to find an upper limit of the heave motion of the pontoons subjected to the presented wave spectrum. An upper limit with an exceedance probability of $6,68 \cdot 10^{-2}$ in a period of 100 years is 0,012 m.

Both the translations and rotations of the pontoons show that the response is significantly influenced by the FRF in comparison to the wave transfer function. A clear peak is visible around the second eigenfrequency. Looking at the translations of the superstructure, the response is negligible compared to the translations of the pontoon.

The rotational response spectra are identical for the pontoons and superstructure. Only a peak is visible around the resonance frequency, but its magnitude is considerably smaller than the one of the translation of the pontoon.

The extreme difference between the response of the translation of the pontoons compared to the other DOFs can easily be explained by the difference in the FRF (figure E.3). The peaks of the FRFs corresponding to the translation of the pontoons are in the order of 10^3 higher than the other FRFs. This is the same order of difference between the response spectra.

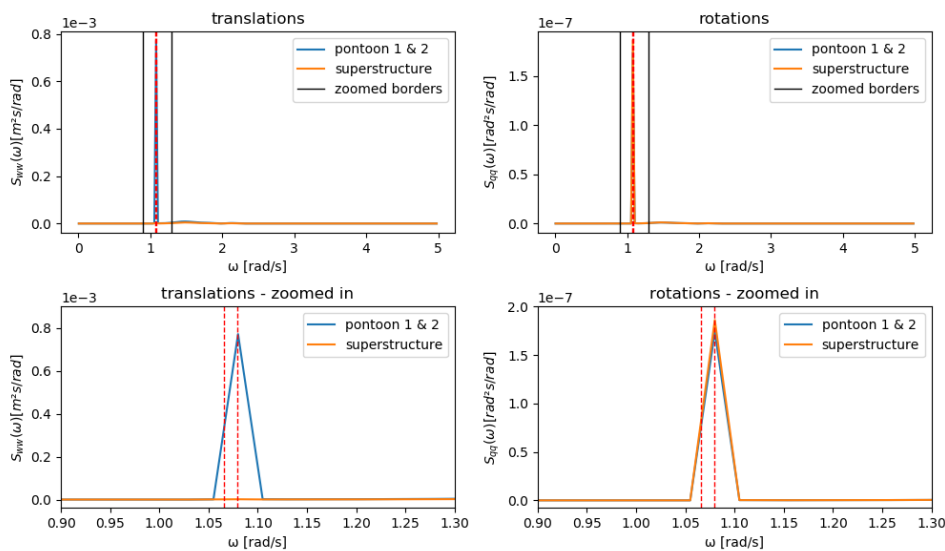


Figure E5: Response spectra of all DOFs of the rigid body model.

To improve the results of this model, a flexible superstructure as well as damping are introduced in the textitTwo pontoon in plane model.

F.2. Two pontoon in plane model

The *Rigid body model* is expanded to the *Two pontoon in plane model*. In this model, the superstructure is replaced with a continuous system consisting of a finite number of Euler-Bernoulli elements. Now the displacements and accelerations of the superstructure can be determined at different locations on the superstructure. Furthermore, surge is included to obtain a full in plane model. To restrain the horizontal motion of the system, horizontal supports are included as well. These are linear springs representing the longitudinal rod at the supports. Furthermore, damping is included in this model. Figure F.6 shows the schematization of the *Two pontoon in plane model*.

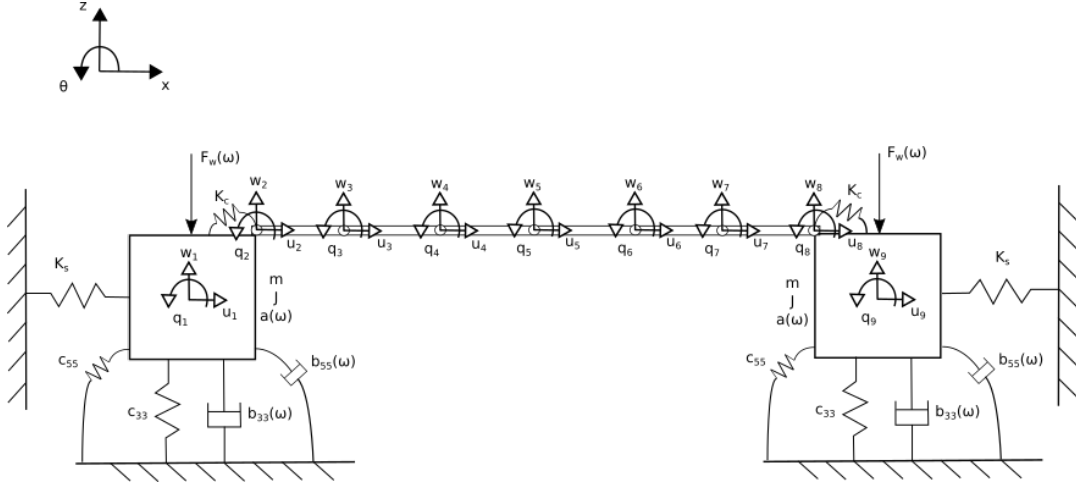


Figure F.6: Schematization of the two pontoon in plane model.

The model shown in figure F.6 contains six Euler-Bernoulli beam elements. This choice is verified in appendix E.5. The mass and stiffness matrices of both systems are computed separately and subsequently they are added in one matrix:

$$\mathbf{M}_{total} = \begin{bmatrix} [M_p + A_p]^{3 \times 3} & & \\ & [M_s]^{3(n_{el}+1) \times 3(n_{el}+1)} & \\ & & [M_p + A_p]^{3 \times 3} \end{bmatrix}^{3(n_{el}+3) \times 3(n_{el}+3)}$$

$$\mathbf{K}_{total} = \begin{bmatrix} [K_p]^{3 \times 3} & & \\ & [K_s]^{3(n_{el}+1) \times 3(n_{el}+1)} & \\ & & [K_p]^{3 \times 3} \end{bmatrix}^{3(n_{el}+3) \times 3(n_{el}+3)}$$

Now mass and stiffness matrices of the system consist of different uncoupled matrices. To couple those matrices into one system, boundary conditions must be composed.

Figure F.6 shows that next to mass and stiffness, also damping is added in this model. The damping matrix will be computed after the system is coupled.

F.2.1. Boundary conditions

The constraints imposed by the connections of the system are represented by specific boundary conditions. In this case the ends of the superstructure are connected to the corner of the pontoon with a rotational spring. The translations of the corner of the pontoon and the end of the superstructure are connected rigidly. Rotations are allowed, but are restrained by the rotational spring. The motion of a specific point on the rotating pontoon can be described using a rotation matrix:

$$\begin{bmatrix} u' \\ w' \end{bmatrix} = \begin{bmatrix} \cos(q) & -\sin(q) \\ \sin(q) & \cos(q) \end{bmatrix} \begin{bmatrix} u \\ w \end{bmatrix}$$

Under the assumption of small angles, this rotation matrix can be simplified. The boundary conditions

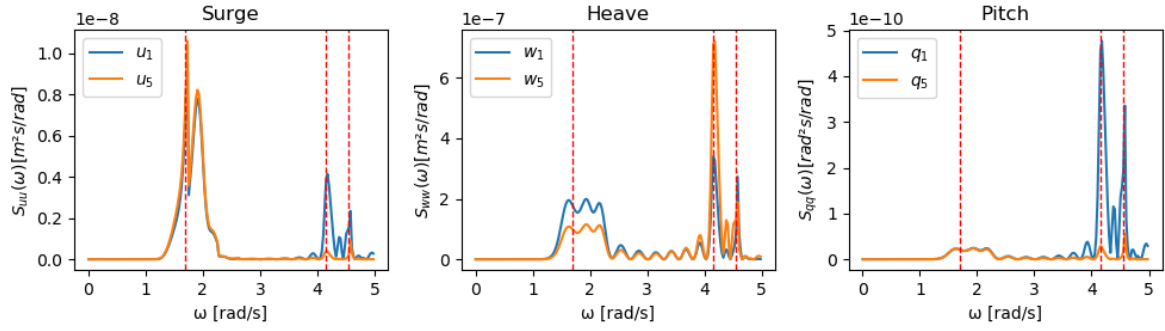


Figure E.7: Reponse spectra of the left pontoon.

Immediately it becomes clear that the response of the pontoon and the superstructure are show a strong correlation due to the coupling. All wave transfer functions (figure 9.4) show no correlation, but still all peaks are located at the same locations. Three different eigenfrequencies are present in the frequency range of interest. At all eigenfrequencies, peaks are present in the response spectra. However, the lowest eigenfrequency only leads to a peak in surge. This eigenfrequency seems to have no effect on heave and pitch. The wide peaks in the lower range of these response spectra are explained by the influence of the wave force spectra (figure 9.7). The corresponding wave force spectra show peaks coinciding with the peaks in the response spectra.

The question remains why the first eigenfrequency only effects surge. This becomes clear looking at the eigenvectors which are plotted in figure E.8. The eigenvectors are found by solving equation 4.12 and represent the modes of the system. The first three eigenvectors are plotted here and represent the relative excitation of all DOFs, which are indicated at the x axis. This is a different notation than the mode shape plots in the main report (figure 9.10) There only the same DOFs are included in the plots. Here the complete eigenvector is used to be able to compare different modes in one figure. The blue line, representing the first mode which corresponds to the first eigenfrequency, shows only excitation at the surge motion. Again, the eigenfrequencies vary over the frequency and must be found iteratively (figure E.8).

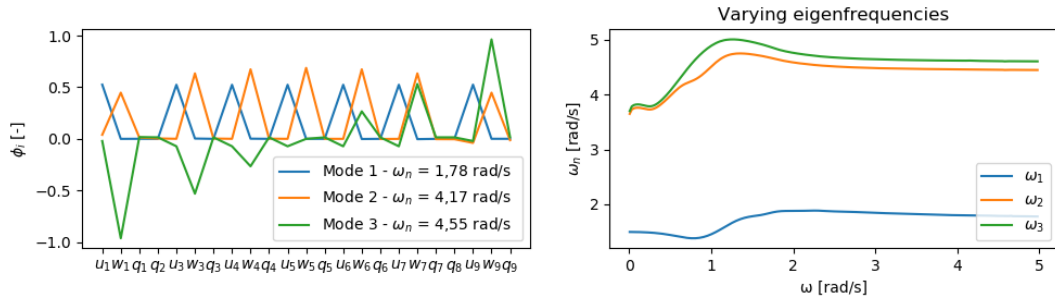


Figure E.8: Eigenvectors and eigenfrequencies of the first three modes.

The second mode is clearly visible in the heave spectrum. Heave of the pontoons (w_{1-9}) shows lower peaks than the middle node of the superstructure (w_5) at the second eigenfrequency which is according to the second mode shape. The influence of the third mode is relatively smaller than the influence of the second mode due to a lower amount of wave energy at the corresponding eigenfrequency.

Comparing heave of the pontoon in this model with the *Two pontoon in plane model*, shows that the peaks in the response spectrum of the *Two pontoon in plane model* (figure E.7) are approximately 10^4 times lower than the *Rigid body model* (figure E.5). The narrow peaks visible in the latter were a sign of resonance although there was a minimum level of wave energy concentrated at those frequencies. However, due to the absence of damping, still resonance peaks were present in the response spectrum.

This is not the case in the *Two pontoon in plane model*, due to the influence of the hydrodynamic and structural damping. More wave energy is present at the peaks of these response spectra, but the magnitude of the peaks is smaller than those of the *Rigid body model*. Therefore the total response is much smaller in the *Two pontoon in plane model*.

Another interesting observation is the difference in eigenfrequencies between the two models. The two

important eigenfrequencies of the *Two pontoon in plane model* are shifted into a higher frequency range. Damping is usually only responsible for small shifts in eigenfrequencies, so this is probably caused by the addition of the plane frame elements to model the superstructure.

To improve the results of this model, the total number of pontoons will be increased. Additionally, abutments will be introduced in the *Seven pontoon in plane model*.

F.3. Seven pontoon in plane model

The *Seven pontoon in plane model* expands the number of pontoons. The number of pontoons can be adjusted, but seven are used to model the Bergsøysund bridge. Figure F.9 shows a schematization of this model to illustrate the number of nodes. In contrast to the *Two pontoon in plane model*, the abutments are now modeled with a horizontal and vertical spring, which are connected to a superstructure node instead of a pontoon.

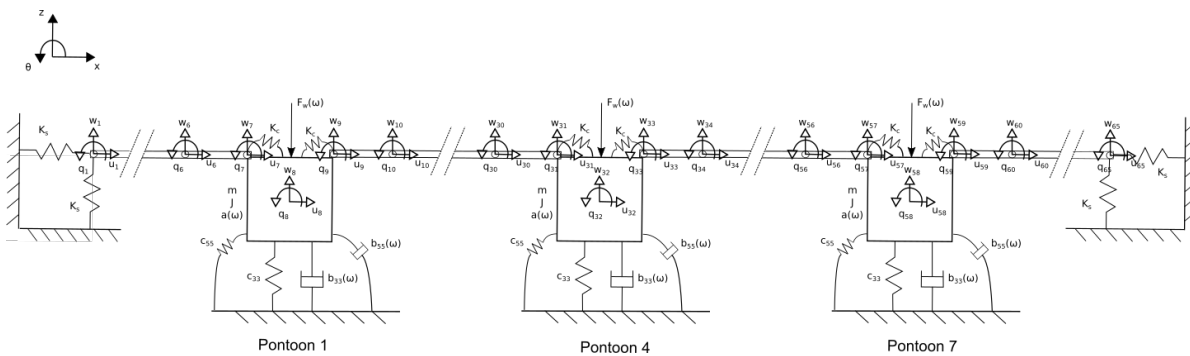


Figure F.9: In plane model with seven pontoons

Similar as with the *Two pontoon in plane model*, the boundary conditions are imposed on the system using the master slave method. Every pontoon adds four extra boundary conditions, because both sides are connected to a part of the superstructure. The mass, damping and stiffness matrices are of size:

$$\begin{aligned}
 [M] & 3((n_p-1)(n_{el}+1)+n_p+2n_{el}) \times 3((n_p-1)(n_{el}+1)+n_p+2n_{el}) \\
 [C] & 3((n_p-1)(n_{el}+1)+n_p+2n_{el}) \times 3((n_p-1)(n_{el}+1)+n_p+2n_{el}) \\
 [K] & 3((n_p-1)(n_{el}+1)+n_p+2n_{el}) \times 3((n_p-1)(n_{el}+1)+n_p+2n_{el})
 \end{aligned}$$

F.3.1. Results

The seven pontoon in plane model can produce 161 response spectra. Only motions of the pontoons and the middle nodes of the superstructure are presented here, because those motions represent the whole system the best. First the results of the pontoons are discussed, followed by the results of the superstructure.

Figure F.10 shows the response spectra of the pontoons in all DOFs. The number of eigenfrequencies present in the frequency range of interest increases significantly compared to the *two pontoon in plane model* and therefore they are now plotted with dotted lines. Eight eigenfrequencies are plotted in this figure. The lowest eigenfrequency is clearly visible, but the remaining seven cluster together and are therefore difficult to distinguish.

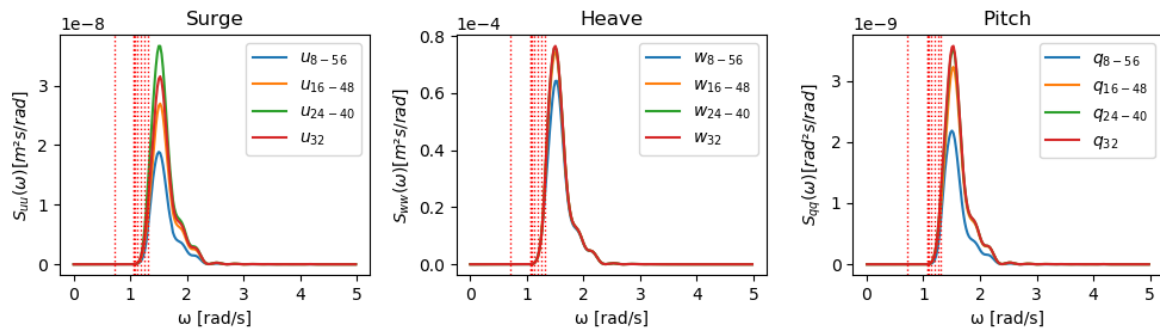


Figure F.10: Reponse spectra of all pontoons.

All response spectra show roughly a similar shape with a wide peak at 1,5 rad/s. All eight eigenfrequencies which are presented here lie up to this 1,3 rad/s. Furthermore, the magnitude the peaks of heave are in order of 10^4 times larger than surge. Pitch remains small as well. The theoretical displacements with a exceedance probability of $6,68 \cdot 10^{-2}$ in a 100 year of all pontoons are summarized in table F.1. As expected, surge is negligible compared to heave.

Node	Surge [m]	Heave [m]	Pitch [rad]
Pontoon 1 & 7	0,00059	0,034	0,00019
Pontoon 2 & 6	0,00071	0,037	0,00025
Pontoon 3 & 5	0,00083	0,037	0,00026
Pontoon 4	0,00077	0,037	0,00026

Table F.1: Displacement of the different DOFs of the pontoons with an exceedance probability of $6,68 \cdot 10^{-2}$ in a 100 year

All response spectra increase at the clustered eigenfrequencies. However, no narrow peaks are present at the eigenfrequencies. This means that those peaks are not only influenced by resonance. The peaks are a result of an approximately equal influence of the FRF and the wave force spectrum. To look into the influence of the FRF, the mode shapes corresponding to the eight eigenfrequencies are plotted in figure F.11. The complete eigenvectors are plotted in this figure. The numbers on the horizontal axis represent the number of the DOF of every node.

Modes two to eight do show that indeed that heave of the pontoons is excited. Especially the middle five pontoons ($x = 40, 60, 80, 100$ and 120) are amplified more than the pontoons at the edges of the bridge ($x = 20$ and 140) in mode eight. The heave response of the latter two pontoons is mainly excited by mode five. However, no wave energy is located at this eigenfrequency. Therefore the peak of these pontoons is lower than the rest.

The mode shapes show that only mode 1 excites surge and that non of these modes excites pitch. No wave energy is concentrated at the first eigenfrequency, so this mode is not present in the response.

The first peak of the surge spectra coincides with the first peak in the wave force spectrum of surge, which explains this peak of the response. No peak is present in the wave force spectrum of pitch. The response spectra of pitch are mainly influenced by heave through motion coupling. Pitch of the first pontoon (q_{8-56}) is mainly caused by heave of the second pontoon (w_{16-48}). This makes sense, because a vertical motion of the second pontoon will apply a moment on the first pontoon through the rotational springs. This moment causes the pitch of this pontoon.

Vice versa is the pitch of the second pontoon (q_{16-48}) influenced by the heave motion of the first pontoon (w_{8-56}). This explains the shapes of these response spectra.

The response spectra of all middle nodes of the superstructure are shown in figure F.12. A comparison is made between these response spectra and the response spectra of the pontoons. Surge stands out at first sight. All middle nodes of the superstructure have exactly the same response spectrum for surge. A wide peak with three narrow parts are present, which coincide exactly with the wave force spectrum of surge.

Heave of the superstructure shows peaks at a similar frequency as the pontoons at the edges (w_{8-56}). The mode shapes (figure F.11) reveal that the middle nodes of the superstructure ($x = 10, 30, 50, 70, 90, 110, 130$ and 150) are amplified significantly less than the middle pontoons. This results in relatively less influence of

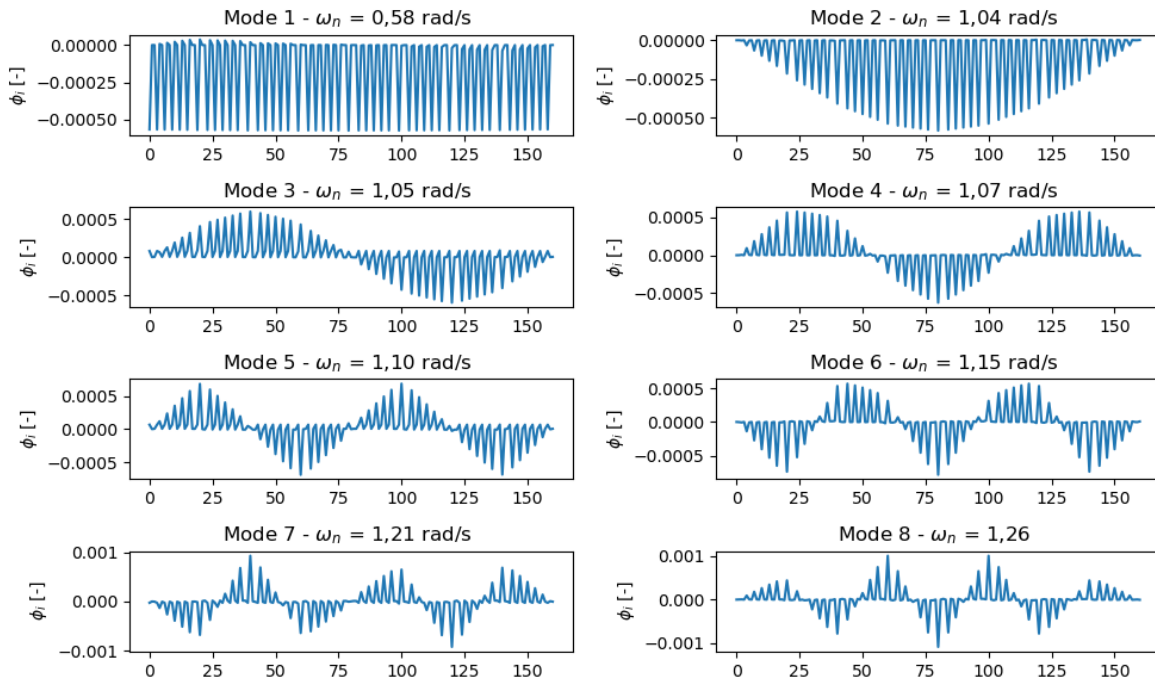


Figure F.11: Mode shapes.

the FRF and more influence of the wave force spectrum. This explains why these peaks are smaller than those of the pontoons.

Pitch of the superstructure is again correlated to the heave of the pontoons, but larger in magnitude. This makes sense, because this motion is influenced by the adjacent pontoons.

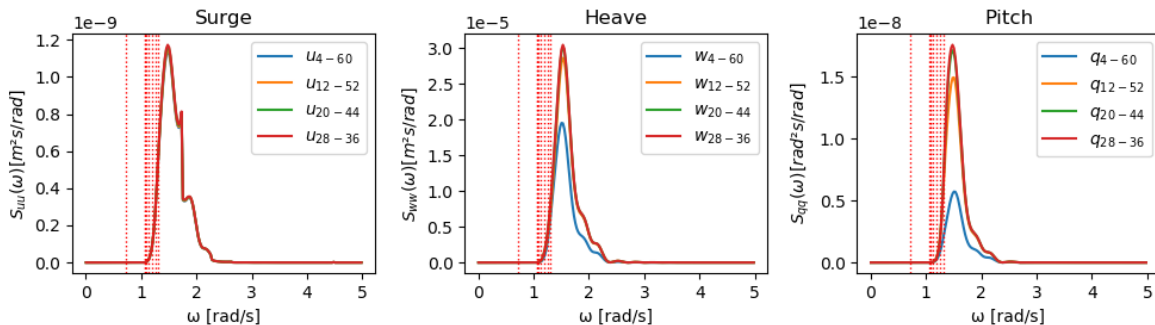


Figure F.12: Reponse spectra of the middle nodes of the superstructure.

F.4. Three dimensions model

Several results of the *Three dimensional model* are presented here. The theoretical accelerations with an exceedance probability of $6,68 \cdot 10^{-2}$ in a 100 year of the sway, surge and roll of all pontoons are summarized in table E.2.

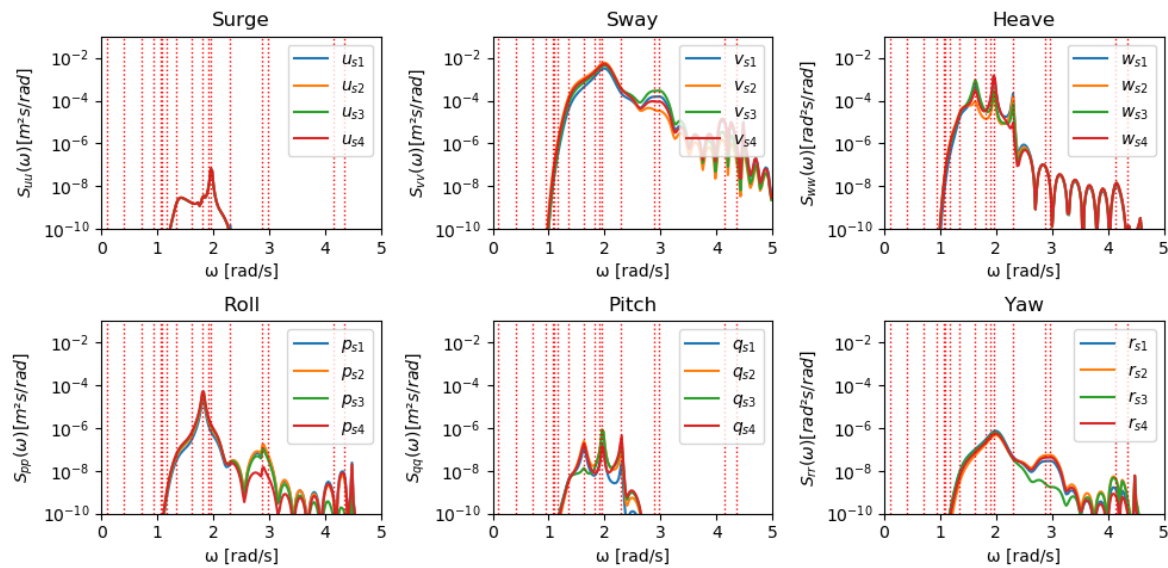
F.4.1. Superstructure response

The response spectra of all DOFs of all middle nodes of the superstructure of the *three-dimensional model* are presented in figure F.13. Again 17 eigenfrequencies are included in these plots. The theoretical displacements with a exceedance probability of $6,68 \cdot 10^{-2}$ in a 100 year of the sway, surge and roll of all middle nodes of the pontoons are summarized in table E.3. The responses of the middle nodes of the superstructure are smaller than the responses of the pontoons. This makes sense, because the pontoons are excited by wave forces and

Pontoon	Sway [m/s^2]	$\frac{Sway}{Threshold}$	Heave [m/s^2]	$\frac{Heave}{Threshold}$	Roll [rad/s^2]	$\frac{Roll}{Threshold}$
1 & 7	0,59	1,17	0,13	0,19	0,015	0,14
2 & 6	0,27	0,55	0,15	0,22	0,017	0,16
3 & 5	0,55	1,10	0,13	0,18	0,019	0,17
4	0,32	0,63	0,12	0,17	0,019	0,18

Table F2: Accelerations of sway, heave and roll of the pontoons with an exceedance probability of $6,68E^{-2}$ in a 100 year.

the nodes of the superstructure only experience excitation through the motion coupling with the pontoons. The shapes of the superstructure's response spectra are in general very similar to those of the pontoons. One difference is that deviations between the response spectra of the different nodes is smaller. For every DOF the response spectra are very similar. It is assumed that the same explanation is valid for the superstructure's response spectra as for the pontoon's response spectra, because of the similarities in shape.

Figure F.13: Reponse spectra of the middle nodes of the superstructure of the *Three dimensional model*.

Between pontoons	Sway [m]	$\frac{Sway}{Threshold}$	Heave [m]	$\frac{Heave}{Threshold}$	Roll [rad]	$\frac{Roll}{Threshold}$
abutment - 1 & 7 - abutment	0,12	0,38	0,13	0,11	0,0048	0,11
1-2 & 6-7	0,16	0,51	0,02	0,06	0,0060	0,14
2-3 & 5-6	0,14	0,45	0,04	0,13	0,0069	0,16
3-4 & 4-5	0,15	0,48	0,04	0,13	0,0073	0,17

Table E3: Displacement of sway, heave and roll of the middle nodes of superstructure with an exceedance probability of $6,68 \cdot 10^{-2}$ in a 100 year

E.5. Mesh sensitivity analysis

A mesh sensitivity analysis is performed to determine the minimum required number of beam elements. The superstructure between two pontoons consists of a finite number of discretized elements. This is called a mesh. Increasing the mesh means that the number of elements is increased. The choice of a mesh is usually a trade-off between accuracy and computation time. A fine mesh improves the accuracy, but also increases the amount of time which is used to complete the simulation.

A mesh sensitivity analysis is performed to find the minimum number of elements required to find accurate results. The *two pontoon in plane model* is used to perform the mesh sensitivity analysis, because this is the most simple model including a FE superstructure (appendix F.2). The number of elements is in-

creased and the difference in response between the simulations is compared. The eigenfrequencies of the system are used as a quantitative measure to analyze the effect of the number of elements. The first three eigenfrequencies are taken into account, because those lie in the frequency range of interest (figure E8).

Δ between number of elements	$\Delta \omega_1$ [%]	$\Delta \omega_2$ [%]	$\Delta \omega_3$ [%]
Δ 2-3	0,0000560	0,00124	0,000107
Δ 3-4	0,000020	0,00021	0,000022
Δ 4-5	0,000009	0,00006	0,000006
Δ 5-6	0,000005	0,00002	0,000002

Table E4: Results of the mesh sensitivity analysis.

The mesh sensitivity analysis shows that the effect of using two and three elements on the first three eigenfrequencies is already negligible. All differences remain smaller than 0,01 %, which is very accurate. However, based on the following arguments still six elements are used:

- The simulation time using six elements is still only 2 minutes, which is assumed to be acceptable.
- Using six elements provides more detailed mode shapes of the whole floating bridge. This can be used to explain results better.
- This sensitivity analysis is performed with the input parameters of the Bergsøysund bridge. Using other parameters might change the results of this analysis. Hence, choosing a conservative number of elements is sensible.

G

FRP alternative

This appendix elaborates upon the design of the FRP alternative and the assessment methods which are explained in chapter 12. Section G.1 addresses the preliminary design and the different loads which are used in the SLS and ULS assessments. Section G.2 presents the results from the simulations of the floating bridge model. Finally, section G.3 contains additional information about the ULS assessment.

G.1. Preliminary design

The superstructure of the FRP alternative is a truss structure. Figure G.1 shows the type of truss structure. The diagonals are loaded in tension and the verticals are loaded in compression. The angle between a vertical and a diagonal is always 45° . A preliminary design of the superstructure is made based on basic design rules. The following requirements and design principles are used to come up with a preliminary design:

- The length over height ratio of the global dimensions should lie between 6 and 16.
- The bridge must provide room for two lanes of 5 m. The total width is assumed to be 11 m.
- Only vertical loads are taken into account without load factors or eccentricity.
- Only normal forces are assumed to be present in the members. The normal force in the top and bottom chord is found by dividing the moment over the height of the truss.
- Stiffness (SLS) and strength (ULS) are assessed to find the dimensions of the preliminary design. The stiffness criteria prescribes that the total deformation must be smaller than $\frac{L}{350}$. The strength criteria checks whether the maximum tension stress remains below 223 N/mm^2 . In this preliminary design a unity check of 0,7 is presumed.

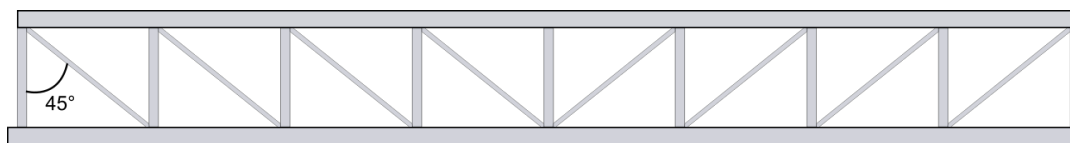


Figure G.1: Layout of the truss bridge used in the parameter study.

Only the dead weight of the structure and traffic loads are taken into account in these SLS and ULS assessments. The following values are assumed for these loads:

For the preliminary design, the truss is assumed to be simply supported. The governing moment is now calculated with:

$$M = \frac{1}{8} qL^2 \quad (\text{G.1})$$

Load type	Specified load	Value	Unit
Dead weight	Truss	19	kN/m3
	Deck	2	kN/m2
	Pavement	2,3	kN/m2
	barriers	2	kN/m
Traffic loads	Concentrated	600	kN
	Distributed	21,2	kN/m

Table G.1: Values of loads which are taken into account in the preliminary design. Provided by Royal HaskoningDHV.

All loads are taken into account to compute the governing moment. When the deformation is calculated, only the traffic loads are taken into account. The potential deformation of the permanent loads can already be compensated for with an initial upward curvature in the design. The deformation is determined with:

$$w = \beta_w \frac{5}{384} \frac{qL^4}{EI} \quad (\text{G.2})$$

where:

$$\beta_w = \text{Reduction factor for deformation check} \quad [-]$$

The final dimensions of the cross section of the superstructure are presented in chapter 12.

G.1.1. Other loads

Besides the dead weight and the traffic loads, other loads are taken into account to assess the preliminary design. An overview of the loads is given in table 12.1. The current and wind loads are found using:

$$F = \frac{1}{2} \rho C A v^2 \quad (\text{G.3})$$

In the case of the wind load, the constant C is assigned with a value of 0,8. For the current load a value of 0,76 is used. The velocity v is assumed to be 10 m/s for the wind load and 1 m/s for the current load. The density of air and water are assumed to be 1,28 and 1025 kg/m^3 respectively. and All these values are based on a feasibility study of a floating bridge in the Sognefjord (Jakobsen, 2013).

G.2. Simulation results of FRP alternative and the Bergsøsund bridge

When the preliminary design of the superstructure is found, more detailed SLS and ULS assessments are performed on the complete floating bridge. Wave, wind and current loads are included in this assessment. The developed model is used to model the wave loads here. In this assessment the governing deflection and moments are required. To obtain these, relative response spectra are computed. The two pontoons with the maximum relative displacements are used in this assessment. The relative response spectrum includes the random phase angle of the wave elevation. This means that every simulation results in different outcomes. To be able to obtain a representative value from several simulations in a dynamic calculation a statistical analysis can be used according to Bureau Veritas (2015). The following statistical approach is used to find representative values:

$$w = \mu + a\sigma \quad (\text{G.4})$$

where:

$$\begin{aligned} \mu &= \text{Mean value} && [-] \\ a &= \text{Multiplication factor of the standard deviation used in dynamic analysis} && [-] \\ \sigma &= \text{Standard deviation} && [-] \end{aligned}$$

The value of a depends on the type and the number of simulations. In a dynamic analysis with 10 runs, a value of 0,3 is assigned to a . The results of the SLS and ULS simulations for both the FRP alternative and the ULS alternative are shown in the tables below.

Simulation	ΔV [m]	$\Delta\psi$ [rad]	ΔW [m]	$\Delta\theta$ [rad]
1	2,19	0,022	1,33	0,0081
2	2,07	0,023	1,47	0,0086
3	2,07	0,022	1,47	0,0084
4	2,25	0,022	1,26	0,0082
5	2,13	0,024	1,34	0,0093
6	2,01	0,023	1,36	0,0087
7	2,19	0,022	1,35	0,0079
8	2,13	0,022	1,26	0,0094
9	1,98	0,023	1,50	0,0078
10	2,22	0,022	1,30	0,0093
St. dev.	0,09	0,0007	0,08	0,0006
Average	2,12	0,0224	1,36	0,0086
Total	2,15	0,0226	1,39	0,0088

Table G.2: Simulation results of the dynamic response of the FRP alternative in ULS conditions.

Simulation	ΔV [m]	$\Delta\psi$ [rad]	ΔW [m]	$\Delta\theta$ [rad]
1	1,39	0,0087	0,85	0,0061
2	1,52	0,0084	0,78	0,0059
3	1,51	0,0091	0,80	0,0062
4	1,46	0,0088	0,78	0,0055
5	1,53	0,0085	0,84	0,0059
6	1,44	0,0088	0,87	0,0058
7	1,51	0,0086	0,95	0,0057
8	1,51	0,0081	0,87	0,0055
9	1,52	0,0081	0,83	0,0060
10	1,47	0,0088	0,86	0,0066
St. dev.	0,04	0,0003	0,05	0,0003
Average	1,49	0,0086	0,84	0,0059
Total	1,50	0,0087	0,86	0,0060

Table G.3: Simulation results of the dynamic response of the Bergsøsund bridge in ULS conditions.

Simulation	ΔV [m]
1	0,41
2	0,41
3	0,38
4	0,43
5	0,39
6	0,41
7	0,39
8	0,38
9	0,41
10	0,39
St. dev.	0,02
Average	0,40
Total	0,40

Table G.4: Simulation results of the dynamic response of the FRP alternative in SLS conditions.

Simulation	ΔV [m]
1	0,28
2	0,27
3	0,27
4	0,27
5	0,26
6	0,25
7	0,28
8	0,28
9	0,26
10	0,26
St. dev.	0,01
Average	0,27
Total	0,27

Table G.5: Simulation results of the dynamic response of the Bergsøysund bridge in SLS conditions.

G.3. ULS assessment

A distinction is made in the ULS assessment between the horizontal direction and the vertical direction. The two main differences are the loads and the schematization of the floating bridge. In horizontal direction the floating bridge is schematized as a simply supported beam with only two supports at the abutments. In vertical direction the pontoons are schematized as seven intermediate supports. Only the part of the floating bridge where the moments are the largest is taken into account in this direction.

In the ULS assessment, the maximum stresses which occur in the members are calculated. To be able to find the maximum stresses, the maximum moment is first determined. In chapter 12 the moment lines under influence of the dynamic wave loads are presented. From the model simulation it appears that the relative displacements between pontoon 1 and 2 are governing. Therefore this part of the structure is evaluated to find the maximum moment in vertical direction. For the envelope moment line, this moment line should be added to the moments which are caused by the dead weight and the traffic loads.

The distributed traffic load is schematized in figure G.2. The superstructure is supported by rotational springs. This means that the moment line will be a combination of the moment line in a clamped-clamped situation and a simply supported situation. Because the rotational springs are assumed to be relatively stiff, the clamped-clamped situation will give a better representation of the actual moment line. Furthermore, in this case this will be a conservative approach, because the envelope moment line contains the largest moments at the supports. This is indicated in figure G.3. The red dot represents the maximum moment in this figure.

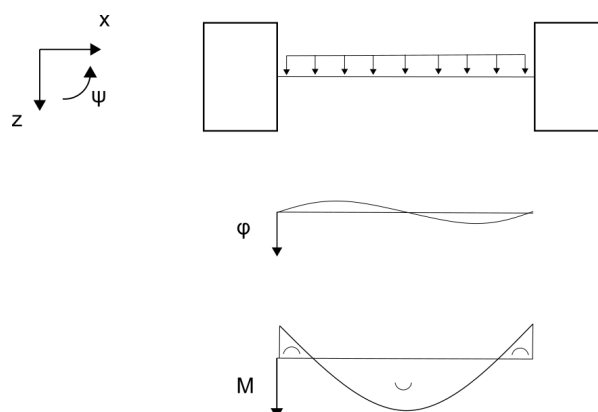


Figure G.2: Moment lines caused by traffic loads.

To find the moments caused by the current and wind loads, the whole floating bridge is evaluated. Figure G.4 shows the moment line under the influence of the current loads. Because the section between pontoon

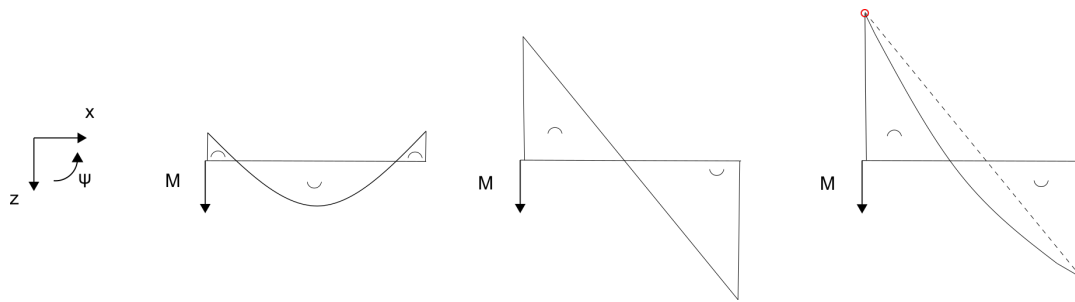


Figure G.3: Envelope moment line in vertical direction.

1 and 2 proved to be governing, these moments are used in the ULS assessment. A similar approach is used to find the moments caused by the wind load. The concentrated loads are replaced with a distributed load in this case.

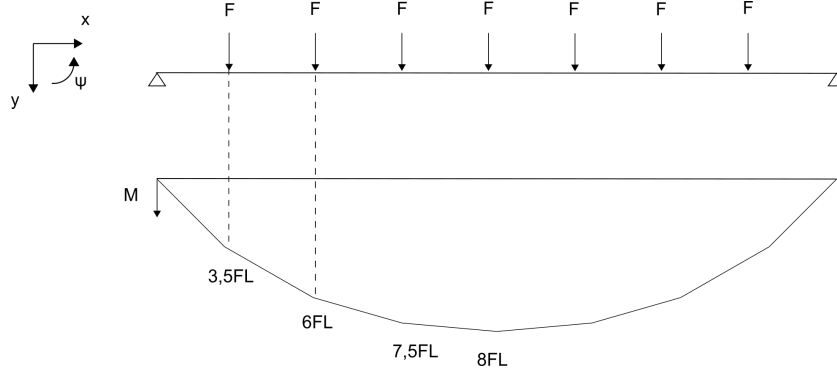


Figure G.4: Moment lines caused by current loads.